Fatigue performance of over-stressed beadweld due to pulling on the bead

Master of Science Thesis

Malwina Anna Witczak

Techische Universiteit Delft

This thesis is confidential and cannot be made public until 28/03/2024.

Fatigue performance of over-stressed beadweld due to pulling on the bead

By

Malwina Anna Witczak

To obtain a degree of
Master of Science
in Materials Science and Engineering

at the Delft University of Technology,
to be defended publicly on March 28th, 2019 at 11 AM.

Student number: 4633660
Email: malwina.aik@gmail.com
Project duration: March 2018- March 2019

Thesis committee: Dr. Vera Popovich   TU Delft: section Material Science & Engineering, supervisor

Prof. Dr Ian Richardson   TU Delft, graduation committee chair
Dr. Miguel Bessa   TU Delft, committee member
Ir. Patrick Rijneveld   Allseas Engineering BV, supervisor

This thesis is confidential and cannot be made public until 28/03/2024.

Acknowledgements

Abstract

The pipeline production rate and the pipeline's superior mechanical properties are the crucial parameters for the offshore pipe laying company. Pulling on the bead, i.e. the action of moving the pipe on the firing line to the subsequent weld stall as the vessel moves forwards allows a fast and reliable pipe welding process. During this movement, the ends of the pipes are intermittently not supported and the bending moment in the weld is created as a consequence. Such operation imposes tensile loads in the welds, that are especially high for the 3 mm thick beadweld and the subsequent 3 mm thick hot pass (6mm thick in total). An important question arises whether imposing loads above the beadweld material yield capacity affects the overall fatigue performance of the girth weld. It is in the best interest of the offshore industry to assure that the pipeline welds properties during their 20-30 years operation lifetime are not adversely affected during its installation. This study investigates the effect of pulling on the bead on the weld's fatigue behaviour.

The overstressing simulation of the test coupons, Finite Element Analysis (FEA) of the loaded beadweld and the small-scale specimens comparative fatigue study were conducted to investigate the effect of straining history on the full girth weld fatigue performance. Additionally, the holistic approach was implemented to investigate the consolidated effects of other factors: local weld root misalignment (Hi-Lo), weld porosity and microstructure quality. Four test coupons were welded together and overstressed to simulate the pulling on the bead action. To assess the stress-strain state in the beadweld and hot pass during the overstressing simulation the FEA analysis was done. The FEA results allowed to quantitatively determine the exact locations of the elastically and plastically strained beadweld material. Full welds were checked against the porosity and subsequently, 46 fatigue specimens were fabricated and tested in the 4-point-bending fatigue loading setup. Additionally, the fatigue crack observation techniques were implemented in order to separate fatigue crack initiation and growth phases out of the total fatigue life. The optical observations (with the optical-digital microscope) and the Potential Drop techniques were used. Tensile and hardness tests were done to compare the strength properties of specimens with different straining and porosity histories. Finally, the microstructure and fracture surfaces of the fatigue broken specimens were studied.

The research done in this study gives a good overview of the fatigue behaviour of the girth welds and provides insights into the straining history effects. Plastic straining was found not to affect the fatigue performance more than currently acceptable elastic straining does. Moreover, plasticity was found to reduce the negative effect of porosity. Additionally, the prevalent influence of Hi-Lo on the crack initiation phase was confirmed, making it the driving negative factor for the fatigue resistance.

Contents

1. Theoretical background

This chapter provides the problem statement and literature review required to fully answer the research question.

1.1. S-lay pipeline installation

Due to the growing oil and gas market, followed by an increasing number of pipelaying projects and contractors, many pipelaying methods have been developed. S-lay, a pipeline installation method used by Allseas, proved to be fast and versatile thanks to ingenious horizontal pipeline assembly.

With time being the crucial factor for the pipelaying company, Allseas put a lot of effort to optimize the S-lay pipelaying. The method (see Figure 1.1), currently used on all their pipelaying vessels, is based on the horizontal firing line and a supporting element called a "stinger", whose length and curvature is adjusted to water depth in which the pipeline is installed (Allseas, Introduction to Pipelaying, 2004).
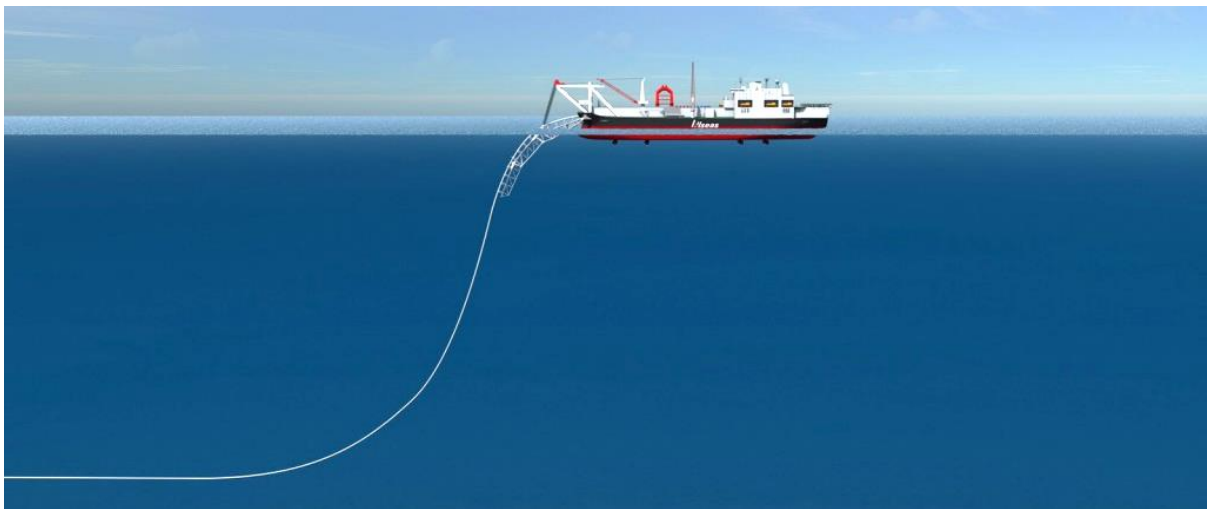
Figure 1.1 Schematic of pipeline installation using the S-lay technique (Allseas, Pipeline Installation, 2019)

The pipeline is assembled horizontally on the firing line inside of a vessel, by welding of 12,2 m pipe segments. After a segment is being welded to the main pipeline the vessel moves 12,2 m forward, pulling on the pipe that is laying on the welding nest (firing line). The efficiency of this process is measured in kilometres of a pipeline laid per day. Thus how quickly a pipeline can leave a stinger is governed by the speed of the welding process and pipeline pulling.

1.2. Pulling on the bead

For the highest pipelaying operation efficiency it is desired to start pulling on the pipeline as early during the welding process as possible. The horizontal firing (assembly) line comprises of several welding stations, followed by the coating and NDT stations. When a new pipe segment enters the firing line it is directed on the first welding station, known as the beadstall. There the segment is aligned with the main pipeline using the Internal In Line Clamp (ILUC) and the first weld pass, defined as the "beadweld", is performed. Once the beadweld is finished the vessel moves forward and consequently, the pipeline is moved in the longitudinal direction. This action is described as a "pull". During the pull, the above-mentioned segment moves from the beadstall to the next station where the next weld pass, defined as the "hot pass", is being performed. As the pipe end leaves the beadstall the next pipe segment is lowered down, aligned with the main pipeline and joined. The pipe is subsequently pulled in steps (single pulls, see Figure 1.2) until it reaches the last station and is released on the stinger. In such a way, as the vessel moves forward, it "pays out" the pipeline.
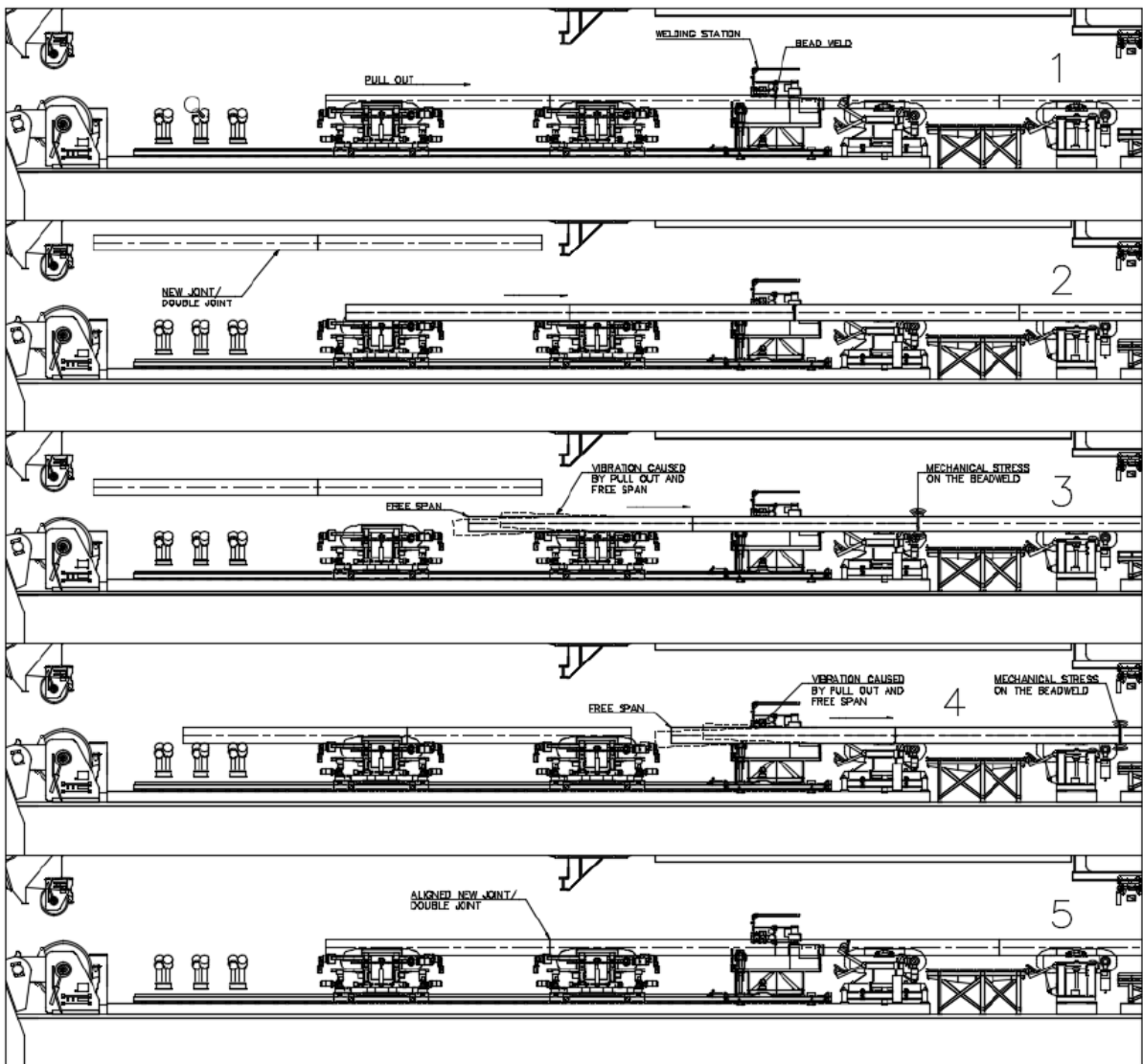
Figure 1.2 The schematic pull steps (1-5) during "pulling on the bead" operation (Karman, 2017)

The pipeline is supported by weld stalls and rollers as it travels towards the stinger. However, as the pipe end leaves the station it becomes unsuspended and subjected to loads due to its own weight and length. Hence, "pulling on the bead" load is caused mainly by the bending moment due to the pipe weight. The highest peak stresses caused by pulling on the bead are present in the thinnest (3 mm), first weld pass, i.e. the beadweld. Beadweld is defined as the single pass of filler material deposition

The magnitude of stresses present in the beadweld during pipeline installation arise from the combination of several parameters:

- Pipe material, diameter, wall thickness, weight and length
- The temperature of the beadweld and the environment
- Support and bead stall coordinates in the firing line
- Beadweld thickness and geometry

Even though the pipeline pulling is timewise crucial for the installation efficiency, safety and mechanical integrity cannot be compromised. According to Allseas operation standards, the level of stresses in a beadweld resulting from pulling "shall be lower than allowable to allow for pulling on the bead" (Allseas, Introduction to Pipelaying, 2004). If pipeline analysis prior to installation indicates that pulling subjects the beadweld to higher than allowable stresses, then pulling on the bead is forbidden and the pipeline is being pulled after the hot pass weld is finished- resulting in "pulling on the hot pass" action.

Stresses imposed on the beadweld shall not exceed the characteristic material yield strength that is given by the DNVGL Submarine Pipeline Systems standard (DNVGL-ST-F101, 2017):

$$f_y = \left(SMYS - f_{y,temp}\right) * \alpha_U \tag{1.1}$$

Where:

SMYS- specified minimum yield stress

$f_{y,temp}$ – de-rating value of the temperature of the yield strength

α_U- material strength factor

The values of α_U and $f_{y,temp}$ should be chosen according to DNV guidance so that they represent the material and the environment.

The above statement is the standard conservative approach currently used in operations. However, questions have been raised about the beadweld performance in case occasional "overstressing" occurs during pulling on the bead. It is assumed that beadweld is "overstressed" when it is subjected to stresses higher than allowable stated by Equation 1.1. Currently, it is assumed that such overstressing is not detrimental to the mechanical performance of the pipeline, especially in terms of beadweld performance (Karman, 2017). In this study, the beadwelds will be intentionally overstressed to simulate the over critical pulling on the bead. The overstressing operation, i.e. loading of the test coupons with stresses above their yield capacity, will be designed and conducted to create beadweld material for further fatigue testing.

1.3. Research goal

The aim of this research is to determine whether single loads above the yield capacity of the beadweld have negative effects on beadweld mechanical properties, especially in terms of fatigue performance and tensile strength. To investigate this problem, the extensive comparative fatigue study has been planned, modelled and executed. Previous theoretical "pulling on the bead" report (Karman, 2017) has been taken as a starting point for this study. Four test coupons (pieces of pipes with complete girth welds) have been fabricated to simulate pulling on the bead and pulling on the hot pass operations. Then small- scale specimens have been cut from the coupons, mechanically tested and their results compared and analysed.

Additionally, the effect of weld misalignment (Hi-Lo) and the porosity on the overall fatigue performance will be investigated. The mutual relationship between the investigated factors: straining, Hi-Lo and porosity will also be studied to provide the holistic overview of the girth weld performance in pipeline installation-like environment.

It is important to note that the analysis and modelling in this thesis are limited only to a comparative study on small- scale specimens and cannot be directly related to full- scale structures.

1.4. Pipe material and properties

The pipe used for this research is a high- strength low-alloy steel grade API -5L- X60, which is a material widely used in the oil and gas industry for conveying petroleum products. API 5L X60 (API, 2018) is a member of Product Specification Level (PSL) 1-grade family, with specific notch toughness, yield strength and tensile strength. The strength specification provided by API is stated in Table 1.1. The chemical composition requirements for API 5L X60 grade are listed in Table 1.2.

It should be noted that metals suited to requirements of the petroleum industry are generally referred to as High Strength Low- Alloy (HSLA) steels. HSLA provide a desirable combination of strength, weldability, toughness and corrosion resistance.

Table 1.1 Tensile requirements for grade X60

Yield Strength, minimum		Ultimate Tensile Strength, minimum	
MPa	ksi	MPa	ksi
414	60	517	75

Table 1.2 Chemical composition requirements of API 5L X60 steel (by percentage of weight)

C, max	Mn, max	P	S, max	Ti, max	other
0,28	1,4	0,045- 0,03	0,03	0,04	adjusted by manufacturer

The desired combination of favourable mechanical and manufacturing properties of the X60 steel is obtained by thermomechanical processing. The goal of those processes is to create a

distinct, banding type microstructure of fine grains. Banding refers to microstructure that consists of alternating bands of different microstructures. In the case of X60 grade presence of ferrite/pearlite banding is observed (Godefroid L. B., 2014). This fine grain, regular microstructure, together with low carbon equivalent, is desirable for good weldability of the X60 grade pipeline.

The pipe pieces used for the experimental part of this thesis are the remaining material from one of Allseas' commercial projects. The pipe was manufactured by UOE (Uing and Oing) forming, hence it has a so-called "long seam" weld in the longitudinal direction. The properties of the pipeline are shown in Table 1.3

Table 1.3 The commercial pipeline properties

Outside diameter OD	609,6 mm (24 inches)
Inside diameter ID	577,8 mm
Wall thickness WT	15,9 mm
Steel density	7850 kg/m^3

Beadweld strength

The yield strength of the beadweld was determined with modified Equation 1.1 so that the weld material strength overmatch *OM* is taken into account:

$$f_y = SMYS * OM - f_{y,temp} * \alpha_U \tag{1.2}$$

Values of $f_{y,temp}$ and α_U were determined according to DNV-OS-F101 as 30 MPa and 0,96, respecively. Weld strength overmatching is simply the ratio of weld metal to base metal yield strength:

$$OM = \frac{Re \ weld}{Re \ base \ metal}$$

Two approaches- theoretical and experimental- can be used to determine the characteristic beadweld yield strength. Theoretical approach calculations are based on the standard values for given types of material, whereas experimental approach calculations are based on material manufacturers' certificates. The differences in values are clearly visible in Table 1.4.

Table 1.4 Comparison of theoretical and experimental calculations of beadweld yield strength

property	theoretical	experimental (average)
SMYS (or R_e)	413 MPa	475 MPa
R_e of weld metal	483 MPa	508 MPa
OM	1,17	1,07
f_y	435 MPa	459 MPa

It can be deducted from Table 1.1 that the exact magnitude of the beadweld yield strength can be only approximated and that it is higher than minimum values indicated in the standard.

1.5. Phoenix welding method

For all their commercial projects Allseas uses an in-house developed automated welded system called Phoenix. The automation was introduced to meet increasing industry requirements for fast, repeatable superior quality welding. Phoenix welding system consists of an automated welding bug that is operated by an experienced welder. The bug, with one, two or three torches, travels along the rail attached to the outer diameter of the pipe. Each weld pass requires two welding tools that operate simultaneously and are controlled by two separate welders.

The commercial pipeline, as well as pipe pieces used for this research, were gas metal arc (GMAW) welded using Phoenix single torch method. The pipe pieces were welded in a horizontal position (5G) with the same welding parameters as used during the original commercial project. The welding record sample, including detailed welding parameters, can be found in APPENDIX B.

Welding procedure starts with pipe ends preparation. Both pipe pieces have to be machined so that their ends are identically bevelled. Automatic welding, such as Phoenix, requires precise J- bevel preparation, see Figure 1.3:
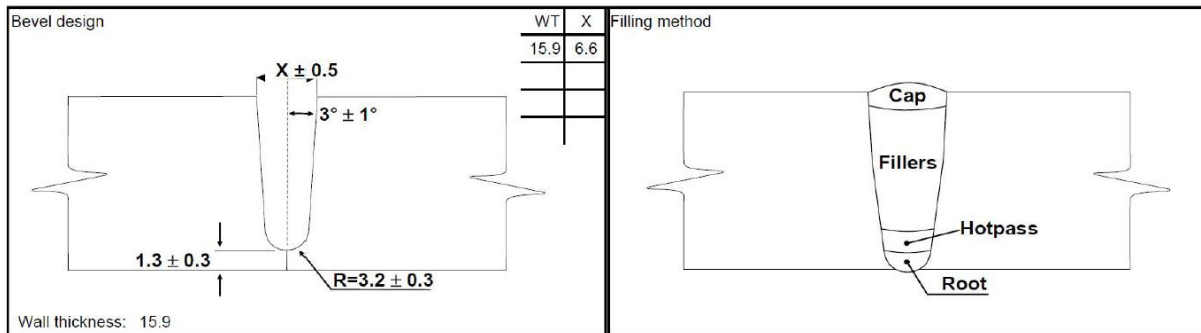
Figure 1.3 Pipeline bevel design and filling method (see APPENDIX B)

The bevel shape and size are especially important for the beadweld geometry and, consequently, its stress distribution. Based on Figure 1.3, in this study, the beadweld thickness was assumed to be 3 mm. Both bevelling and subsequent pipe pieces alignment has to be done precisely as they influence further beadweld geometry. Especially the pipe pieces alignment on the bead stall has a significant role. Once the pipe is J-bevelled and placed on the pipe nest, the second pipe is aligned with it using ILUC. For the better control of the beadweld geometry, especially to reduce the Hi-Lo (a high-low weld misalignment defect) along the girth, both pipe pieces should be placed with their long seams aligned on 12 o'clock position. However, in normal welding operations aligning of the weld seams is considered a bad engineering practice and in offshore production seam welds are alternating with 10 and 2 o'clock positions.

1.6. Properties of girth welds

The chemical composition of steel grade, welding position and especially the parameters of mechanised GMAW welding process play a crucial role for microstructure evolution of pipeline girth welds. Welded joints exhibit distinct microstructural regions, whose mechanical properties vary greatly. In the heart of a joint, a region associated with melting (the fusion

zone) is located. Outside of this central phase, other zones can be distinguished, of material that was not melted but severely affected by temperature effects: the heat affected zone (HAZ). More detailed investigations revealed that both fusion zone and HAZ can be further subdivided, see Figure 1.4.
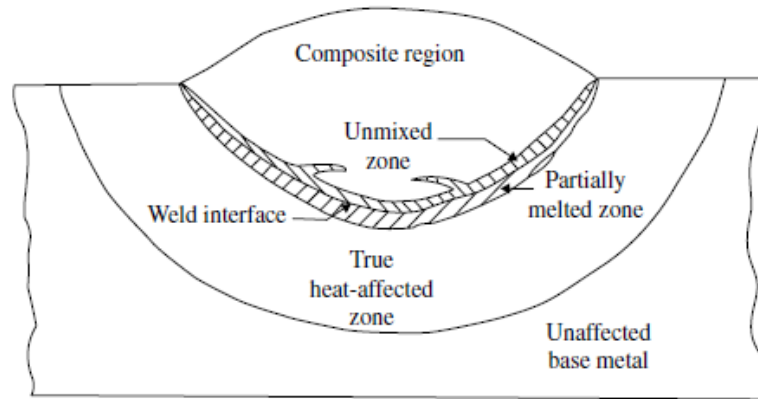
Figure 1.4 The schematic of all distinguishable zones in a typical weld (Lippold, 2015)

The properties (and microstructure) of HAZ are extremely sensitive to temperature changes during the welding process. In steel, material within the HAZ region can undergo phase transformation which results in mechanical properties extremely different from surrounding base material and fusion zone. Because of these reasons, as well as the fact that HAZ can spread relatively wide from the fusion zone, it plays the most important role in the overall weld properties.

In multipass steel welds, the prediction of mechanical properties becomes especially challenging as the evolution of microstructure in HAZ is very complicated (Lippold, 2015). Even within the same weld, different locations can experience different temperature cycles during the welding process. There are one or more metallurgical phenomena that can occur in steel HAZ during multipass welding, that mostly depend on peak temperatures experienced by the material. Those are, namely:

- Recrystallization
- Grain growth
- Phase transformations
- Dissolution/over ageing of precipitates
- Precipitate formation
- Residual stress and stress relaxation

Equilibrium phase diagrams, continuous cooling transformation (CCT) diagrams together with detailed thermal history can provide guidance on what kind of reactions within HAZ can be expected. However, one has to keep in mind that such diagrams are developed for continuous (slow rate) cooling transformations. Due to extremely rapid thermal changes associated with multipass welding, thermal simulations (using, for example, Gleeble or Smitweld simulators) are recommended. Also, post- mortem optical and scanning electron microscopy of a specific HAZ location within a specimen of interest can provide accurate information of microstructural features and chemical composition.

15

As mentioned, the microstructure of HAZ in steel can be predicted, to some extent, with phase diagrams. As explained in Figure 1.5, when different regions get heated up to certain temperatures, the morphology of microstructure changes. Consequently, we can distinguish the intercritical heat affected zone (ICHAZ), where base material starts to transform to austenite when heated above A_{C1} (lower critical temperature). Closer to fusion line (FL), when the material is heated above A_{C3} (upper critical temperature), it becomes fully austenitic and higher temperatures cause austenite grains to grow, resulting in the formation of first fine grain HAZ (FGHAZ) and, subsequently, coarse grain HAZ (CGHAZ).
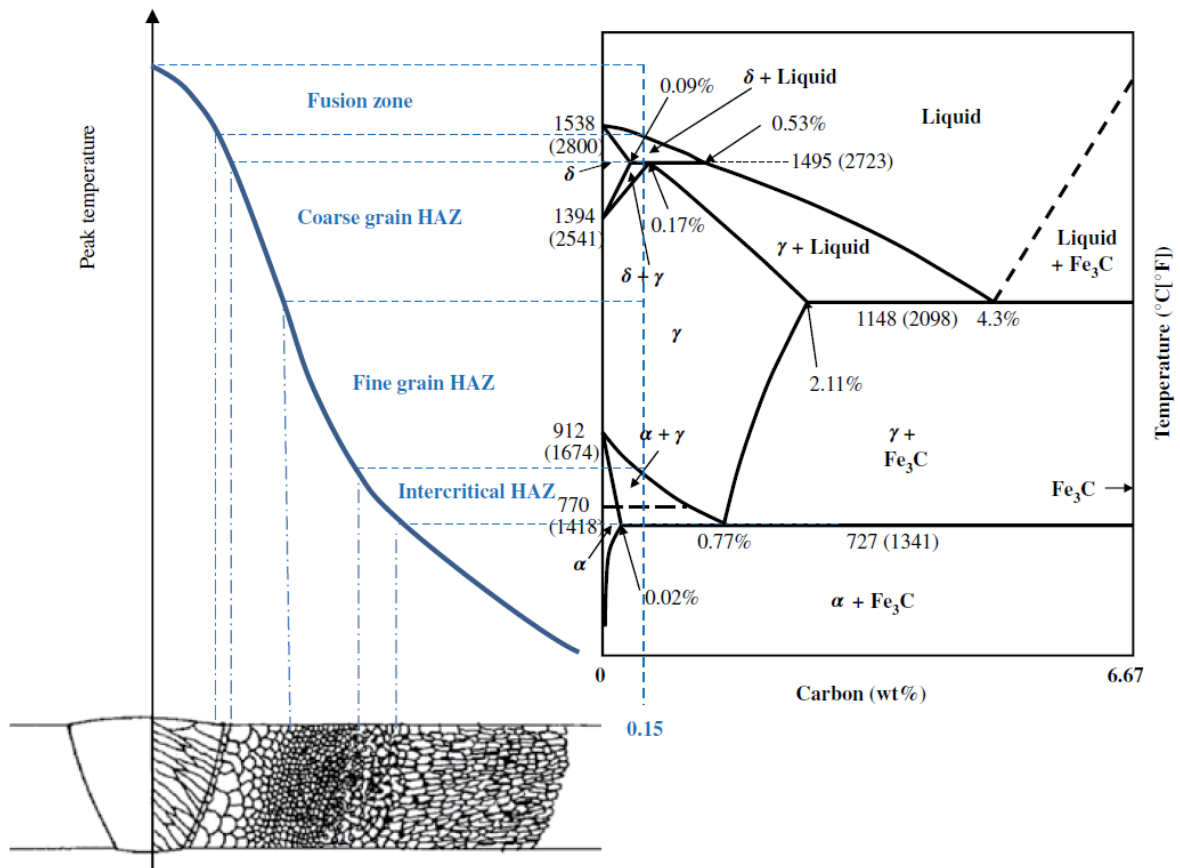
Figure 1.5 Overview of HAZ composition in relation to peak temperatures upon heating. Here, A_{C1} temperature equals 727 °C and A_{C3} equals 912 °C. (Lippold, 2015)

Final formation of austenite is governed not only by heating but also by the second part of each thermal cycle- cooling. In multipass welding, when each location within the weld experiences overlapping thermal passes, its microstructure becomes extremely complex and can be only approximated as shown in Figure 1.6.
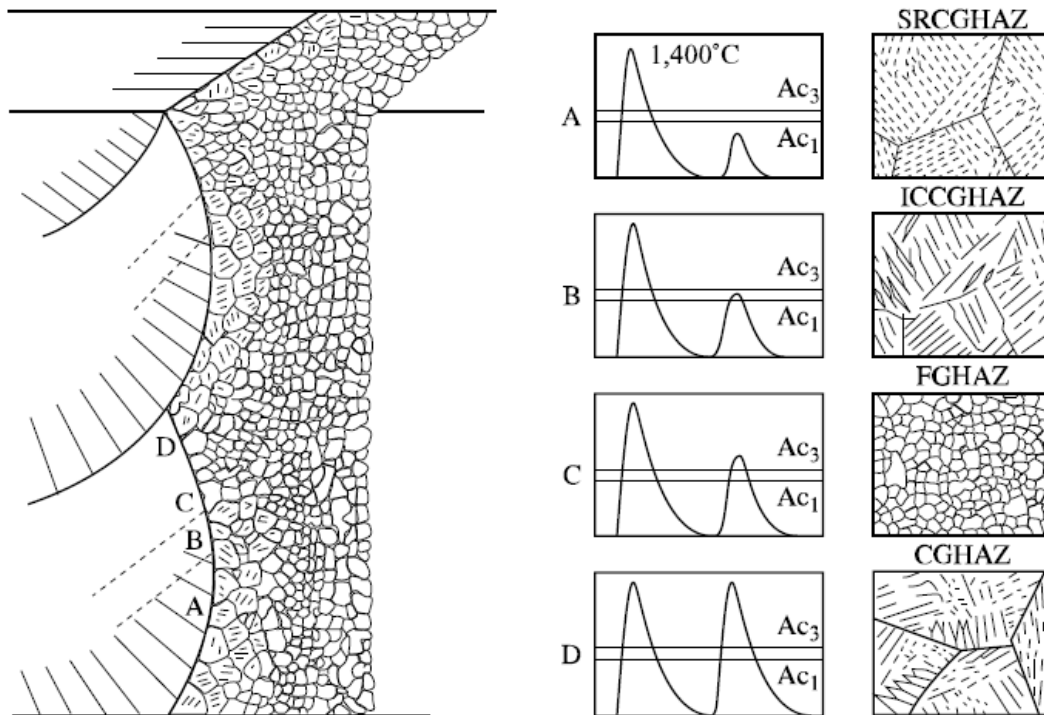
Figure 1.6 Schematic evolution of HAZ microstructure in multipass steel welds (Blondeau, 2001)

From the point of view of mechanical properties modification, multipass welding can be seen as an extremely rapid post- weld heat treatment (PWHT). Because of that, microstructural zones in multipass welding are altered compared to single pass ones, presented in Figure 1.5. Especially the coarse- grain region experiences severe changes, which depend mostly on reheating temperature during subsequent passes.

If a coarse grain zone, during the subsequent pass, is reheated below A_{c1} temperature (when austenite formation starts) it remains unchanged. Such microstructure zone is called SRCGHAZ (subcritically reheated coarse grain heat affected zone, zone A on Figure 1.6) which is very similar, in morphology and mechanical properties, to CGHAZ zone of metal in a rough state (zone D).

When CGHAZ is reheated above A_{c1} but below A_{c3} another subzone can be distinguished, namely ICCGHAZ (intercritical reheated coarse grain heat affected zone, zone B). This subzone is of particular interest in the steel industry because this is where the austenite → ferrite transformation occurs in favourable locations. Also, so-called M-A compounds (martensite- austenite coexistence) can be formed, which is associated with a decrease in toughness according to many studies on HSLA steels (Blondeau, 2001), (X.L. Wang, 2017). The local brittleness of this zone (sometimes referred to as LBZ, local brittle zone) is considered to show the least toughness within the whole heat affected zone.

FGHAZ, fine grain heat affected zone (zone C) is formed when grains are reheated above the A_{c3} temperature. This fine microstructure can be associated with normalization treatments occurring in high temperatures. Excellent mechanical properties of this subzone have been shown. It is desired to maximize this zone, which in combination with M-A compounds present in the heat affected zone, can result in a favourable combination of toughness and strength.

17

1.7. Fatigue of welds

Welded structures are much more sensitive to fatigue damage than they are to static loads, due to their stress concentrating nature. Thus, even though yield strength of a weld may be comparable to this of its base metal, more strict safety coefficients must be applied for design against cyclic loading. In fact, welds must be considered as severe stress concentrators (similar to notched structures) and their severity differs depending on many factors. It is extremely difficult to uniquely determine the weld fatigue effect of an actual structure. A realistic approach is to determine thoroughly the actual stress level at the weld (including assembly type and size, structure loading mode and local stress concentrators) and relate it to a fatigue data corresponding to a given joint configuration. One of the most used standards for fatigue design of welds, also used by Allseas Engineering B.V., is the (DNVGL, 2016).

In the case of transverse butt welds (see Figure 1.7), i.e. two plate members with a transverse weld perpendicular to an external load, fatigue cracks start at the weld cap or root.
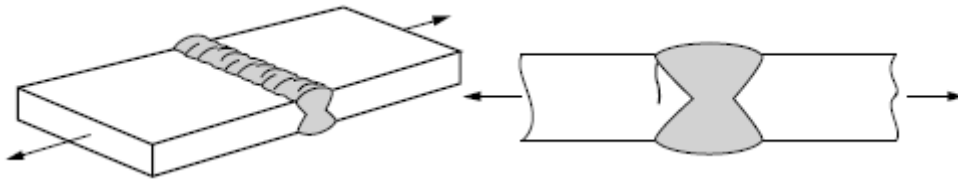
Figure 1.7 Transverse butt weld; cracking mode indicated on the right (Blondeau, 2001)

In such case, a crack always starts at the weld surface (if no internal large defects are present) and propagates through a wall thickness, perpendicular to load direction. Thus, crack initiation always yields from stress concentrators at a weld surface, not from the welding quality or material properties.

One of the most basic fatigue analysis methodologies is the nominal stress S-N curve analysis. This concept principle is that an elementary weld in a structure can be considered as a notched structure, where beadweld represents a notch. This approach takes into account all the local stress concentrators generated by the weld itself. Nominal stress in a body is the stress resulting from a simple static theory such as beam theory. Thus, in this stress approach, the design stress resulting in the local component under consideration is nominal stress with all the local notch effect (noted as stress concentration factor SCF) taken into account:

$$\sigma_{local} = \text{SCF}\sigma_{nominal} \tag{1.3}$$

Resulting local stress σ_{local} can be then used together with a relevant S-N curve, see Figure 1.8. To use those curves for a particular welded component under consideration one needs to only choose the right detail classification, as the SCF related to the weld type and assemblage quality is already incorporated in those curves.
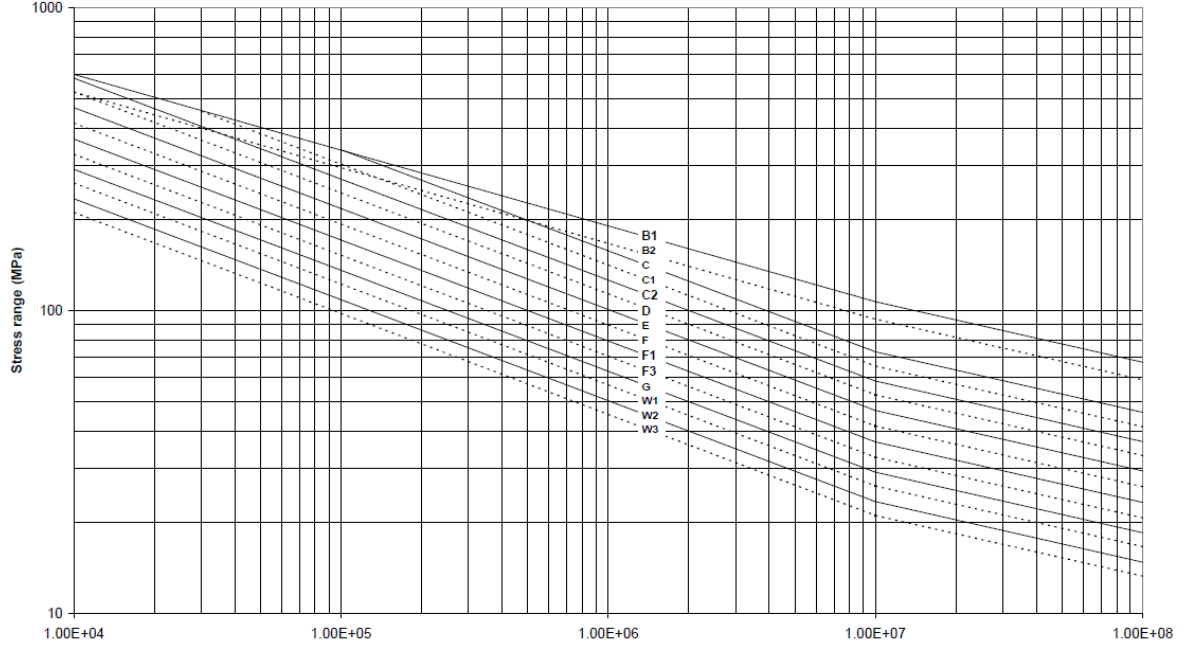
Figure 1.8 S-N curves in the air, for different weld classifications (DNVGL, 2016)

The classification of welded joints (from A to W, as per (BSI, 2014)) depends on joint geometry, the direction of loads acting on a joint and methods of joint fabrication. Curves presented in Figure 1.8 are the design S-N curves, which provide 97,7% probability of survival for a given welded detail under consideration. A formula for basic design curve is given:

$$\log N = \log \bar{a} - m \log \Delta \tag{1.4}$$

where N is the number of cycles to failure, $\log \bar{a}$ is intercept of N- axis by the curve (parameter depending on a standard deviation for a given curve), m is the negative inverse slope of a curve, and $\Delta\sigma$ is the nominal stress range [MPa].

The idea of design curves is that one specific curve can be used to characterize fatigue life of different structural details (as long as they fulfil the classification requirements) for constant amplitude considerations. However, there is always some uncertainty involved when developing design curves as tests on specific details always present some scatter. DNVGL and other regulatory bodies recommendations provide values of standard deviations representative for each curve.

Mean curve is an S-N curve that provides a 75% probability of survival for a given detail. Design curve is derived as a mean curve minus two standard deviations obtained from sufficient experimental data carried out in a lab environment:

$$\log \bar{a} = \log a - c S_{\log N} \tag{1.5}$$

Where $\log \bar{a}$ is intercept of the mean value of the n test data with the log N axis; $S_{\log N}$ is the standard deviation of the n test data of log N, and c is a factor determining how many standard deviations should be subtracted to obtain a design curve from a mean curve.

19

For E class of welds the standard deviation S_{logN} equals 0,2 and the c factor equals 2. Both design and mean curve have the same slopes and m parameter equal to 3 in Equation 1.4 The $log\,\bar{a}$ value for a design curve is given by the DNV recommendation and equals 12,010. However, Allseas Engineering adjusts this parameter for the root weld by incorporating the $SCF_{root} = 1,07$ factor (see Equation 1.7). Thus, $log\,\bar{a}$ for analysis of root weld fatigue used by Allseas (and in this research) equals 11,926. Such adjusted E type S-N curves, both design and mean, can be seen in Figure 1.9.
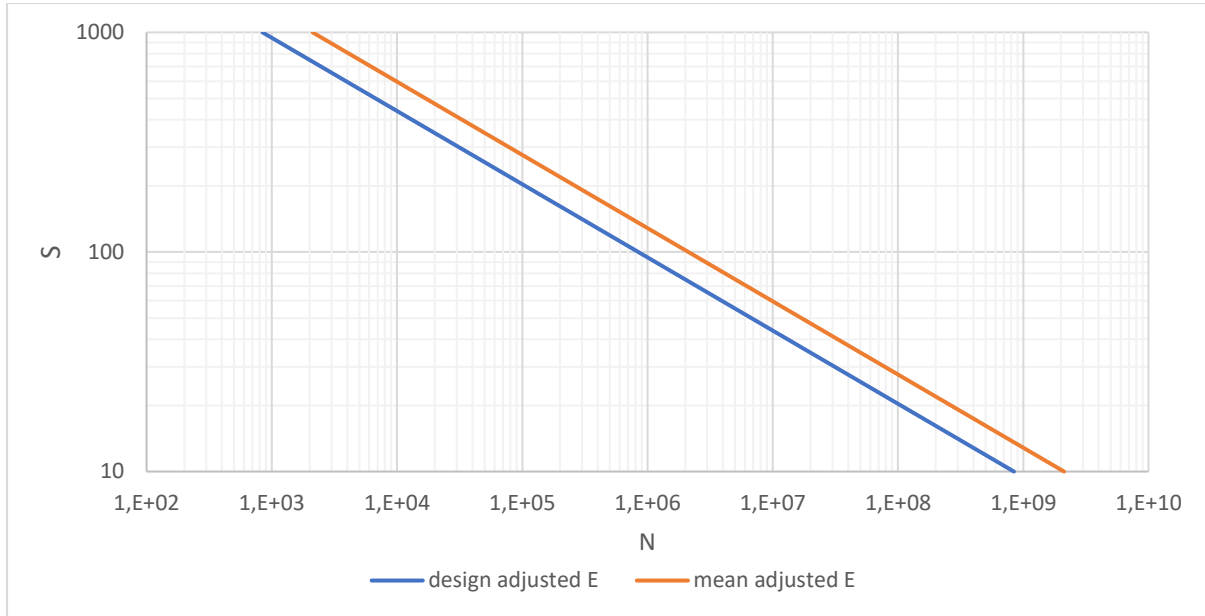
Figure 1.9 Design and mean S-N curve that was used as a benchmark for fatigue testing in this research.

Smooth, unnotched and unwelded plates are generally considered to have fatigue life comprised of two phases: crack initiation and crack propagation (growth). Crack initiation phase starts with the nucleation of microcracks and their growth as long as it can be considered a surface phenomenon. Then those microcracks start growing into the material, away from the surface, and fatigue life enters the crack propagation phase. However, in the case of welded plates, fatigue life is considered differently. Crack initiation phase in welded components is believed to start because of weld or geometry defects on the surface and therefore is usually much shorter than in a case of unwelded components. Hence, the fatigue life of welds is usually mainly covered by the crack growth phase (Schijve, 2009).

1.8. Factors influencing beadweld fatigue performance

From the static resistance point of view, welded joints have similar strength as the base material (provided that weldment is of good quality). However, the fatigue performance of welded joints is always poorer than that of base metal. Fatigue strength of welds varies greatly and depends on many factors, mainly on a type of assembly, welding process itself, HAZ, local properties of the bead and stresses, see Figure 1.10.
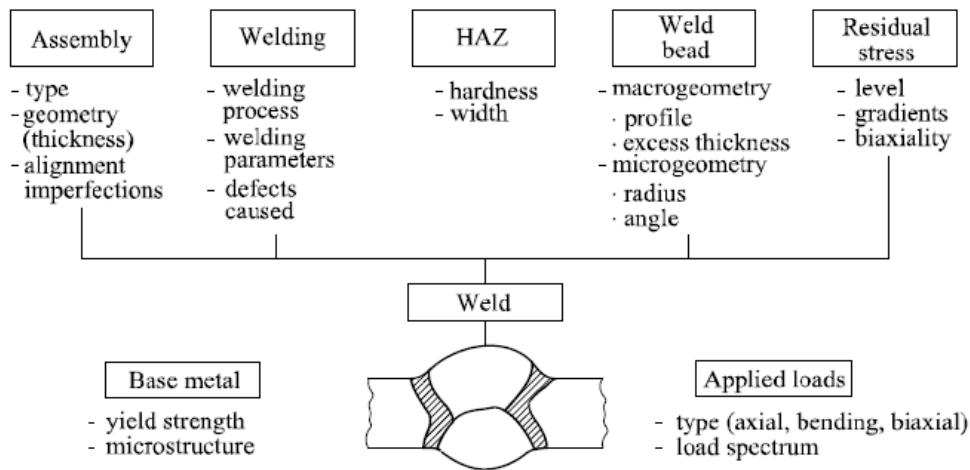
Figure 1.10 Overview of factors affecting fatigue strength of welds (Blondeau, 2001)

Weld assembly

Type of weld assembly has to be carefully examined and matched with a corresponding S-N curve. Many standards, for example, BS7608, DNV-RP-203 or recommendations by the International Institute of Welding (IIW) provide comprehensive weld classification based on assembly geometry. The beadweld investigated in this research can be categorised as a single side transverse butt weld, with a mean Hi-Lo value lower than 1 mm (DNVGL, 2016). This corresponds to class E welds. S-N curves for class E weld in the air (Figure 1.8) will be used as a benchmark for overstressed beadweld investigation.

Residual stress

In welds, thermal cycles introduced during welding produce local plastic strains. In principle, they are created as cooling metal contracts but is restrained by adjacent material that is further away from the weld. As a consequence, after a weld is cooled down to room temperature, tensile residual stresses are present in the weld metal and compressive residual stresses are present further away from weld metal. Other factors, like joins type and size or welding process parameters, can influence the magnitude of those strains, too. Residual stresses are especially important in case of multipass welds, where, due to multiple thermal cycles, residual stresses can build up and even reach the yield strength of a material. However, it is important to remember that small scale specimens do not contain the same amount of residual stresses as full-scale structures they are cut out from (DNVGL, 2016). Upon cutting, residual stresses present in weld may get relaxed (released) as there is less adjacent material constraining the weld. Test data used to create a given S-N curve is usually obtained in a lab environment, using small scale specimens. Therefore, for the purpose of this comparative fatigue study, S-N curves can be applied without corrections for the presence of residual stresses. Hence, fatigue testing on specimens in this research can be performed without high mean stress, i.e. with low R ratio.

Weld bead

On a macroscopic level, a beadweld profile (geometry) is virtually even and uniform. Pipe end J bevel and the welding process is designed this way that results in 3 mm thick beadweld. Both bevelling and welding are automated processes, optimized for pipelaying operation and checked during production. Microscopic thickness changes or hi-low, when within acceptable ranges, are acceptable in daily operation as they do not influence the pipelay properties. However, local misalignments and/ or change in thickness cannot be neglected for detailed fatigue study in a lab environment. Presence of joint misalignment (or a so-called Hi-Lo) introduces secondary bending moments when a joint is loaded in tension. Those moments are added to nominal stress which decreases fatigue life. Misalignments, or local change in weld geometry, can act as stress risers in that particular location. Stress concentration factor and local bending stress for such misaligned joint can be determined when a weld shape is known and defined, as presented in Figure 1.11.
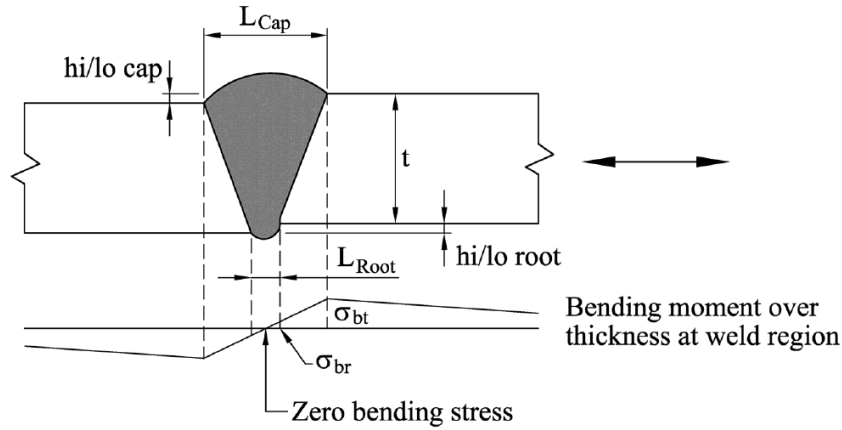
Figure 1.11 Stress distribution resulting from weld misalignment in pipes (DNVGL, 2016)

Bending stress found in the weld root, resulting from a moment found at a transition from the weld to the base metal is defined as:

$$\sigma_{b_r} = \frac{3\delta_m L_{root}}{t L_{cap}} e^{-\sqrt{\frac{t}{D}}} \sigma_m \tag{1.6}$$

Where δ_m is the mean of two values of Hi-Lo at the cap and root, t is the wall thickness, D is the outer diameter of a pipe and σ_m is the membrane stress.

Therefore, this resulting stress at the weld root can be included in the stress concentration factor (SCF) for the weld root:

$$SCF_{root} = 1 + \frac{3\delta_m L_{root}}{t L_{cap}} e^{-\sqrt{\frac{t}{D}}} \tag{1.7}$$

Welding process and defects

Welding parameters used for automated GMAW welding (using Phoenix system) are virtually the same for every location of the beadweld along the pipe circumference. For this comparative

fatigue study, the same welding parameters for every test coupon for every weld location are assumed. The heat input (HI), resulting from travel speed of the weld tool and voltage and current provided may vary slightly per location. HI data obtained from welding of test coupons (see Figure 2.8) proved to vary too little to affect material properties per location, thus HI effects are negligible for this research.

Weld defects, however, cannot be neglected when investigating fatigue performance of a material. Different defects can affect total fatigue life differently. Lack of penetration in a weld increases the risk of crack initiation on the surface, especially at the root. Inclusions or pores also reduce fatigue strength as they affect the crack propagation phase. It is then desirable to compare fatigue strength between completely defect- free specimens, which in practice can be hard to achieve. In a general pipelaying operation each weld is inspected with Non-destructive Tests (NDT), usually Automated Ultrasonic Tests (AUT) before pipelay installation. Some small level of porosity is allowed and is considered not harmful for pipeline mechanical performance. However, there is a so-called "size effect" involved when comparing between defects influence in full-scale structures and small scale specimens. It is assumed that cracks always (in good quality welds) initiate from the surface micro defects, usually at the transition zone from base to weld metal. Naturally, the "volume effect" of the given specimen/ structure plays a role as the longer the weld, the bigger the potential surface and more potential defects are available as initiation locations. This aspect of a size effect is another reason (next to residual stresses mentioned previously), why small scale specimens performance cannot be readily compared with full-scale structures. As long as the weld length and the specimen volume is kept the same within the specimen research population, comparative fatigue study can be performed.

From the point of view of beadweld fatigue performance, investigated with small- scale specimens, both beadweld porosity and misalignment play an important role, however they influence fatigue life differently:

- Porosity present in the weld can negatively affect the total fatigue lifetime. Depending on pores location, size and shape they can affect the crack growth rate. In this study, it is especially important that all the investigated specimens have no pores in the beadweld pass or if the porosity presence is known and determined. Some porosity in filler passes is acceptable, but the amount and size of pores need to be controlled and documented with NDT. Surface defects such as lack of penetration or undercuts are highly undesirable as they influence crack initiation and may undermine the effect of overstressing on total fatigue life. In this study, it is desirable that all cracks initiate at the weld root.
- Hi-Lo misalignment in a specimen can influence the crack initiation phase as it introduces stress concentration factor at the weld root (according to Equation 1.4). Hi-Lo values of each specimen can be measured but its effect on total fatigue life cannot be controlled. As local root geometry affects only the surface it has a great effect on the crack initiation phase. However, contrary to surface defects, the effect of local root geometry on fatigue life cannot be avoided. Beadweld material properties are the core interest of this study and therefore cannot be machined (ground) flat from the specimens. Class E welds are considered as "as-weld" joints, without root or cap

removed. One has to realise that even samples cut out from the same girth weld can have different local micro geometries, which can result in wide scatter in fatigue life results. Thus, it is desired that the crack initiation phase is separated from the crack propagation phase.

1.9. Plasticity and the stress-strain curve

During the pipeline installation, there are different types of loads- tension, bending and shear-acting on pipeline components. For this research tensile loads in the longitudinal direction of the pipeline are further considered. During "pulling on the bead" action the beadweld is subjected to peak tensile stresses, as already discussed in section 1.2. The magnitude of those stresses (and corresponding strains) is carefully controlled during normal pipelaying operation. It is necessary for this research to understand the mechanical behaviour of the beadweld material under external uniaxial tension exceeding a certain value, defined as "yield".

Material's response to stress is deformation (or strain), i.e. displacement of atoms from their original positions. This displacement can be reversible- elastic or irreversible- plastic. Also, the material's deformation upon acting stresses can be time depended or time independent. For the scope of this research time- independent irreversible deformations will be considered, determined as "plasticity". When beadweld is overstressed it can experience local or global plasticity, i.e. change in shape. For small strains, as in the case of pulling on the bead, the main mechanisms of plasticity would be a slip and mechanical twinning. Those two modes of plasticity are considered conservative, which means that upon deformation material experiences change in shape but its crystal structure remains unaltered.

To understand the mechanical behaviour of X60 grade steel and beadweld, a stress-strain curve for structural steel has to be studied (Figure 1.12). Such a curve is a result of a tensile test and represents the elastic-plastic behaviour of a given material.
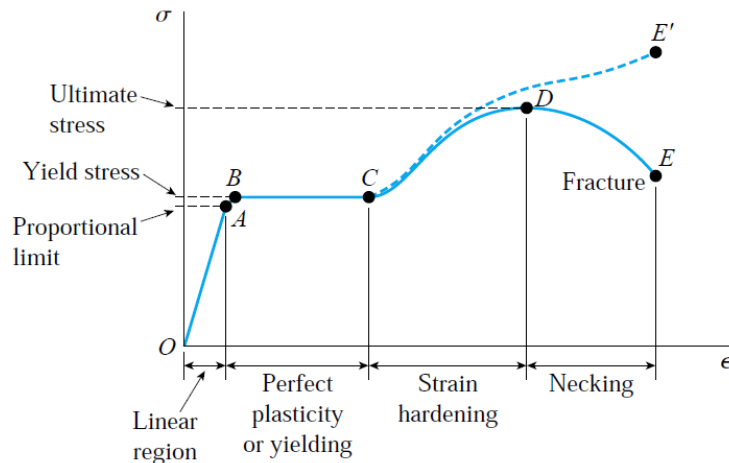

Figure 1.12 Engineering (solid line) and true (dashed line) stress-strain diagram for a structural steel specimen loaded in uniaxial tension (not to scale) (Gere, 2004)

It is known that usual, "not overstressed" pulling on the bead action is contained within the *proportional limit* part of the material response (section O-A on the curve). This is where the stress-strain relationship in the material is linear and proportional and any deformations experienced in the beadweld are gone after pulling on the bead action stops. As the stress imposed on material increases beyond the proportional limit, the relation between stress and strain is no longer linear and strain increases more rapidly with stress. This is where material reaches its *yield point* (point B on the curve). At this point considerable deformations can occur in the material without increase of stress- material starts to *yield*. In reality, it is impossible to determine a single stress value at which plasticity starts because yielding is a transition phenomenon and develops gradually (Bäker, 2007). For engineering applications, it can be assumed that material starts to deform plastically when irreversible deformation reaches 0,2% (corresponding to ~0,5% total strain at the yield point for steel). Stress associated with this point is then called *yield strength $R_{p0.2}$* Section B-C in Figure 1.12 depicts the perfectly plastic behaviour of a material, which elongates without any increase in applied stress. For the case of structural steel the elongation in region B-C can be 10- 15 times of this experienced during elastic deformation (linear region O-A).

Once a material experiences extensive portion of yielding, it starts to harden in a process called *strain hardening*, represented by section C- D. During that process the strains experienced by material are large enough to cause its crystal structure to change. Generated in this way dislocations strengthen a material as they make it more resistant to deformation. Increase in applied stress is required to further elongate material. At point D stress finally reaches its highest value, called *the ultimate stress*, after which material (specimen used for the tensile test) starts *to neck,* i.e. experiences reduction in its cross section. Such lateral contraction, which always accompanies stretching, is negligible up to point C, thus it is virtually not present before strain hardening. The change of cross-sectional area can be taken into account for stress calculation which results in true stress-strain curve (dashed line on Figure 1.12), which is obviously different from engineering curve, where the cross-section area assumed constant for simplicity. For modelling and predictions of structural components' mechanical behaviour, which are not expected to experience large strain in their operation, engineering curve can be applicable.

1.10. Techniques to monitor crack initiation and crack propagation

Total fatigue life comprises of two phases and each of those phases is governed by different factors. Crack initiation phase is governed by surface parameters such as weld geometry (notch), surface defects, surface roughness etc. The crack growth phase is controlled by material (weld or base metal, depending on the location) properties away from the surface. In defects- free materials the initiation phase can take up the majority of the total fatigue lifetime, especially at low-stress amplitudes. The size of "initiation cracks" is relative for the application or industry, but in general, microstructurally small cracks are considered to belong to the initiation phase. Once the cracks reach the size of physically small cracks (0,1-1 mm) they are considered to belong to the growth (propagation) phase (S.-T. Tu, X.-C. Zhang, 2016). Since the focus of this research is fatigue properties of the overstressed weld, not the surface (notch) effect, it is desirable to investigate only the crack growth phase and to exclude crack initiation

25

phase from the considerations. To do so, a method to determine (and distinguish) those two phases is needed. There has been a lot of research effort put into monitoring and understanding fatigue crack growth, resulting in developing various monitoring techniques: optical observations, acoustic emission pick- up method, potential drop measuring systems, strain gauges, just to name some of them. Literature suggests that for better, more reliable results, multiple techniques based on different principles should be applied simultaneously.

Optical observation

One of the most straight forward techniques for crack initiation and crack growth determination is observations with an optical microscope. This method allows observations of a (polished) specimen surface, hence only surface defects can be detected. Such a microscope, usually digital, should be portable and equipped with stands or grips that allow it to be positioned in the vicinity of an investigated specimen. The biggest limitation of this method is the small observable field so that an operator has to know exactly where to expect a crack. Once the microscope's lens is pointed at the area of interest, it can detect small cracks, depending on its magnification, and (or) follow the crack propagation. It is up to the technical capabilities of equipment and the operators wish to either pause testing for optical observation or observe during continuous testing. Due to its simplicity and technological advances of today's digital cameras and microscopes, this is a widely used and versatile technique for fatigue cracks observations.

Potential drop technique

An even more powerful method for crack growth measurement is the potential drop (PD) technique. This method, when properly calibrated and fit for the purpose, can be very effective and sensitive for crack length changes. The basic principle of PD measurement is relatively simple: a specimen has to be subjected to a stable constant (DCPD) or alternating (ACPD) current supply. As the crack grows in the material it reduces its cross-section and the electric resistance of the specimen increases. A well calibrated (sensitive) PD instrument is able to detect not only the surface but also inner cracks of only 1 μm or less. To effectively measure crack length changes, suitable electrodes and a sensitive voltmeter are needed. Increasing resistance in a specimen is measured by placing two wires as close to the crack initiation area as possible. They are then connected to the voltmeter. Often one or two additional reference wires are attached to the specimen, further away from the crack, in order to reduce the noise in the output signal. The output signal from the electrodes is determined as $10 * \frac{V_{crack}}{V_{ref}}$ where V_{crack} is the output from the "crack" electrodes and V_{ref} is the output from the reference electrodes. The ratio is multiplied by 10 so that the output potential is within the range supported by the machine.

Schematic set-up of the DCPD measurement on a tensile specimen is shown in Figure 1.13.
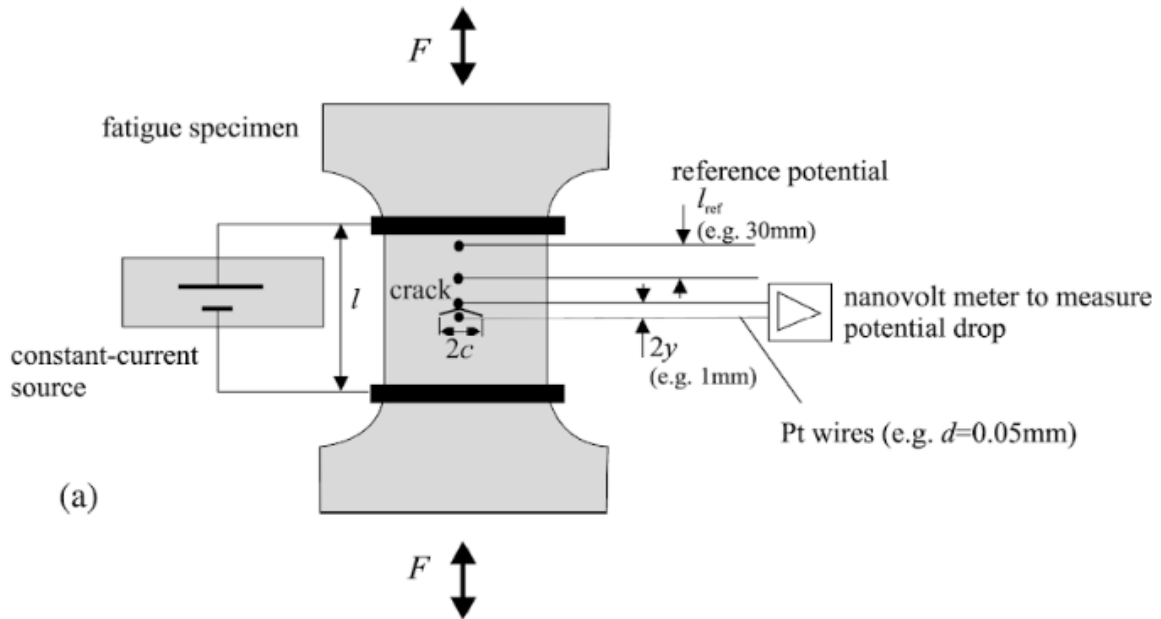
Figure 1.13 Schematic set-up of a DCPD measurement (Krupp, 2007)

Since the resistance response of the specimen is affected by many factors (wires position, temperature, specimen geometry, type of materials used, electric effects such as eddy currents, thermoelectric effects etc.) the PD system calibration is challenging and crucial for good output. It is recommended to analyse the fracture surface post- mortem in order to obtain a calibration curve for a given specimen geometry. Such curve correlates potential-drop data [V] with crack length [mm] and is necessary for reliable crack growth observations.

For slow crack growth rates, in the crack initiation phase, special care must be taken to account for the voltage noise generated by PD set-up itself. Modern DCPD systems are designed to minimize the noise, especially thermoelectric effects at the wire/specimen interface, by pulsing the current. Thermoelectric effects at the wires attachments are known as "thermal voltage" effects. Thermal voltage is generated at this interface due to the thermocouple effect and can be even of the same magnitude as voltage changes generated by crack growth. Hence it is important to separate thermal voltage from actual crack growth data and this can be done by cyclic turning the current on and off. Such pulsed DCPD takes two measurements of the voltage: one during the actual pulse (current on) and the other one after that (at zero- current). Then the off-current reading is subtracted from the on-current one. Current pulsing can be synchronized with the external loading wavefunction so that pulse-peak reading is taken at the load peak or valley, depending on the operator's research goal. Another way to account for thermal voltage is to manually measure it when current is supplied to the uncracked, unloaded specimen, in the same environment as the actual fatigue test takes place. The measured voltage then becomes an offset (H. Kuhn, 2000).

For the reasons mentioned earlier, crack propagation monitoring is not needed for this research. Thus the potential drop technique will be set-up to approximate the moment (in terms of cycles) of crack initiation. Care should be taken to obtain an electrically stable set-up, with sensitivity adjusted to detect as small cracks as possible. Also, a pulsated DCPD equipment will be used to account for thermal voltage.

2.   Methodology and test set-up

This research comprises two main experimental phases:

1) Coupons fabrication & overstressing simulation, i.e. fabricating test coupons by welding and then applying high loads, that took place on board of *Brightspark*- one of the Allseas vessels. Additionally, the FEA analysis of the overstressing simulation was done.
2) Fatigue testing of specimens, i.e. fabrication of test specimens from the coupons and performing fatigue test at TU Delft laboratory, including crack initiation measurements, microstructural analysis, hardness and tensile testing plus data processing.

Details of those activities are explained in the following sections.

2.1 Coupons overstressing

To investigate overstressed material fatigue performance, test specimens would be extracted (ideally) from a weld subjected to pulling on the bead operation. Because this operation takes place during pipelay installation only, it was more practical to simulate such operation on pipe pieces, in controlled conditions. For the reliability of test results, it was chosen to use unused pipe pieces that were left from one of the commercial pipelaying project completed by Allseas. The overstressing simulation comprised pipe pieces preparation, bevelling, bead welding, applying the loads and then finishing the welds. It was chosen to fabricate four test coupons in total, from which the test specimens will be extracted.

Since the yield of the overstressed beadweld material is known it was possible to calculate the force needed to load the test coupon above the yield point. All the calculations below assume the uniform stress distribution along the girth weld, i.e. that each location of the beadweld will experience the same magnitude of stress during overstressing. However, it must be noted that neither the beadweld overstressing simulation, nor the FEA study, represent the uniform stress distribution in the beadweld. The stress state in the pulling on the bead, caused by the bending due to unsupported pipe weight, is not uniform either. In the loading mode introduced by the jacks (overstressing simulation and the FEA) the force and pressure located on the force application points are in fact higher than those calculated below.

Overstressing load calculations

To determine loads that were used in the overstressing operation (and corresponding pressure subjected by the jacks) the following calculations were done:

$\sigma_y = 380\text{MPa}$ is the yield point based on the Ramberg $-$ Osgood stress $-$ strain relationship for the X60 steel

$OD_{root} = 583,8$ mm is the outer diameter of the beadweld

$ID_{root} = 577,8$ mm is the inner diameter of the beadweld, based on pipe manufacturer

$A_j = 213,8246 \text{ cm}^2$ is the area of the jack's cylinder exerting the pressure ($\emptyset = 165 \text{ mm}$)

Area of the 3 mm thick beadweld is $\text{A3} = A_{OD_{root}} - A_{ID_{root}} = 5473,91 \text{mm}^2$

Total force needed to trigger yielding in the 3 mm thick beadweld is $F3 = \sigma_y * A3 = 2080085,8[N]$. Thit amount of force would have to be applied in case of a flat plate. However, the coupon is a tubular joint, containing a beadweld that creates a type of misalignment. The presence of the beadweld disrupts the geometry and acts like a stress concentration, resulting in effectively higher stresses located in the beadweld. The formula for a stress concentration factor at a girth weld with such a misalignment was developed by Conelly and Zettlemoyer (L.M. Conelly, 1993):

$$SCF_{CZ} = 1 + 2,6 * \frac{e}{T_1} * \left[\frac{1}{1 + 0,7 \left(\frac{T_2}{T_1} \right)^{1,4}} \right] \tag{2.1}$$

Where: e- eccentricity (offset of centrelines of equal thickness plates in the misaligned joint), T_1- thinner plate, T_2- thicker plate. Pipe pieces used for the overstressing come from the same bigger pipe segment, thus they have the same wall thickness. In such case, $T_1 = T_2$ and Equation 2.1 can be rewritten as:

$$SCF = 1 + 1,53 * \frac{e}{T} \tag{2.2}$$

The geometry of the misalignment (eccentricity e) differs from the beadweld geometry, see Figure 2.1

Misalignment configuration   Beadweld configuration
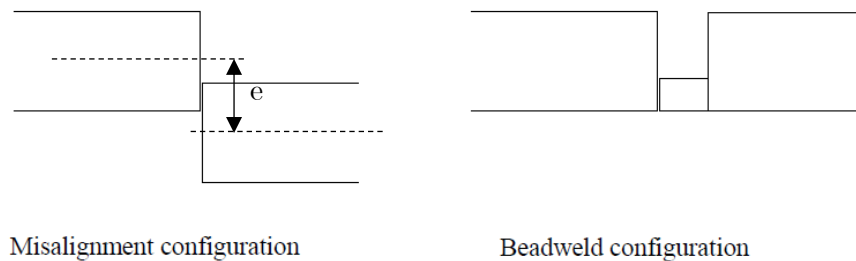
Figure 2.1 Eccentricity e vs. beadweld geometry.

Equation 2.2 can be rewritten for the beadweld configuration, with the 3 mm beadweld thickness bt and zero misalignment:

$$SCF = 1 + 1,53 * \left(1 - \frac{bt - e}{T} \right) = 1 + 1,53 * \left(1 - \frac{3}{15,9} \right) = 2,24 \tag{2.3}$$

This approach to calculating the SCF value is used by Allseas in their standard "pulling on the bead" assessment in any pipelaying operation. The SCF of 2,24 has to be incorporated in the total force needed for beadweld yielding so that $F = \frac{F3}{2,24} = 928609,7[N]$.

The force needed to be exerted by one jack equals $\frac{F}{2} = 464304,9[N]$. This can be expressed in terms of pressure p [bar] applied by one jack:

$$p = \frac{F}{2} * \frac{1}{A_j} * \frac{1}{10} = 217,14 [bar]$$

In other words, each jack has to exert a pressure of at least 217,14 bars to the test coupon to cause the beadweld material to yield (100% of the yield capacity). Since the hydraulic jacks were operated manually by two operators, each responsible for one jack, their movement had to be as synchronised as possible. To facilitate that the target pressure of 300 bars was chosen, to be sure that there is a sufficient overstressing load applied to the coupons. 300 bars correspond to $\frac{300}{217,14} = 1,38 = 138\%$ of the yield. Assuming the uniform stress distribution the entire circumference of the beadweld would be stressed 38% above the yield. In case of the loading mode with jacks, the force point locations most likely will be stressed more than 138% of the yield, with stress decreasing further away and the minimum stressed less than 138% above the yield (see Sections 3 - 3.6 for details).

The broken test coupon- incorrect load calculations

Coupons fabrication and their overstressing took place on board *Brightspark*, the Allseas' training vessel. During initial preparations for that operation, an error was made in the target pressure calculations. The SCF was not taken into account in the initial load calculations (Karman, 2017) resulting in too high target pressure, i.e. too high loads applied to the coupon.

The 120% of yield capacity was incorrectly determined as $F_i = 1,2 * \sigma_y * A3 = 1,2 * 386,13 MPa * 5473,91 mm^2 = 2536369N = 2536,37kN$ (Karman, 2017). This value was then converted into acting pressure of cylinders, with each cylinder applying a half, i.e. 1268184,5N per jack. Pressure per jack was calculated as $p = \frac{0,5F_i}{A_j} = \frac{1268184,5N}{213,8246mm^2} = 593,1 \, bar$. In other words, it was believed that 593 bars of pressure applied by each jack are needed to stress the beadweld 20% over the yield. With those calculations 100% of yield capacity would be reached with applying $\frac{593,1}{1,2} = 494,25 \, bars$. The correct calculations (with the SCF incorporated) show that 100% of the yield is actually reached with 217,14 bars. Thus, in reality, applying 494,25 bars per one jack would result in overstressing of $\frac{494,25}{217,14} = 2,28 = 228\%$ of the yield.

At the moment the first overstressing simulation was performed the above error was not yet known. Target pressure for each jack operator was set to 593,1 bar. Before that value was reached the first overstressed coupon (with 3 mm beadweld) broke at the girth weld when each of two pressure gauges showed around 500 bars (approx. 1000 bars applied in total). That corresponds to approximately $F_a = A_j * p * 10 = 213,8246mm^2 * 1000bar * 10 = 2138,246kN$ of total force applied to the structure at the moment of failure, which is about 1,6 times more than loads experienced by coupons A, B and C, see Table 2.1.

After the unwanted test coupon rupture, the calculations were revised and the error has been found. The corrections were made by incorporating the SCF (see Equation 2.3) and the overstressing operation was continued. The error, however unwanted, provided an interesting insight for the SCF evaluation. Since we approximately know the force to failure of the beadweld (read from the pressure gauges in the moment of rupture) and the estimated UTS of the beadweld material the actual acting value of SCF at the location of rupture can be estimated. The average UTS of the pipe material, as certified by the pipe manufacturer, is 559

MPa. The characteristic material ultimate tensile strength can be calculated with the same approach as presented in formula 1.1. Hence, the value of actual UTS of beadweld can be estimated to 545 MPa. Force needed to cause such stress in the beadweld can be calculated simply by multiplying this value with the surface area of the beadweld $A3 = 5473,91 mm^2$, which gives F_{UTS} = 2983,280 kN. Since we know the force to failure applied by the jacks (F_a = 2138,246 kN) and we estimated the force needed to rupture the beadweld, we can estimate the actual SCF value that was acting in the moment and location of the coupon weld failure: $SCF_f = \frac{F_{UTS}}{F_a} = \frac{2983,280}{2138,246} = 1,39$. This value is only an estimation, since the exact jacks pressure at the moment of rupture was not precisely recorded. This estimation also applies to the uniform stress distribution along the girth weld. As we already know the actual stress distribution is ununiform, with symmetrical maximums and minimums along the circumference. We can conclude that the stresses in the beadweld acting in the moment of rupture were even higher in the maximum location than estimated here, indicating that most likely the actual SCF is even lower than 1,39. Nevertheless, it can be concluded with a high level of certainty, that the Allseas' standard assessment of SCF being 2,24 is conservative.

Coupons fabrication

It was decided to fabricate 4 test coupons for the overstressing simulation, based on the *Overstressing load calculations*. This amount of coupons ensured there would be enough material to fabricate desired sets of fatigue specimens. The overview of test coupons is given below:

- Coupon 0- being the reference coupon. This test coupon was not subjected to overstressing load and represented the conditions of the undisturbed, standard weld. Because of that this coupon was fabricated without the load supports and comprised only two pipe pieces welded together, each 700 mm long.
- Coupon A- test coupon comprising two 700 mm long pipe pieces, equipped with steel support plates for the load application, see Figure 2.2. This coupon was loaded with a total of 631 bars applied to it by use of hydraulic jacks. The load application took place after the beadweld (3 mm thick weld) was finished.
- Coupon B- has the same design as coupon A and was subjected to the same loading conditions. Load application also was applied after finishing the beadweld. The pressure gauges showed applied pressure of 621 bars. Coupons A and B are virtually identical.
- Coupon C- has the same design as coupons A and B. Overstressing loads of approx. 626 bars were applied directly after a hot pass (6 mm thick weld) was finished. It was chosen to apply loads to the hot pass of the weld (thus after the second pass, not only the first one) to be able to compare between pulling on the bead and pulling at the hot pass in terms of fatigue properties.

Coupons A, B and C were loaded for 120 seconds each, which is the actual pulling on the bead time during offshore pipelaying. After the overstressing simulation was finished, coupons were placed back on the welding station and the welds were finished with the same standard Phoenix welding operation as used previously for the bead welding.

31

Table 2.1 The summary of each test coupon characteristics. The actual loads applied are given, readings are taken during overstressing operation from hydraulic jacks' pressure gauges.

Table 2.1 Overview of test coupons used in overstressing simulation

Coupon	loaded	Loaded weld type	Pressure [bar]	Corresponding force [kN]
0	no	Not loaded	Not applicable	Not applicable
A	yes	3 mm thick beadweld	631	1349,233
B	yes	3 mm thick beadweld	621	1327,102
C	yes	6 mm thick beadweld + hot pass	626	1339,846

2.2 Test coupons

To simulate the pulling on the bead operation, a custom made test coupon has been developed. Since design for coupon 0 is straight forward and does not require the addition of support plates, this paragraph will focus on the design of coupons A, B and C. The main purpose of this design was to assure that there is a known, desired and controlled stress field introduced to the beadweld during overstressing. The original idea proposed by (Karman, 2017) involves the use of two hydraulic jacks, mounted in between support flanges designed as integrated parts of the test coupon. Such design implies that loads provided by the jacks, mounted symmetrically, are evenly distributed in the beadweld.

The use of two identical hydraulic jacks was dictated by a number of reasons, main of them being the simplicity of the design and cost of the overstressing simulation. However, one must be aware that the load case introduced by jacks differs significantly from the load case present in beadweld during the standard offshore pipelaying operation. The difference emanates from different points of force application. This will be explained in details later in this chapter.

The visualisation of a test coupon used for beadweld overstressing simulation can be seen in Figure 2.2. Detailed drawing of the test coupon design can be found in APPENDIX E.
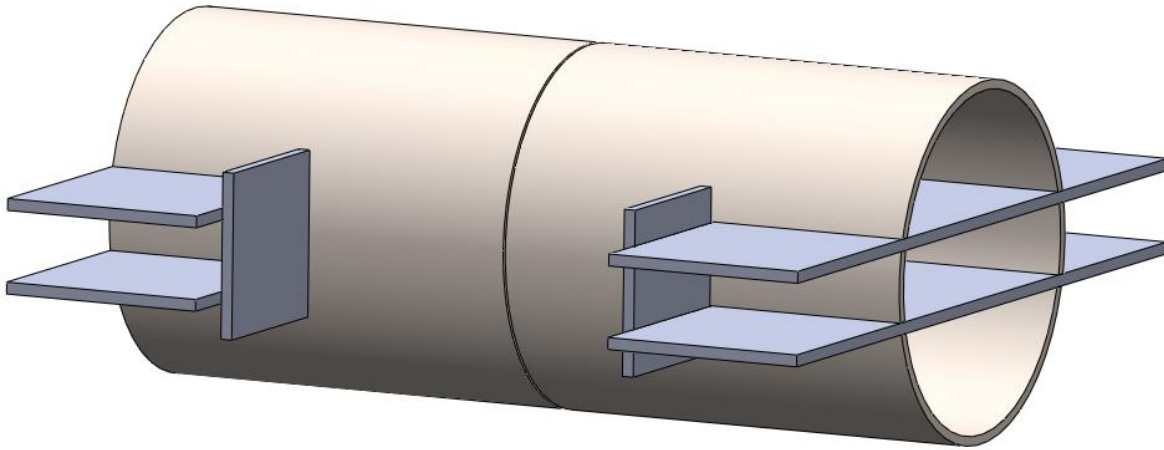
Figure 2.2 Test coupon visualisation, with support plates marked in blue

There are four square support plates, tangent to the pipe outer surface, which is the force application points. They are welded to bigger plates, that are inserted and welded to pipe slots. In such design, loads are applied to square plates and transferred through "slotted plates" into the pipe body, and hence to the girth weld. The square flanges are located at 3 and 9 o'clock of the pipe, 350 mm away from the girth weld each. Points of force application were set to 350 mm away from the beadweld because of three reasons: i) the jacks' stroke capacity, ii) the load distribution and iii) enough room for the welding equipment in between the flanges. The supports set-up geometry influences the final load distribution in the beadweld- the four force points create four maximum stress points along the circumference. Due to this loading mode, one can expect stress maxima and minima along the beadweld, which will be discussed in detail in section 3.

The square flanges were designed big enough to fit the commercial hydraulic jacks (see Section 2.3) that were used to apply the desired pressure to the test coupon. Due to simplicity and because of the safety reasons the coupons were placed vertically for the overstressing operation. The visualisation of the coupons, with the jacks mounted on the support flanges, is shown in Figure 2.3.
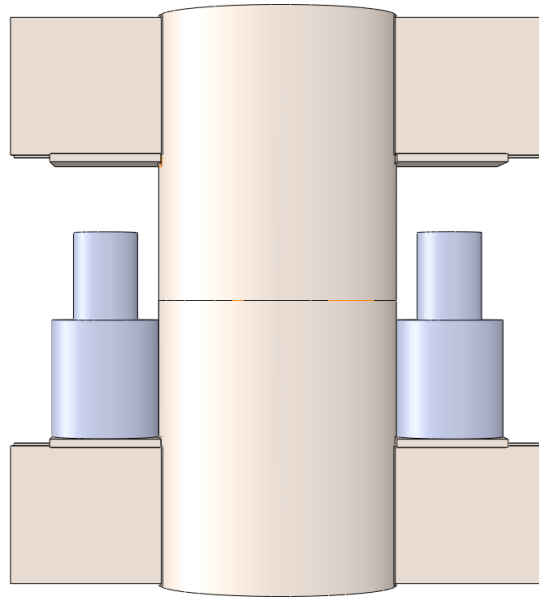
Figure 2.3 Visualisation of a test coupon with jacks mounted on the support flanges, ready for the overstressing operation.

Due to safety reasons, all test coupons were welded to the deck and had a steel cage placed over the top of the coupon. The cage itself was also welded to the deck. Such prevention measures were necessary because of the magnitude of pressure used to overstress the coupon.

2.3 Hydraulic jacks

Hydraulic jacks were selected for the overstressing operation based on their tonnage capacity and maximum stroke range. The distance between the flanges is 700 mm and the pressure exerted by the jacks on the support flanges should be big enough to assure that at least some parts of the beadweld are stressed above the beadweld yield strength. The target pressure per jack was determined as 300 bar (see Section 2.1). Commercial hydraulic jacks (see Figure 2.4) were found suitable for the purpose of this research.

For the proper load application additional hydraulic equipment was needed, i.e. a hydraulic pump, system of hoses and two digital pressure gauges to control both of the jacks working simultaneously. Schematic of the system set-up is presented in Figure 2.5. The jacks were connected with hoses to the same single main manifold that was connected with a single hose to the hydraulic pump. Such setup ensures that oil flows from the pump to the manifold and then branches evenly to both jacks. There are two digital pressure gauges mounted at each jack's feeding pump. Since both jacks are sharing the same main oil manifold the oil pressure evens out as soon as the jacks reach the constraints (i.e. become subjected to loading).

Figure 2.4a High Tonnage Cylinder, Enerpac model CLR25013, used for coupons overstressing (Enerpac, 2018); b) Test coupon C, just before the overstressing load application.
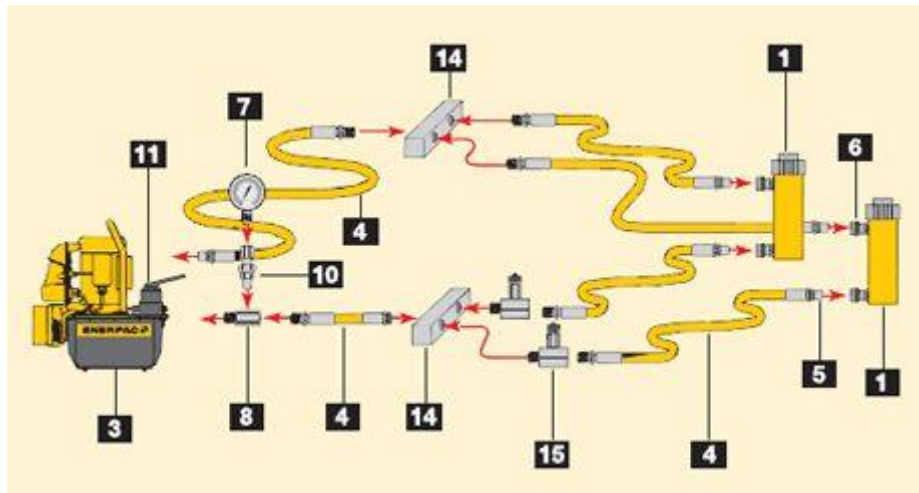

Figure 2.5 Double-acting cylinder set-up used in a push/pull the application. 1- cylinder, 3- pump, 4- hydraulic fluid hose, 5, 6- couplers, 7- pressure gauge, 8- gauge adapter, 10- auto-damper valve, 11- 4-way directional control valve, 14- manifold, 15- needle valve. (Enerpac, Enerpac, 2018)

Figure 2.4b shows the test coupon C ready to be loaded. The yellow hydraulic cylinders are mounted on the support flanges and secured around the coupon with a rope. The coupon itself its welded to the ground, as well as the steel frame around it. The hoses are channelled out to the pump, outside of the operation site, approximately 5 m away from the coupon. The pump operators were operating the pump manually, opening/closing the valves and recording the gauge's readings.

2.4 Non Destructive Test- Automatic Ultrasonic Testing

A standard Non-Destructive Technique of weld checks has been requested after full welds on coupons have been finished. Weld scanning took place directly after welding, on board of *BrightSpark.* The NDT used by Allseas is the Automated Ultrasonic Test (AUT). The standard AUT service provided by Allseas is able to detect weld flaws of at least 1 mm size and can locate them in terms of weld depth. Only checks of beadweld and hot pass were requested (thus at the depth of 6 mm from the weld root) as only those parts of the weld are investigated in this study. A detailed NDT report can be seen in APPENDIX C.

2.5 Samples matrix- locations, parameters, quantity

To satisfy the research goal the appropriate number of samples had to be fabricated. Because of the comparative nature of this study, it was important to obtain subsets of specimens of distinct sets of features. As explained in Table 2.1 and in Section 3.5, the overstressing simulation resulted in coupons (material) that differ in terms of loading history (experienced strain state), welding features, porosity and loaded beadweld geometry. Subsets of specimens were chosen from appropriate coupons and appropriate girth locations based on FEA results, welding parameters log and the porosity report provided by Allseas NDT service.

Experienced strain

The leading parameter for the comparative fatigue study is the strain level experienced by the weld during the overstressing simulation. To satisfy the research question it is desirable to compare specimens that differ only in the strain levels. Since the FEA results show that there was a symmetrical stress distribution along the girth in all the coupons, we can distinguish between locations (areas) where the material was strained elastically only or plastically, see Figure 2.6. Based on this the reference stress and plastic strain level experienced by the material in each specimen will be reported.
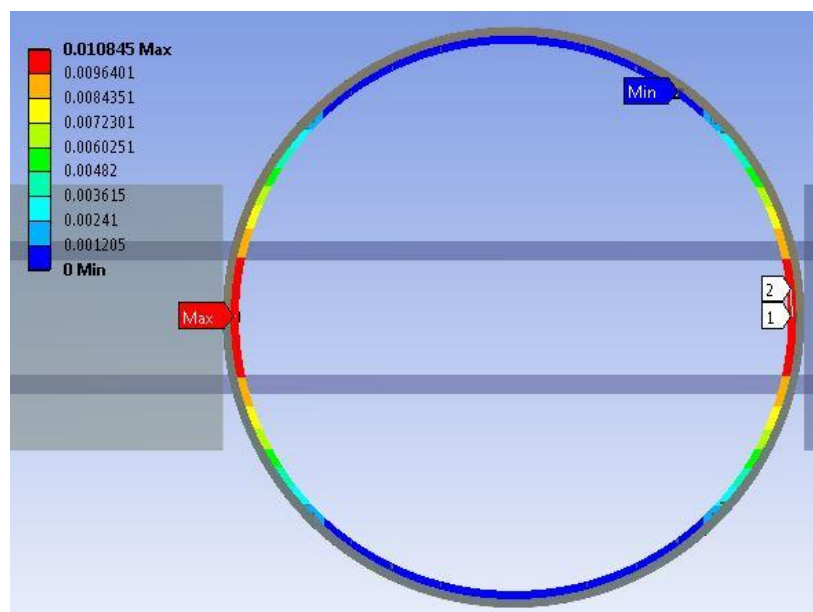

Figure 2.6 Plastic strain along the beadweld OU path, 3 mm thickness beadweld model; elemental results.

The quantitative representation of the stress and plastic strain is presented in Figure 2.7. The distribution is presented starting at 12 o'clock, going counter-clockwise. Based on this graph the reference values of strain and stress will be assigned to each specimen from coupons A and B in Table 2.3. Analogously, a similar stress/plastic strain distribution graph was done for coupon C to find a reference stress/strain values for the C-group specimens.
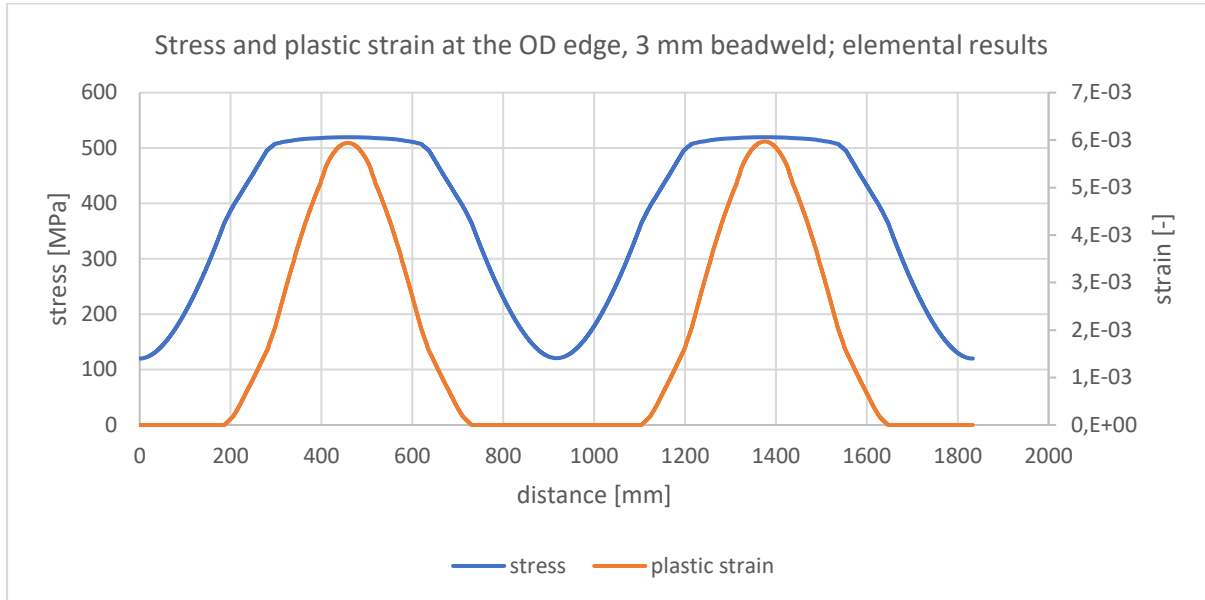

Figure 2.7 Stress and plastic strain along the OD edge of the 3 mm beadweld. Elemental averaged results are presented. Distribution starts at 12 o'clock, proceeds counter-clockwise.

Welding features

Parameters of welding procedure (travel speed, voltage and current), as mentioned in section 1.8, can be quantified as heat input (HI). HI was measured for every weld pass during welding of each coupon. The output of this measurement proved negligible changes of HI along the girth weld. The only locations along the coupon circumference that experience higher variations of the HI were the welding tool start and stop positions. The HI distribution along the pipe circumference during Phoenix welding is shown in Figure 2.8. Sharp drops at 10 o'clock and 12 o'clock correspond to stop and start positions, respectively, of welding bug nr 1 and nr 2. Slight HI fluctuations between 12 o'clock and 10 o'clock (from 355 J/mm to 316 J/mm) are considered irrelevant for the resulting weld metal microstructure and, subsequently, final fatigue performance. Therefore, there will be no distinction regarding the experienced HI in the fatigue specimens.
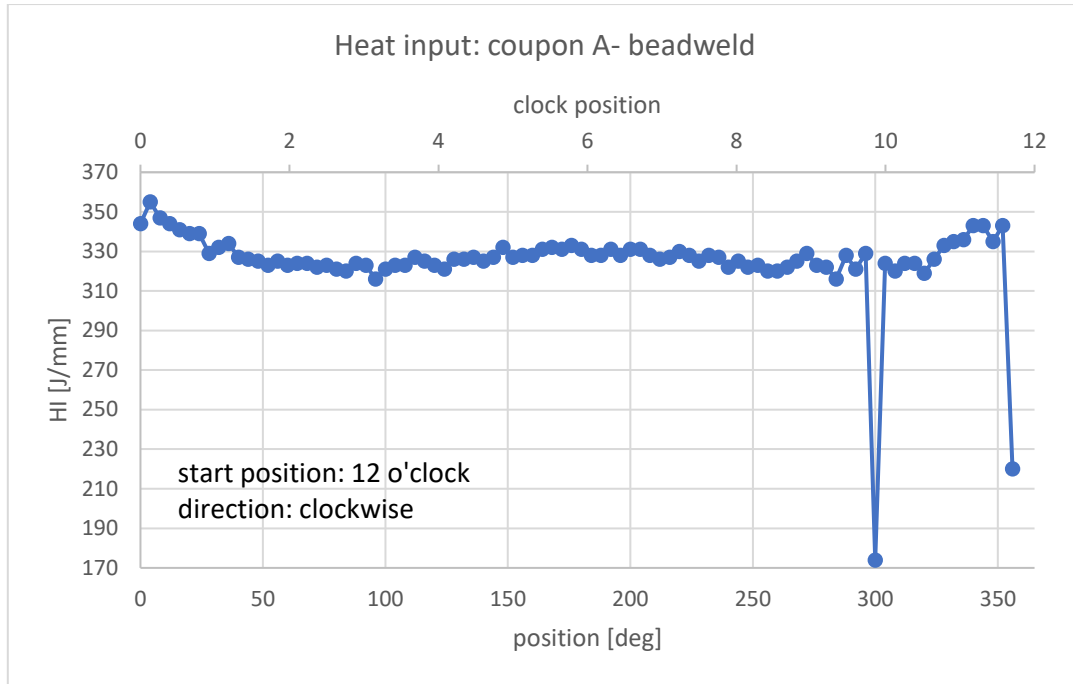
37

Figure 2.8 Heat input distribution during beadweld of coupon A.

Porosity

As explained in section 2.4, the AUT can reveal the presence of pores in a certain location of the weld. The porosity report was focused on the beadweld and hot pass of all the coupons, as those are the weld parts of interest. Based on this report (APPENDIX C) there was a distinction made between locations "with porosity" and "without porosity previously reported". However, one has to keep in mind the limitations of the AUT method regarding the size of the pores. The post mortem analysis of fracture surfaces is advised to check for the presence of pores below the minimal detectable size in AUT scans.

Specimens selection

The above parameters, combined with the loaded weld type (beadweld or hot pass) were taken into account when creating specimens subsets (groups) for the comparative study. There have been 6 groups of specimens indicated:

- "Reference" group: specimens extracted only from the coupon 0. They experienced no overstressing loading and had no previously reported porosity. They represent the case of a pipe that experienced no pulling on the bead during installation. Those specimens will serve as a benchmark for the remaining subsets.
- "Elastic, no pores" group: those specimens come from the coupons A and B, which experienced loading on the beadweld. They were extracted from the locations along the circumference that experienced stresses below the yield, i.e. were strained elastically only. According to the porosity report, there are no pores present in the beadweld or hot pass of those specimens. Those specimens represent the case of a pipe subjected to acceptable pulling on the bead action.
- "Plastic, no pores" group: a group of specimens taken from coupons A and B. Those specimens were extracted from the beadweld material that was loaded above the yield point, hence was strained in the plastic regime. They contain no previously reported

38

pores. Samples in this group represent the case when the beadweld is pulled above its acceptable limits.

- "Elastic, pores" group: samples extracted from coupons A and B, from locations where the beadweld was strained in an elastic manner only and where the NDT report revealed the presence of pores. This subset will allow investigating the influence of pores on the fatigue performance.

- "Plastic, pores" group: similarly, this subset of specimens is intended to investigate the influence of porosity on fatigue performance of specimens containing beadweld that was previously strained in a plastic manner. Specimens in this group were extracted from coupons A and B, from the locations indicated by FEA results and porosity report.

- "6 mm, no pores," group: those specimens are extracted from the coupon C only. They are made of a material that contains hot pass subjected to loads. Since the hot pass and beadweld material is 6 mm thick the stress distribution found along the coupon C girth was of magnitudes two times lower than coupons A and B. This subset represents the case when pulling is performed after the second pass (hot pass), not after the beadweld only. Those specimens also are free from pores to assure no other features influencing their fatigue behaviour.

The amount of specimens in each group is listed in Table 2.2. The rule of thumb is to have at least 3 data points to experimentally investigate any property and the bigger the sample, the better. At least 6 specimens per subset were chosen as a balance between a number of data points and testing time.

Table 2.2 Number of fatigue specimens fabricated for each group (subset).

group	Reference	Elastic, no pores	Plastic, no pores	Elastic, pores	Plastic, pores	6mm, no pores	total
amount	6	12	6	6	6	6	42

The locations of the coupons, from which given specimens were extracted, was based on FEA results and porosity reports. Each specimen was taken from the previously determined position that was carefully indicated in terms of distance from the 12 o'clock [mm]. A visual representation of specimens located along the girth weld of coupon 0 is presented in Figure 2.9. The total number of specimens (as per design explained in Section 2.6) that can be extracted from once coupon is 34 (marked as grey contours on the picture). Specimens of interest are marked in yellow and they are tagged according to their position relative from the 12 o'clock (top) in terms of degrees. For example, the specimen at 3 o'clock is marked as 0-90, since it comes from coupon 0 and is positioned at a 90 degrees angle. This notation will be used for all the subsequent specimens. The areas in between red lines, concentrated around 3 and 9 o'clock, indicate the approximate extent of plasticity along the girth weld of coupons A and B (based on FEA results, see sections 3.5 and 3.6).
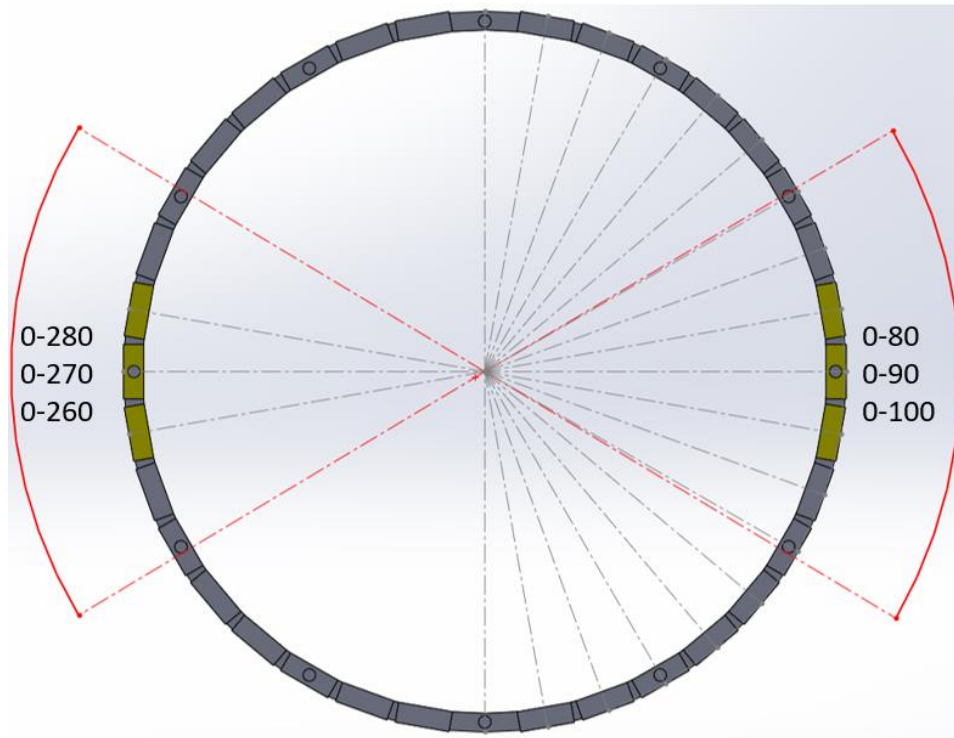
Figure 2.9 Visual representation of 6 specimens locations along the coupon 0 girth weld (highlighted in yellow). Little grey circles represent full hours. The specimens and the pipe are up to scale.

The specimens matrix, containing all 42 specimens selected for fatigue testing, is given in the overview Table 2.3

Table 2.3 A complete fatigue specimens overview, including their unique tag and location as the distance from 12 o'clock. Specimens marked in red were discarded from the results due to reasons explained in Section 4.4. Elemental stress-strain values per location are given according to the discussion in Section 3.6

number	specimen tag	location [mm]	group	Experienced FEA stress [MPa]	Experienced FEA plastic strain [%]
1	0-80	425	reference	-	-
2	0-90	479	reference	-	-
3	0-100	532	reference	-	-
4	0-260	1383	reference	-	-
5	0-270	1436	reference	-	-
6	0-280	1489	reference	-	-
7	A-20	106	elastic, no pores	-	-
8	A-30	160	elastic, no pores	311	0
9	A-40	213	elastic, no pores	406	0,030
10	A-80	425	plastic, no pores	519	0,572

11	A-90	479	plastic, no pores	519	0,584
12	A-100	532	plastic, no pores	517	0,477
13	A-140	745	elastic, pores	333	0
14	A-150	798	elastic, pores	231	0
15	A-160	851	elastic, pores	159	0
16	A-200	1064	elastic, pores	283	0
17	A-210	1117	elastic, pores	387	0,012
18	A-220	1170	elastic, pores	458	0,103
19	A-260	1383	plastic, no pores	520	0,596
20	A-270	1436	plastic, no pores	518	0,510
21	A-280	1489	plastic, no pores	515	0,367
22	A-320	1702	elastic, no pores	254	0
23	A-330	1755	elastic, no pores	172	0
24	A-340	1809	elastic, no pores	125	0
25	B-20	106	elastic, no pores	212	0
26	B-30	160	elastic, no pores	309	0
27	B-40	213	elastic, no pores	406	0,031
28	B-60	319	plastic, pores	512	0,282
29	B-70	372	plastic, pores	517	0,447
30	B-110	585	plastic, pores	513	0,321
31	B-120	638	plastic, pores	493	0,152
32	B-240	1277	plastic, pores	516	0,416
33	B-250	1330	plastic, pores	519	0,554
34	B-320	1702	elastic, no pores	254	0
35	B-330	1755	elastic, no pores	172	0
36	B-340	1809	elastic, no pores	125	0
37	C-80	425	6mm, no pores	506	0,130
38	C-90	479	6mm, no pores	508	0,152
39	C-100	532	6mm, no pores	500	0,111
40	C-260	1383	6mm, no pores	508	0,159

41

41	C-270	1436	6mm, no pores	507	0,132
42	C-280	1489	6mm, no pores	480	0,088
additional	tag	location [deg]	group		
43	0-1	110	reference	-	-
44	0-2	120	reference	-	-
45	0-3	130	reference	-	-
46	EX A	190	elastic, no pores	371	0,004

During fatigue testing, a few of the "reference" and "elastic, no pores" specimens failed at the support points, instead of at the root weld. Four additional specimens (three of the "reference" type and one "elastic, no pores" type) have been manufactured and tested. See Section 4.4 for more details.

2.6 Fatigue testing

Fatigue tests can be carried out for different purposes, for example, to verify fatigue predictions models, investigate various environmental effects or to collect fatigue properties data for component design purposes. The vast majority of fatigue tests, including this one, aims to compare fatigue properties of material different conditions. Once the goal of fatigue test is established, three main variables have to be determined: specimen type, loading mode and testing procedure (Schijve, 2009).

Specimens and loading mode

Specimen type and design were determined based on (ISO, 2012). The standard allows types of specimens suitable for two loading cases: tension and bending. Design of specimen loaded in bending was chosen, see Figure 2.10. Detailed drawing, including dimensions and surface finishing, is presented in APPENDIX A. As stated previously in section 1.8, class E S-N curve will be used for comparative fatigue testing. As stated in (DNVGL, 2016) this class refers to welds without a root weld being ground (hence, the root remains intact- as weld). Since the specimens are extracted from a pipe they contain the original curvature. This is undesirable from the bending test point of view, due to rollers positions. For accurate stress state during bending it is required that faces of the specimens, where the rollers touch, are flat and exactly parallel. This was solved by machining flat only the upper face of the specimen and its ends at the bottom face, leaving the middle approx. 70 mm area (containing the root) intact (see Figure 2.10).The transition between the as-weld middle and ground ends was smoothed out (filleted) to minimize stress concentrations.
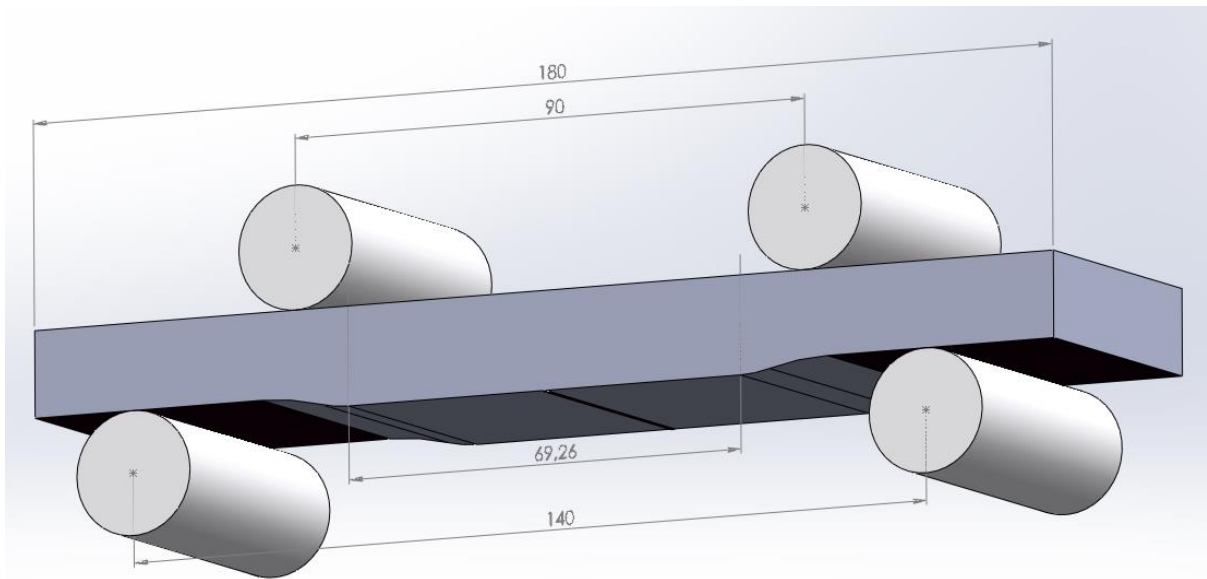
Figure 2.10 A visualisation of a fatigue specimen in a four-point bending test. The root of the beadweld has been marked for clarity as the dark centreline on the bottom face of the specimen. Faces marked in dark colour indicate the machined-flat areas. Important: the root area remained intact.

Four point bending loading mode was chosen as a suitable method for fatigue testing of a beadweld, see Figure 2.10 It was chosen due to the stress distribution offered by this testing mode: there are compressive stresses (normal to the cross-section) at the upper face of the specimen and tensile stresses at the bottom face, where the beadweld is located. This setup guarantees that maximum external tensile loads are applied to the root weld. Moreover, due to the constant moment distribution between the inner force point, the stress distribution is constant across that area. It guarantees the same stress state in every tested specimen, independent of the manual specimen alignment.

Testing procedure

To imitate fatigue conditions experienced by pipe girth welds during pipeline installation and operation, the following fatigue testing parameters were chosen:

- Low R- the ratio of loading, as there is no need to account for residual stresses (released while specimens were cut). All fatigue tests in this research were performed with R=0,1.
- Applied stress amplitude- to optimize testing time a relatively high-stress amplitude was considered. The maximum nominal stress is limited by the yield strength of the material and the stress amplitude σ_A was chosen to be 300 MPa.

Given the above, the specimens will be loaded in a cyclic manner between 33,3 MPa and 333,3 MPa. Those are the minimum and maximum tensile stresses, respectively, experienced by the specimen on its bottom (tension) face.

The well-known relationship between bending moment and stress takes the form:

43

$$\sigma = \frac{My}{I} \tag{2.8}$$

where σ is stress (tensile or compressive), M is the bending moment, y is the distance from a neutral axis and I is area moment of inertia $I = \frac{bh^3}{12}$. For four-point bending setup the moment M can be derived as (NPTEL, 2018):

$$M = \frac{F(S_o - S_i)}{4} \tag{2.9}$$

where F is the total applied force, S_o is the distance between outside rollers and S_i is the distance between inside rollers (see Figure 2.10). Combining equations (2.8) and (2.9) we can derive that, in order to stress the bottom face of the specimens with 333,33 MPa, they have to be subjected to a total force of:

$$F = \frac{4\sigma I}{y(S_o - S_i)} \tag{2.10}$$

Above equation (2.10) was used to calculate the maximum (load peak) and minimum (load valley) force for the testing using the following values:

Table 2.4 Parameters used for maximum loading force determination.

σ_{max}	333,3 MPa
b	46 mm
h	15 mm
$y = 1/2\,h$	7,5 mm
S_i	90 mm
S_o	140 mm

Substituting the above values into equation (2.10) :

$$F_{max} = \frac{4 * 333,3\text{MPa} * 46\text{mm} * (15mm)^3}{12 * 7,5mm * (140mm - 90mm)} = 45995,4\ N \approx\ 46\ kN \tag{2.11}$$

and

$$F_{min} = 0,1F_{mx} = 4,6\ kN$$

Above maximum (F_{max}) and minimum (F_{min}) values of load were set for the fatigue testing of all the samples. The frequency of cyclic loading was set to 15 Hz.

2.7 Crack initiation measurements

A custom made optical crack observation setup was made, consisting of a simple optical microscope with the minimal detectable object of 200 μm and a digital camera connected to a Raspberry Pi computer, see Figure 2.12. The camera was mounted at the microscope lens so that the view from it would be captured and stored. A piece of software was written for the camera to take 3 pictures every 5 minutes, starting from the beginning of the test. After a fatigue test was finished the pictures were stored in the correct order, labelled with exact date and time they were taken and were manually analysed. The setup was immobile and was

pointed out at a certain, previously determined point at the root weld, at the polished face of the specimen, see Figure 2.11. It was expected the cracks will initiate at the highest Hi-Lo location so the microscope was always pointing at that spot. However, in some cases the crack initiated outside of the microscope view, resulting in no useful optical data. Provided the crack initiated at the expected location and the picture quality was good, it was possible to observe a crack formation of 200 μm and its subsequent growth (with 5 minutes time increment).
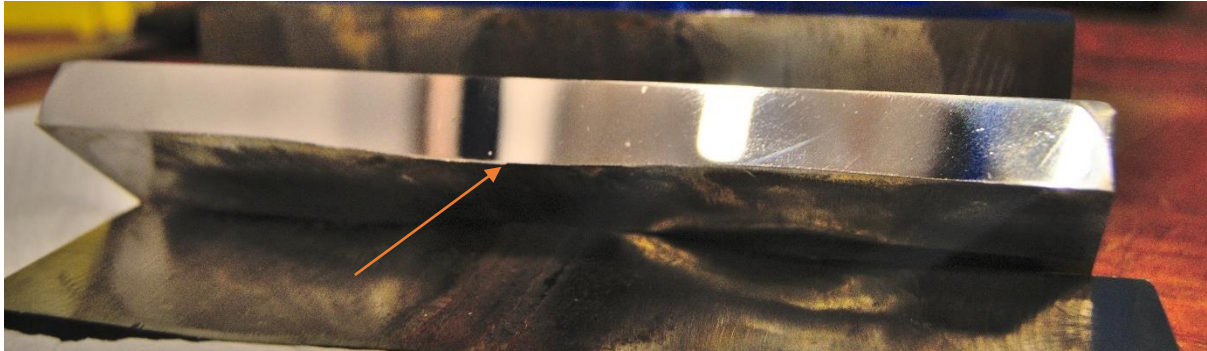
Figure 2.11 The polished face of the specimen, ready for the optical crack observation. The observed point is marked with the arrow.
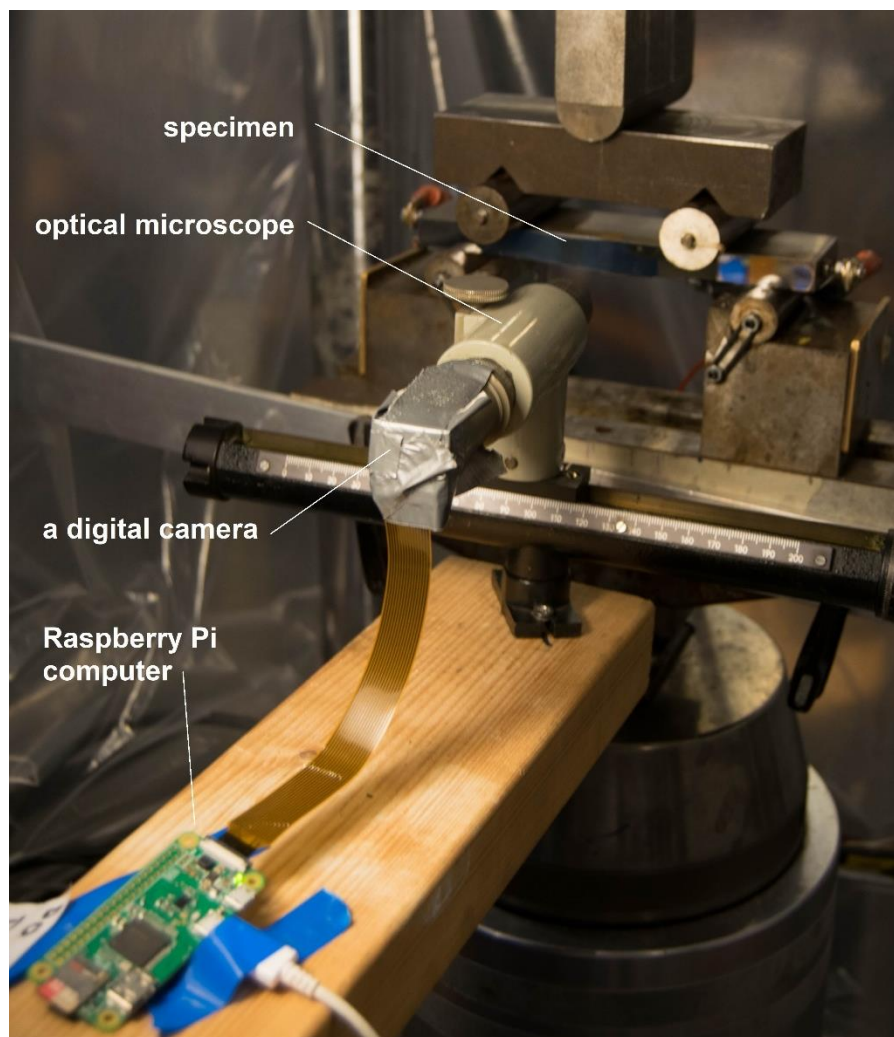
Figure 2.12 A full optical observations setup during the fatigue test

For the Potential Drop (PD) measurement four electrodes were spot welded to the root side of the specimen- two on both sides of the root (expected crack initiation site), as close to it as possible. The other two electrodes (reference ones) were placed at the far ends of the specimen, see Figure 2.13. A DC current was applied to the specimen by two cables screwed tight into the material. Despite many efforts, it was impossible to properly isolate the specimen from the testing machine. No isolation material available could withstand the high loads (approximately 4,6 tonnes) when inserted between the specimen and the rollers. It was decided to proceed with the uninsulated setup, compromising on the PD sensitivity. Most of the tests yielded satisfying results, however, some PD measurements failed during fatigue testing. Most common errors that occurred were: detached electrodes or short circuits due to lack of isolation. Unfortunately, such disturbed PD measurements had to be discarded. In the case of PD measurement, the correct output is the curve representing the potential in the function of time. Once that curve changes its slope, the crack growth starts.

In the case of both PD and optical measurements were available for a given specimen, their correlation was checked. In case they both were in accordance then their average value was concluded as the initiation phase determination. In case the PD reading was very different from the optical results, the PD was considered as the more reliable one. Optical observation results were only chosen when there was only the optical value available for the given specimen.

Total lifetime, crack initiation and the growth phases are represented in terms of hours or minutes. The crack growth phase was determined by subtracting the initiation part from the total lifetime.
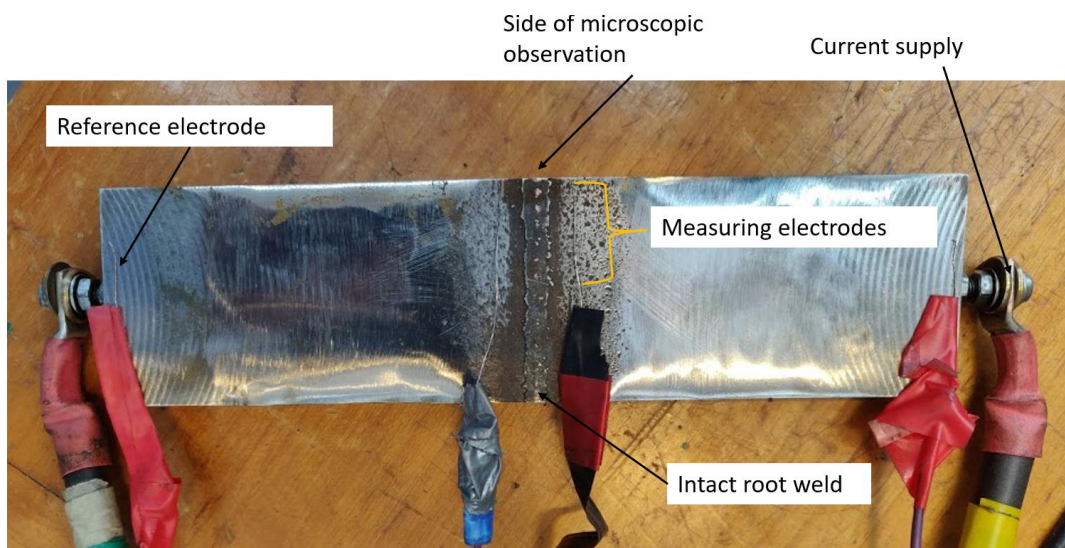
Figure 2.13 The PD setup with spot welded electrodes visible on the root (tension) side of the specimen.

2.8 Microscopy observations

Low magnification microscopy was used to determine each specimen's Hi-Lo magnitude and to determine whether the crack started (and/or propagated) at the base or weld material.

Keyence Digital Microscope VHX-6000 was used for metallographic observations and low magnifications observations of fracture surface (FS). Additionally, Scanning Electron Microscope (SEM) JEOL JSM-IT500 was used to observe fracture surfaces of selected specimens.

Metallography preparations were carried out on specimens destined to optical microscopy observations. The focus was on crack, weld and its surroundings. After fatigue test was finished a broken specimen was cooled down in liquid nitrogen and subsequently broken through with one rapid overload. This enabled FS observations of both failed halves, with a clear distinction between FS and forced overload, see Figure 2.14a-b.

Figure 2.14 a) Specimen A-220, just before overload application, b) two halves of the specimen, with a clear distinction between FS (rusty area) and overload. Crack growth anisotropy clearly visible.

Crack propagation, as well as a base material, HAZ and weld microstructure, were investigated on two planes: edge plane and centre plane, see Figure 2.15. Next, both halves of the cracked metal were embedded in resin, polished (up to 1 μm polishing cloth) and etched with Nital 2%.
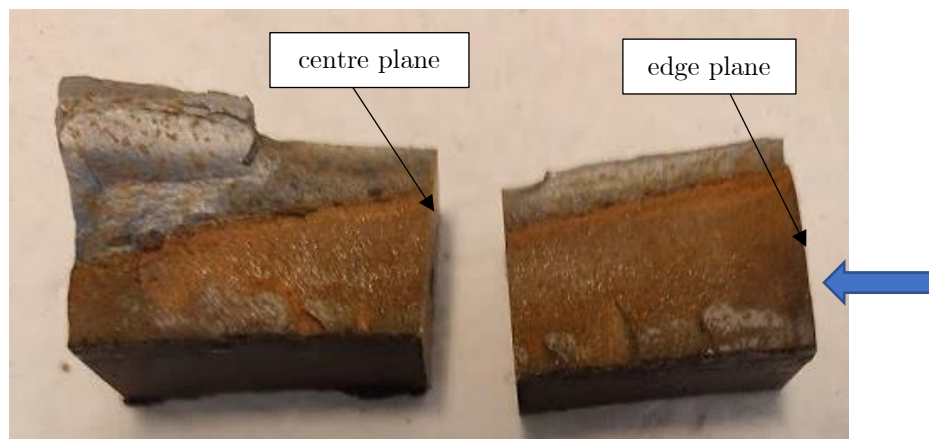
Figure 2.15 Halved fatigue cracked specimen, ready for polishing and etching. Blue arrow indicated the direction of observation.

Selected specimens (see Table 2.5) were chosen for the microscopic observation so that every specimen group has been represented. Those specimens who showed unusual (extreme) results

or crack growth anisotropy (faster crack propagation on one side) were also included in microscopy observations. Some of the selected specimens were also subjected to hardness testing.

Table 2.5 Overview of specimens subjected to microscopy investigations and hardness testing.

specimen	Keyence	SEM	FS	Hardness	group	remarks
A-270	x		x	x	Plastic, no pores	
B-70	x		x		Plastic, pores	
A-160	x		x	x	Elastic, pores	
A-280		x	x		Plastic, no pores	
C-270	x		x		6mm, no pores	
extra A			x		Elastic, no pores	
0-2	x		x	x	reference	
A-320	x	x		x	Elastic, no pores	Long fatigue life
A-200	x		x	x	Elastic, pores	Not uniform crack growth
B-240	x		x	x	Plastic, pores	Not uniform crack growth

2.9 Hardness tests

Vickers hardness tests were performed on selected specimens, using Struers DuraScan automatic hardness tester. Selected specimens were subjected to series (line) measurement at different locations, in order to investigate hardness of base metal, HAZ and weld metal. Hardness HV1 was measured on one plane (either edge or centre plane), in two series: across the beadweld and across the middle of the weld (filler pass), see Figure 2.16. Hardness tests were carried out on flat, polished surfaces, with an applied load of 1 kgf. The choice of load guarantees the result is averaged across the grains and pores, if any. The distance between two indents was 300 µm, the average diagonal of the indentation was 90 µm and each series consisted of 15-20 points. Each indentation was manually assessed with the DuraScan software.
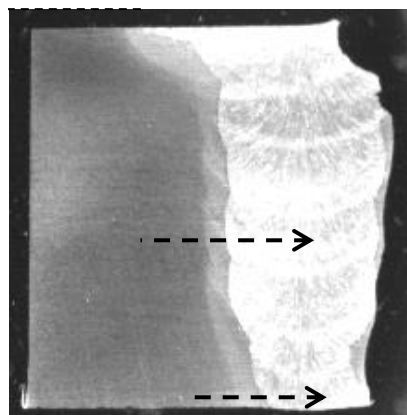
Figure 2.16 Setup of line hardness measurement. A polished and etched edge plane of a specimen is shown, with bead series and middle series marked with dashed lines. The indenter follows the marked points advancing from the left (base material) to the right (weld material).

A total of six specimens were selected for hardness testing, from the groups of specimens that were previously subjected do microscopy observations, see Table 2.5.

2.10   Tensile tests

A total of 10 tensile tests have been performed, on reference-material ("0"), elastically ("E") and plastically ("P") strained material. Tensile specimens were extracted from the leftover test coupons material, from the locations with no previously reported porosity. The overview of specimens is shown in Table 2.6. The specimens within one type group are virtually the same. It was decided to have at least 3 specimens per group to average out results.

Table 2.6 Overview of specimens for tensile testing

type	Reference (0)	Elastic (E)	Plastic (P)
quantity	3	3	4
Location [deg]	210-230	Coupon A: 120, 230, 240	Coupon B: 260-280
Name tags	0-1, 0-2, 0-3	E-1, E-2, E-3	P-1, P-2, P-3, P-4

The tensile specimens were designed as per ASTM E8, with the thickness adjusted so that the whole weld is included in the specimen cross section, see Figure 2.17. The length of the specimen was chosen to fit in the testing machine, with the gauge length as per the standard.
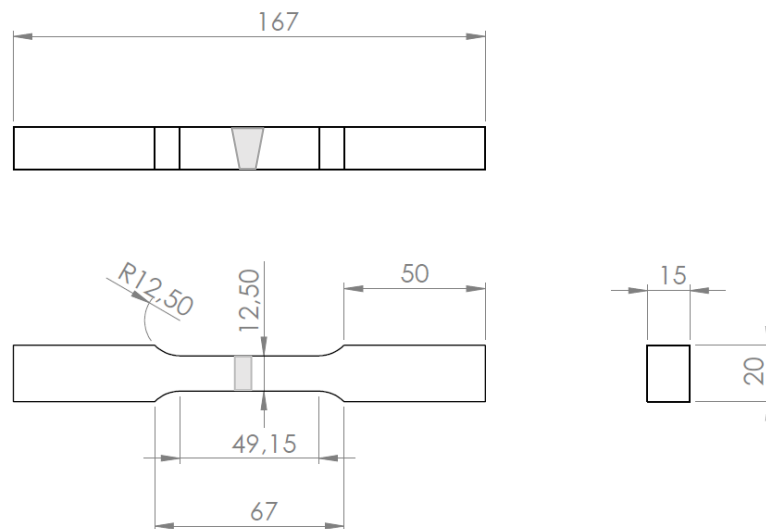
Figure 2.17 Design drawing of the tensile specimen. Weld contour is marked with a grey area.

Standard tensile tests were performed with the Instron tensile machine, with the maximum load cell capacity of 100 kN. A Zwick clip-on extensometer was attached to the specimen at the test start and then removed when 4% of total strain was reached (just before the onset of necking).

Tensile tests were performed in order to evaluate strength differences between strained and reference material. The tensile curves obtained from the testing were used for the material input for the FEA modelling.

3. Finite Element Analysis of the test coupons

A three- dimensional mechanical Finite Element Analysis (FEA) was conducted to assess the stress field in the test coupon during overstressing simulation- with refining in the weld and its vicinity. The FEM model was developed with ANSYS software (Ansys 19.0, 2017).

The rate- independent elastic-plastic constitutive equation was considered together with the Von Mises yield criterion and multilinear kinematic hardening rule. Since the material response, in this case, was described as non- linear, the software solver was set to account for the non-constant stiffness matrix [K]. Because of that, the solving process took place in multiple iterations and for each iteration, the stiffness matrix was adjusted. Contrary to the linear structural analysis, where [K] is constant and the solution is calculated in one iteration, the non-linear solution requires multiple iterations with updated stiffness matrix. Such an algorithm is called the Newton-Raphson method and it applies a load in steps and performs an equilibrium iteration at each load increment. Iterations continue until the difference between internal and external load vectors are negligibly small (within the limit).

This non-linear analysis was classified as originating from material non-linearity (N.G. Gokhale, 2008). The structural tangent stiffness matrix for material non-linearity case (without geometric non-linearity), that is updated at every equilibrium iteration, takes the form of (Criesfield, 2000):

$$\mathrm{K} = \int B^T C_1 B dV \tag{3.1}$$

where B is a strain/nodal displacement matrix, C is the constitutive matrix of tensors and dV is the volume increment. Geometric non-linearity stems from stiffness changes caused by geometric deformations. It can emerge as large strains, large rotations, stress stiffening or spin softening. None of those geometric non-linearities is related to the case under this study.

Another important difference between static linear and non- linear simulations is the choice of stress-strain definition of material behaviour. While for the linear FEA engineering stress-strain curves can be readily applied, their use for non-linear studies is limited. The choice of a correct stress-strain definition depends on the investigated material, geometry, loading case and, most importantly, the expected range of strains. For small strains (approximately up until twice the yielding strain) engineering and true strains are equal (ANSYS, 2010). Thus for non- linear analysis contained within small strain ranges, the engineering stress-strain curve can be used as well. If larger strains (exceeding twice the yielding strains) are expected in the model, the true stress-strain curve should be considered.

3.1 Material model

Building up the FEA model began with determining the right set of material properties. Each testing coupon consists of virtually three different materials- the pipe base metal, being X60 grade steel, the material of the beadweld and the supports material, being S460 structural

steel. From the modelling point of view, it was important to implement the correct material properties at the beadweld. As it was shown in Table 1.4 the beadweld is virtually stronger than the X60 base pipe metal. It would be then logical to model the beadweld material with the theoretical properties of the stronger grade from the same family, in this case, the X65 steel. However, the theoretical (as per steel standards) approach, based on the engineering stress-strain curve obtained from the Ramberg- Osgood formula (Bäker, 2007), only approximates the strength properties of the material in the study. Such approximation is good enough to be used widely in the industry when the dedicated tensile tests are not available. It must be noted, that in the case when the tensile test output data is available, it is always preferable to use it over the numerical approximations, as it provides better accuracy.

There were 10 tensile tests done in this research, on reference, elastically and plastically strained material. The results from those tests are the excellent source of input for the material model required by ANSYS to model the pipe body and beadweld material. A tensile test output of the reference-material tensile specimen was used (see Section 4.7).

The theoretical approach, based on the Ramberg- Osgood formula was implemented to obtain the elastoplastic behaviour of S460 steel that was then assigned to the supporting parts of the coupon. The S460 steel is the standard structural steel and its properties were sourced from the ANSYS material database.

The material input required to provide for the FEA non-linear analysis should approximate the real behaviour of the material as adequately as possible. The tensile test results of the investigated material are the best input solution for the pipe body and beadweld material model. Based on the input provided the software determines the elastic and elastoplastic behaviour of steel, taking hardening into account. The isotropic elasticity is derived from the Young's Modulus and Poisson's ratio, being 200 GPa and 0,3, respectively. Next, the kinematic or isotropic hardening has to be determined. Kinematic hardening rule shifts the yield surface while isotropic one increases the yield surface (keeping its centre unchanged). The choice of the correct rule depends on the type of material and is valid only for the cyclic loading (and unloading). For the monotonic loading, both rules should yield the same results. Usually, the kinematic hardening is recommended for steels as it allows for the Bauschinger effect (when unloading). Hence, the kinematic rule was chosen. Then, a bilinear or the multilinear curve has to be determined. A bilinear curve consists only of the yield stress point (when the plasticity is determined as 0) and the tangent modulus, which determines the slope of the curve past the yielding. Bilinear curve usually allows for faster computation but can yield less precise results. A multilinear point is then a good option if the computation time is not crucial and the multilinear data is available. Taken above into account the multilinear kinematic hardening (MKH) was chosen as the best possible material input for the simulation of the beadweld and the pipe body.

The true stress-strain curve, based on the tensile test of the reference material was used, see Section 4.7. A very detailed and data-dense curve had to be adjusted for the ANSYS input. The software requires the data in the true stress-true plastic strain form. The MKH curve must start with the yield point (0 plastic strain) and can be extended up to the true UTS, as

the true data cannot be approximated in the necking region. A seven-point curve was chosen from the dense data-set (APPENDIX I), see Figure 3.1.
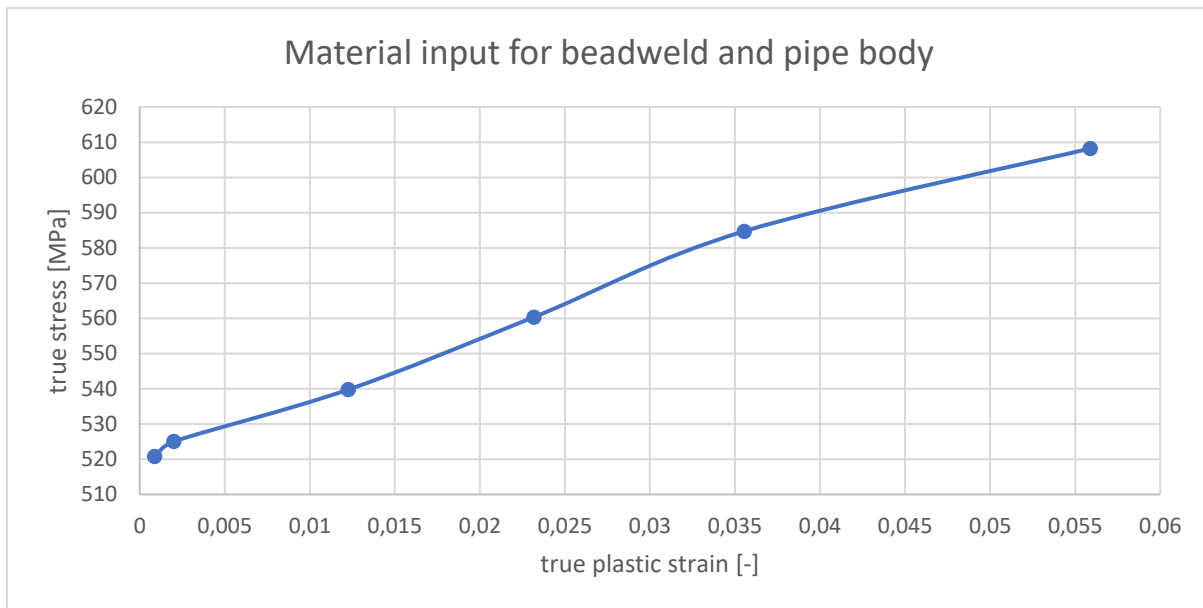

Figure 3.1 Multilinear Kinematic Hardening of beadweld material, input material curve for the FEA simulation.

3.2 Model geometry

Two coupon geometries have been considered in the FEA modelling to differentiate between two beadweld thickness cases. One case represents pulling on the beadweld, i.e. pulling on the 3 mm thick weld. The other case represents pulling on the hot pass, i.e. stressing the 6 mm thick weld. Each case was modelled separately with the same material parameters and a similar mesh.

Model geometry ought to simulate the real testing coupon as precisely as possible, with the main focus being on the beadweld. The coupon model has been virtually divided into 32 bodies, seamlessly connected into one part (see Figure 3.2). This operation allowed precise meshing around the beadweld area and saved computation time. Beadweld is essentially the contact between two pipe pieces (parts) that has been welded together (rigid bond). The bonded type of contact has been chosen for the beadweld as well as other contacts in the body as no sliding or gap openings are allowed.

Beadweld was modelled with the 3,2 mm fillet radius, to simulate the actual geometry that is created at pipe ends bevelling operation, see Figure 3.3. Even though the actual beadweld shape may differ from the bevel it was decided to model it with a constant 3,2 mm radius (like the original bevel) for the consistency and ease of modelling.
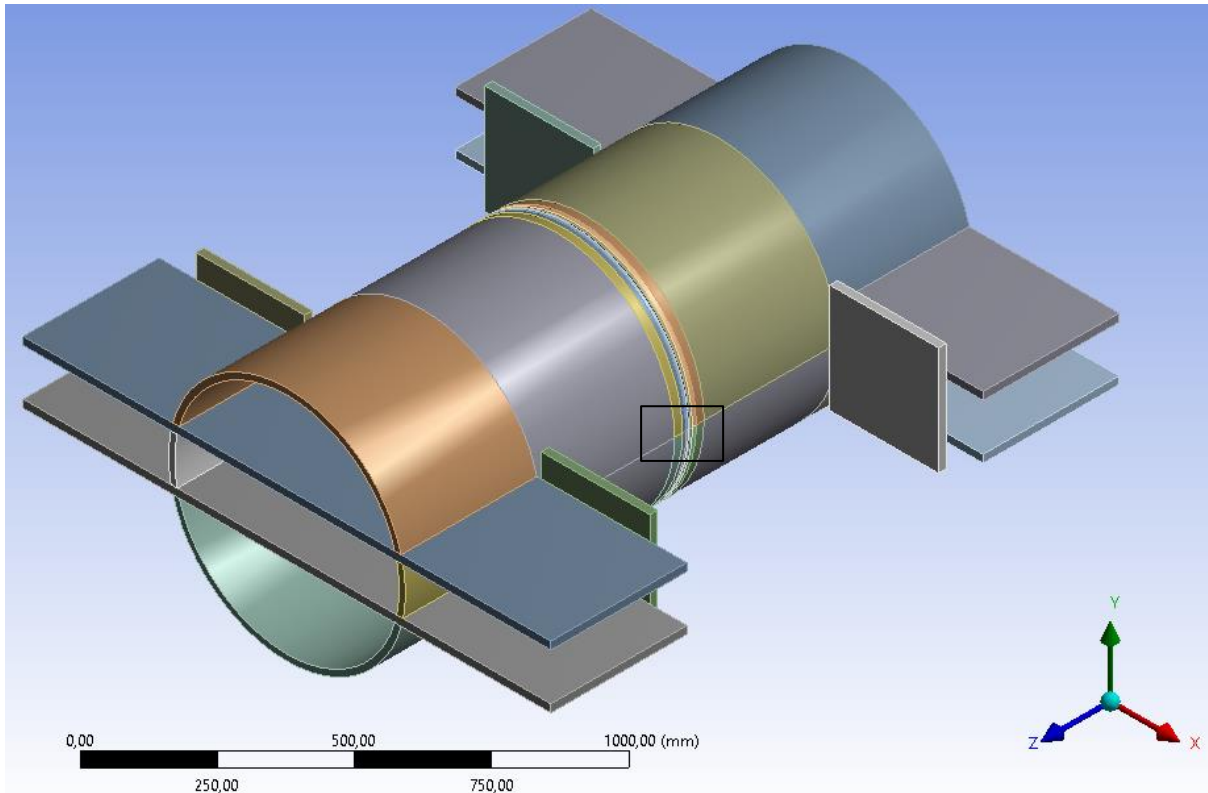
Figure 3.2 Test coupon geometry modelled for FEA simulation. Different colour indicates virtual parts. Detail from Figure 3.3 is marked with the black rectangle.
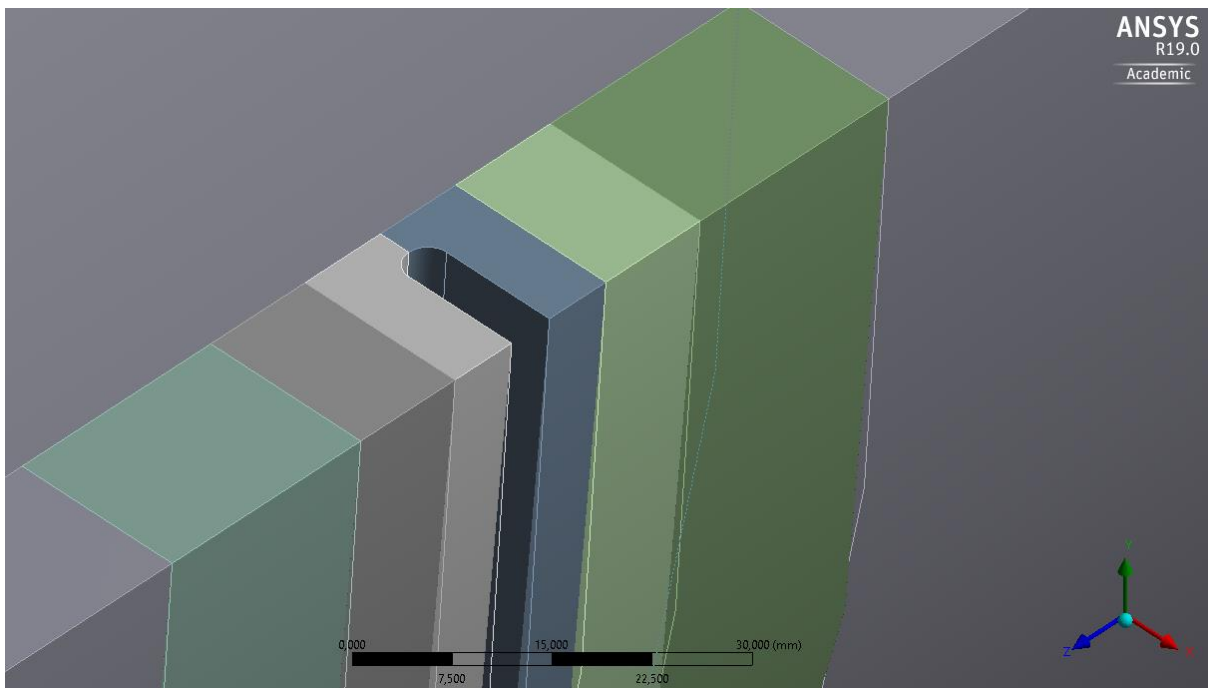
Figure 3.3 Cross-section view of pipe wall thickness including the 3 mm thick beadweld.

To save computation time different model variations were considered, namely modelling a half or a quarter of the model. Modelling only a part of the total coupon was possible thanks to its symmetry. A half model was created by splitting the full geometry in Figure 3.2 along the YZ plane. Half model computation time was shorter than the full model, however, the difference

was not drastic. The computation time of a full model, with optimized mesh, was satisfactory, thus it was decided to proceed with the full model geometry.

3.3 Mesh

For reliable stress and strain distribution results, it was important to obtain a uniform, fine and conformal mesh at the beadweld. To save computation time it was desired to create a coarse mesh (element size 10 mm) far away from the beadweld and at the supports. Smooth element size gradient was achieved by separating the model into virtual parts and by using adequate meshing techniques (body sizing, edge sizing).

Hexahedron elements were chosen as the most suitable for precise beadweld stresses investigation. Ansys references those elements type as SOLID186 Homogeneous Structural Solid (HEX20 in short). Those elements contain 20 nodes, each having 3 degrees of freedom. This higher- order element is recommended for non-linear models as it supports plasticity well. Only hexahedron (HEX20) elements were allowed in the beadweld and in its direct vicinity. Further away small numbers of other element types, like SOLID187 3-D 10-Node Tetrahedral Structural Solid (TET10), WED15 (wedges) and PYR13 (pyramids) were also allowed.

The same meshing approach and techniques were used for all the models used in this study- full ones, half ones, of 3 mm and of 6 mm bead thickness. The slight changes in geometry resulted in slightly different meshes, however, sensitivity study showed that with the appropriate mesh refinement the results are mesh independent. The optimal mesh refinement at the beadweld was found to be 1 mm (element size). The example overview of meshing made for the models is shown in Figure 3.4.
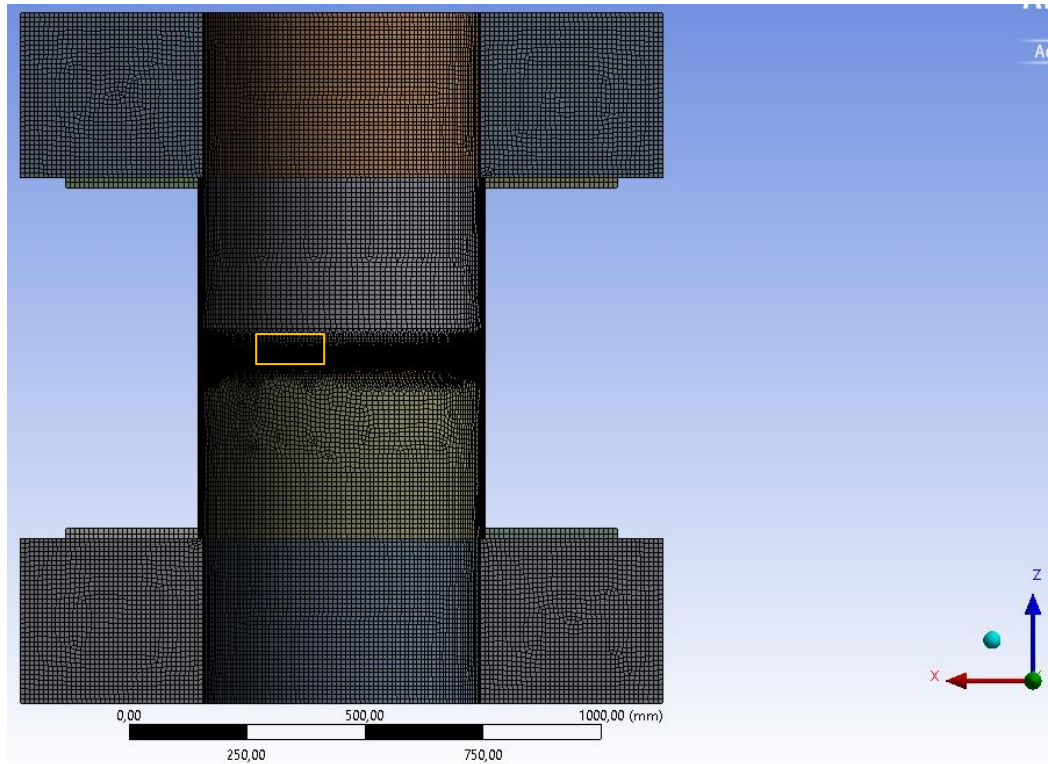
Figure 3.4 Overview of a mesh of the full model, with 3 mm beadweld. Detail from Figure 3.5 is marked with the yellow rectangle.

Meshing with Sweep Methods and adequate, gradual sizing for virtual (transition) parts were used to obtain a smooth element size gradient, see Figure 3.5. A gradual element size transition from 10 mm, through 8 mm, 4 mm, 2 mm to 1 mm is visible.
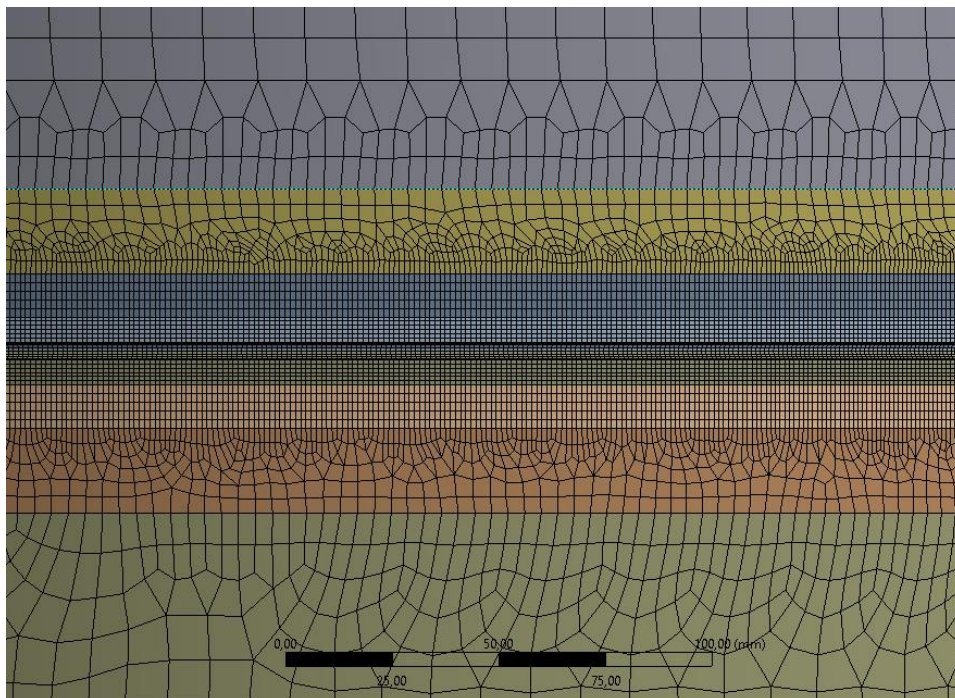
Figure 3.5 Zoom in at the beadweld area. The transition between coarse mesh and refinement is visible.

An additional look inside the body thickness is needed to assess the mesh quality, see Figure 3.6. A section along the plane across the coupon was made. It revealed that the beadweld and its direct vicinity consists of uniform and conformal hexahedron only elements.
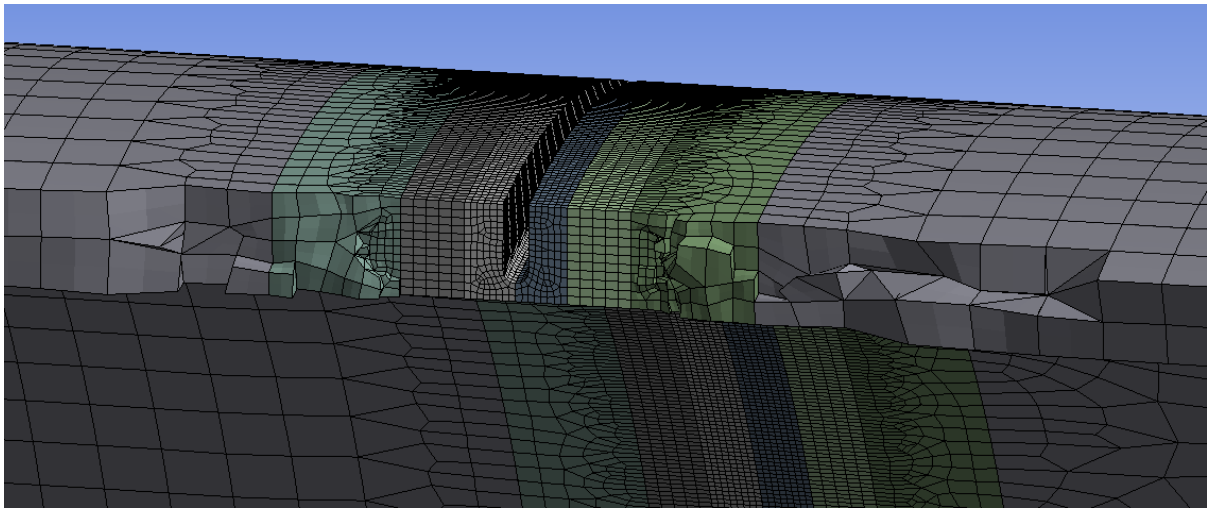
Figure 3.6 A section through the pipe to see the inside of the mesh; 3 mm beadweld model.

Some element type and size irregularities were revealed at the transitions. Those mesh aberrations were unavoidable at the transition points. However, dividing the model into parts allowed to keep the unwanted element types (prisms, wedges) away from the beadweld. Presence of alien elements among majority oh hexahedron is unwanted as it may disturb the stress distribution. Highlighting only the unwanted types of elements in the mesh shows that they are located far away from the beadweld, see Figure 3.7 for the example of tetrahedron elements. This guarantees that stress and strain results will not be affected by mesh quality.
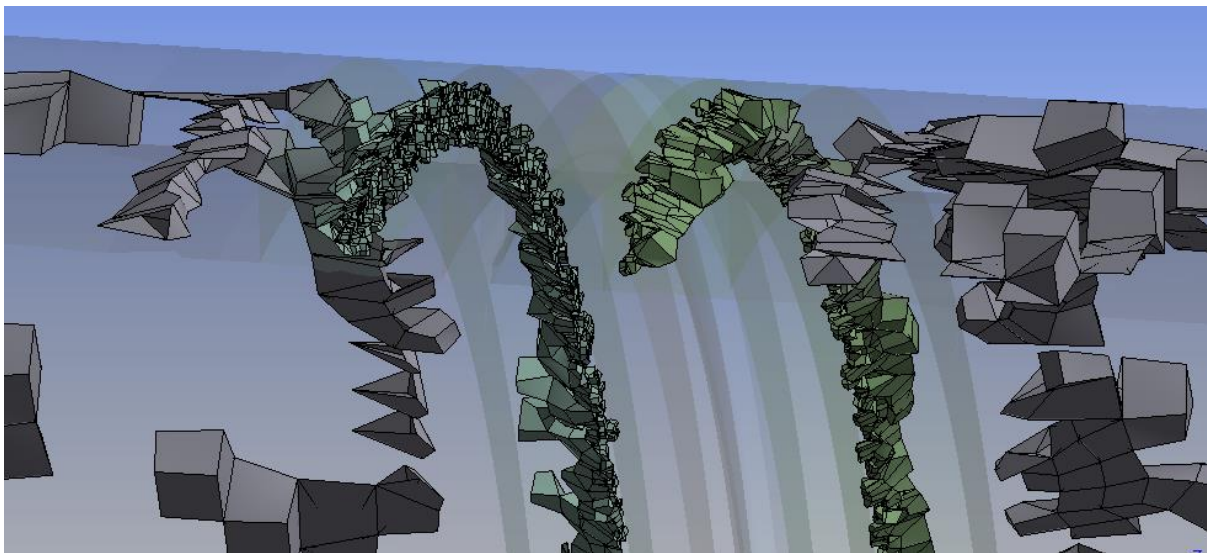
Figure 3.7 Section view of the mesh with only tetrahedron elements visible. The middle part- beadweld- is clear from tetrahedron elements.

As mentioned before, mesh for a 3 mm beadweld model and the 6 mm beadweld model can be slightly different due to a slight change in geometry. A cross section of the 6 mm beadweld

mesh is shown in Figure 3.8. When compared with Figure 3.6 the similarity in both mesh types is clear.
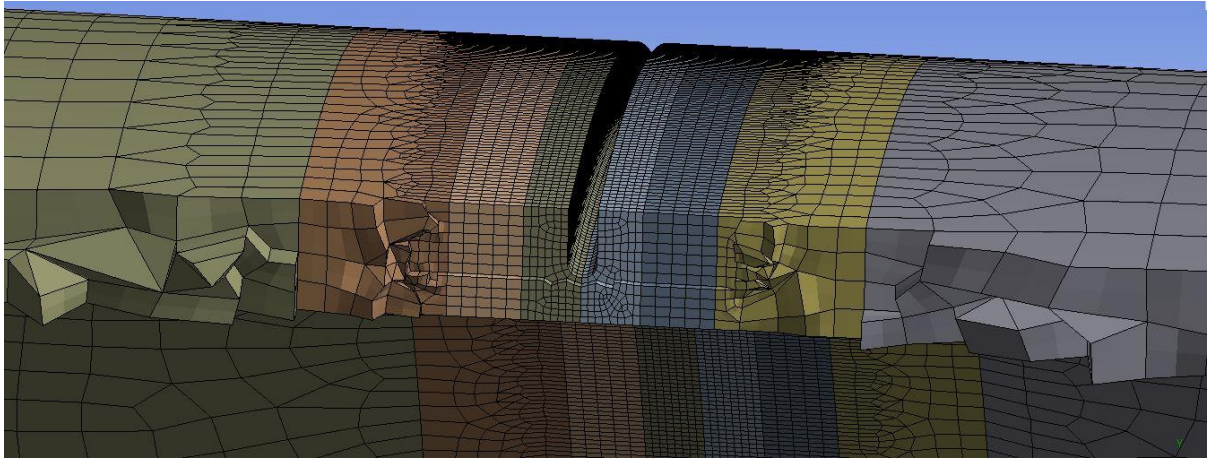
Figure 3.8 A section through the pipe to see the inside of the mesh; 6 mm beadweld model.

For each model studied the mesh quality was checked. Parameters used to asses that quality was the number of elements, the number of nodes, aspect ratio and Jacobian ratio. Rule of thumb specifies that the average aspect ratio should not exceed 10 and the Jacobian ratio (which indicates how much elements diverge from their ideal shape) should be kept as low as possible, with 1 being the lowest (meaning that all elements have a perfect given shape). Those parameters for both 3 mm and 6 mm models are shown in Table 3.1.

Table 3.1 Overview of mesh quality parameters for the 3 mm and 6 mm beadweld models.

model	# of elements	# of nodes	Average aspect ratio	Average Jacobian ratio
Full 3 mm	864695	3539273	2,53	1,51
Full 6 mm	880239	3575279	2,58	1,52

The mesh was optimized and its good quality was confirmed. It can be concluded that the results of the FEA simulation are mesh- independent.

3.4 Boundary conditions and loading

Forces were applied to the model in such a way to simulate the loading mode described in section 2.2. Four force points were located at the square support flanges in the Z direction (longitudinal coupon direction). Since two identical jacks were used for the overstressing simulation it was assumed the force was equally distributed over all four flanges, see Figure 3.9. Hydraulic pressure [bars] applied to the coupon was then converted to the force [N] input used in the FEA model. Example calculations for the coupon A are shown below:

According to Table 2.1, 631 bars were exerted on the coupon. The equivalent force F [N] can be calculated as $F = 10 * p * A$ where p is the pressure of one jack [bars] and A is area of the jack cylinder touching the flange. Jacks of cylinder diameter of 165 mm were used and their area was calculated as follows:

$$A = \pi * \left(\frac{d}{2}\right)^2 / 100 \ [cm^2] \tag{2.6}$$

Which resulted in the area of one cylinder being $A_j = 213{,}82 cm^2$. Force exerted by one jack was then determined as:

$$F = 10 * 615{,}5 bar * 213{,}82 cm^2 = \mathbf{674{,}6021 \ kN} \tag{2.7}$$

Thus total force the coupons were subjected to equalled 1349,2042 kN (see Figure 3.9). Presented loading mode was used for each force application in all models (representing coupons A, B and C).
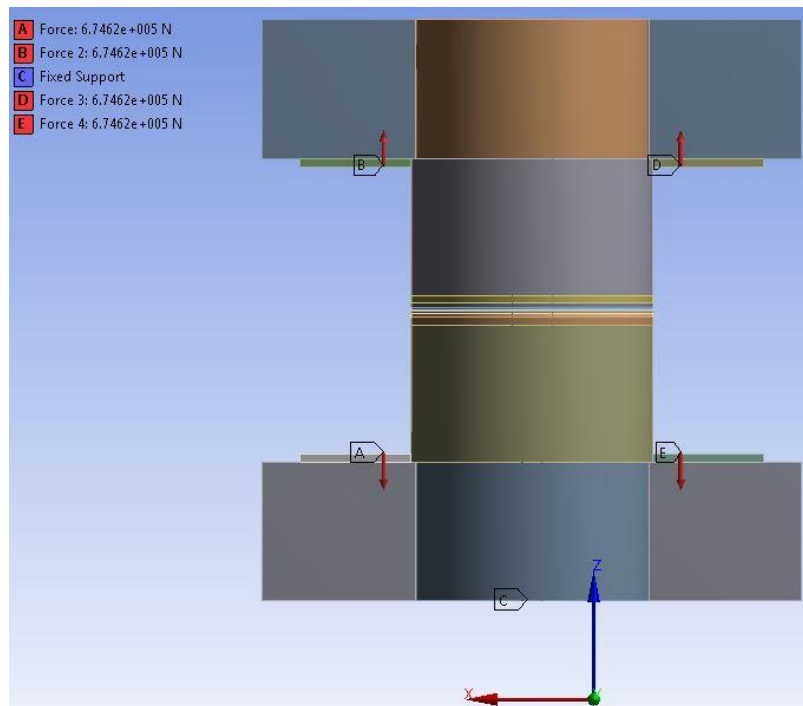

Figure 3.9 Load application and boundary conditions applied to a 3 mm beadweld, full geometry model. Red arrows indicate on which surfaces the force was applied, they do not indicate the exact point of load application.

Full coupon geometry was modelled in all simulations, which allowed for simple modelling of boundary conditions. During the overstressing operation the coupon was welded to the steel deck of the vessel. This situation can be simply modelled as fixed support in ANSYS, assuming rigid body behaviour with no displacement or rotation in any axis. Fixed support was applied to all model surfaces in the XY plane of the coupon, see point C on Figure 3.9. The force reaction and the moment reaction can be used to check the adequacy of the chosen boundary conditions. Both of those reactions should be zero or negligible to confirm no unwanted movements or displacements occurred. For the "3mm" model the reaction results are presented in Table 3.2.

Table 3.2 Force and Moment reactions recorded for the full geometry "3mm" model.

	Max total value over time	Min total value over time
Force reaction	8,842 N	0,0544 N
Moment reaction	25499 Nm	2516,5 Nm

Even though the reactions are non-zero, their magnitude is small enough when compared to the applied loads and can be negligible. The registered moment reaction may be the consequence of the secondary bending induced in the structure by the beadweld geometry. The applied boundary condition is then considered adequate.

3.5 FEA results- stress and strain distributions

Results of full models of 3 mm beadweld and 6 mm beadweld were considered for the sake of this research. The 3 mm full model represents the case of coupons A and B, while the full 6 mm model represents the case of the coupon C. The analysis was focused on stress and strain distribution along the beadweld inner and outer edges and through the beadweld thickness. Additional studies were carried out with different material models (true and engineering curves based on Ramberg-Osgood approximation for the X60 steel), different beadweld geometries (with removed bevel so that the beadweld upper surface makes the right angle with the wall), partial (half or quarter) coupon geometries and with different (severely refined) mesh. All those studies led to the final, optimal models, that best represent the stress-strain state during the overstressing simulation and are the most computationally efficient.

The obtained FEA results will be presented for the 3 mm and 6 mm beadweld thickness models. Additionally, comparisons between nodal and elemental stress/strain results, beadweld shape (rounded with a 3,2 mm fillet and no fillet designs), kinematic/isotropic hardening and stress evolution in steps will be presented.

The 3 mm beadweld, full geometry model

Figure 3.10 shows the overview of all von Mises stresses in the model. It is clear that the construction can easily sustain the applied loads, with maximum local stress located at the beadweld and the minimum at the end of the support plate. Slightly higher stresses (but still below the yield) are also found at the support/pipe body interface, where the plate geometry generated stress concentrations. Nevertheless, the test coupon proved to be structurally safe during the overstressing simulation.
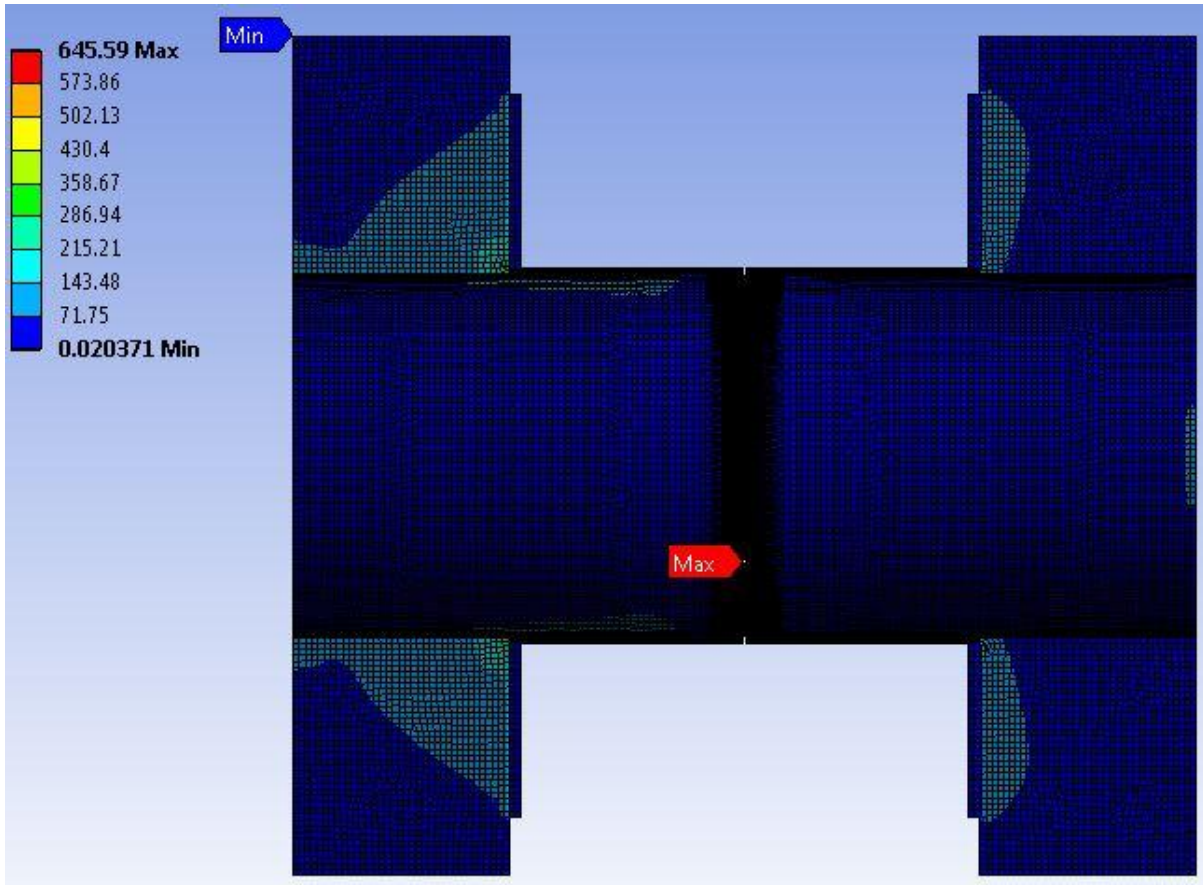
Figure 3.10 An overview of von Mises stresses; 3 mm, full model, X-axis view

A more in-depth look into the beadweld area stresses (Figure 3.11) shows that von Mises stresses above ~500 MPa (determined as the onset of plasticity, see Figure 3.1) are found exclusively at the beadweld outer area. Stress distribution shown in Figure 3.12 indicates that the highest stresses are located on the outer surface (edge) of the beadweld, with much lower von Mises stresses distributed on the inside surface of the coupon. This figure also presents how the stresses spread out from their source (force application points) at 3 and 9 o'clock.
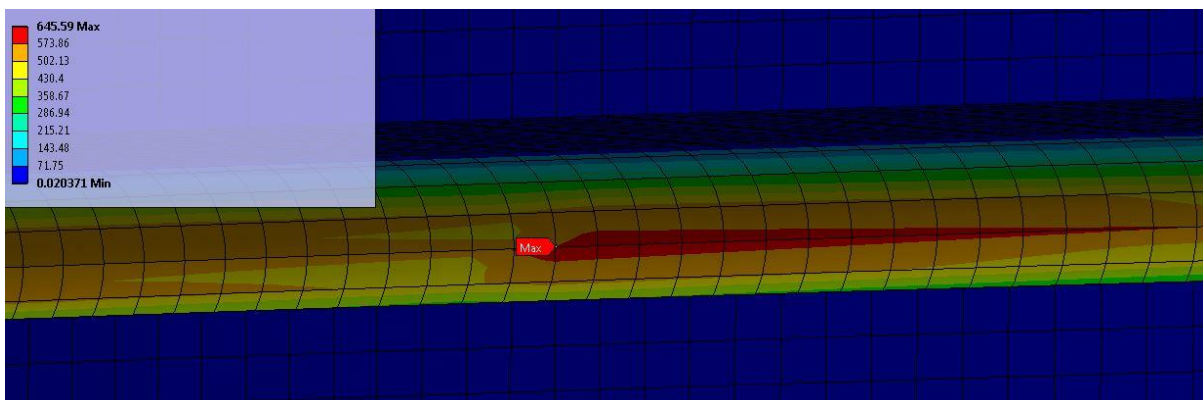
Figure 3.11 A zoom-in view at the maximum stress location showed in Figure 3.10. The outer side of the coupon.
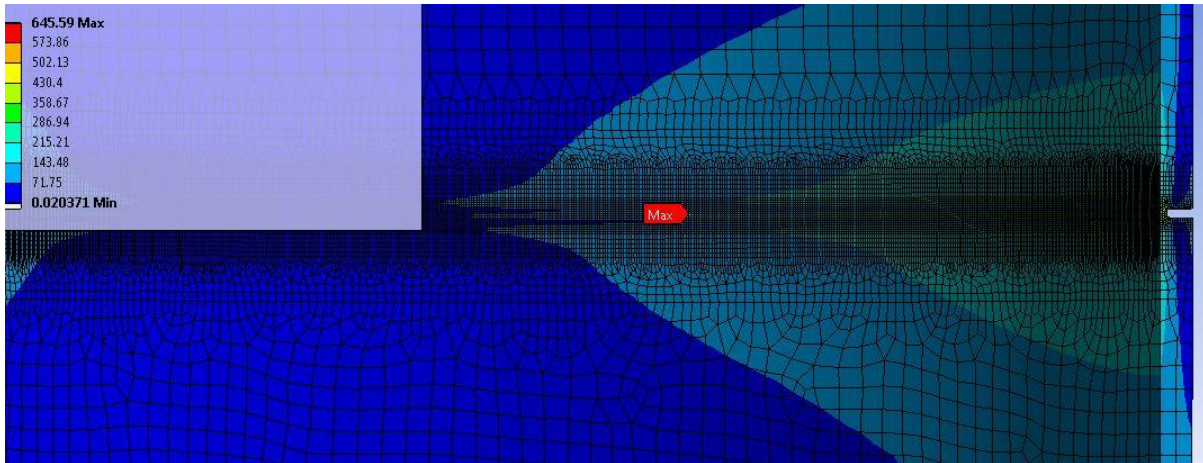
Figure 3.12 A zoom-in view at the maximum stress location showed in Figure 2.15. The inner side of the coupon. The red "Max" indicator, though still visible, indicates values located on the other side of the pipe wall.

It was found that the maximum von Mises stresses are located at the beadweld outer diameter (OD), which is the outer edge of the 3 mm beadweld, shared by two pipe bodies (see Figure 3.13). It was then decided to investigate stress-strain distributions along both, the inner and outer edges of the beadweld (ID and OD). Two virtual paths were created on those edges so that stress and strain results can be scoped to those paths.
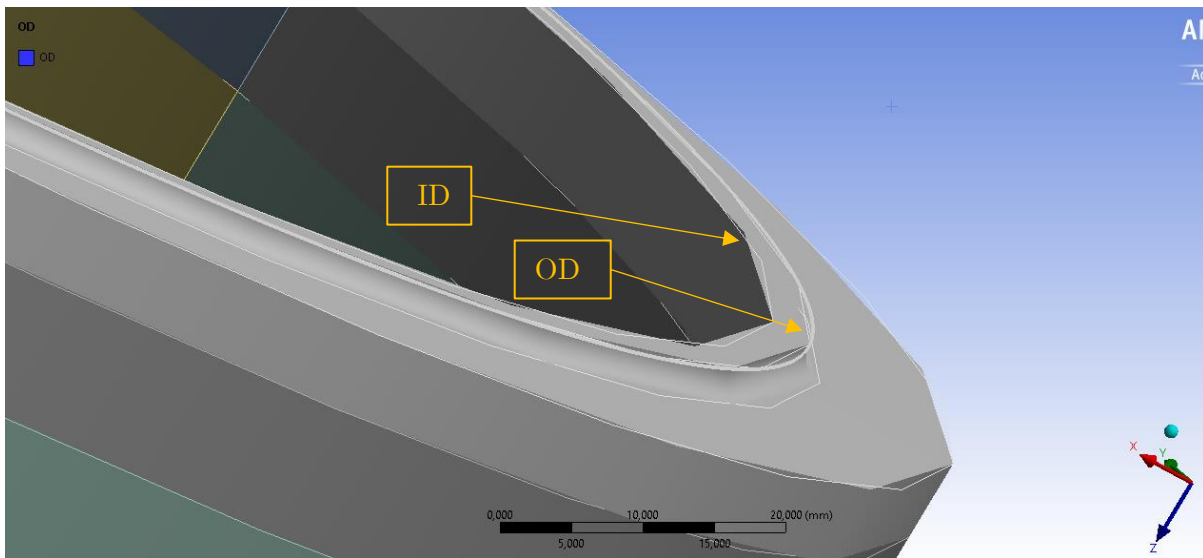
Figure 3.13 The bevelled end of one pipe body (the other pipe body is hidden on purpose for the clear view). ID and OD paths are marked on the inner and outer edge of the beadweld, respectively.

Von Mises stress distribution along the OD path is shown in Figure 3.14. The results displayed here are the *averaged elemental nodal* results. The maximum stress in the structure is found on that edge, which confirms that the loads applied to the supports were concentrated in the beadweld. Figure 3.14 shows the von Mises stress distribution along the OD edge. The distribution starts at point "1" (at the 9 o'clock) and proceeds counterclockwise to finish at the same point. The areas marked with red on Figure 3.14 has been stressed above 510 MPa (yield point), thus are strained plastically. As it was expected, areas further away from the

61

force application points experienced gradually lower stresses, up to the minimum values (215 MPa) at 12 and 6 o'clock.
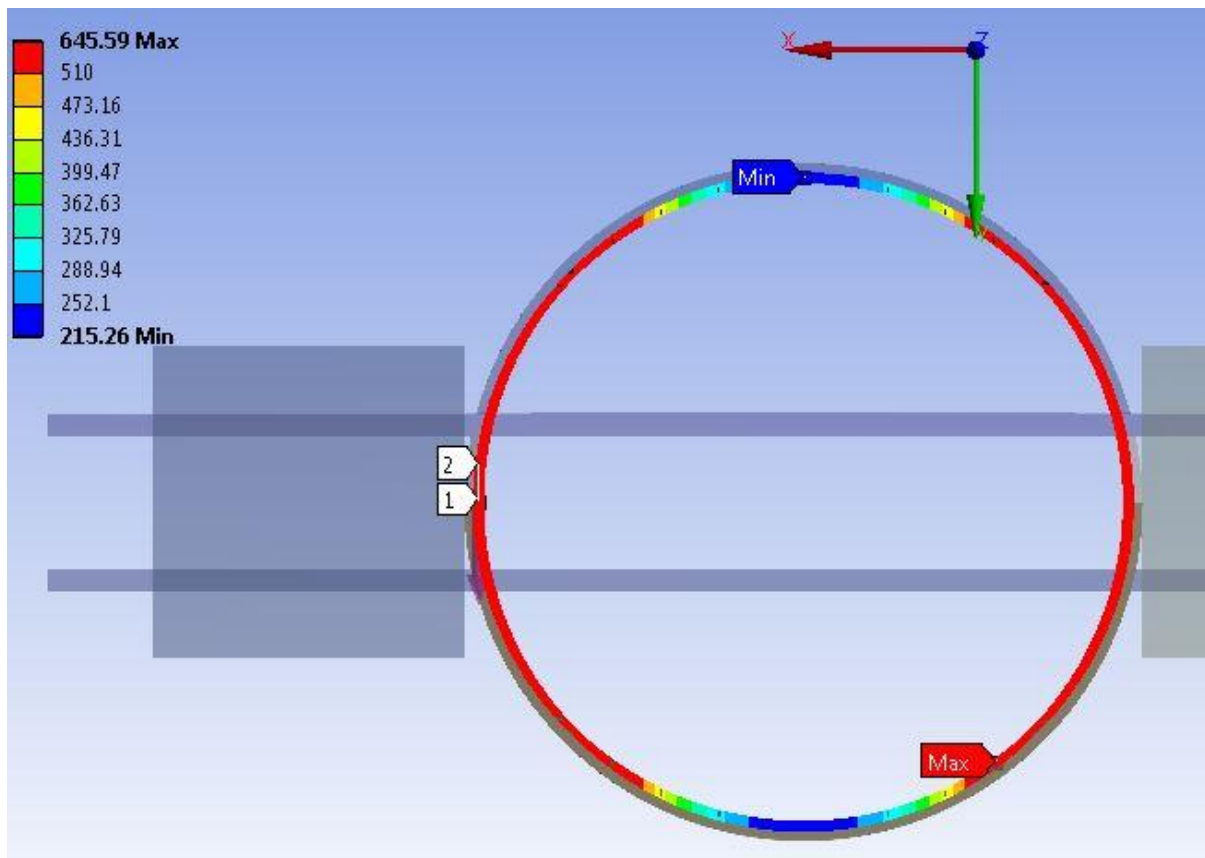
Figure 3.14 Von Mises stress distribution along the OD path of the 3 mm beadweld full model. Z-axis direction plane view. 1 and 2 indicate the OD path start and finish locations, respectively. The nodal averaged results are shown.

An interesting profile of the stress distribution (*average nodal display*) was observed, see Figure 3.15. The von Mises stress at the OD edge is presented in terms of distance [mm] from point "1" to point "2" (9 o'clock), counterclockwise direction (see Figure 3.14). We observe four symmetrically located maximum stress points and two minimum points located symmetrically at 6 and 12 o'clock. Maxima (~645 MPa) are located on both sides of force application points. After each maximum a sudden stress drop is observed, followed by a more steady stress increase up to 3 (or 9) o'clock position. After that the stress decreased slowly again to peak suddenly again at the other maximum location on the other side of the force application point. This twofold symmetrical distribution clearly emanates from the loading mode and the whole setup geometry.
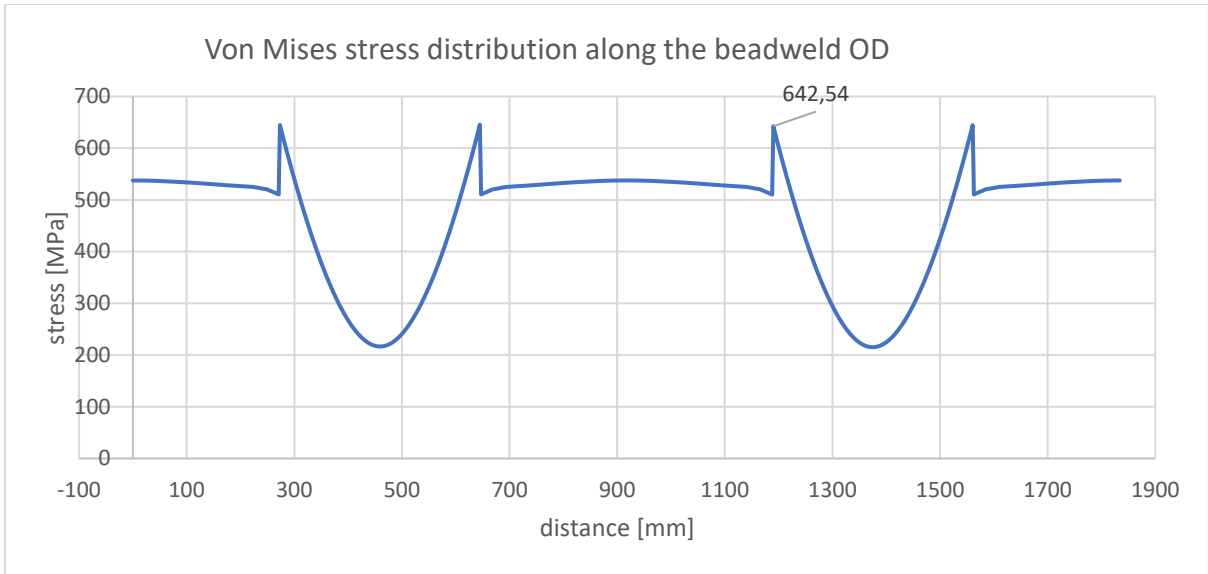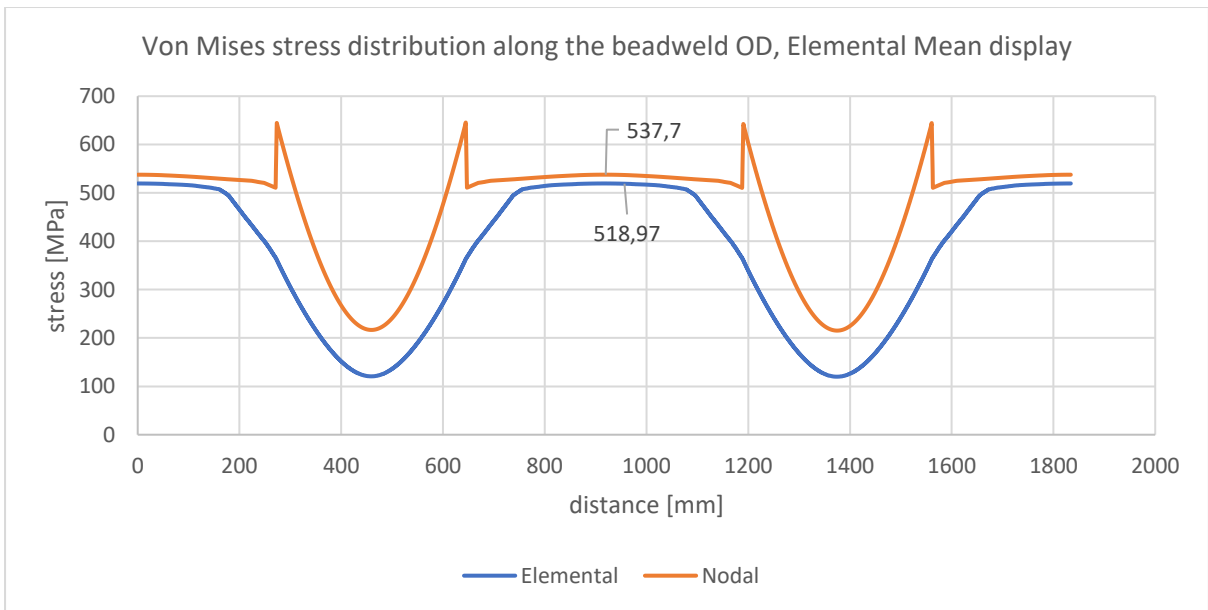
Figure 3.15 Equivalent von Mises stress distribution along the beadweld OD; 3mm model. Average nodal display. The starting point (0 mm distance) is the point "1" marked in Figure 3.14. Such profile was observed exclusively in case of plastically strained material.

An interesting change is introduced when we look differently at the same results. Another than default- average nodal- results display option is introduced. Figure 3.16 presents the Von Mises stress distribution at the OD edge, this time in terms of the *elemental mean* results (blue curve). The default nodal results (orange curve) are kept for comparison.

Figure 3.16 Equivalent von Mises stress distribution along the beadweld OD; 3mm model. Elemental mean and averaged nodal displays.

To understand the cause of the differences between the curves an explanation of the average *nodal* and *elemental* results is needed. Those displays are virtually two ways of looking at the same results. During FEA the solver evaluates stresses (and strains) at the Gaussian points, i.e. specific locations inside the elements. The number of those points in each element is determined by the element quality and type. Then, the results at those points are extrapolated

to the element's nodes. In a 3D body, each node is shared by multiple elements. Hence, Gaussian points from many elements can contribute to the result at one node. *Nodal* values are the average of all nodal results from the elements contributing to that node, see Figure 3.17 (Nodal versus Elemental Stresses, 2008).
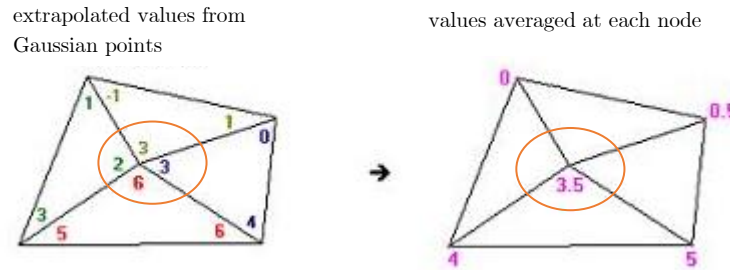
Figure 3.17 Graphical explanation of the nodal average results computing.

Another way to look at the Gaussian results are the *elemental* values. In this approach, the result at the element is considered as the average over the nodes of this element, see Figure 3.18.
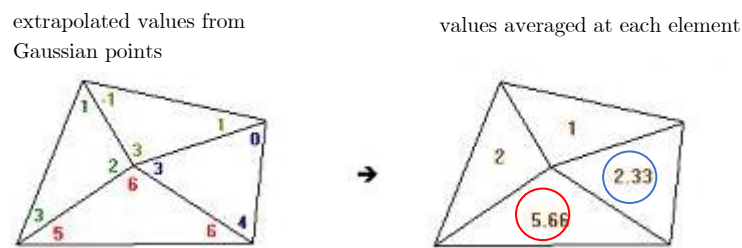
Figure 3.18 Graphical explanation of the elemental average results computing.

Since the approach to averaging the results is different for those two methods, that explains the stress values differences in Figure 3.16. The comparison between both results is usually recommended to check the coarseness of the mesh. By the rule of thumb, the good refinement is reached when the maximum stress difference between nodal and elemental results is not higher than 10%. However, this is true in the general cases of stresses across bodies and surfaces. In the case of singularities or edges, i.e. entities with big local stress gradients across the elements, it is not always the case. In the presented case (Figure 3.16) the ratio of nodal/elemental results at the 3 o'clock is 538/519 thus 3,7%. However, the ratio measured at a different location, say 6 o'clock, is higher (80%). The recommendation, in that case, is to change the element type to the higher order and to decrease the element size (locally, in the area of interest). However, the mesh in consideration here is already built of HEX20 (a high-order element) with a fine size (1 mm). The differences in stress may also stem from another factor- the results scope. It must be remembered that the results in Figure 3.15 and Figure 3.16 are scoped to the edge, thus averaging across the elements and nodes is limited to that edge only. Less number of points in the sum may result in less precise results.

Keeping the above explanation in mind it is easier now to understand the stress behaviour at the OD beadweld edge. The nodal results present the stresses registered at the nodes belonging to the OD path only. The elemental results present the stresses of the elements belonging to

the path, thus average across more points. It explains the four sharp stress peaks present in the nodal results and their absence when the stress is averaged within the elements. The stress peaks in the nodal results are the consequence of the plasticity in the material. Plastic deformation is not a threshold phenomenon but a gradual process. With that in mind, the nodal stress curve can be explained starting from the 3 o'clock position (equivalent to approx. 913 mm distance). This is the location where the plasticity first started when the yield point was reached and then, as the applied load increased, the plastic region spread out further away towards 12 and 6 o'clock. The evolution of the plasticity distribution can be well seen when the total load is applied in steps, see Figure 3.19.
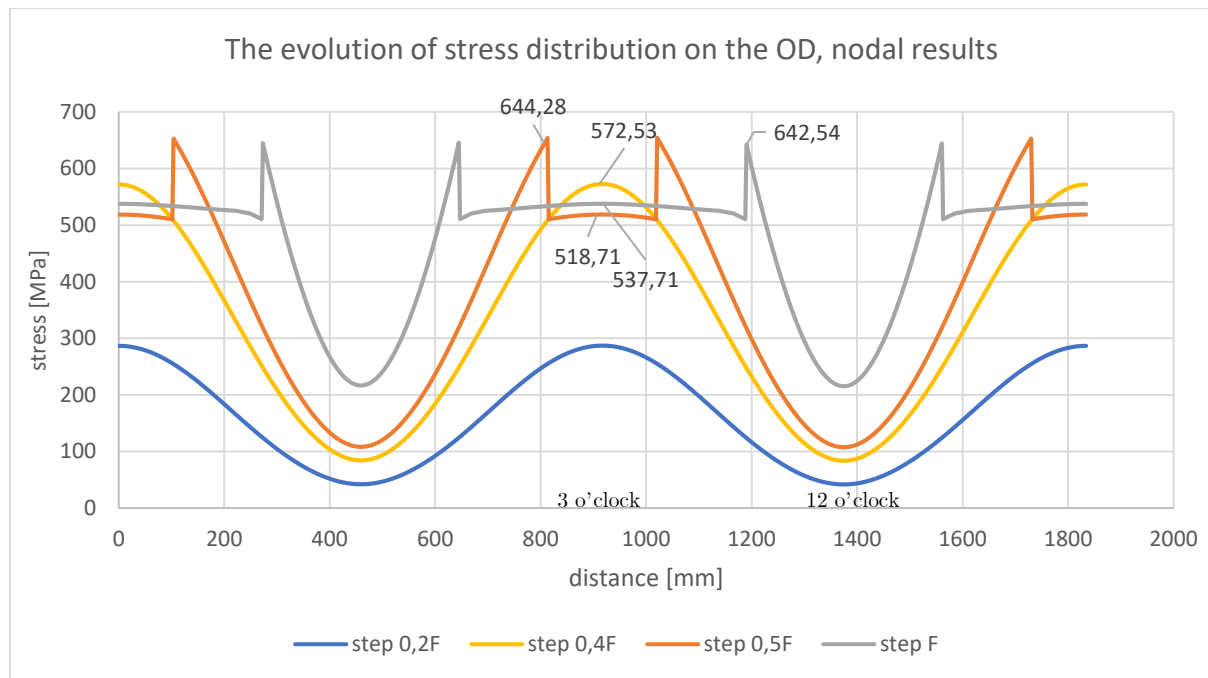
Figure 3.19 Evolution of the stress distribution profile when the load is applied in steps.

Total load F determined in *Boundary conditions and loading* was applied in 4 steps: 0,2F, 0,4F, 0,5F, F, corresponding to 1,35E5 N, 2,62E5 N, 3,37E5 N and 6,75E5 N, respectively. When the 0,2F load was applied the beadweld was stressed entirely below the yield, hence only elastic deformation occurred. It is also true for the 0,4F step, which corresponds to the amount of load that stresses the beadweld just below the yielding. Both curves, blue and yellow, present a smooth, undisturbed distribution profile. When the load is slightly increased (up to 0,5F) then the very different stress profile is observed. The transition from the smooth stress profile to the "sharp peaks" stress profile is then triggered by yielding. The maximum stress values of 0,4F are different from the 510 MPa yield point determined in the kinematic hardening curve, however, one has to keep in mind that the results presented by ANSYS are the averaged ones (nodal averaged in this case). Increasing the load even further to the full capacity (step 1F) results in a similar stress profile: identical 4 stress peaks are observed but their location is shifted- they are located even further away from the force application point. The (almost) constant stress area between the peaks for the 1F step increased slightly compared to the 0,5F load step. The maximum stress values at the peaks in steps 0,5F and 1F are virtually the same. It means that stressing above the yield plastically deforms the given element (locally) so that it cannot bear the loads anymore and the loads are distributed

65

between the adjacent elements. The cause of it is that after yielding the material behaves (almost) perfect plastically and deforms without a real increase in applied load. The noticeable change is the stress distribution to other (adjacent) elements.

The maximum stress values, registered for the steps in the plastic regime (0,5F and 1F), indicate stresses of approx. 644 MPa, higher than the UTS value defined by the material input (608MPa). To understand that two explanations are needed: first, how does the software behave when it reaches the end of the material curve and secondly, the physical explanation of the material behaviour. The situation of a beadweld loaded in tension can be compared to the notched bar during a tensile test. It is important to realize that the state of stress in the beadweld (acting as a notch) is triaxial, in contrary to the uniaxial stress state in a smooth bar loaded in tension. The material input, which is the benchmark data, has its source in a tensile test made with smooth specimens. Thus, the values of maximum stress in the notched (beadweld) case cannot be readily compared with the true stress-strain curve used as input data. The differences in yield and tensile strength, between the smooth case (material input) and a notched beadweld, are caused by the stress triaxiality, which increases with the notch radius (Chang-Kyun Oh, 2007). The software deals with this behaviour by adopting a bi-linear behaviour at the end of the material curve, i.e. it assumes the material behaviour based on the last tangent modulus (almost horizontal) and the yield strength.

Clearly, we observe two very different material behaviours in the steps 0,5F and 1F: plastic behaviour in between the peaks (around 3 and 9 o'clock) and elastic behaviour outside of the peaks (around 6 and 12 o'clock). A look into equivalent strain distribution along the OD edge, for the 1F (total) load, confirms those findings, see Figure 3.20.
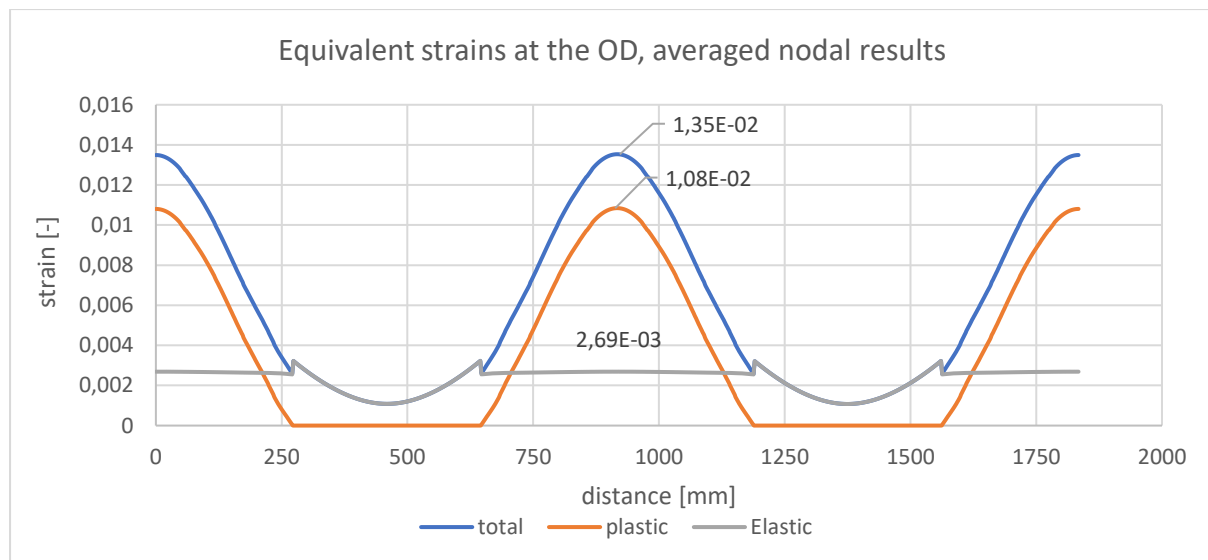

Figure 3.20 Distribution of strains along the OD path, 3 mm full model. Nodal results displayed.

Total, plastic and elastic (equivalent) stresses are plotted against distance from the beginning of the OD path (the same as in the case of stresses). The averaged nodal results are presented. The plot of plastic strains clearly indicates that only some parts of the weld are plastically strained. Those are, indeed, the areas around the 3 and 9 o'clock already identified earlier. The occurrence of plasticity (around 270 mm, 645 mm, 1200 mm and 1560 mm) coincides with

the sharp peaks in the elastic strain distribution. Comparing Figure 3.16 and Figure 3.20 it becomes clear that the shape of the elastic strain profile overlaps with the shape of the stress profile. Also, between the peaks, the elastic strain is constant. Plastic strain is maximum at the 3 and 9 o'clock, decaying until it reaches 0 at the locations where elastic strain and stress experience the abrupt peaks.

The aggregate graphs of strains and stresses allow identifying the cause and nature of the stress and strain sudden peaks. The locations of the peaks along the OD path indicate the interface between the yet-elastically-strained and just-plastically-strained material. This interface is so local that it is only abruptly noticeable on the nodal scale and is much less profound on the elemental scale (see Figure 3.16). Scoping to only edge nodes makes it possible to see how neighbouring nodes at that specific location differ in terms of stress (and strain) as a consequence of the drastically different properties of the material. Looking at both results- nodal and elemental- is beneficial as it gives the broader understanding of the simulation's results and hence, the actual stress states in the construction.

Nodal results show the severity of the extremums, whereas elemental results give a more reliable overview of the stresses at the location of interest. However, the question now is which scoping and results evaluating approach is most suitable for determining the reference stresses in the beadweld. The discussion above concerns only the OD edge of the beadweld. However, the interest of this research is in the 3 mm thick volume of the material at the beadweld, not only I n a particular edge. Because of that, the additional analysis of stresses at the beadweld inner diameter (ID) and of stresses through the beadweld thickness were conducted.
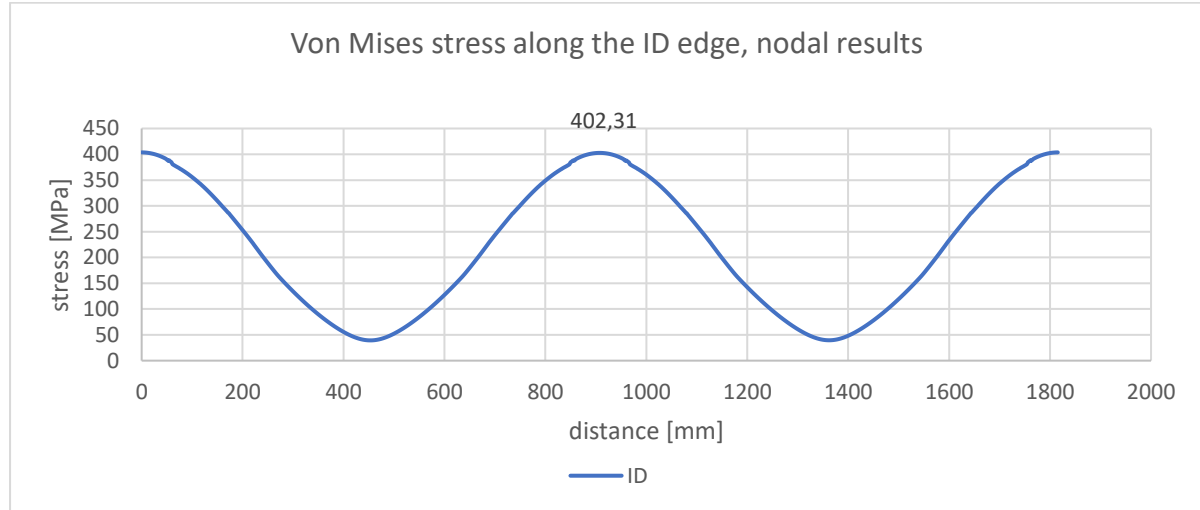

Figure 3.21 Equivalent stress distribution along the ID edge, nodal results displayed.

Figure 3.21 shows the Von Mises stress distribution along the ID edge of the beadweld, the nodal results are shown. The maximum stress value is much lower than at the OD at the same location (402 and 537 MPa, respectively). Due to the absence of the stress concentrators at the inner wall of the pipe, the lower stresses at the ID were, indeed, expected. Lower stresses at the ID edge result in the "smooth" distribution, specific to the elastic distributions shown in Figure 3.19 for the lower load steps. The stresses at the ID edge are low enough so that this edge entirely remains in the elastic range. Such a difference between stresses at the OD and ID indicates that the stress gradient is present across the 3 mm beadweld thickness. It can be

67

concluded from the graphs that the magnitude of this gradient most likely varies per location. Hence, it was decided to analyse the through thickness stress at the maximum stress location (around 4:30 o'clock) and at 12, 3, 4 and 5 o'clock, see Figure 3.22. Since the stress results are symmetrical, the results at those locations can be expected on the other quadrants of the circumference. The gradient was measured from the OD to the ID (see the arrows showing the direction).
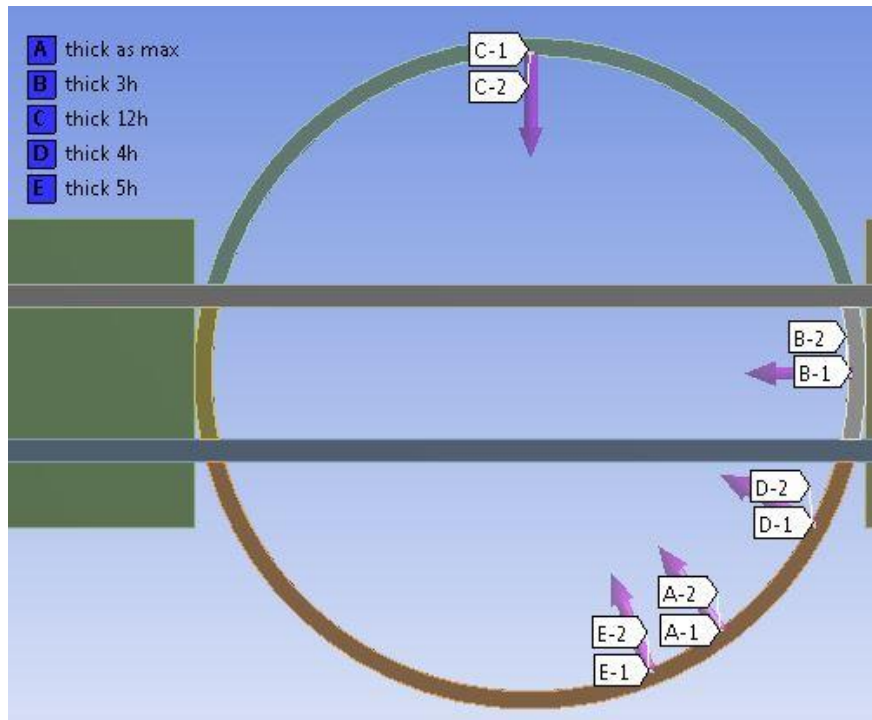

Figure 3.22 Locations of the through- thickness stress a.

Figure 3.23 shows the combined results of all the through- thickness stress results at the given locations. The results are shown as the Von Mises stress, averaged nodal values.
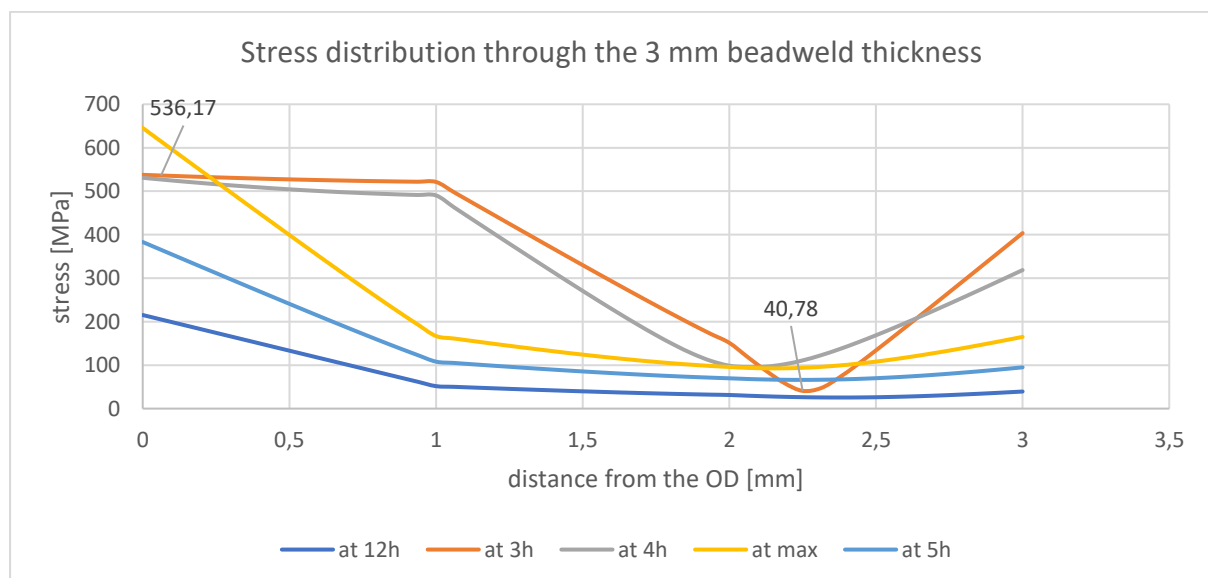
Figure 3.23 Stress distribution through the 3 mm beadweld thickness at five specific locations. "At max" refers to the gradient analysed at the maximum stress location.

Different positions along the circumference experienced different stress gradient through the beadweld thickness. Figure 3.24 compares the magnitude of the stress differences at those positions.
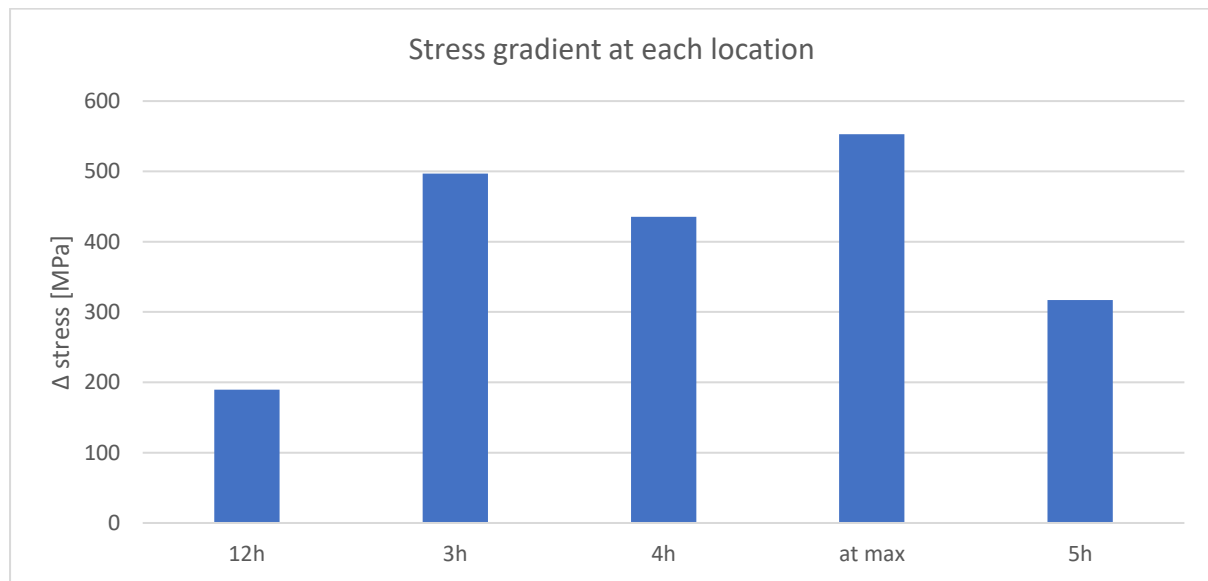
Figure 3.24 Stress gradient at each position. $\Delta stress = stress_{max} - stress_{min}$ at a given location.

The biggest stress gradient is seen at the maximum stress location (around the 4:30 o'clock). The smallest is located at the minimum stress location (12 and also 6 o'clock). The 3 and 4 o'clock have the same stress values at the OD but different at the ID. It is because those locations are within the plastically strained region (between the stress peaks) at the OD, whereas the ID edge does not experience the plasticity. The higher value of the OD stress at the maximum stress location emanates from the nodal average results evaluation. Interestingly, the maximum stress gradient curve is similar to the "elastic" locations curves (12 and 5 o'clock). Apparently, the elastic behaviour prevails at the transition locations (at the elastic/plastic material interface). The 3 and 4 o'clock curves, fully contained in the "plastic" behaviour at the OD edge show a different gradient profile. Up until 1 mm deep in the beadweld, the stress is approximately constant at those locations and then it decreases to reach the minimum at the depth of approximately 2 mm, then increases again until it reaches its ID value. Such gradient shape is the consequence of the secondary bending, which is caused by the loading mode and the wall thickness geometry. From the shape of distributions in Figure 3.23, it can be concluded that the neutral axis is located approximately 2 mm deep from the OD edge (no compression part is visible as presented results are the von Mises stresses, which are always positive). The stress increase is not found at the "elastic" locations (12 o'clock, 5 o'clock, at maximum stress). There, the stress also decreases from the maximum value at the OD up to the 1 mm depth in the beadweld and then reaches an approximately constant value until the end of the beadweld at the ID. The differences in stress between the OD and ID (inside of the beadweld) stem from the geometry of the beadweld acting as a stress concentrator at the OD. The fact that the stresses in the plastically strained region are constant up to 1 mm deep is also related to that same SCF effect. As the SCF rises the stresses close to the OD, the higher stresses there trigger the plasticity and in this regime the stresses are constant. Further away from the OD (deeper in the beadweld) the effect of the SCF decays, as well as the stresses,

and only elastic strains are present. Hence, effectively, only the 1 mm of the beadweld total thickness, in certain areas, experienced plastic straining.

The beadweld shape study

Two options of the beadweld shape were considered: with and without the fillet. The "with fillet" design represents the situation when two pipe pieces have their ends bevelled and the bevel shape is preserved after the beadweld deposition. The bevelling is done by the automated machines with the 3,2 mm radius. The "no fillet" design represents the situation when the 3,2 mm fillet is not preserved after the bead welding and the beadweld makes the right angle with the pipe wall. Two designs are presented in Figure 3.25.
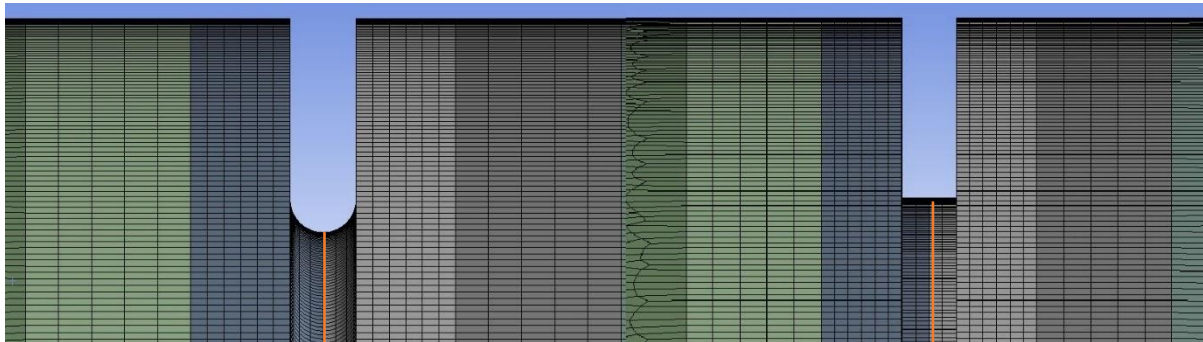
Figure 3.25 The comparison between the rounded beadweld design (3,2 mm fillet radius) and the right-angle (no fillet) design. The OD edge is highlighted in orange.

The Von Mises stress along the OD edge was compared (Figure 3.26) for the "with" and "without" fillet beadweld design. The displayed results are the nodal average.
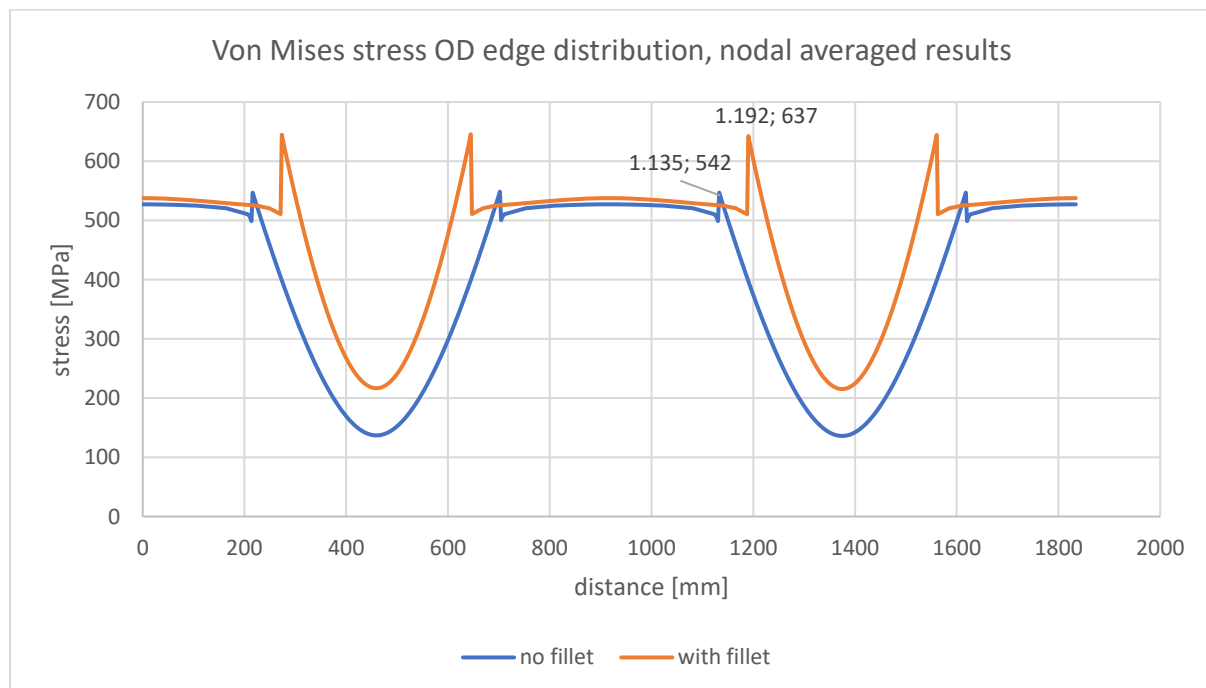
Figure 3.26 A comparison of the stress distribution along the OD edge for two beadweld geometries, nodal results.

The change of the beadweld shape changes the maximum stress values and their positions, with the "no fillet" results being 95 MPa lower and 57 mm closer to the force point locations. The stress in the plastically strained area remains the same in both cases. The minimum stresses in the "no fillet" case are also lower than their counterparts in the "with fillet" design.

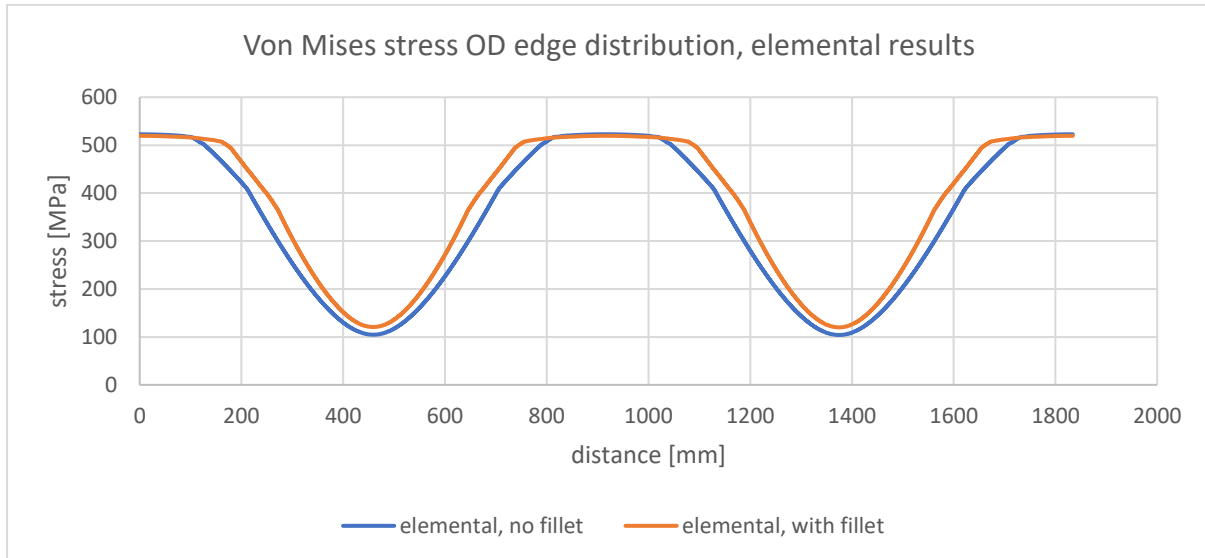The same comparison was made with the averaged elemental results, see Figure 3.27.

Figure 3.27 A comparison of the stress distribution along the OD edge for two beadweld geometries, elemental results

Little difference in stress distribution is introduced with the beadweld changes. The "no fillet" design has slightly narrower areas of plastic straining. The values of maximum stresses, however, remain unchanged.

In conclusion, the stress at the OD of the beadweld is not greatly affected by the beadweld shape. At first glance, this might be counter-intuitive, as the "no fillet" beadweld geometry clearly introduces higher SCF to the structure. However, one must remember that the actual OD edge is located 3 mm away from the SCF created at the right angle with the pipe wall. In actual fact, the geometry at the OD edge is smooth. This is why the stresses registered there are slightly smoother (less abrupt) than at the OD edge with the beadweld fillet. The OD edge in the latter case is located on a curved, not flat, geometry (see Figure 3.25).

Stress distribution across the beadweld was also studied in this case. The distributions at the same locations (3, 4, 5, 6 o'clock and the maximum stress location) for the "no fillet" beadweld design are presented in Figure 3.28.
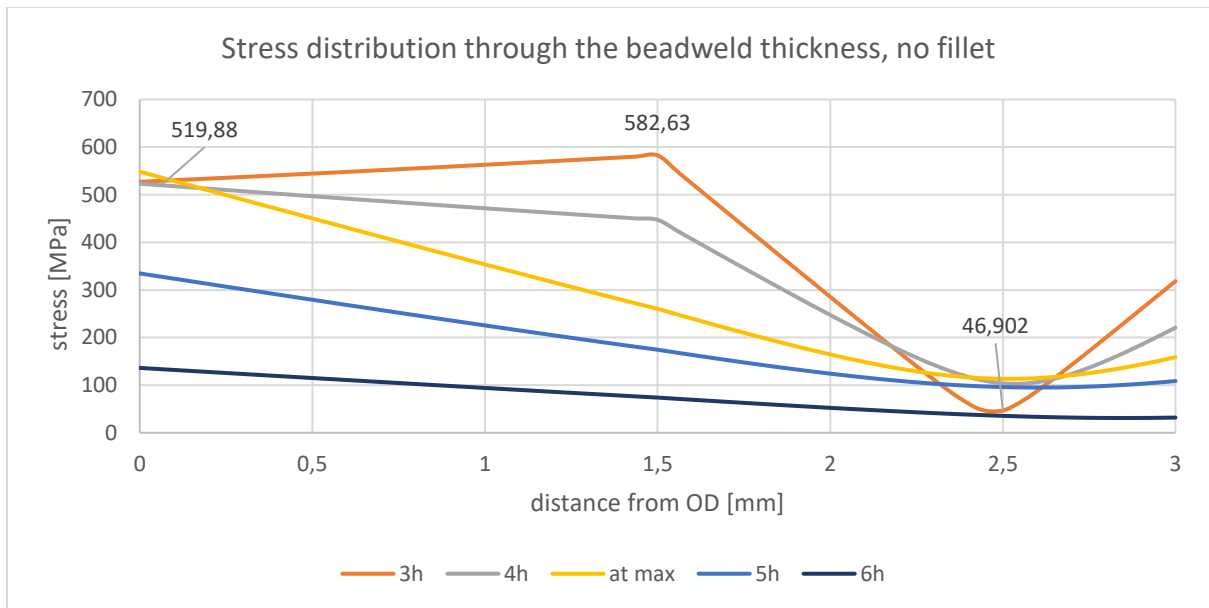
Figure 3.28 Stress distribution through the beadweld thickness, no fillet beadweld design; nodal results

Slightly different stress gradients are observed, comparing to the "with fillet" design results (see Figure 3.23). Here, the maximum stress is found 1,5 mm deep in the beadweld, not on its OD edge anymore. Apart from that, the distribution of stresses at a certain location is similar in both cases. Again, the effect of secondary bending is visible, with the neutral axis located approximately 2,5 mm deep from the OD. The changes of stress in the "no fillet" case, however, seem to have a smoother distribution, decreasing in a more steady manner up to 2,5 mm depth.

Negligible differences were found between the flat (no fillet) and rounded (with fillet) beadweld design. Hence, it was decided to base the results and discussion on the rounded design model, as its calculation time was slightly shorter.

The 6 mm beadweld, full geometry model

The same as the above steps and reasoning were applied to investigate the 6 mm beadweld thickness model. Based on the findings in the "3 mm model" study the "6 mm model" was designed with a 3,2 mm fillet radius, the kinematic hardening rule for the material model and the elemental and nodal result displays. The structure was loaded in the exact same way as the 3 mm model (with F= 674620 N total load). The area of the 6 mm beadweld can be calculated as $A6 = A_{OD_{6root}} - A_{ID_{6root}} = 11004,4\ mm^2$.

The overview of von Mises stresses in the coupon are shown in Figure 3.29. Also, in this case, the coupon is structurally safe, with the maximum stress located at the beadweld and the minimum located at the support plate's end
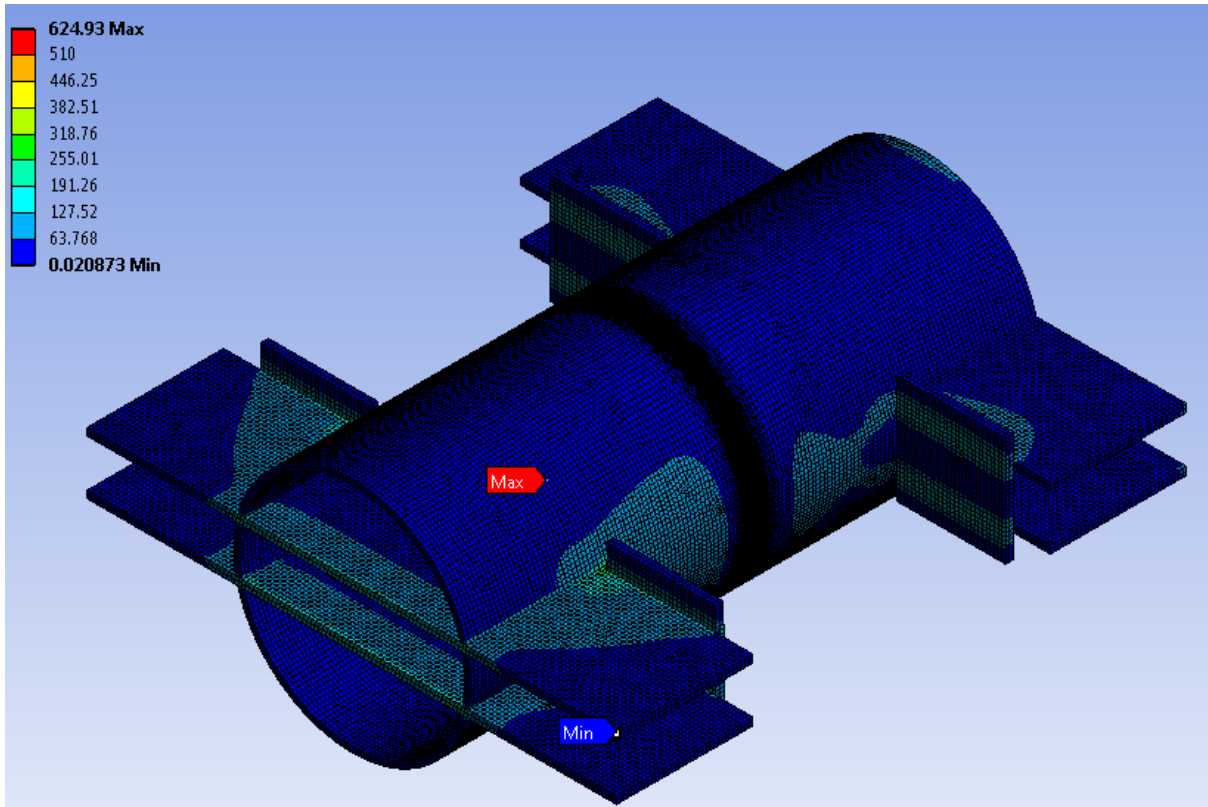
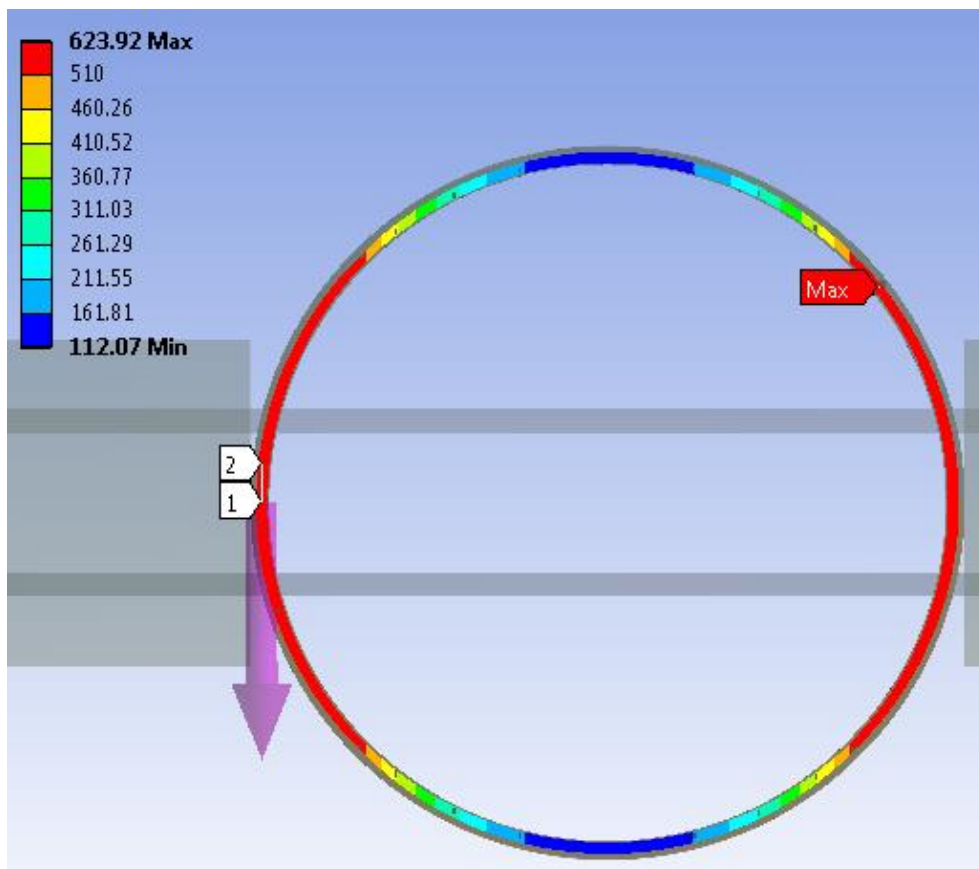Figure 3.29 The overview of the von Mises stresses in the "6 mm" model; nodal results

Figure 3.30 Von Mises stress distribution at the OD edge, 6 mm model, Z axis view. Nodal results display.

Again, the OD edge of the beadweld was investigated in terms of stresses and strains, in the nodal and elemental display. The comparison of both results displays, for the OD edge stresses, is presented in Figure 3.31.
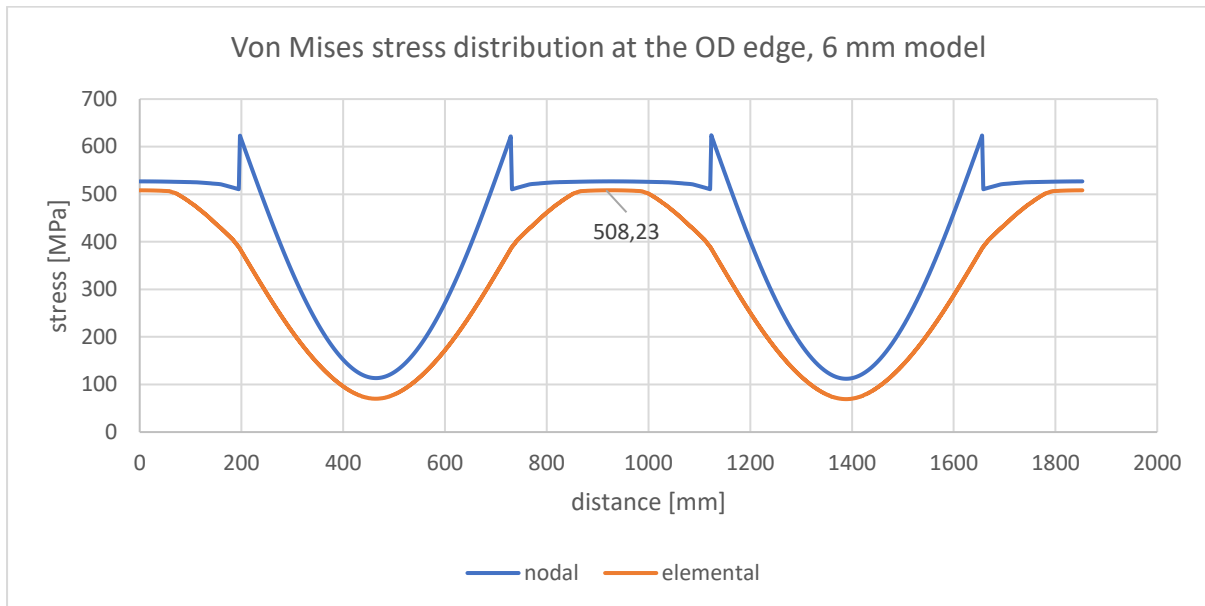

Figure 3.31 Von Mises stress distribution along the OD path of the 6 mm beadweld model. The averaged nodal and elemental results are compared.

Presented stress distributions can be readily correlated with those in Figure 3.16. For both display modes, the distribution profiles are very similar. However, in the 6 mm beadweld model the stresses registered are lower. This can be easily explained by the bigger beadweld area (6mm thickness vs. 3 mm thickness), which, loaded with the same force, results in lower stresses. Those stresses, however lower, were high enough to trigger the onset of plasticity at the most heavily loaded locations (3 and 9 o'clock). The shape of the nodal stress distribution indicates the presence of plasticity, which, indeed, is confirmed with the strains distributions at the OD edge. The elemental display is presented, see Figure 3.32.
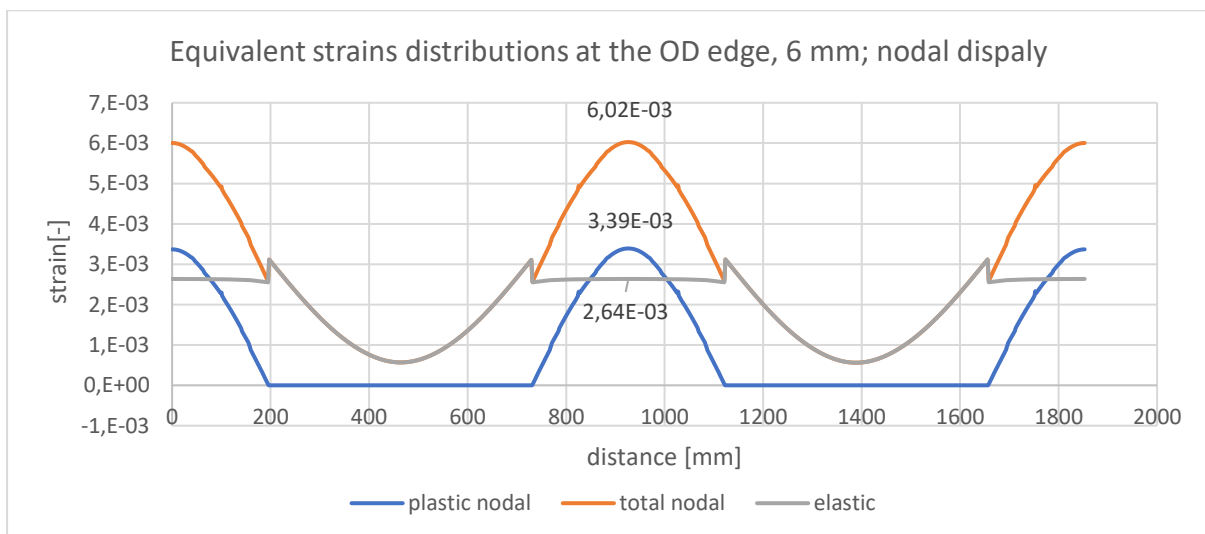

Figure 3.32 Equivalent strains distribution (total, elastic and plastic) at the OD edge of the 6 mm beadweld. Nodal results are presented.

Plasticity is present at the same locations as in the case of the 3 mm model. The magnitude of plastic straining is much lower (0,339% vs 1,08% see Figure 3.20). The characteristic sharp peaks in the total and elastic strain distributions are present. The onset of plasticity overlaps with those peaks. To adequately assess the extent of the plastic area a similar graph of strains was done, this time presenting the elemental results, see Figure 3.33.
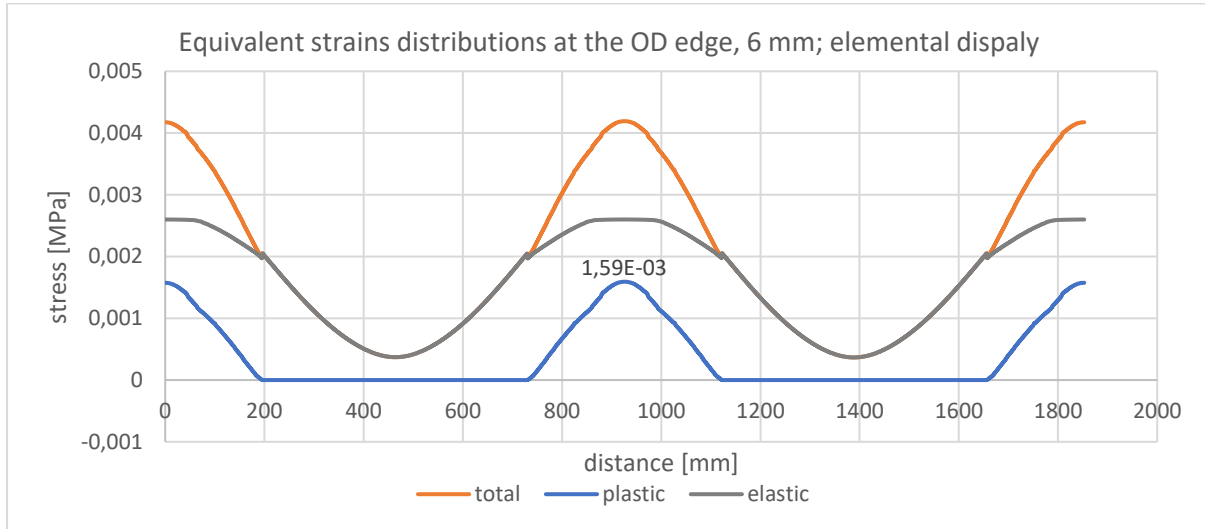

Figure 3.33 Equivalent strains distribution (total, elastic and plastic) at the OD edge of the 6 mm beadweld. Elemental results are presented.

Displaying the plastic strain results in an elemental manner decreases the result to 0,159%.

As in the 3 mm model case, the through-thickness stress distributions on sensitive locations were plotted in the 6 mm beadweld model. The nodal results are presented in Figure 3.34.
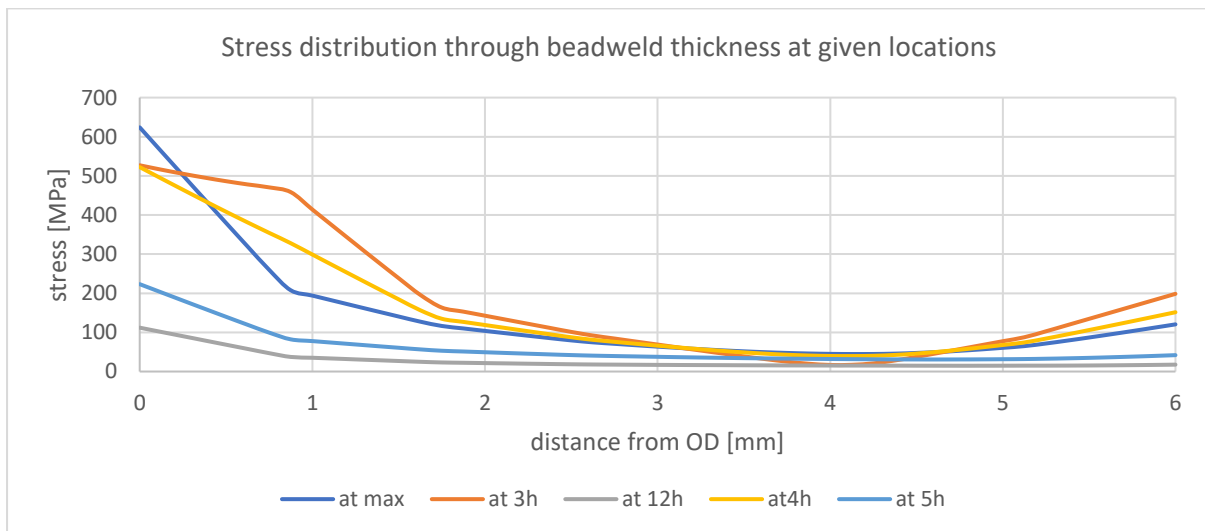

Figure 3.34 Through 6 mm beadweld thickness Von Misses stress distribution at the specific locations; nodal results are presented.

The stress gradients at all investigated locations are steady, without abrupt peaks. Wider beadweld allows for this smoother stress evolution from the OD edge to the ID edge. The biggest stresses are observed at the OD and then they decrease, with the most dramatic

decrease observed for the maximum stress location. At all locations, the stress reaches its minimum at approximately 4 mm beadweld depth and then slightly grows towards the ID edge. The stress gradient is believed to represent the bending moment in the weld, with the neutral axis being located approx. 4 mm deep in the weld. Findings of the stress gradient at in the 6 mm beadweld thickness correlate with the results observed for the "3 mm" model.

3.6 FEA results- discussion

The above results and their analysis were the departure points for the fatigue specimens' location and quantity determination. The FEA simulation presented, being a numerical approximation of the real experiment, was designed, conducted and analysed in a careful manner so that its results are reliable and adequate for the subsequent fatigue testing.

The paramount goal of the FEA was to identify the locations (and their stress-state) at the beadweld that were plastically strained and to determine the extent of straining a particular location experienced. The exact location of each specimen and their unique stress-strain state are presented in Table 2.3.

Different simulation parameters and geometries were presented. As confirmed by the stress and strain distribution results, the exact shape of the beadweld affects the results at the locations of interest to a negligible extent. The through- thickness stress distribution in the "no fillet" and "with fillet" designs was checked, proving that the exact curvature of the beadweld does not greatly affect the local stress gradients. This is a fortunate finding, as the exact shape of the beadweld during the overstressing simulation can only be approximated- the pipelaying practice shows that it can be concave, flat or even convex. Results for the rounded beadweld design (with a 3,2 mm fillet radius) was then assumed.

Once the beadweld shape model was determined, the adequate results display must be chosen. Based on the discussion presented in the previous sections it was concluded that the elemental mean results best depict the actual stress state in the beadweld. The elemental results at the OD edge, together with the through- thickness stress gradients, provide a full overview of the stresses (and plasticity) at a certain location. Those results, in contrary to the nodal ones, represent the values averaged across more points on a more representative area of the beadweld. Since the focus of this analysis was on the beadweld thickness, not on its edge, the elemental results are considered as the reference stress-strain state per each fatigue specimen extracted from the coupon. The plastically strained fraction of the OD edge in the 3 mm full model, based on the elemental results, equals 1085 mm in total. The nodal results at the OD and ID edges, due to their scoping sensitivity, may yield less reliable values at the sensitive locations of the elasticity/plasticity interface.

The analysis of the 6 mm beadweld model revealed plastic straining of the beadweld at the locations around 3 and 6 o'clock. The plastically strained fraction of the OD edge, based on the elemental results, equals 763 mm in total, which is much less than in the case of the 3 mm model. Based on those findings the reference OD elemental stress and plastic strain will be reported for the C-group specimens.

4. Results and discussion

4.1 Optical crack initiation observation

From 38 successful fatigue test, 27 of them gave useful optical crack observation results, see APPENDIX D. Example results are presented in Figure 4.1a to Figure 4.1d.
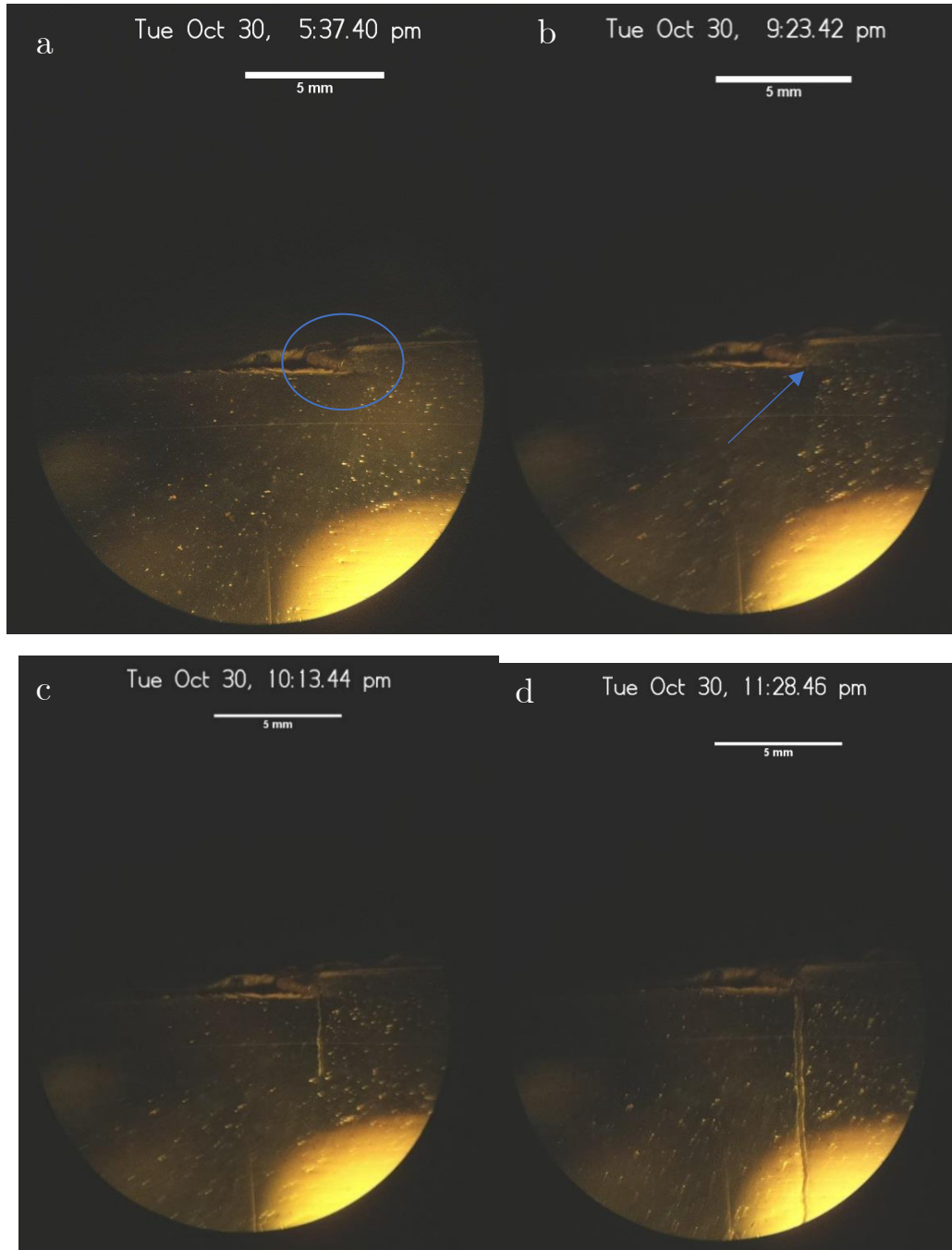

Figure 4.1 a) Start of observation of specimen A-150; no crack yet; b) First observed change at the Hi-Lo corner- the moment considered a crack initiation; c) Crack propagation almost 1 hour after initiation was observed. Crack is about 3,2 mm long; d) The last recorded image before failure.

As visible on the above pictures, the observation of a crack initiation strongly depends on the surface preparation, lighting conditions and a favourable crack location. The case of specimen

A-150 presented above is a good example of a successful optical crack observation. There were 217 pictures taken from the test start until the test finish, only 4 are presented as an example. The crack initiation phase is determined as the time from the observation start until the first observable change appears. After that, the subsequent photographs show the steady crack growth, until the failure. For the specimen A-150, the initiation phase lasted 2h 15 minutes which accounts for 38% of the total lifetime of 5h 53 minutes. Thus, the growth phase accounted for 62% of a total lifetime.
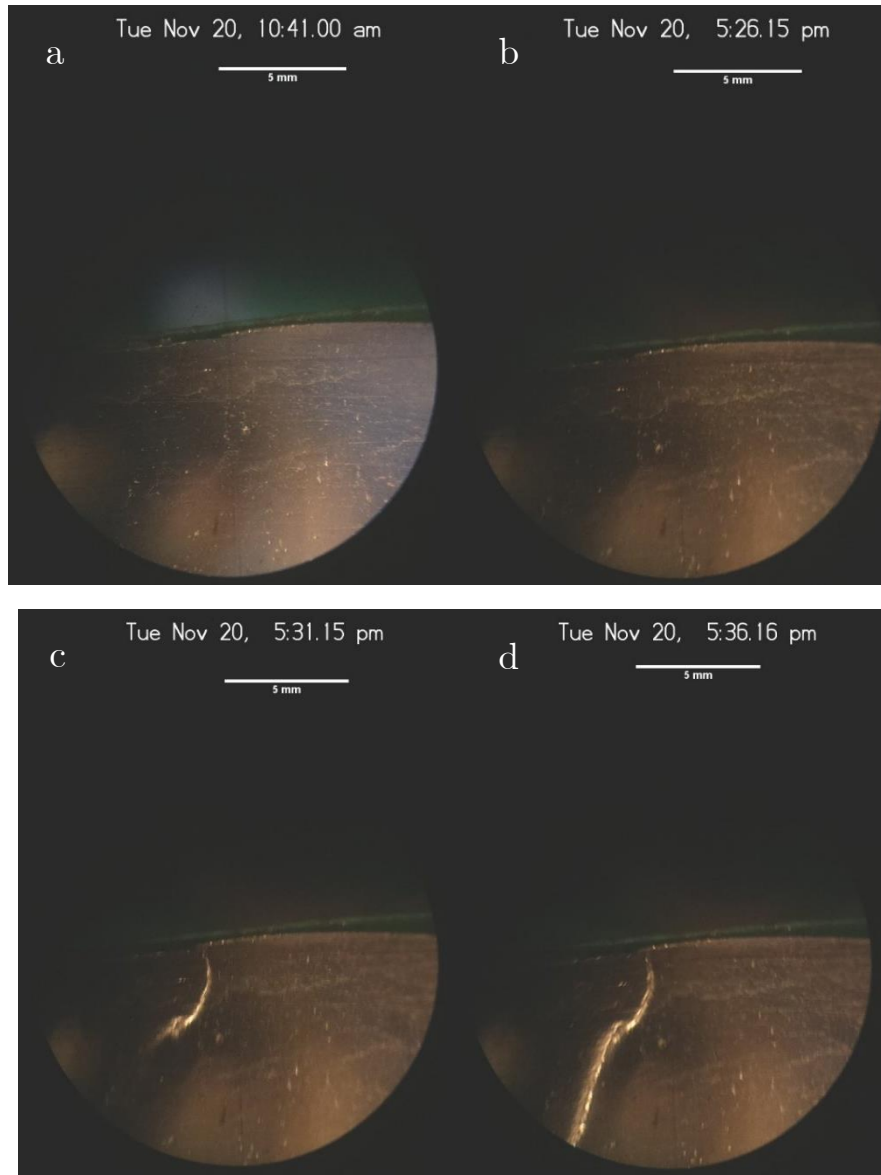
Figure 4.2 a) Start of observation of specimen A-100; b) First observed crack occurrence at this side of the specimen; c) Almost 7 hours later still no crack is visible; d) The last registered picture before the specimen failure.

Unfortunately, in some cases (for example, specimen A-100) the initiation started on the other specimen face than observed. Then, even though the set of good quality pictures was available, it did not show the actual steady crack growth. Such case is presented in Figure 4.2a-d

It was a challenge to correctly determine the failure location prior to the test due to the very low Hi-Lo of the A-100 specimen. Unfortunately, in this case, the crack propagation occurred elsewhere than the observed spot. Figure 4.2 show how a big, curved crack appeared suddenly on the surface within only 5 minutes. Clearly, no steady growth was observed. The total failure occurred just 5 minutes after. In such a case, the optical measurement suggests the initiation time took 90%, which cannot be assumed reliable and the PD measurement result has to be used as a backup.

4.2 Potential Drop method observations

There have been 27 successful PD measurements, out of all 38 successful fatigue tests. Some PD results correlate with the optical measurements results, however, not always. The output from the PD electrodes is the potential [V] as the function of time. It was impossible to present potential as the function of crack length because the crack length (and, ultimately, its growth rate) has to be measured with a precise instrument such as extensometer, attached to the crack mouth. Such set up was not feasible in this study.

An example output curve from the PD measurement, taken from the specimen A-280, is presented in Figure 4.3.
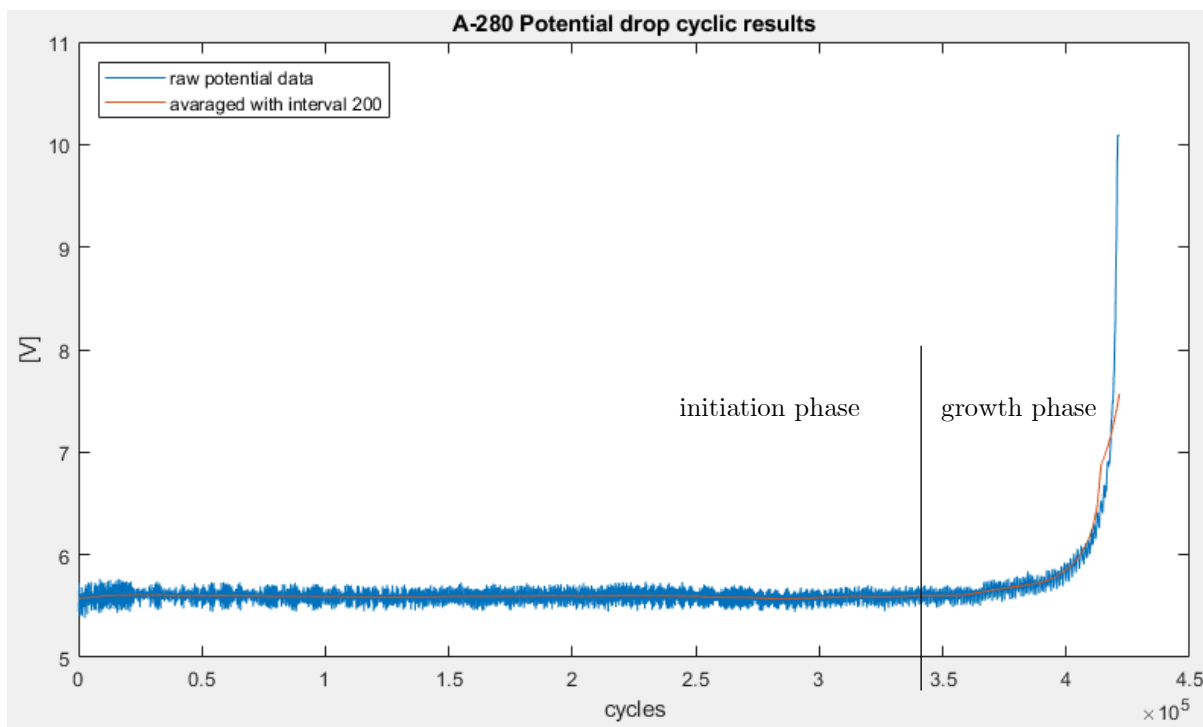

Figure 4.3 PD curve from the crack observation of specimen A-280

The blue curve represents the raw signal from the electrodes, the potential fluctuations are clearly visible. To account for this signal noise the results can be averaged out, which is represented by the orange curve. The moving average interval over which the results can be averaged is decided with the trial-error approach, by adjusting the optimal interval value so that the curve smooths out but without the loss of important data. In the case of specimen A-280, averaging over 200 points was chosen. For each specimen, the averaging interval was

adjusted individually. The horizontal axis presents the changes in the potential in terms of cycles. The initially flat curve indicates no changes in crack length were detected by the electrodes. The change of slope of the curve indicates that the changes in the crack length are big enough so that the electrodes registered changes in the current. This point in time (cycles) indicates where the crack initiation phase is over and the crack growth begins. The curve stops when the signal from electrodes breaks, meaning the specimen failed under fatigue. The total lifetime of this specimen was 421644 cycles, from which the initiation took 328882 cycles (78%) and the growth phase took 92762 cycles (22%). Another example of a successful fatigue test with a PD measurement is specimen C-280, see Figure 4.4.
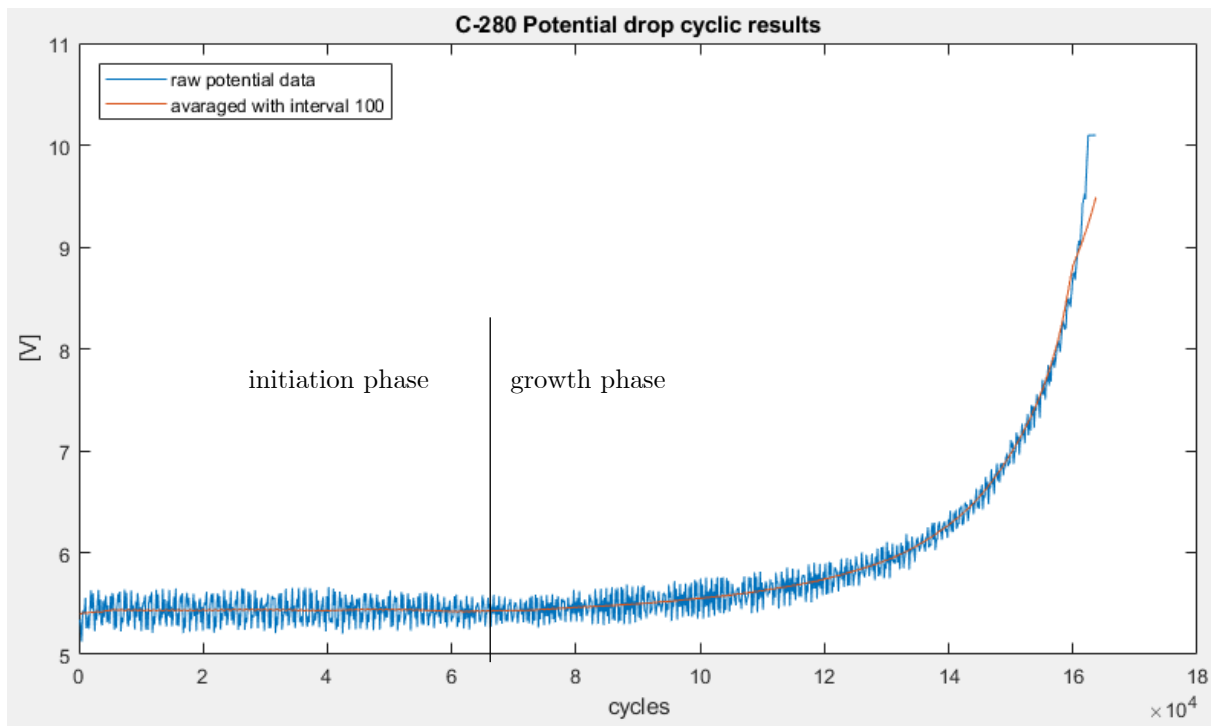

Figure 4.4 PD curve from the crack observation of specimen C-280

This time it was enough to average out the signal over 100 data points. Similar curve shape is observed, with signal fluctuations and the initial constant slope of the averaged output signal. The change of slope is observed at around 40% of a total lifetime, accounting for 65492 cycles. Total lifetime of specimen C-280 was 163729 cycles, over than 2,5 times less than the previously presented specimen A-280.

As mentioned before, not all PD results were successful. An example of a failed PD measurement is presented in Figure 4.5. For unknown reasons the signal was aberrant, making the initiation phase impossible to determine. The output load signal from the fatigue machine, Figure 4.6, proves there was no force aberration that could cause such potential deviations. One probable explanation could be the electrodes touching each other or the machine set up due to the vibration of the machine.
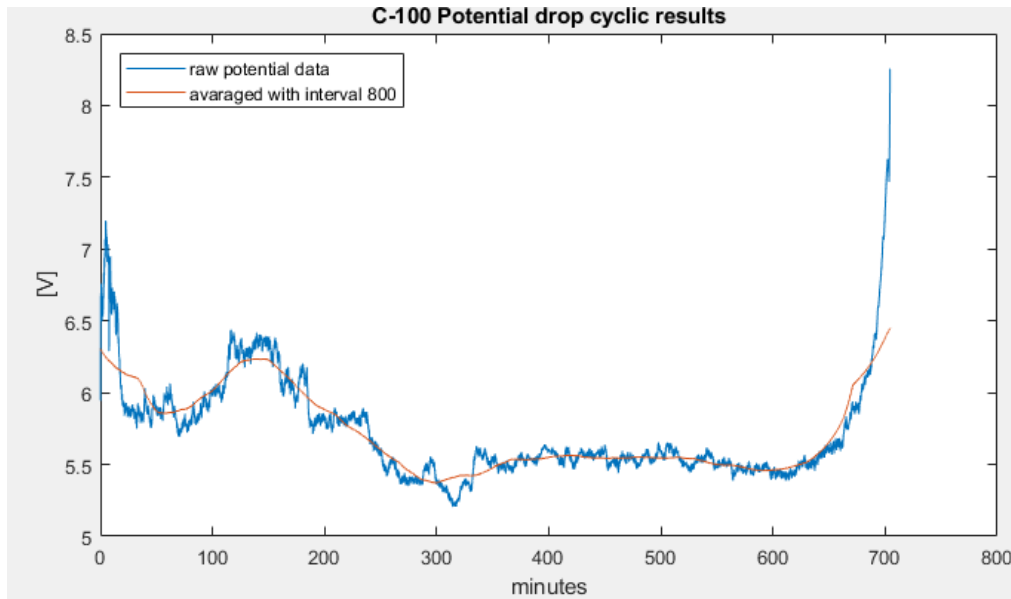
Figure 4.5 An example of erroneous reading from the PD measurement.
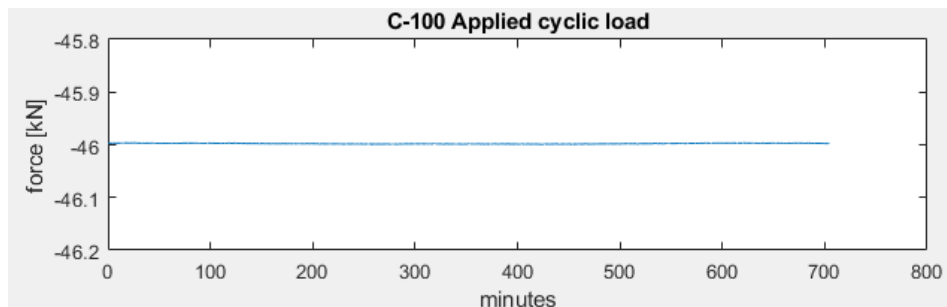

Figure 4.6 Force peaks registered during fatigue testing of specimen 0-2

PD results (graphs) for the remaining specimens can be found in APPENDIX G.

4.3 Optical & PD measurements: discussion

Table 4.1 presents the combined results of the crack initiation phase determination done by the optical and PD method. Invalid measurements were marked with "x". Additionally, the Hi-Lo value of each specimen was included in the table. Figure 4.7 presents the duration of the initiation phase in the function of Hi-Lo, measured for each individual specimen, by two methods. Similarly, Figure 4.8 presents the relationship between the initiation phase duration and the total fatigue lifetime of each specimen.

Table 4.1 gives an overview of the performance of both used crack observation methods. In some cases both of them failed for the same specimen (ex. 0-260, C-100, A-220), in other cases, they yielded different results (ex. A-260, C-260), finally, for some specimens, their results were well correlated (ex. 0-2, A-270, A-40). Despite its imperfection, the obtained data set allows drawing certain conclusions coming from the crack observation, which are better presented in Figure 4.7 and Figure 4.8. The average initiation time measured by optical observations was

63 (±10,5)% whereas this measured by the PD setup was 60 (±6)% (both averaged across 27 points, regardless of the initiation location).

Table 4.1 An overview of both PD and optical measurements results combined. Initiation phase as a fraction of total fatigue lifetime is presented.

| Specimen	Optical	PD	Lifetime [cycles]	Hi-Lo [mm]
0-280	x	50%	3,05E+05	0,42
0-270	x	46%	4,23E+05	0,39
0-260	x	x	3,14E+05	0,44
0-100	x	59%	3,29E+05	0,58
A-20	93%	62%	3,06E+05	0,33
A-40	52%	57%	1,51E+05	0,87
A-320	70%	63%	6,91E+05	0,32
A-80	x	52%	4,42E+05	0,47
B-40	x	63%	6,35E+05	0,48
B-30	x	63%	7,00E+05	0,32
B-340	x	48%	1,82E+05	0,52
B-320	44%	65%	1,80E+05	1,15
B-330	38%	50%	1,81E+05	1,03
A-140	x	x	2,91E+05	0,17
A-150	65%	x	3,18E+05	0,38
A-220	x	x	3,87E+05	0,2
A-160	78%	73%	2,83E+05	0,42
A-210	85%	x	4,42E+05	0,48
A-200	75%	x	3,71E+05	0,55
B-240	33%	x	2,74E+05	0,53
B-70	67%	75%	4,10E+05	0,25
B-120	48%	x	2,33E+05	0,46
B-110	35%	x	1,95E+05	0,48
B-250	70%	52%	4,24E+05	0,26
C-100	x	x	6,34E+05	0,21
C-270	70%	80%	1,80E+05	0,77
C-280	66%	40%	1,64E+05	0,72
C-260	21%	64%	1,95E+05	0,76
A-90	78%	59%	2,78E+05	0,1
A-280	78%	85%	4,22E+05	0,5
C-80	84%	63%	2,75E+05	0,52
A-270	29%	32%	3,23E+05	0,14
A-260	92%	74%	3,51E+05	0,16
A-100	90%	70%	3,76E+05	0,15
extra A	77%	70%	1,36E+05	0,83
0-1	76%	59%	8,47E+05	0,4
0-3	24%	x	5,66E+05	0,4
0-2	60%	57%	3,24E+05	0,88
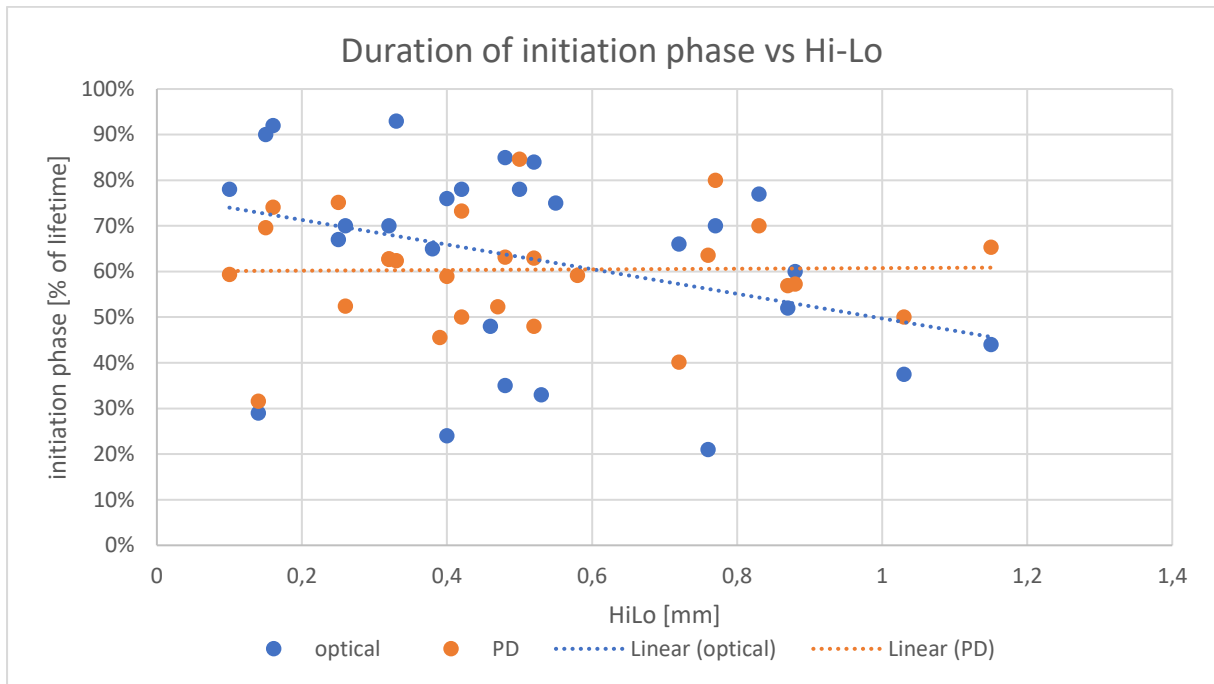
Figure 4.7 Duration of the initiation phase of individual specimens in the function of Hi-LO, measured by two methods- optical one and the PD method.
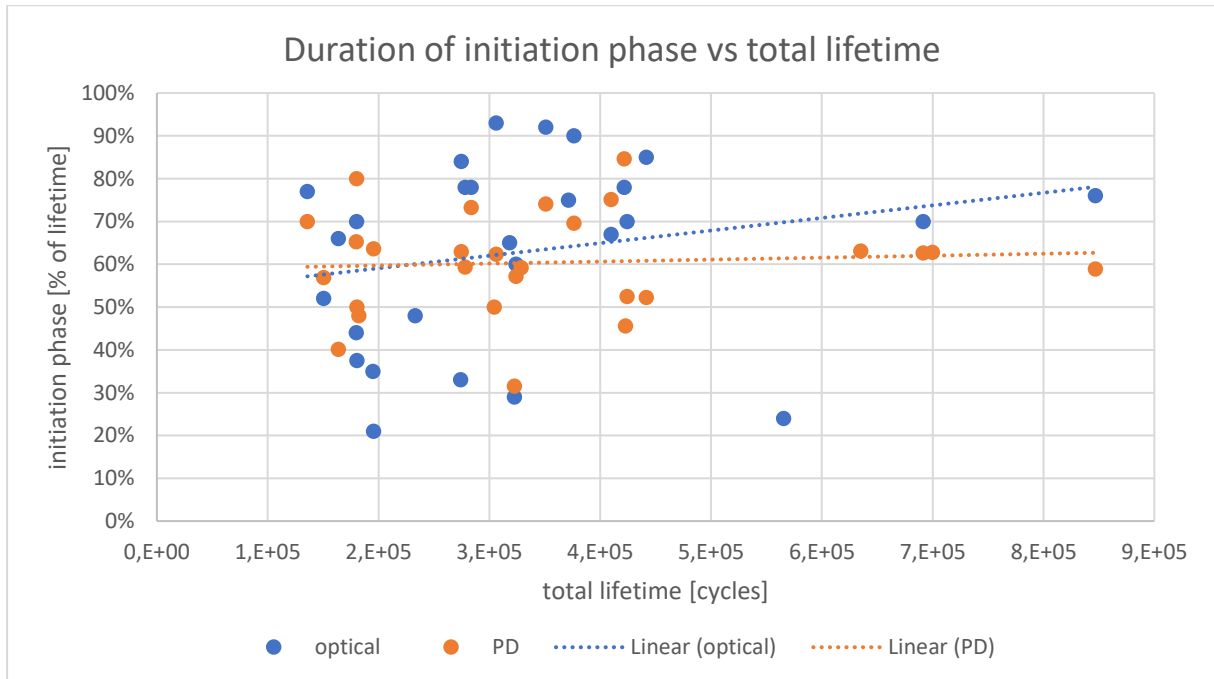

Figure 4.8 Duration of the initiation phase of individual specimens in the function of a total lifetime, measured by two methods.

As explained in Section 1.7, the initiation part of the fatigue lifetime is sensitive to the surface geometry of the weld. This is confirmed in Figure 4.7. Optical observations of the crack captured the general tendency of decreasing initiation phase duration with increasing Hi-Lo value. In other words, it took more cycles for a microcrack to nucleate and then grow into a

macrocrack for specimens with smoother surface geometry. Interestingly, the PD machine failed to capture this tendency, most likely due to insufficient sensitivity of the electrodes or their inadequate placing.

Intuitively, the more cycles it takes to form microcracks, the longer the total fatigue life, see Figure 4.8. For specimens with longer fatigue life, it is the growth phase that governs the overall fatigue performance. The influence of factors other than surface or geometry irregularities should be then investigated considering the growth phase only. Additionally, Figure 4.8 confirms that also in this case the optical method proved more accurate than the PD measurement, which fails to show that tendency, most likely because of the reasons mentioned earlier.

Additional insight was made into the relationship between the initiation phase duration and the location of the crack. The overview is presented in Figure 4.9. The optical measurement registered a slightly higher numbers for the initiation crack duration than the PD instrument. However, the difference (7 and 3 percentage points) is smaller than the standard deviation associated with the results thus can be negligible. No difference in average initiation phase duration for weld- and base-cracked specimens indicates that the initiation part is not affected by the material strength.
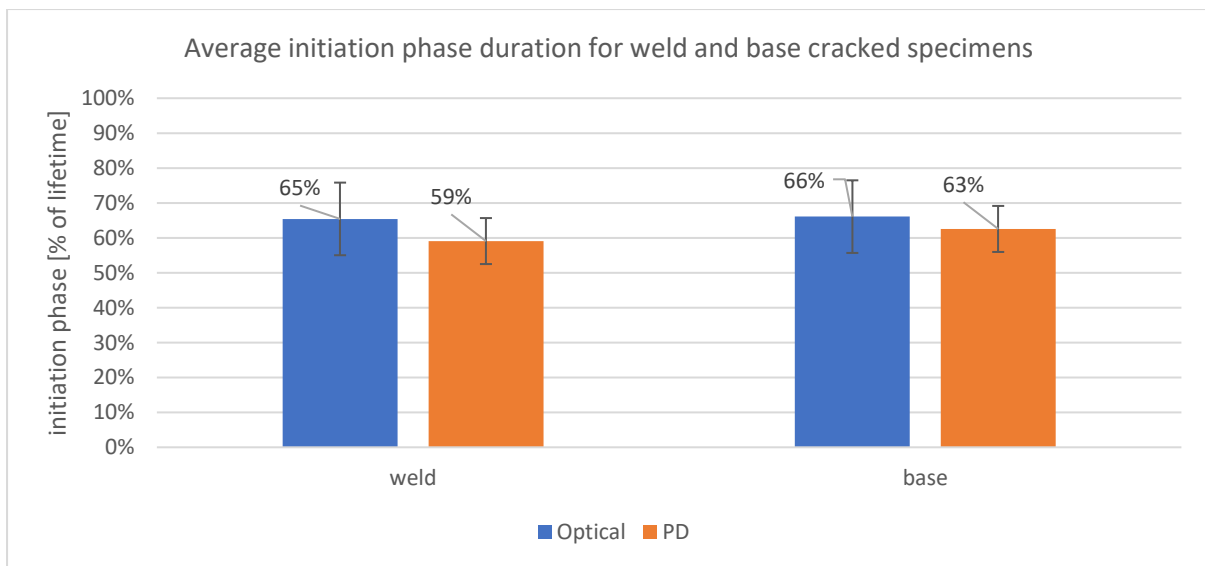

Figure 4.9 Graph showing how does the location of the crack initiation (base or weld metal) affects the average initiation phase.

4.4 Fatigue testing

Forty-six fatigue tests were performed in total- 42 originally planned specimens plus 4 additional ones, see Table 2.3.

It should, however, be noted that not all fatigue tests were successful. There were 8 discarded tests results because of failures during testing, namely: rotation of the machine crosshead resulting in non-uniform stress distribution in the specimen (2 specimens) or crack forming at the support points instead of the root (6 specimens). Failed specimens are marked in red in

Table 2.3. 38 test results in total remained and were considered for further analysis. The overview of all those tests can be found in APPENDIX D, including parameters such as lifetime (in terms of cycles and hours), measured Hi-Lo value, the location of crack initiation, determined initiation and growth phases as fractions of a total lifetime, also in terms of hours and minutes.

Total fatigue lifetime of 38 successful results was compared against the adjusted E type S-N curve, explained earlier in Figure 1.9. The specimens' lifetime in relation to the curve is shown in Figure 4.10. Each green dot represents the number of cycles to failure of a specimen, for the effective stress amplitude calculated for each specimen with SCF at the root taken into account (see Equation 1.7). The entire population of investigated specimens falls to the right from the mean S-N curve, which means that all the welds had better fatigue properties than the minimum required by the standards. Despite the scatter and different factors dependencies discussed later, the superior quality of the pipeline girth welds fabricated in this study can be already confirmed.
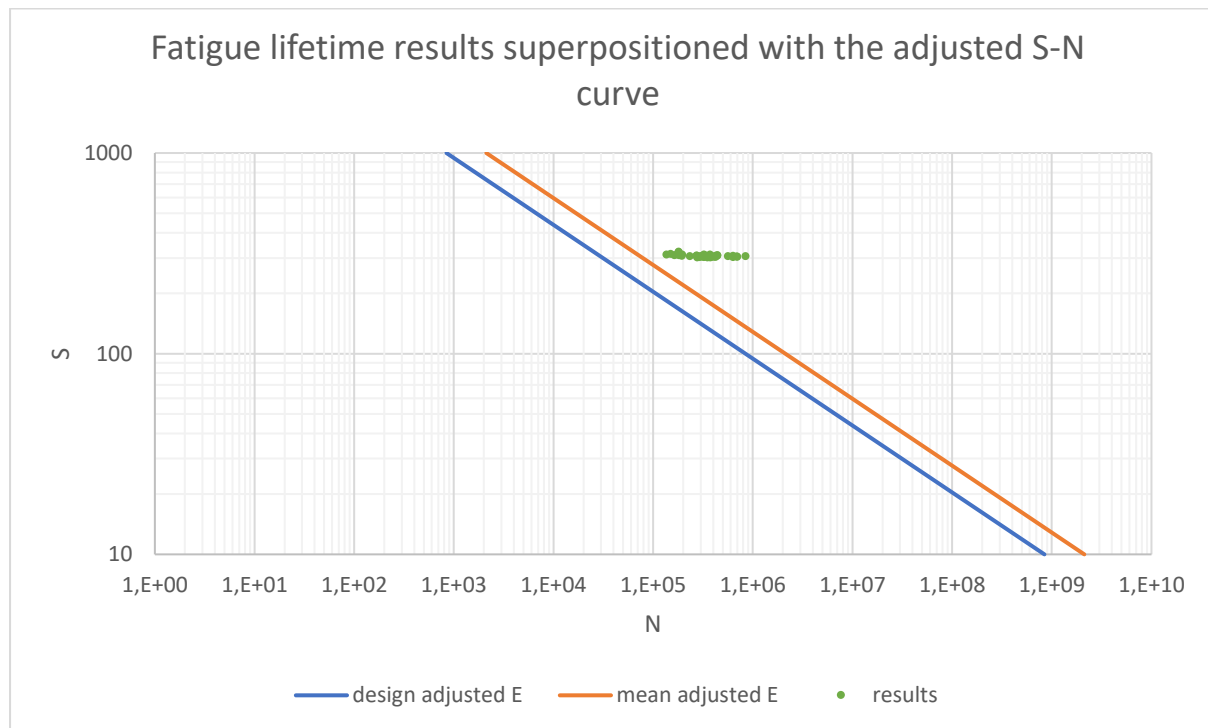

Figure 4.10 The specimens' fatigue lifetime in relation to the S-N curve

Effect of Hi-Lo and porosity
To investigate the effect of Hi-Lo only, the lifetime results were investigated within a given specimen group. Six graphs, one for each group, were created, comparing the lifetime of a given specimen as a function of Hi-Lo value, see graphs from Figure 4.11 to Figure 4.16. Each solid colour dot on the graph represents the total lifetime of one sample. Each faded colour dot represents the growth phase of one sample. Each sample is also labelled with the crack initiation location (weld material or base material). For easier identification, each group of specimens has its own assigned colour (see APPENDIX D).

It is important to note that the number of specimens per group is not equal. Also, the distribution of Hi-Lo values is different in every group.
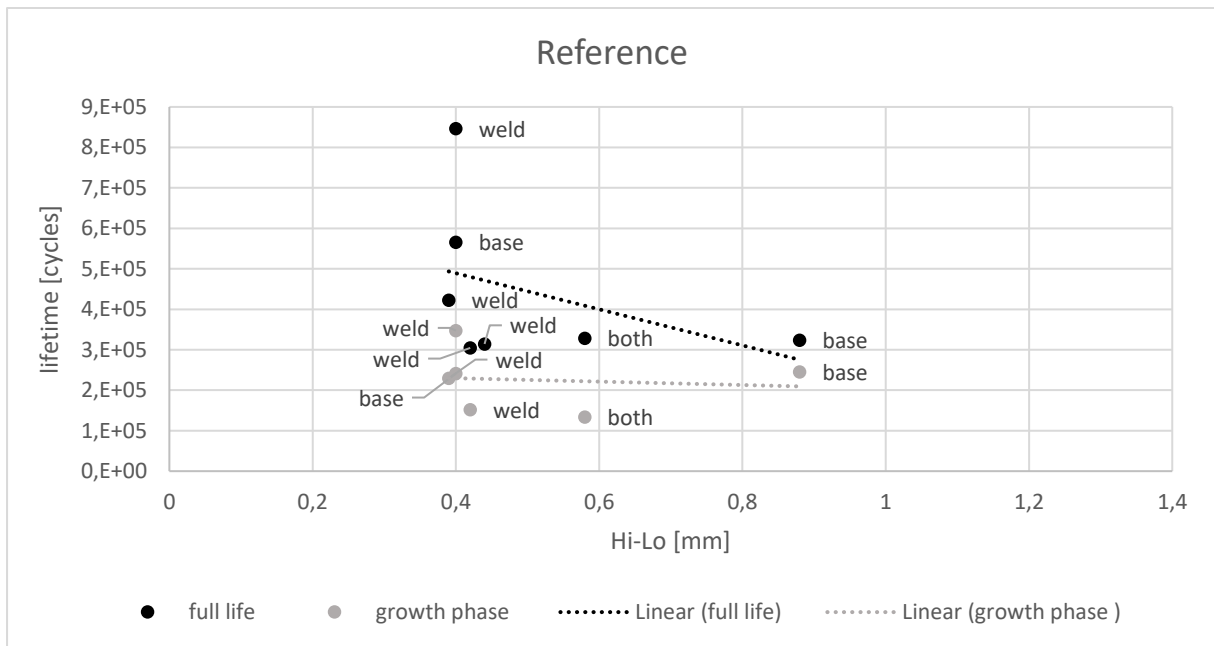

Figure 4.11 "Reference" group: The effect of Hi-Lo on lifetime

There were 7 specimens in the reference group, with Hi-Lo values from 0,39-0,88 mm. The lifetime varied from 846879 to 304520 cycles. High dispersion of the data points is visible in Figure 4.11, with extreme points removed when only the growth phase is present. Much lower scatter is observed for the crack growth phase, with no dependency on Hi-Lo visible.
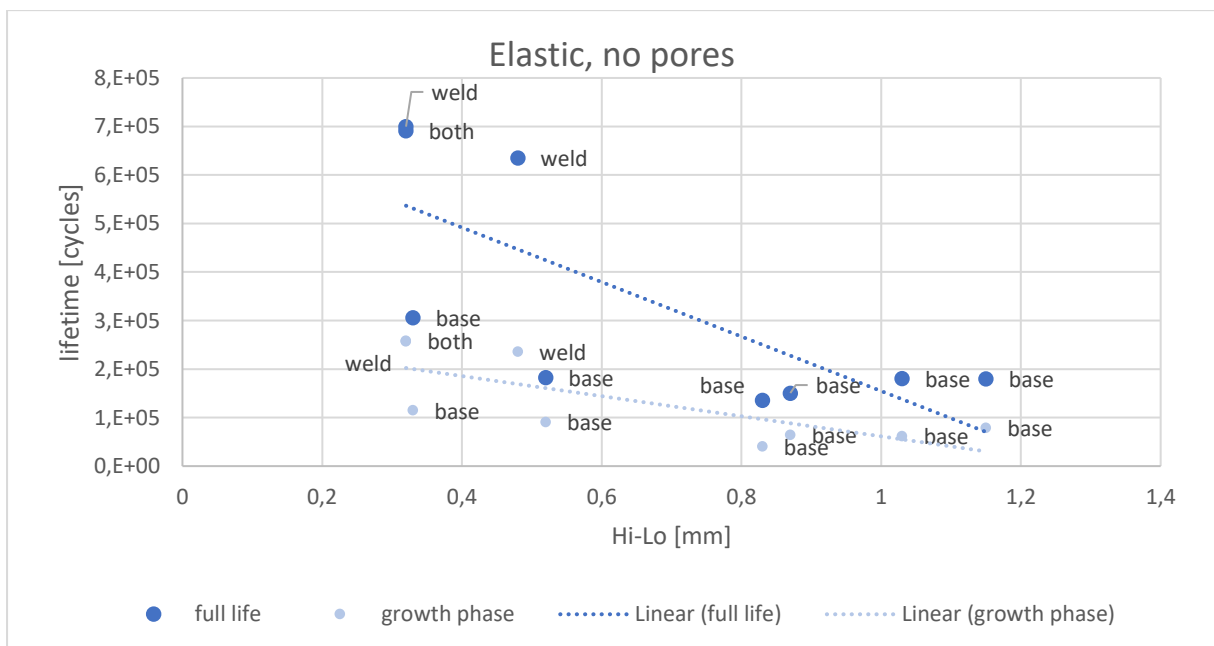
Figure 4.12 "Elastic, no pores" group: The effect of Hi-Lo on lifetime

9 specimens of properties similar to the reference are shown in Figure 4.12. The range of Hi-Lo in the case on "elastic, no pores" group is higher- 0,32-1,15 mm, as well as the scatter of total lifetime- 135799 to 691396 cycles. After removing the initiation phase the strong dependency on Hi-Lo also disappears.
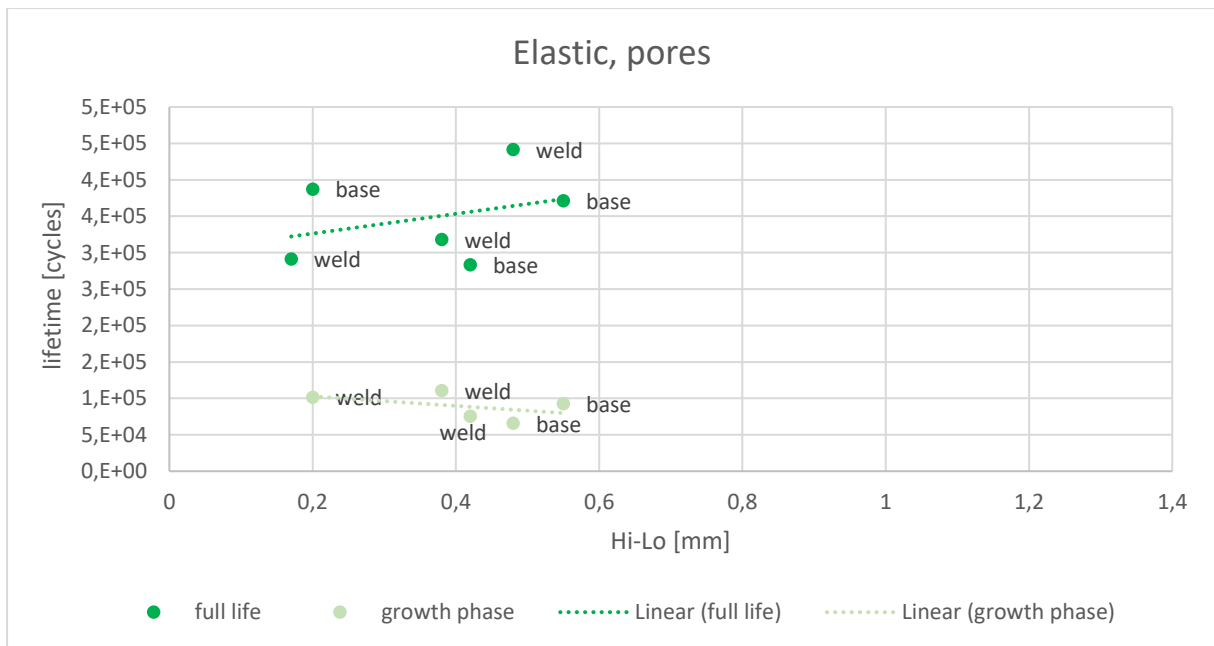

Figure 4.13 "Elastic, pores" group: The effect of Hi-Lo on lifetime

6 specimens from the "elastic, pores" group are visible in Figure 4.13. Hi-lo varies from 0,17 to 0,55 mm, lifetime- from 283475 to 441665. Surprisingly, there is an inverse dependency on Hi-Lo for total lifetime observed. Again, it disappears once the growth phase only is considered. The counter-intuitive increase of lifetime with increasing Hi-Lo can be explained with the relatively small data set for that group and low values of Hi-Lo.
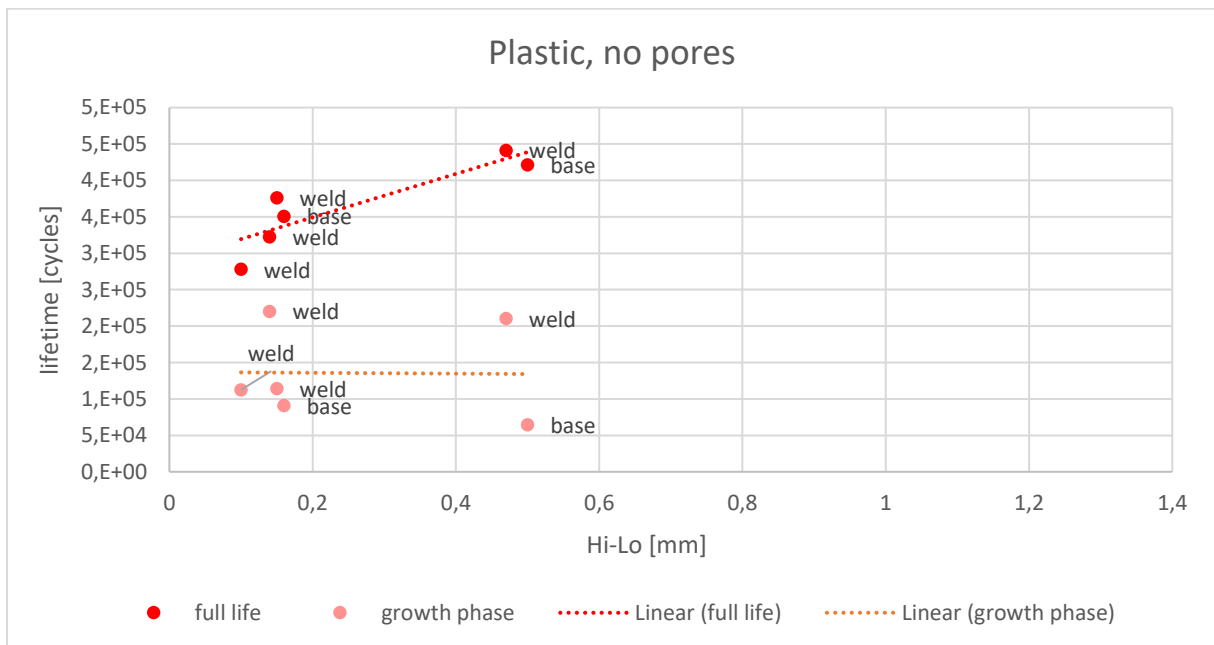

Figure 4.14 "Plastic, no pores" group: The effect of Hi-Lo on lifetime

A similar situation is observed for the "plastic, no pores" group, see Figure 4.14. This data set comprises of 6 specimens as well. Hi-Lo is scattered from 0,1 to 0,5 mm, the very low average compared to all groups. Lifetime varies from 278103 to 441500 cycles which is also the smallest dispersion within all groups.
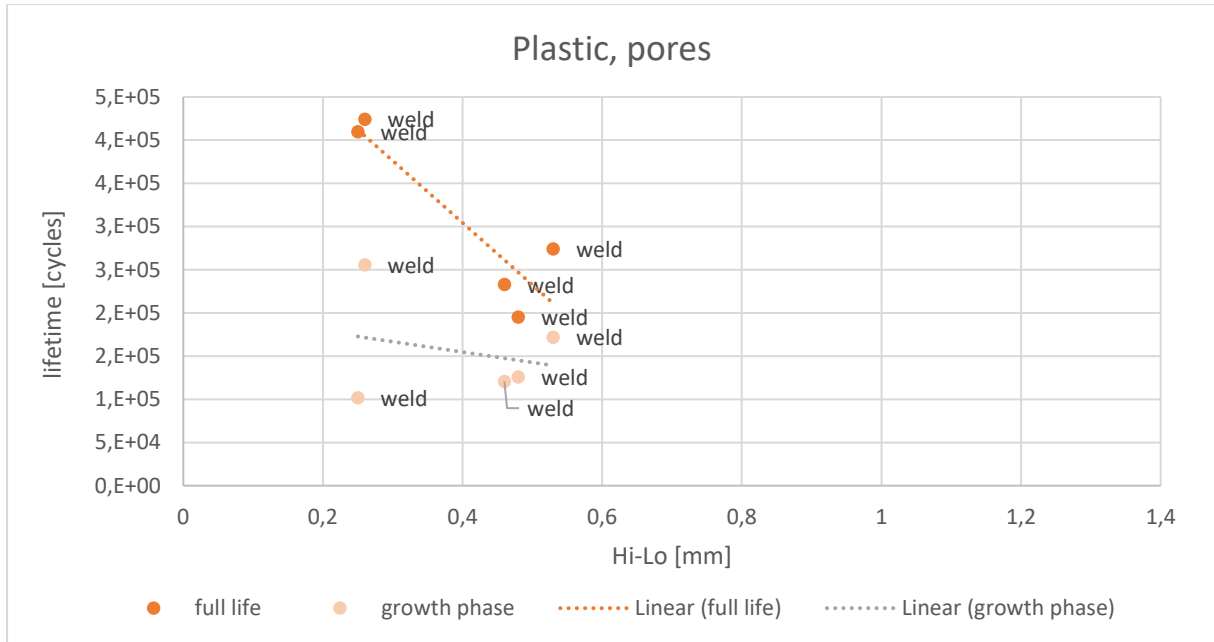

Figure 4.15 "Plastic, pores" group: The effect of Hi-Lo on lifetime.

Only 5 specimens are included in the data set presented above, with Hi-Lo from 0,25 to 0,53 mm, being the smallest scatter within all groups. Lifetime varies between 409925 and 195041 cycles. This group shows similar behaviour to the reference group.
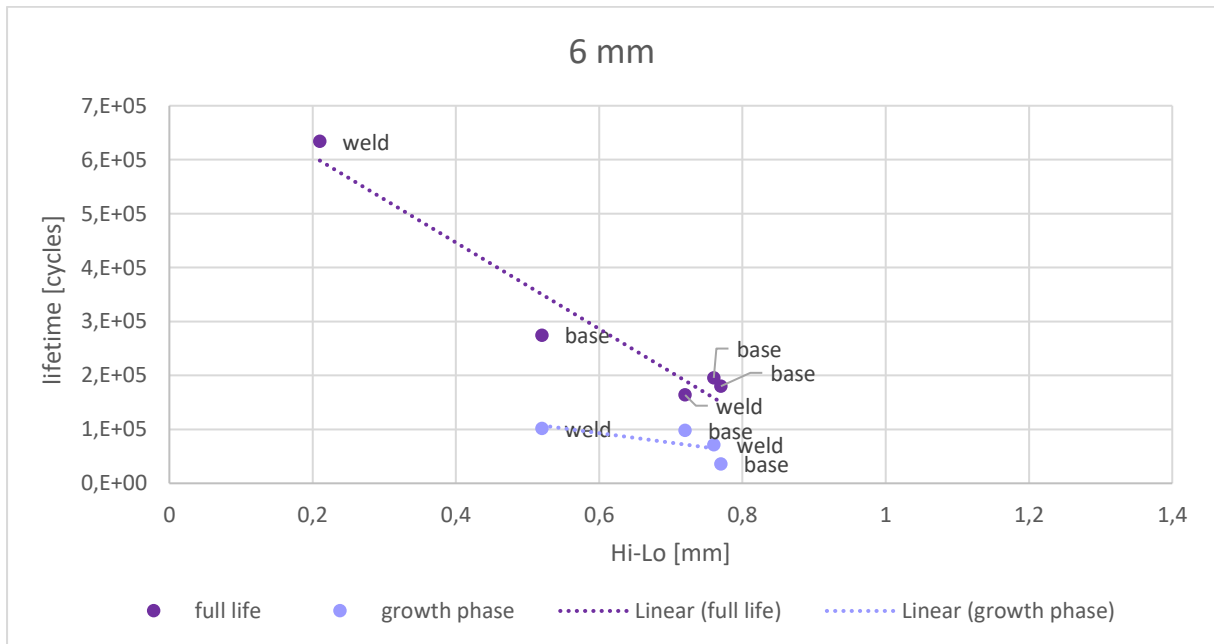

Figure 4.16 "6 mm" group: The effect of Hi-Lo on lifetime.

The results 5 specimens from the 6 mm beadweld coupon, that experienced lower plastic strains are presented above. Figure 4.16 confirms a very similar tendency to the reference or elastic, no pores group. The Hi-Lo scatter is rather average, being 0,21-0,77 mm, with majority of specimens having higher Hi-Lo values. The lifetime is rather scattered, being from 163729 to 633983 cycles.

The comparison between the average number of cycles (of total lifetime and growth phase) of each group has been made in order to discover other (than Hi-Lo) factors that may affect the fatigue lifetime. Figure 4.17 shows the differences between the average total lifetime of specimen groups. This figure combines information from Figure 4.11- Figure 4.16 into one graph. The average total lifetime is expressed in a number of cycles to failure. There are two additional features presented on the graph: the average Hi-Lo per each group (represented by a grey dot inside of a column) and the number of specimens that compose each group (indicated by a number callout above a column). It is also worth noting that within each group (column) there are both weld- and base-cracked specimens present.
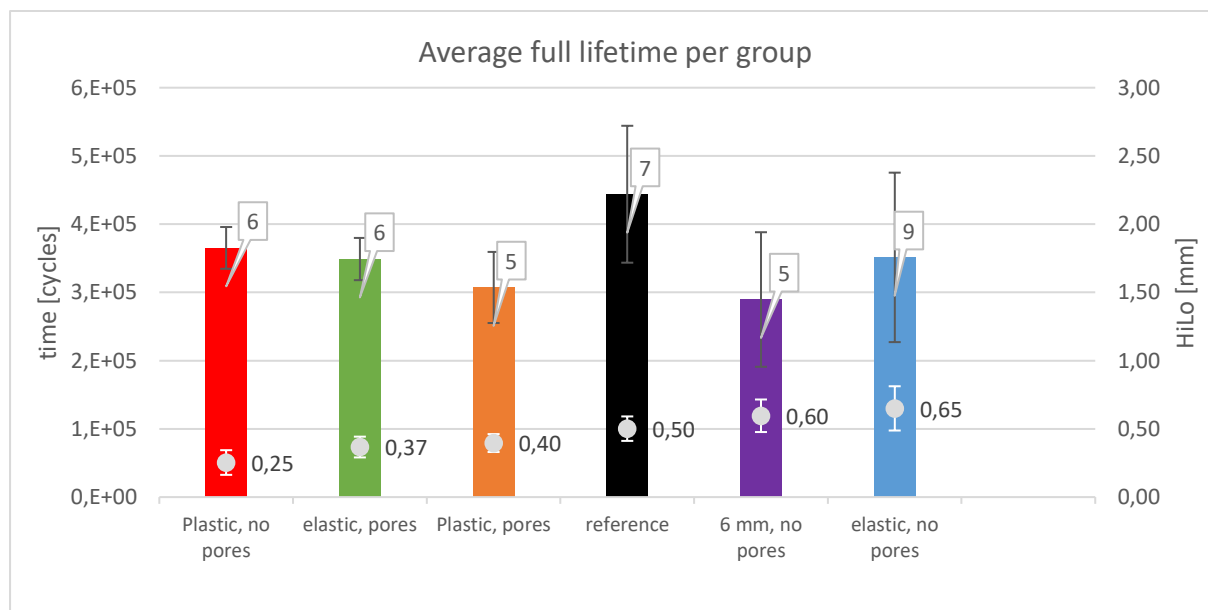

Figure 4.17 Average total lifetimes of all investigated groups, including lifetime scatter. Grey dots within columns represent the mean Hi-Lo values, associated with the scatter given by white scatter bars. The number of specimens per investigated group (column) is given by a digit in a call-out above it.

There is a similar graph presented in Figure 4.18. In this case, each bar represents only the part of the lifetime, namely the growth phase. As previously, the average Hi-Lo information is included and the number of samples in the data set as well. One may note that in some cases there are fewer samples in the "growth only" groups than in full lifetime ones- this is because of the crack propagation monitoring techniques' imperfections. All data on the graphs (average number of cycles and average Hi-Lo) are also accompanied by the error bars, being the standard deviations.
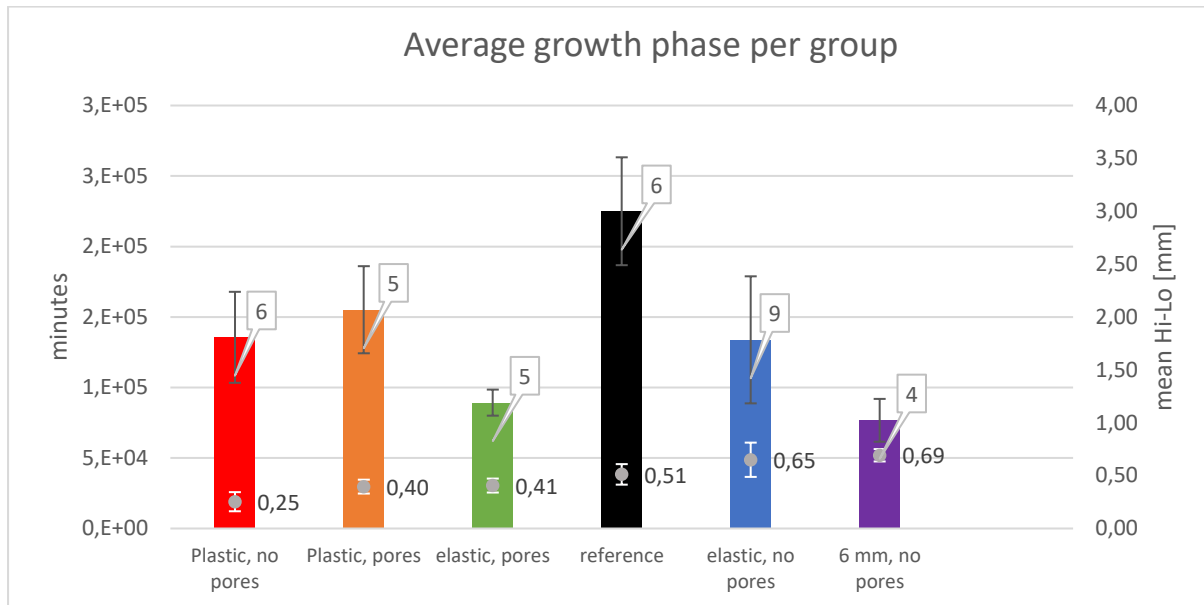
89

Figure 4.18 Average growth phase of all groups, including growth scatter. Grey dots within columns represent the mean Hi-Lo values, associated with the scatter given by white scatter bars. The number of specimens included in investigated group (column) is given by a digit in a call-out above it.

First look at Figure 4.17 and Figure 4.18 immediately brings the observation that the reference specimens had the longest total lifetime (i.e. the best fatigue resistance). However, the scatter associated with this data is high compared to the remaining groups. High scatter is associated with Hi-Lo: we can see in Figure 4.17 (and also in Figure 4.19) that results scatter increases with mean Hi-Lo value. The tendency of decreasing lifetime with increasing Hi-Lo, visible across Figure 4.11 to Figure 4.16, is noticeable, however, not as profound in Figure 4.17. We see that trend for red, green, orange and purple columns, however, two groups (black and blue) do not follow that tendency. It is also worth noting that those two groups have the biggest scatter, which can explain this deviation. The "increasing Hi-Lo - decreasing lifetime" trend is naturally not visible in Figure 4.18 since the crack initiation phase is excluded from those results.

In the case of elastically strained samples, the porous ones show worse fatigue resistance when only the growth phase is considered. The full lifetime graph does not show this behaviour because the Hi-Lo effect is apparently more profound than the porosity effect.

Interestingly, there is an inverse tendency observed for the plastically strained samples (red and orange bars). When the growth phase only is considered there is a counter-intuitive relationship of porous "plastic" specimens having better fatigue resistance. However, looking at the scatters of both groups on both above graphs it can be concluded that there is, in fact, no influence of porosity on fatigue life. The effect of pores on crack propagation can only be confirmed with fracture surface observations (see Section 4.4). Microscopy observations confirmed some pores are present on the FS of "plastic, pores" specimens. Their interference

with the crack, however, seem to have a far smaller effect on the fatigue resistance than the Hi-Lo.

The "6 mm" group (purple bars) shows the lowest fatigue resistance. It also has very big mean Hi-Lo values and relatively high results scatter. In fact, almost all of those specimens (except from one) have Hi-Lo above 0,5 mm (average of 0,69 mm), which is high compared to other groups. Hence, the fatigue life is greatly negatively affected by the Hi-Lo Because of that, it is hard to unambiguously draw conclusions of this group's fatigue behaviour in relation to other factor. The FS observations in Section 4.4, *Specimen C-100; 6 mm, no pores*, suggest that specimens from this group might be affected with pores that interfered with the crack growth, decreasing their fatigue life. High values of H-Lo, together with unwanted presence of pores on the crack's path, explain the poor fatigue resistance of the "6 mm" group specimens.

A similar pair of graphs for weld cracked specimens only was prepared, see Figure 4.19 and Figure 4.20. It was desired to obtain data of specimens that had the fatigue crack initiated and developed in the beadweld (or HAZ) material so that it guarantees the effect of straining was included. However, as mentioned earlier, due to the intact beadweld root (not machined) and various local weld profiles, it was not possible to control whether the crack initiates and propagates in weld or base metal. The number of weld- cracked specimens varies per group, with all of them included in "plastic, no pores" group (orange) and only 2 of them in the "6 mm" group (purple). The only solution to that would be to manufacture and test more specimens, however, this was not feasible for this study. Because of this reason, there are less weld-cracked specimens in all groups than in the groups presented in Figure 4.17 and Figure 4.18. This, together with the material homogeneity, has an advantage of generally less scatter in results of the weld-scatter results.

There can be a similar (to Figure 4.17) descending fatigue lifetime trend observed in Figure 4.19. We see the '6 mm' group (purple) shows a much different behaviour, however, the only 2 specimens included in that group have very high scatter (both for the mean lifetime and Hi-Lo values). The rule of thumb is that a fatigue data set should not have less than 3 specimens, thus the "6 mm" group in Figure 4.19 and Figure 4.20 cannot be accurately analysed.

Looking at the relationship between elastically strained samples, the non-porous ones seem to have much higher fatigue resistance. Thus, pores have a strong effect of elastically strained samples, especially in the growth phase, but only if the weld-cracked specimens are considered. In the previous graph pair the porosity effect was much less profound because as the microscopy showed (Section 4.4), the pores are found only in the weld or HAZ metal. Interestingly, pores seem not to affect the plastically strained samples (red and orange bars) to such a big extent, which can indicate that there was little crack interaction with the pores. As previously, this is be confirmed with fracture surface observation, which showed that a small amount of porosity was discovered on the FS surface of a plastically strained specimen.

Interesting information is revealed when we compare the very high fatigue lifetime (almost $3,5*10^5$ cycles) of the "blue" group in Figure 4.20 with the same group in Figure 4.18(around $1,3*10^5$ cycles). The weld cracked specimens were more fatigue resistant, thus the weld material proves to be stronger than the base metal if the growth phase only is considered. The 3 weld- cracked elastically strained samples have much higher fatigue resistance compared to

the remaining 6 base cracked ones. This is why the blue bars in Figure 4.19 and Figure 4.20 are much higher than in Figure 4.17 and Figure 4.18.
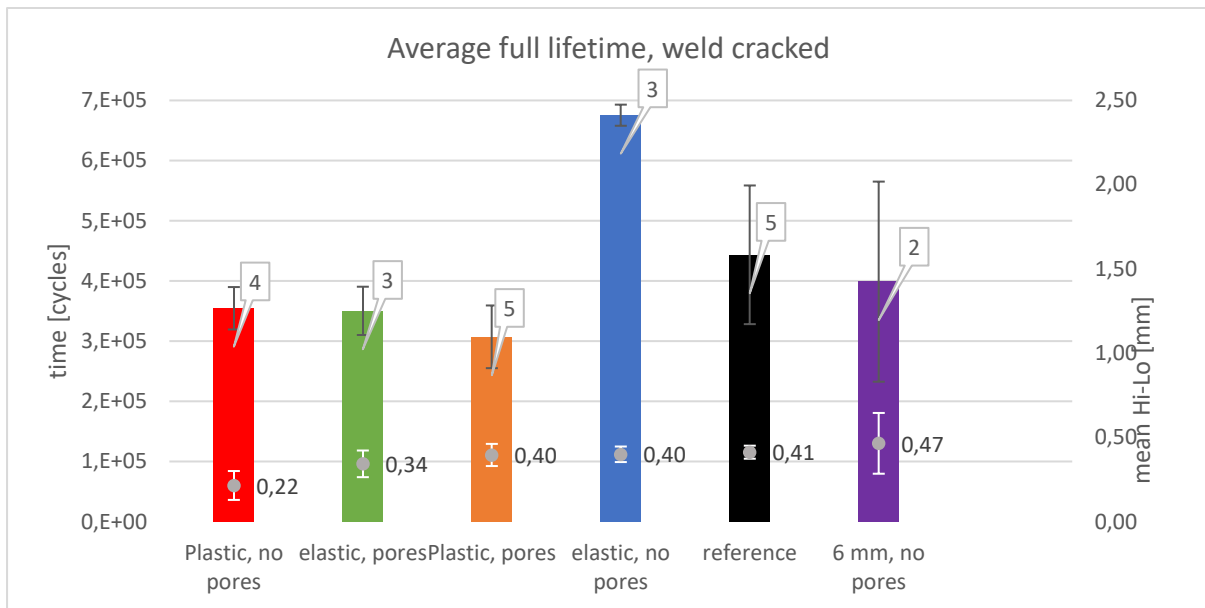

Figure 4.19 Average total lifetime of only the weld- cracked specimens. Grey dots within columns represent the mean Hi-Lo values, associated with the scatter given by white scatter bars. The number of specimens included in investigated group (column) is given by a digit in a call-out above it.
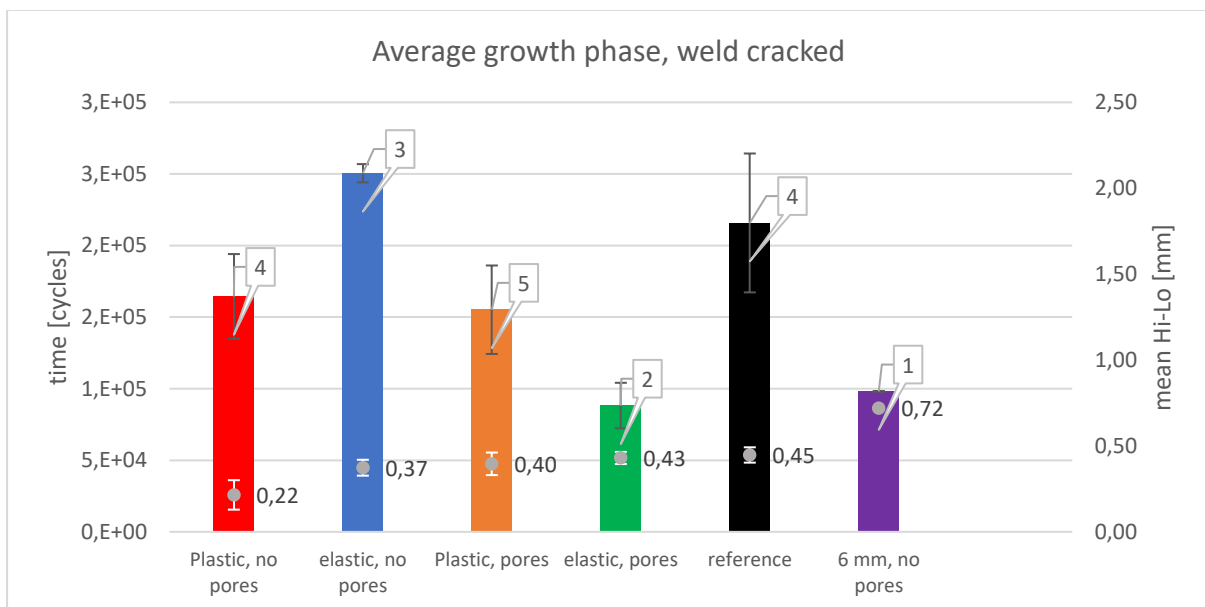

Figure 4.20 Average growth phase duration of only the weld- cracked specimens. Grey dots within columns represent the mean Hi-Lo values, associated with the scatter given by white scatter bars. The number of specimens included in investigated group (column) is given by a digit in a call-out above it.

Effect of Hi-Lo and porosity: discussion

There is a clear dependency of a total lifetime on Hi-Lo observed in each group. This relation disappears (or strongly decreases) when the initiation phase is excluded. Thus, regardless of porosity and strain history of the material, it can be concluded that the Hi-Lo affects strongly the initiation part of a lifetime. The crack growth phase remains unaffected by this surface geometry defect.

Hi-Lo has such a profound influence on total lifetime that this factor has to be accounted for to make an investigation of stress influence possible. Crack growth phase only was investigated further to examine the influence of other factors, like porosity and straining history.

The location of crack initiation, specified as "weld material", "base material" or "both" (interface between the two) was reported post mortem but was impossible to predict or to control. There was 20 weld cracked, 16 base cracked and 2 interface- cracked specimens. Crack would always initiate at the location of the biggest Hi-Lo, however, that location might have been shifted from the fusion line. Such non uniform conditions could not have been avoided due to the choice of the specimen's finish- the beadweld root was left intact on purpose to simulate the real-life conditions. Because of the non-consistent location of the crack initiation (and its initial growth) the beginning of the propagation was not always located in the weld or HAZ. Thus, the first 3 mm of crack propagation were not always located in the strained material.

Study of Figure 4.17 to Figure 4.20 compares the general behaviour of specimen groups relative to each other. Figure 4.17 presents the results that are the closest to the real-life conditions. Indeed, we see that the reference samples, representing the non-strained, undisturbed weld are the strongest. Fatigue resistance worsens for both elastically and plastically strained material. When the initiation phase is excluded from the total fatigue life the porosity in plastically strained material does not play a role (there is no crack interaction with pores), see Figure 4.17 and Figure 4.18. However, it seems like pores do interact with a crack in the elastically strained groups. This may be assumed as some porosity was confirmed with microscopy or fractography observations.

Figure 4.18 and Figure 4.20 (cases of growth phase only) clearly show that there is no Hi-Lo influence on fatigue resistance once the initiation phase is excluded. Again, looking at those graphs as well, there is a big porosity effect on elastically strained specimens. It indicates that pores may play an important role in fatigue behaviour especially in the growth phase. On the contrary, again we see no porosity effect on fatigue life of plastically strained specimens. This can be explained by the presence of the plastic zone near the pores, that was enhanced by the straining history. The plastic zone is an obstacle on the fatigue crack growth path, which requires more energy for the crack to pass through it (N. Noraphaiphipaksa, 2012). The negligible difference of fatigue resistance for plastically strained porous and pore-free specimen indeed indicated that straining removes (or decreases) the stress state around the pores. Another conclusion that can be drawn from the mentioned graphs is that when the initiation part is excluded from the total lifetime plastic straining seems to in general improve the fatigue resistance (when compared to elastic straining). The very high lifetime of the "blue" group in Figure 4.20 that deviates from this trend can be justified with the small data set for this group.

The analysis of the above graphs greatly helps to answer the research questions. Especially Figure 4.17 may be of the special interest of the offshore industry as it presents the results in conditions most similar to the real life conditions. It can be then concluded that plastic straining does not affect the fatigue resistance to a higher degree than the elastic straining does. Moreover, the quality of welds that were plastically strained, seems to play a smaller role than it is in the case of elastically strained, because the plastic deformations most likely soften the effect of pores. Apart for the straining, this is the misalignment factor that should be best controlled in order to improve the fatigue resistance.

4.5 Microscopic observations results

A number of specimens have been selected for the detailed observation under the optical and SEM microscope. The features of interest for the microscopy were: porosity, fracture surface (FS), base metal, weld metal and HAZ microstructure, fatigue crack location. Specimens selected for the observations are shown in Section 2.8, Table 2.5.

The main goal for the microscopic investigation and hardness testing was to look for pores or microstructure differences between specimens types and, if found, to expose their interference with the fatigue crack.

Specimen 0-2, reference

The measured Hi-Lo of this specimen was 0,88 mm and slight anisotropy of the crack growth was observed, see Figure 4.21
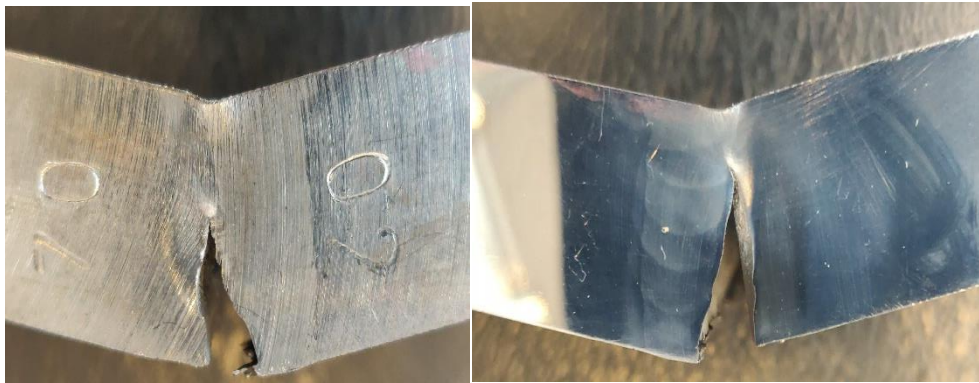

Figure 4.21 Both sides of the cracked 0-2 specimen, just after the fatigue testing. Anisotropy of the crack growth is visible, with the longer crack side on the observed (polished) face.

The investigation started with the fracture surface observation. Once the specimen was broken into halves (with a single overload) the FS was preserved and investigated under the optical microscope, see Figure 4.22. A clear distinction can be made between the flat, shiny fatigue fracture surface (bottom) and the ductile, overloaded remaining upper part of the specimen. The blue arrow indicates the direction of the crack growth: from the root toward the weld cap. A number of characteristic features can be observed in the picture. The look of the fracture surface, together with the specimen shape, allow identifying the plane stress and plane strain areas. The shape of the FS (marked with the yellow line) allows identifying the areas where the shear stresses were predominant.

After the fracture surface observations were completed the specimen pieces were prepared for the microscopic observations.

The overview of the full weld, viewed from the middle plane and the edge plane is presented in Figure 4.23. Differences in microstructures of the base metal, HAZ and weld metal are already visible. The arch-like traces of the subsequent welding passes are also visible. The path of the fatigue crack (the right, vertical edge) can be easily distinguished from the plastic overload, caused when the specimen was forcibly broken into halves after the testing- the cracked edge is smooth and straight, whereas the upper part of the edge is non uniform and heavily deformed. The location of the fatigue crack initiation can be seen in the lower right corner of the weld. We see the crack initiated at the location shifted from the fusion line, caused by the weld misalignment. That misalignment (Hi-Lo) is also visible in Figure 4.21. The crack path is different at the edge and the middle planes. At the edge (observed) plane the crack, once departed from the Hi-Lo location, followed the fusion line. In the middle of the specimen, however, the crack propagated straight upwards, clean-cutting through the columnar microstructure of the fusion zone. It can be explained by the maximum tensile stresses acting in the middle of the specimen during fatigue and the shear stresses prevailing on the sides.
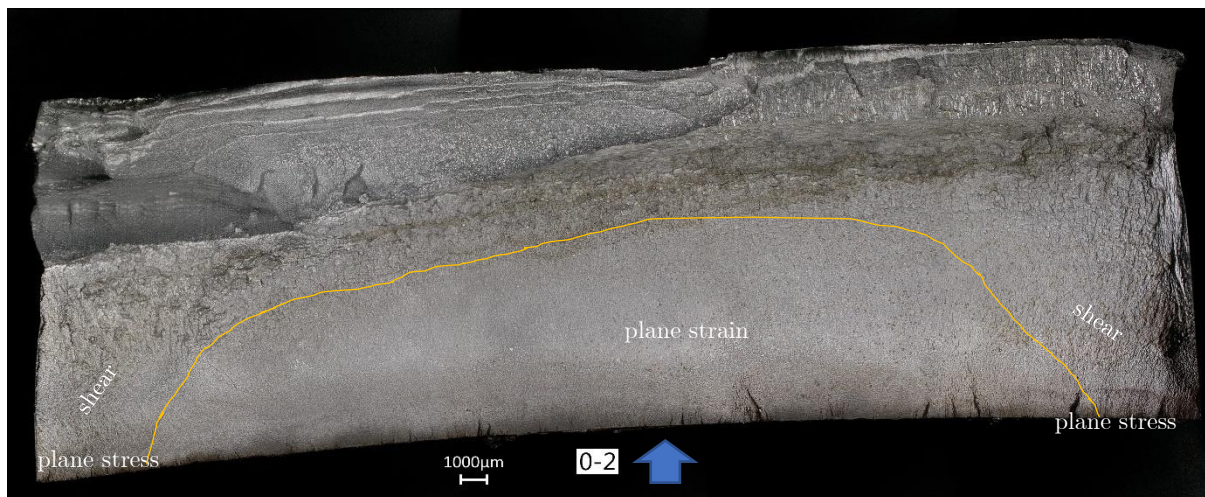

Figure 4.22 Fracture surface of specimen 0-2, magnification x20.

Figure 4.23 Specimen 0-2 edge plane and middle plane views of the full weld. Magnification x50. The beadweld is marked with the arrow.

A zoom-in view into the crack initiation area was made, see Figure 4.24. The columnar microstructure of the weld is revealed. It can be concluded that the crack initiated at the fusion line or in the weld metal and then propagated straight up, entering the HAZ. Scattered porosity is present in the weld and HAZ, which seems to be absent in the base metal.
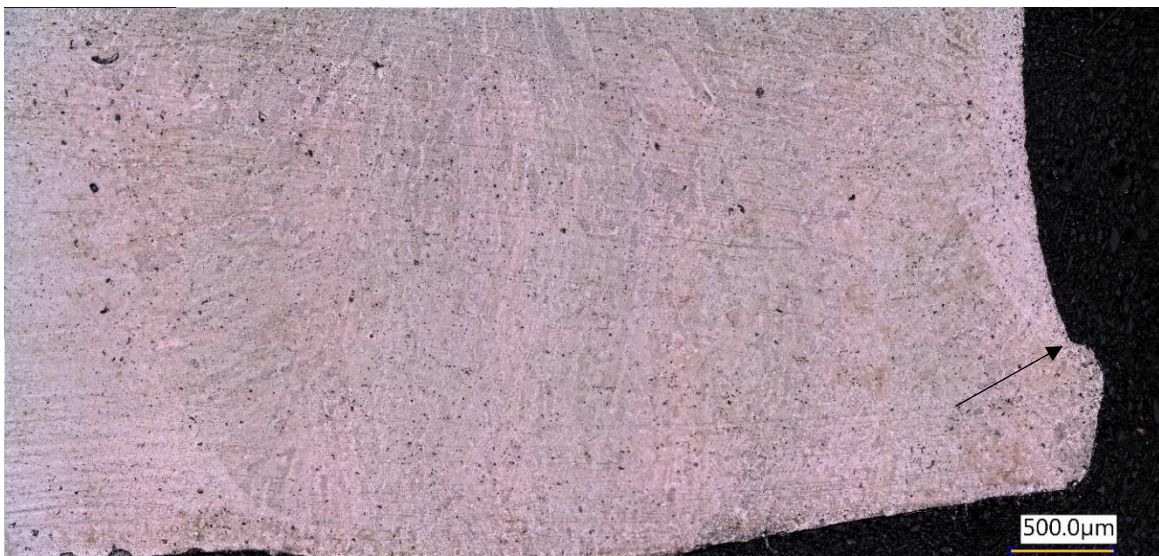

Figure 4.24 Specimen 0-2, the beadweld, magnification x250. Crack initiation point marked with the arrow.

The size of the pores was measured at the interface between HAZ and weld. The porosity of irregular shapes and size between 8-42 µm is revealed. The NDT conducted by Allseas (see

Section 3.6) used to check the weld is unable to detect such small pores, hence it was not previously reported as it is assumed to not affect any fatigue properties of the weld and, ultimately, the pipeline.

Despite the porosity, microscopic observations confirmed the correct microstructure of the weld and HAZ, see Figure 4.25.
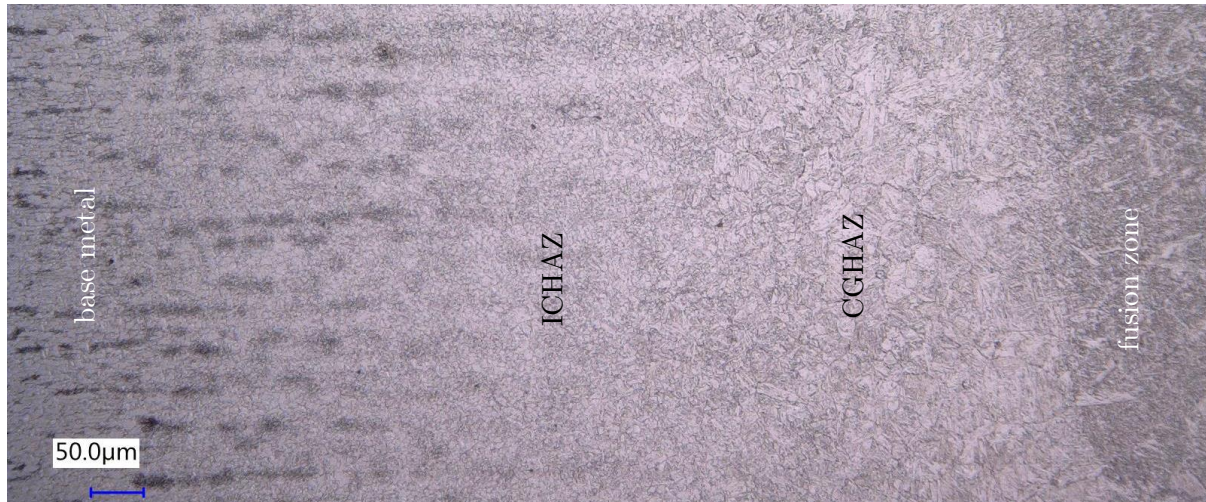

Figure 4.25 Evolution of the microstructure as it approaches the weld centre line. Magnification x300.

The columnar grains of the fusion zone are clearly visible. Further away from the weld the bigger grains of the CGHAZ are visible, gradually transforming into finer grains of ICHAZ. The band-like structure of the X60 steel is visible on the far left of the picture.

The last step of the specimen analysis was hardness testing. The tests were performed on the polished surfaces, as specified in Section 2.9. Figure 4.26 shows the overview of hardness indents points after testing. An example distribution of points over the base metal, HAZ and weld metal, in the beadweld location, is presented in Figure 4.26.

Figure 4.26 Hardness indents across the beadweld of specimen 0-2. Dimensions are given in μm.

Hardness testing results and their discussions, for all six specimens analysed in this chapter, are presented in Section 4.6.

Specimen A-270: plastic, no pores

The same as presented above investigation steps were conducted for this specimen. Special care was made during the analysis, as it belongs to the group of the special interest- plastically strained specimens with no porosity reported. Virtually those specimens represent the material of the overstressed beadweld during the pulling on the bead operation.

The investigation started with the FS observations. Crack growth anisotropy across the specimen thickness was observed. As in the case of the specimen 0-2, characteristic features are visible, too: the ductile overload zone and the flat fatigue fracture, the shear deformations at the sides. Additionally, well pronounced are interesting arch-like features. The arches are located only in the plane strain governed part of the fracture surface and were noticed in almost all other specimens investigated in this study (even though their finding strongly depends on the quality of the FS). Characteristic ratchet marks, typical fatigue macroscopic features, are located along the root edge of the specimen. Their nature will be discussed later in this section. The macrographs of specimen A-270 microstructure can be found in APPENDIX J.

An example of the arch-like features, indicated by the yellow arrow, of the Ex-A specimen, are presented in a zoom-in view, see Figure I., APPENDIX J. Those features can be assumed to be the consequence of the ductile striations perpendicular to the crack growth direction. Relatively high ductility of the investigated steel was confirmed with the SEM observations, see Figure II. What with the naked eye looks like a smooth fatigue fracture surface, under the SEM reveals its ductile nature. The facades of the ductile fatigue failure, perpendicular to the crack growth direction, are visible.

Zoomed-in view of the same area, to the magnification where the striation (microscopic features) usually start to become visible, is presented in Figure III. The extent of ductility is clearly visible. Because of that, no striations can be observed.

Another typical fatigue features, beach marks and ratchet marks, are presented in Figure IV. The ratchet marks are the well-pronounced facades, located at the highly stressed edge (weld root) and aligned parallel to the crack growth direction. Ratchet marks indicate multiple crack initiation sites, usually on different planes in the metal. Once the microcracks initiate, their sites grow and coalescence via tear ridges, creating the well visible ratchet marks. Beach marks often occur together with ratchet marks, making both of them one of the most reliable (macroscopic) features to identify fatigue failure, its nature and its initiation sites. Beach marks are indicated in Figure IV. with the yellow arrows. They are easy to identify as they are aligned in a slightly semi-elliptical manner, perpendicularly to the crack growth direction. Both described macroscopic features of the fatigue, ratchet and beach marks, were found on all fracture surfaces investigated in this research.

Finally, the macrographs of the full weld of this specimen were investigated, see Figure V. An interesting situation is presented in terms of the crack initiation location and the initial propagation. The fatigue cracks clearly initiated at the Hi-Lo, thus within the fusion line area. However, due to the shape of the beadweld (see the edge plane view) its initial path was mostly contained within the HAZ area. Growing deeper in the weld the crack path followed the fusion line again. The investigation of the middle plane view shows that in the middle of the specimen the crack initiated away from the fusion line, in the HAZ (or even the base metal), due to the different beadweld shape. The crack's offset from the fusion line was measured as 972 μm (middle plane view, Figure V.). The crack path in the middle of the specimen is straight and does not follow the fusion line. No interference with microstructure artefacts is revealed.

A big pore, the diameter of 582 μm, was discovered at the edge plane, within the beadweld. The pore was too small to be detected by the NDT, however, big enough to disturb the crack path, if on its way. Despite its size though, the crack did not interfere with the pore, passing it approximately 0,5 mm away. Thus, indeed, the classification of this specimen as previously reported pores-free is adequate.

Hardness results of specimen A-270, along with the others, will be presented all together at in Section 4.6.

Specimen B-240: plastic, pores
FS observation of this specimen revealed the presence of pores, meaning the crack interfered with the pores on its path.

The microstructure of the weld was investigated, see Figure VI, APPENDIX K. Crack initiated in the weld metal shifted slightly from the fusion line. At the edge plane, it propagated along the fusion line, whereas the crack in the middle of the specimen propagated straight upwards, cutting through the subsequent weld passes. Comparisons of the edge-view and the middle plane-view of the crack length indicate the crack growth anisotropy

A zoomed-in view into beadweld microstructure revealed different grain shapes and sizes in the beadweld area. Grains directly adjacent to the beadweld edge are finer compared to the columnar grains inside of the weld. The crack initiation location at the Hi-Lo, within the weld metal, is well visible.

Evolution of the microstructure from the base to the weld metal was assessed. No porosity is revealed in the microstructure. The microstructure evolution corresponds to this reported in the 0-2 reference specimen.

Specimen A-160; elastic, pores
First, the fracture surface of this specimen was investigated. As expected, the presence of pores interfering with the crack is revealed, of sizes big enough to be detected by NDT. Typical macroscopic features of the FS, as discussed before, are present. The golden colouring was found on the surface, being the oxide layer on the FS, which appeared after the specimen was broken into halves.

The overview macrograph of the weld is presented in Figure VII., APPENDIX L The crack initiation is clearly located in the base metal, even though it originated from the Hi-Lo (measured value of 0,42 mm).

Some pores were revealed in the weld, see Figure VIII.1 The pore of the biggest size was approx. 86 μm, while the smaller ones were in the range of 9-17 μm. They were too small to be detected by the NDT. Besides the presence of pores, the microstructure of the base metal, weld metal and HAZ is correct.

Specimen A-320; elastic, no pores

The investigation of this specimen started with the FS observations. Typical macroscopic fatigue features reported in different specimens, like ratchet marks, arch-like fatigue features, shearing, together with the ductile overload are, are seen in this case, too. A big pore was found in the middle of the specimen, in the overloaded area, thus its presence did not interfere with the fatigue crack.

Even though this specimen was expected to have no porosity, the overview picture of the microstructure already indicated that some pores are present. They are better visible on higher magnification macrographs. Macrographs revealed that the location of the crack initiation is the fusion line.

Figure 4.27 shows the revealed porosity in the weld and HAZ, within the size range of 12- 184 μm, yet they are still of acceptable size and are assumed to not affect the performance of the weld. The scattered porosity shown here is similar to the pattern that is shown in the 0-2 (reference) specimen.
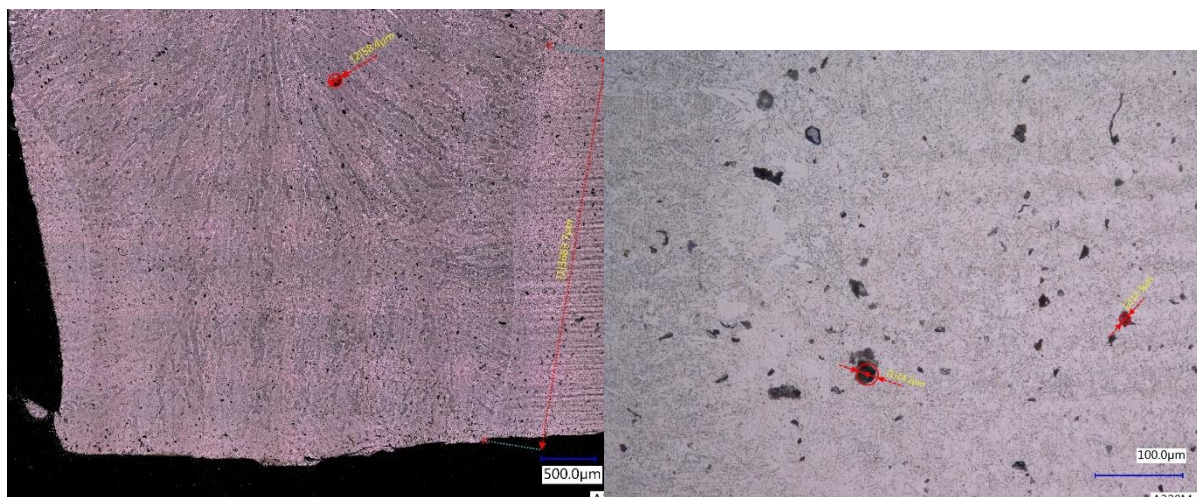
Figure 4.27 Higher magnification macrographs showing porosity in the hot pass (left) and in the HAZ (right), specimen A-320.

Specimen C-100; 6 mm, no pores

Figure 4.28 presents the FS of the specimen from the last investigated group- 6 mm beadweld thickness with no porosity reported. However, a number of pores are visible on the fracture surface, most of them located in the beadweld or hot pass. Clearly, the crack interfered with those defects. Characteristic macroscopic features of the FS, as discussed earlier, are visible too.

Figure 4.29 presents the macro photographs of the full weld, seen from the edge plane and the middle of the specimen plane. Very different crack paths are observed. The edge plane view is the plane that was observed during the microscopic crack growth observation, see the arrow in Figure 4.28. It must be noted that the crack did not initiate on that edge, a situation analogous to specimen A-100, see Figure 4.2. That path of the crack that we observed here is the final fracture of the fatigue failure, not the steady crack growth. Thus the curvature of the

path, very different from the straight, smooth crack growth path presented in the middle plane view, Figure 4.29. It can be concluded that the crack growth in the middle of the specimen was steady, most likely the crack growth on the other, not observed edge as well.

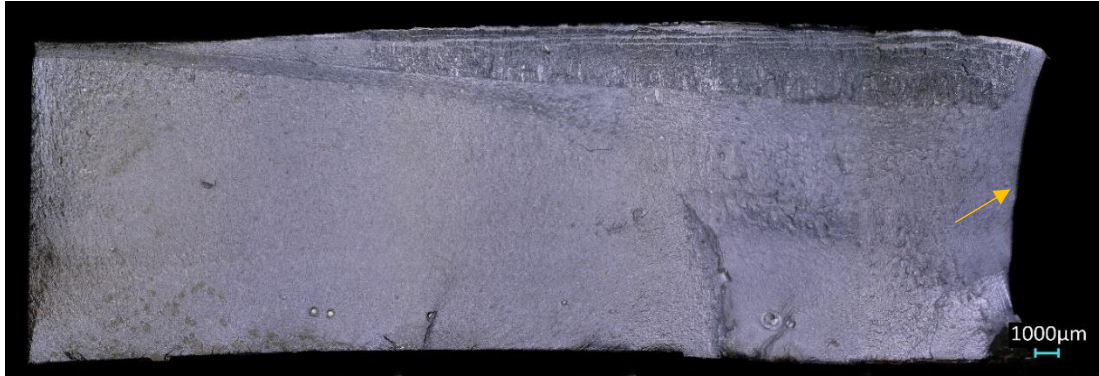No porosity was discovered in the investigated microstructure.

Figure 4.28 Fracture surface of the specimen C-100. The observed edge is marked with the yellow arrow.

Figure 4.29 Specimen C-100, macrographs of the full weld, edge plane (left) and middle plane (right0 views are presented.

4.6 Hardness testing results

Hardness line results, measured across the beadweld and the centre of the weld are presented for each of 6 specimens investigated in Section 4.4. Those results cover the spectrum of one representative specimen per specimen type: reference, elastic- no pores, elastic- pores, plastic-no pores, plastic- pores, 6 mm beadweld.

Full line hardness measurements, taken through the beadweld and taken through the middle weld pass, were made for all six specimens, resulting in 12 single measurements. Each line measurement started in the base metal and ended in the weld metal, passing through the HAZ areas. Differences between results taken in the bead and in the middle weld were investigated. Also, the average hardness results in between the specimens were compared, representing differences between specimen groups. Both hardness line measurements of specimen A-270 will be presented here in detail, as an example (Figure 4.30). The hardness results of the remaining specimens can be found in APPENDIX F

The results of hardness testing at two locations across the weld- at the bead and at in its centre- are presented. It must be noted that the measurement points have different global X and Y coordinates relative to the specimen, i.e. the lines start and end in different positions. The location of points was determined based on the macrographs of the indents made after the testing. Based on those photographs it was possible to determine the exact width (and a number of indents) of the base, HAZ, and weld metal, for all the investigated specimens. The exact description of the hardness testing methodology can be found in Section 2.9.

The ident size (a pyramid with 87-97 μm diagonals) is bigger than the size of grains in the investigated microstructure, thus hardness was measured across several phases and the results are pore-independent. Both line measurements presented, in the bead and in the middle, show a similar tendency of increasing hardness towards the weld centre. It can be concluded that the weld metal is stronger than the base metal.

The "base metal" parts of hardness results, in both distributions (Figure 4.30), (approx. 0,8 mm) are constant. Hardness in the HAZ (approx. 1 mm) increases steadily, in a similar manner for both distributions until it reaches the weld metal. Hardness scatter in the weld metal is higher than in the other zones. Also, the weld metal hardness measured across the middle weld is higher than the one measured across the beadweld. Higher scatter can be associated with the bigger grains of the weld microstructure, resulting in one indent averaging across fewer grains. The microstructure observations proved that weld metal in the beadweld zone especially can suffer from small, scattered porosity.
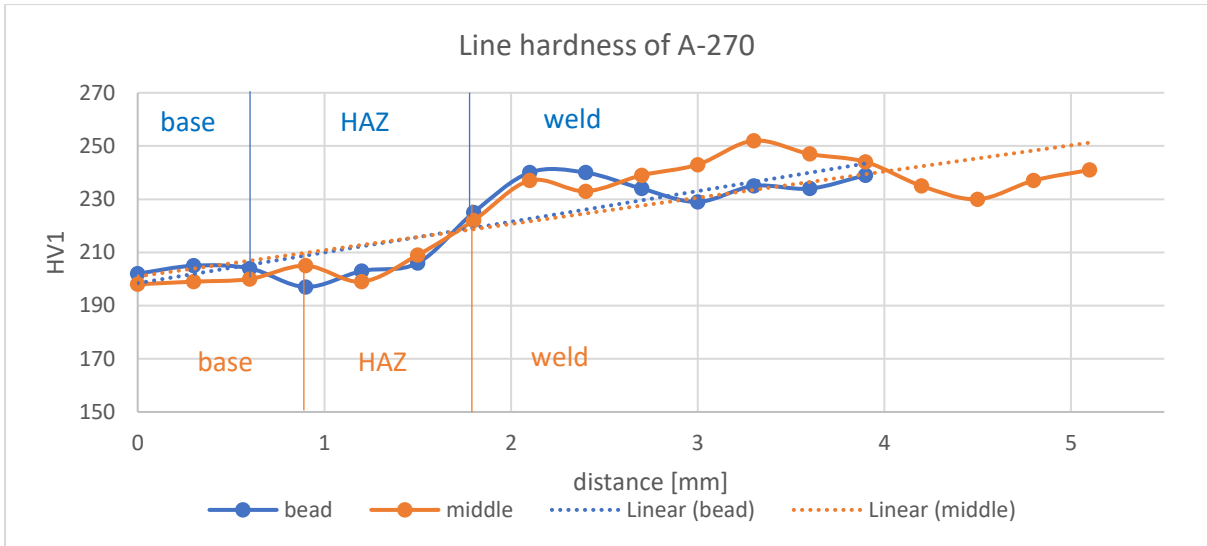
Figure 4.30 Specimen A-270 hardness results. The 0 mm distance refers to the full base metal, the last points are located in the weld. Note: the start and end points of both distributions do not coincide. The bead hardness line measurement is longer as its HAZ is wider and the base part is longer.

The effect of scattered, small size pores, not relevant for the fatigue performance, is rather negligible for the hardness results. The rare presence of individual, bigger pores can affect the local hardness. Thus, the quality of weld (its porosity and homogeneousness) play an important role in its overall microhardness.

The above investigation steps and reasoning were applied to the five remaining specimens, see APPENDIX F. Based on those results the further analysis was done, comparing the average hardness of the base, weld and HAZ metal for all the specimens in the bead and middle weld pass.
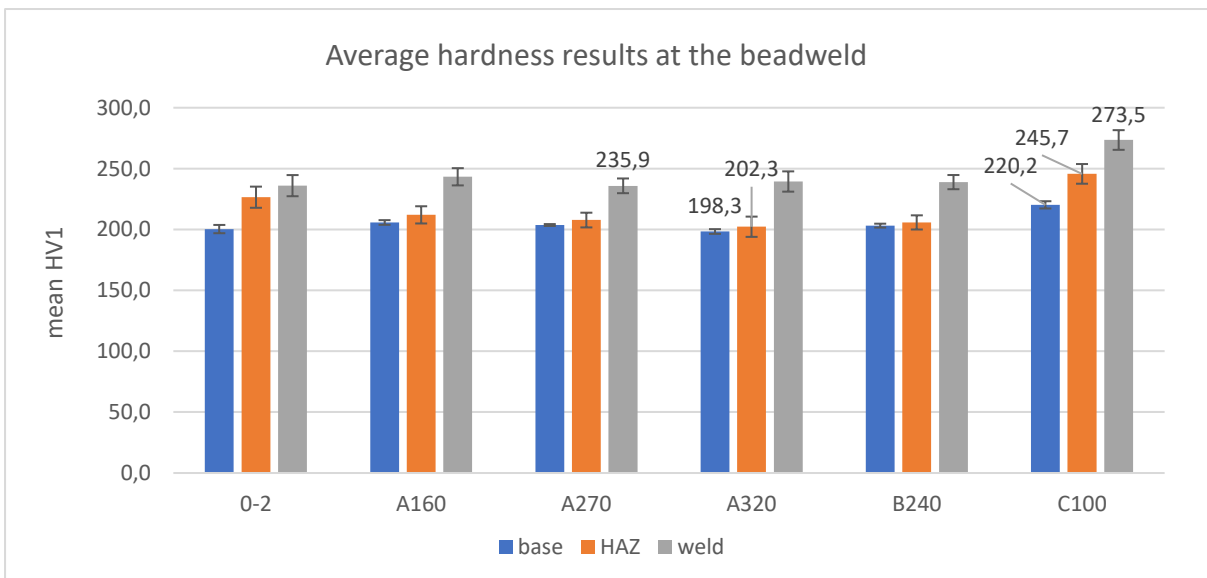
Figure 4.31 Comparison of the average hardness of base, HAZ and weld metal measured at the bead. Maximum and minimum averaged values for the base, HAZ, and weld metal are shown.
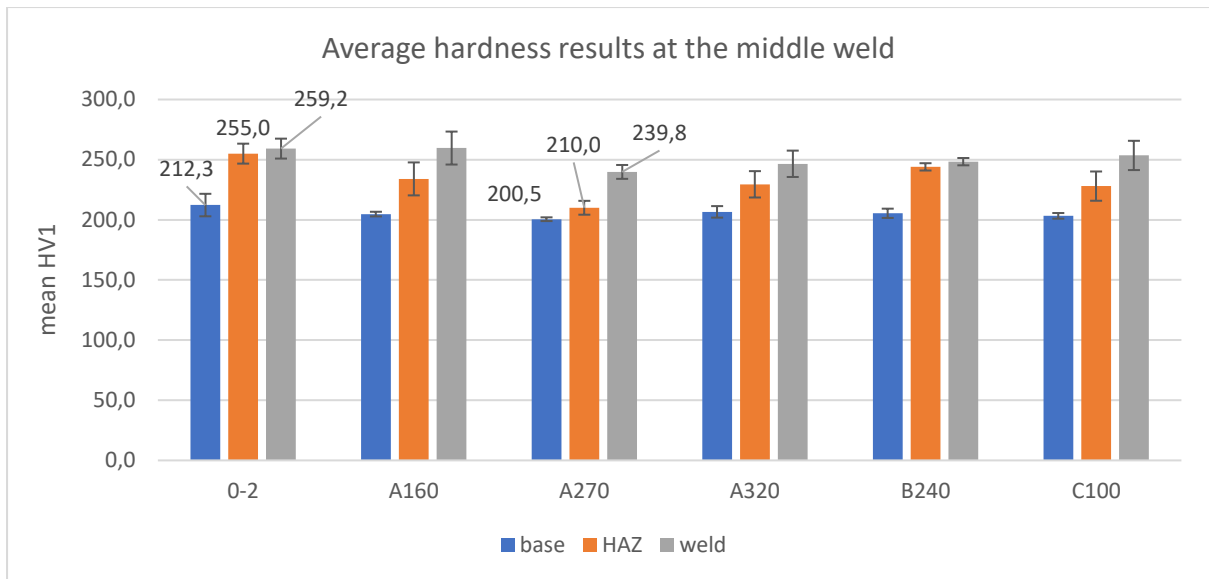
Figure 4.32 Comparison of the average hardness of base, HAZ and weld metal measured at the middle weld. Maximum and minimum averaged values for the base, HAZ, and weld metal are shown.

Results in Figure 4.31 and Figure 4.32 are consistent that the weld material is the strongest within the specimen, HAZ is less strong and the base metal is the weakest, measured both at the beadweld and at the middle weld pass. There are no big differences recorded for the hardness of particular zones measured across the beadweld and the middle weld. For both bead and middle weld results, in all samples, the minimum scatter is associated with the base metal and the biggest with the weld metal. Again, the scattered porosity is the cause.

In the majority of the cases (only except the C-100 specimen), the weld hardness is higher when measured across the middle weld than the beadweld. It is in accordance with the microscopic finding of generally more profound small-size scattered porosity in the beadweld area, that may negatively affect the hardness. Also, slightly higher hardness of the zones measured in the middle weld may be explained by the fact, that the higher located weld material experienced re-heating cycles, compared to the beadweld material that close to the root edge did was re-heated to the smaller extent or not at all. Researchers (X.L. Wang, 2017) proved that the microstructure of the re-heated weld metal differs from the as-deposited weld microstructure- there are large amounts of hard and brittle martensite/austenite constituent found in the re-heated weld microstructure. Thus, the middle weld line measurement, most likely crossing the re-heated zones of weld metal, show slightly higher hardness than the equivalent line measured at the bead.

4.7 Tensile testing results and discussion

All tensile specimens were thoroughly measured before mounting in the machine grips. Table 4.2 gives an overview of their dimensions, with results given in mm. Specimens P are of plastically strained material, E of elastically strained material and "0" of the reference material.

Table 4.2 Overview of tensile specimens' dimensions as measured before testing.

specimen	P1	P2	P3	P4	0-1	0-2	0-3	E1	E2	E3
thickness	13,7	14,1	13,8	13,9	14,0	13,9	13,4	13,5	13,1	12,3
width	12,5	12,5	12,5	12,4	12,5	12,6	12,5	12,6	12,0	12,5
gauge L	51,6	52,3	50,6	52,0	52,4	52,7	52,7	52,5	52,7	52,6
total L	177,6	178,5	177,5	177,5	176,9	178,9	177,1	182,1	179,5	180,3
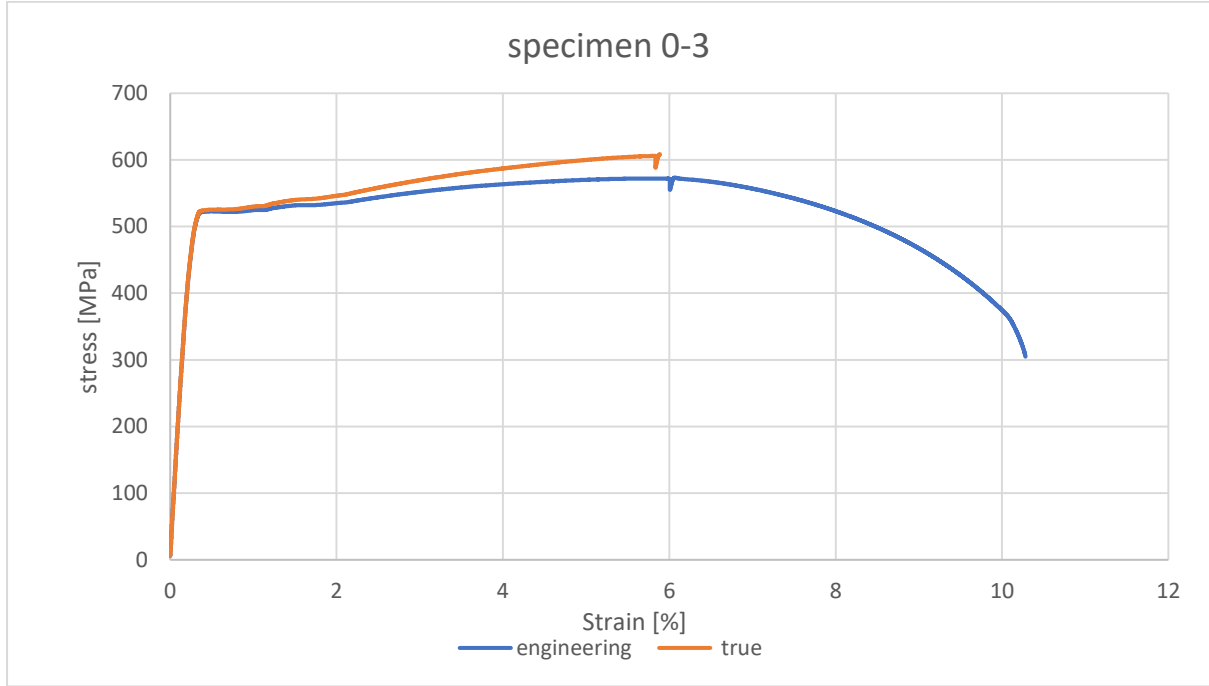
Figure 4.33 Stress-strain relationship of the reference material, specimen 0-3.

The result of tensile tests 10 stress-strain curves were obtained, all can be seen in APPENDIX H. One curve, the result of the reference material testing is shown in Figure 4.33. The output from the tensile test is the *engineering* stress-strain relationship (blue curve), which means that the strain and stress are calculated relative to the initial cross-section of the specimen- the cross section changes during irreversible deformation are not taken into account. This is fundamentally different from the *true* stress-strain curve, where the actual cross section area in each stress increment is considered.

Engineering stress and strain can be converted to the true ones with the following formulas (Bäker, 2007):

$$\sigma_t = \sigma_e * (1 + \epsilon_e)$$

and

$$\epsilon_t = ln(1 + \epsilon_e)$$

where σ_t, ϵ_t and σ_e, ϵ_e are the true and engineering constituents, respectively.

The output from the tensile machine and its conversion to the true relationship can be found in APPENDIX I. The true stress-strain curve was used as an input for the material model in the FEA, see Section 3.1.

The tensile machine was equipped with the software analysing the obtained stress-strain curves. Based on the input specimen dimensions and the applied force the mechanical properties of each specimen were automatically determined. No value of the yield strength for specimen P2 was recorded due to faulty reading from the extensometer.

Figure 4.34 and Figure 4.35 compare the tensile properties of individual specimens and between the groups. Young's modulus is not being compared as all the specimens are of the same material. The properties such as yield and ultimate tensile strength, however, can be affected by the mechanical or thermal history of the material. This can be well seen from the charts below- the reference specimens, virtually without any straining history, exhibit the smallest scatter in their results and are also the strongest. It can be concluded that straining of the material, elastic or plastic, has a negative effect on its mechanical strength. When comparing the plastically and elastically strained specimens, the former seems to have slightly higher strength. The explanation may come from the general mechanical behaviour of steel (see Section 1.9) and the phenomenon of work hardening. Plastically strained material experienced strain hardening to a bigger extent than the elastic one.
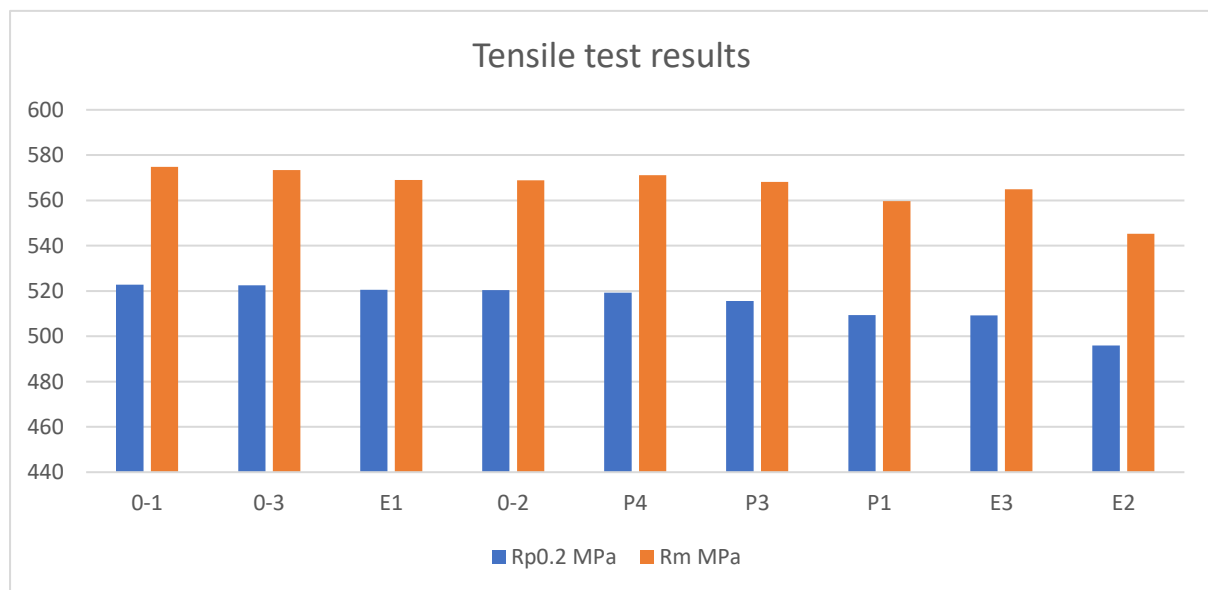

Figure 4.34 Overview of tensile properties of tested specimens range by the yield strength in descending order. 0- reference, E- elastically strained, P- plastically strained.
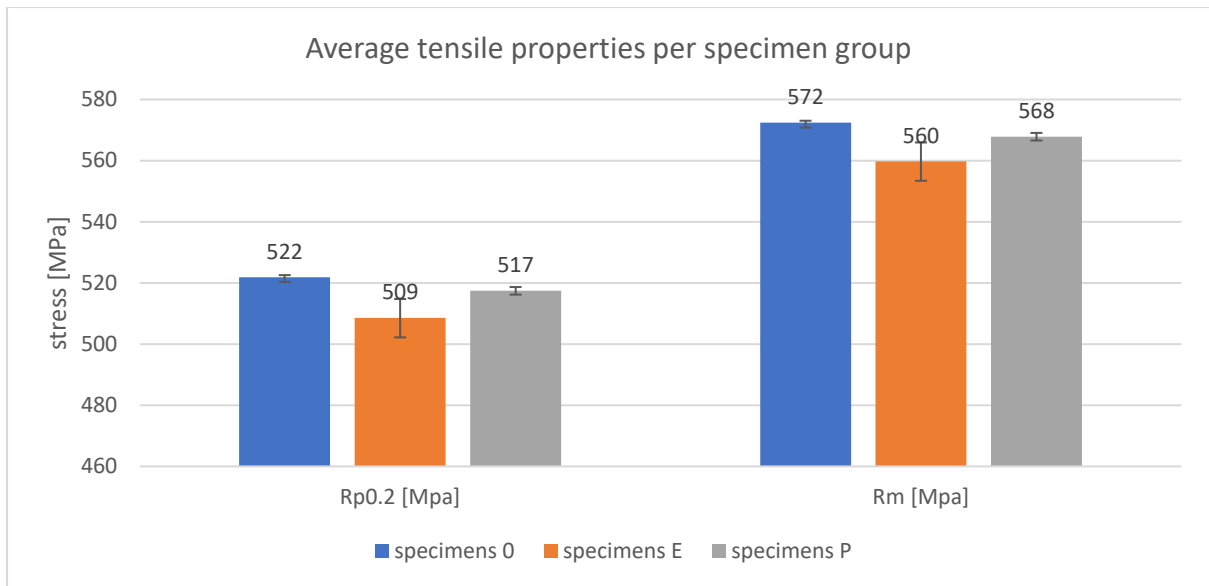
Figure 4.35 Average tensile properties per specimen group: 0- reference, E- elastically strained, P-plastically strained.

An example of the broken tensile specimen is presented in Figure 4.36. The weld is visible as the slight change of colouring in the middle of the specimen.

Figure 4.36 Tensile specimen after testing.

Necking, as well as the final ductile fracture, is not centrally located but shifted slightly towards one end. It is common also for smooth plates to neck away from the centre and the exact location of necking is hard to predict. Knowing the results of hardness, most likely the base metal is the preferable location of necking in this case. It is worth noting that all of the 10 tested specimens necked and fractured away from the middle. All the specimens had the same surface finishing and contained the weld in the middle. The fact that the weld was not a preferable fracture location indicates that the weld metal was stronger than the base metal or HAZ.

4.8 Accuracy and uncertainty

The methodology and testing procedures presented in this research are, to some extent, affected by the inherent accuracy level. This has to be taken into account to critically assess the produced results and the uncertainty related to some aspects. When evaluating the presented results it is important to be aware of the factors influencing them. The overview of those factors is presented in Table 4.3. Such an overview can be a useful departure point of future research recommendations.

Table 4.3 Overview of factors affecting the accuracy of results discussed in this research

factor	effect	proposed solution
Overstressing simulation loading mode	Introduction of the symmetrical peak and low stresses along the girth weld, which is different from the bending-induced stress distribution caused by pulling on the bead	-
The symmetry of loading applied by the jacks	Due to manually applied loading by two valves operators, it might be that the bending moment was introduced to the beadweld during the overstressing simulation.	An automated, machine controlled loading setup with uniform load distribution.
Determination of size and location of porosity	Porosity could only be assessed post mortem, as far as optical microscopy was performed.	Porosity detection per each sample, with, for example, radiography.
Conditions of the start/ stop locations	Welding start and stop positions can have widely different properties than other locations and were not covered in this study.	A separate investigation of the effect of heat input on fatigue performance.
Symmetry and alignment of the 4-point bending setup	The setup was built and operated manually, thus there is a possibility of misalignment and non- uniform stress during fatigue testing, that differs from the FEA.	An automated, 4-point bending setup or a different fatigue loading mode- for example a rotating bending setup.
The accuracy of the PD measurement	Locations of the electrodes attachment and the vibration during fatigue testing influence the output signal.	A different specimen design, with the PD electrodes, screwed into the specimen at exactly the same location.
The sensitivity of the optical crack observations	One camera observes one side of the specimen only. Minimal observable crack size is 200 μm.	Two high magnification cameras would guarantee that the crack initiation is observed regardless of the location
Determination of the crack initiation location	The rough surface of the root makes it hard to predict and control the crack initiation.	A machined-smooth root surface would eliminate the Hi-Lo effect. A small notch introduced in the weld guarantees the crack initiation location.
Numerical modelling of the beadweld	Modelling the beadweld with the same material model neglects different properties of the weld and the HAZ.	An investigation should be done to properly model the properties of HAZ.

Relation to the real-life pipelaying operations	Small-scale specimens were considered, with the released residual stresses that are present in the actual structure after welding.	-

5.   Conclusions

Based on the results and analysis presented and discussed in Chapter 4 the following conclusions can be drawn:

- Plastic straining of the beadweld did not prove to negatively affect the girth weld fatigue performance more than the elastic straining does. A single overstressing that can happen during the pulling on the bead operation will not impair the pipeline girth weld properties related to fatigue resistance more than the currently applied pulling in the elastic regime does. It thus can be recommended to investigate the effect of the plastically strained metal re-melting when the hot pass (and subsequent weld passes) are performed.

- Girth welds that were not subjected to any straining- neither elastic or plastic- and whose welding procedure was not interrupted showed better fatigue resistance than the girth weld with a straining history. Nevertheless, all investigated weld types- strain-free, elastically and plastically strained- show superior fatigue performance when compared to the adequate S-N standard curve, recommended by (DNVGL, 2016) as the benchmark for the weld fatigue assessment.

- The fatigue performance of the girth weld is primarily governed by Hi-Lo and porosity, with the prevailing effect of Hi-Lo. Both of these factors have a negative effect on fatigue lifetime.

- Hi-Lo affects only the initiation phase of the crack growth, with higher values of Hi-Lo having a more deteriorating effect on the initiation phase, hence on the total lifetime.

- Hi-Lo is the most probable location of the crack initiation, especially when located within the weld metal or HAZ.

- The porosity was discovered only in the weld metal and the HAZ. Regardless of the pore sizes, the porosity negatively affected the strength properties of the investigated specimens. The negative impact of pores on the crack growth phase was only present if the pore interfered with the crack path.

- The influence of pores is less profound in plastically strained specimen than in elastically strained ones. Plastic straining interferes with the pores in the metal so that it decreases the influence of pores on fatigue life. It is most likely caused by alternating the local stress state around the pores.

- Despite some extent of the scattered porosity, the microstructure of the base metal, weld metal and HAZ was expected for the given welding procedure.

- Fatigue life of the investigated welds is found not primarily affected by the strength of the metal. It is rather the surface geometry, the weld alignment (assembly) and the porosity that affect the fatigue lifetime the most.

6.   Recommendations

The broad overview of girth weld fatigue performance given in this research provides a good starting point for further research, especially regarding the relationship between plasticity, porosity and material re-melting. The author suggests that a detailed study of a weld and HAZ microstructure evolution in a controlled welding simulation should be done to investigate the effects re-melting and re-heating of the weld regions (X.L. Wang, 2017). A deeper understanding of the microstructure constituents evolution will allow accounting for the re-melting (and re-heating) of previously plastically strained metal. Additionally, a more in-depth microstructure evolution of the porous and pore-free material could be done, to investigate the effect of pores on microstructural changes during multipass welding.

Given the profound effect of Hi-Lo and surface geometry on fatigue life, it may be desirable to conduct a fatigue test on the smooth (or notched) specimen. A fatigue study with smooth specimens (with machined notch) can be done, to eliminate the prevailing Hi-Lo effects for the investigation of solely the straining and porosity influence on the crack growth. The author suggests conducting fatigue test with crack growth rate (da/dN) determination so that the stress concentration range (ΔK) can be characterised in porous and plastically strained welded specimens (for example, as per ASTM E647). It may be especially interesting to investigate the relationship between da/dN and porosity/plasticity above the threshold (K_{th}) regime of the Paris law, as it is believed there is a local plastic zone around the pores (N. Noraphaiphipaksa, 2012), which may affect the situation at the crack tip. Plastic zone size may be then assessed at the crack tip and around the pores and their consolidated effect on the crack growth rate can be characterised.

Even though this research provides a good overview of the topic, a separate investigation of the girth weld material and the welding start and stop positions is recommended in order to enhance its actual industrial application. It should be noted that start/stop positions, being 12, 6 and 10 o'clock locations on the pipe circumference, were excluded from the scope of this study. However, as they are the integral parts of the weld in every pipeline, their fatigue performance should too be characterised for a more complete picture. The author recommends to recreate steps of this research for specimens extracted from these locations, backed up with the heat input data of the welds.
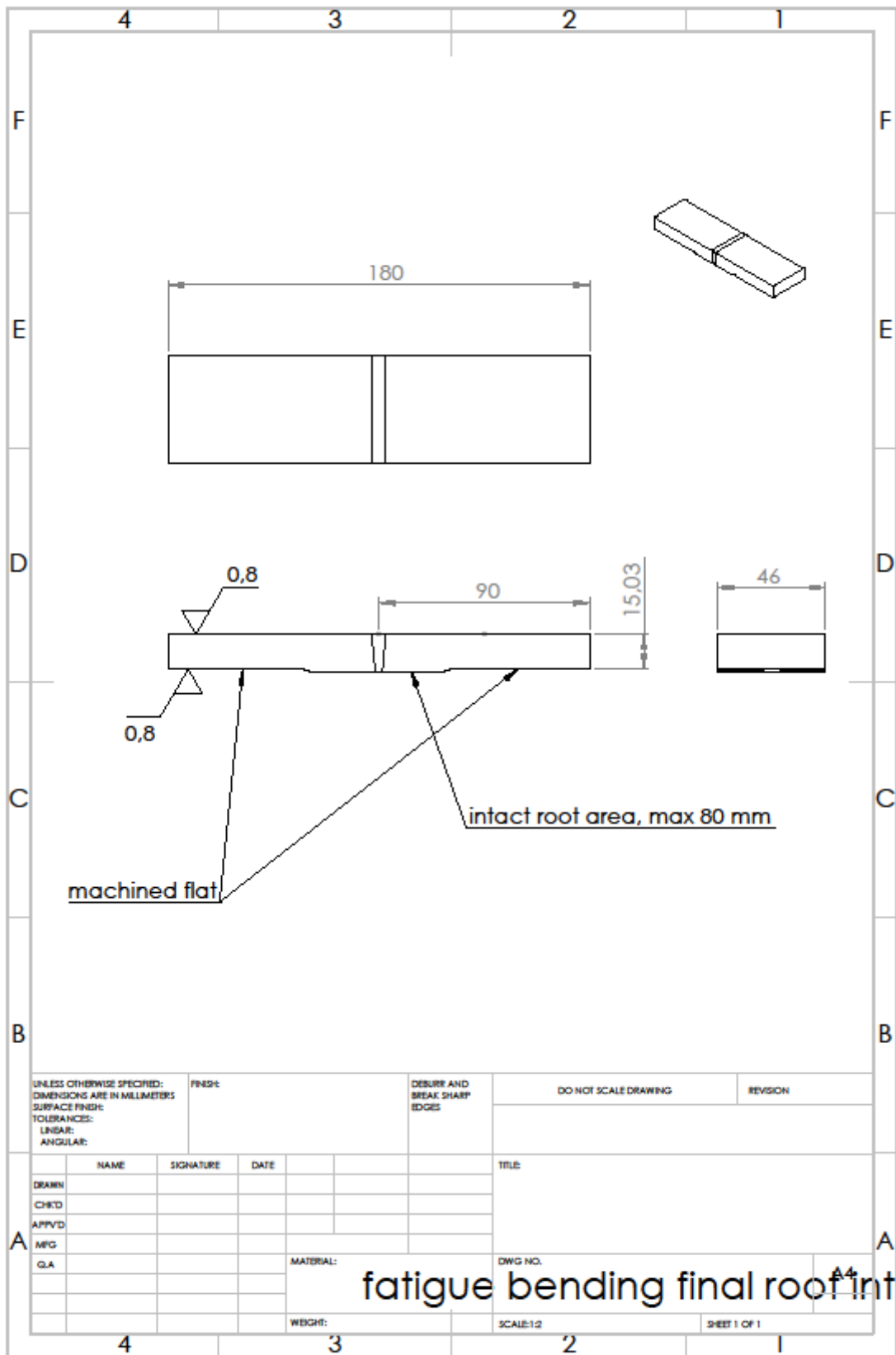
Bibliography

Allseas. (2004). *Introduction to Pipelaying.* Delft: Allseas.

Allseas. (2019, February). Retrieved from Pipeline Installation: https://allseas.com/activities/pipelines-and-subsea/pipeline-installation/

Amiri, A. (2012). *Experimental Investigation of Fatigue Behavior of Carbon Fiber Composites Using Fully Reversed Four Point Bending.*

Ansys 19.0, I. (2017). ANSYS Workbench 19.0. *Release 19.0.*

ANSYS. (2010). *Customer Training Material- ANSYS Mechanical Structural Nonlinearities.* Retrieved from Rate Independent Plasticity.

API. (2018). *API 5L: Specification for Line Pipe.* American Petroleum Institute.

Bäker, J. R. (2007). *Mechanical Behaviour of Engineering Materials.* Berlin: Springer.

Blondeau, R. (2001). *Metallurgy and Mechanics of Welding.* London: ISTE Ltd.

BSI. (2014). *BS 7608: Guide to fatigue design and assessment of steel products.* BSI Standards Limited.

Chang-Kyun Oh, Y.-J. K.-H.-s. (2007, January). Development of stress-modified fracture strain for ductile failure of API X65 steel. *International Jurnal of Fracture.*

Criesfield, M. A. (2000). *Non- Linear Finite Element Analysis of Solids and Structures. Volume 1.* London: John Wiley & Sons.

DNVGL. (2016). *DNV-RP-203C Fatigue design of offshore steel structures.* DNV GL AS.

DNVGL-ST-F101. (2017). *DNVGL.*

Enerpac. (2018, July). Retrieved from https://www.enerpac.com/en-gb/high-tonnage-cylinders/high-tonnage-cylinder/HCR30012

Enerpac. (2018, July). Retrieved from Enerpac: https://www.enerpac.com/en-gb/training/e/basicsystemsetups

Gere, J. M. (2004). *Mechanics of Materials.* Belmont: Brooks/ Cole.

Godefroid L. B., C. L. (2014). Microstructure and Mechanical Properties of Two API Steels for Iron Ore Pipelines. *Materials Research*, pp. 114-120.

H. Kuhn, D. M. (2000). Fatigue Crack Growth Testing. In *ASM Handbook, vol.8: Mechanical Testing and Evaluation* (pp. 740- 757). ASM International.

ISO. (2012). *ISO/TR 14345 Fatigue- Fatigue testing of welded components- Guidance.* ISO.

Karman, S. (2017). *Pulling on the bead overstressed weld performance- fatigue.* Delft: De Haagse Hoogeschool, Allseas.

Krupp, U. (2007). *Fatigue Crack Propagation in Metal Alloys: Microstructural Aspects and Modelling Concepts.* Weinheim: Wiley.

L.M. Conelly, N. Z. (1993). Stress concentration at girth weld of tubulars with axial wall misalignment. *Tubular Structures V* (pp. 309-321). Nottingham: E&FN Spon.

Lippold, J. C. (2015). *Welding Metallurgy and Weldability.* New Jersey: John Wiley & Sons.

Maddox, S. J. (1991). *Fatigue Strength of Welded Structures, 2nd Edition.* Woodhead Publishing.

N. Noraphaiphipaksa, T. P. (2012, July). Interaction of plastic zone, pores, and stress ratio with fatigue crack growth of sintered stainless steel. *International Journal of Fracture.*

N.G. Gokhale, S. B. (2008). *Practical Finite Element Analysis.* Maharashtra: Finite to Infinite.

Nodal versus Elemental Stresses. (2008). Retrieved from Computer Aided Technology: https://www.cati.com/blog/2008/04/nodal-versus-elemental-stresses/

NPTEL. (2018, October). Retrieved from Shear and Flexural Testing: https://nptel.ac.in/courses/101104010/lecture39/39_6.htm

S.-T. Tu, X.-C. Zhang. (2016). *Fatigue Crack Initiation Mechanisms.* Shanghai: Elsevier.

Schijve, J. (2009). *Fatigue of Structures and Materials.* Springer Netherlands.

X.L. Wang, Y. N. (2017). Influence of welding pass on microstructure and toughness in the reheated zone of multi-pass weld metal of 550 MPa offshore engineering steel. *Materials Science & Engineering A*, 196- 205.
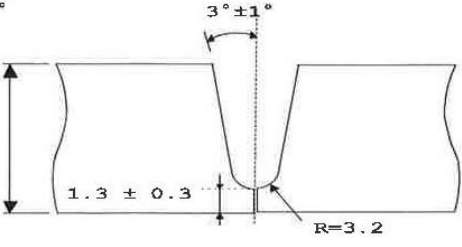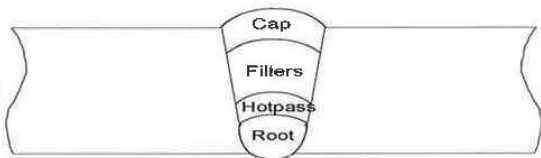
APPENDIX A: Fatigue specimen design

Welding Record

Allseas

Client	:		Sample No	:	EH 24 M1 A (0-180)
Project	:		Description	:	Phoenix GMAW welding procedure
Job No	:				

Pipe O.D.	:	609.6mm (24")	Equipment Type	:	Phoenix System
Wallthickness	:	15.9mm	Welder(s) I.D. No	:	1419
Material Grade	:	SAWL X60 PSL 2	Line-up Method	:	Internal Pneumatic Line-up Clamp
Pipe number(s)	:	DGR00352	Removed after	:	100% completion of first pass
Heat/Charge No	:	412610	Cleaning Method	:	Power wire brushing and/or Grinding

Fit-up

3° ±1°

1.3 ± 0.3   R=3.2

Pass Sequence

Cap
Fillers
Hotpass
Root

Pass No	1	2	3	4	5	6	7 Cap	8 Cap			
Process(es)	GMAW	GMAW	GMAW	GMAW	GMAW	GMAW	GMAW	GMAW			
Test Position	5G	5G	5G	5G	5G	5G	5G	5G			
Travel Direction	Down	Down	Down	Down	Down	Down	Down	Down			
Filler Metal Name	Esab	Esab	Esab	Esab	Esab	Esab	Esab	Esab			
Filler Metal Type	70S-6	70S-6	70S-6	70S-6	70S-6	70S-6	70S-6	70S-6			
Filler Metal Diameter (mm)	1.2	1.2	1.2	1.2	1.2	1.2	1.2	1.2			
AWS Designation	ER70S-6	ER70S-6	ER70S-6	ER70S-6	ER70S-6	ER70S-6	ER70S-6	ER70S-6			
Heat / Batch No	840090	840090	840090	840090	840090	840090	840090	840090			
El./Wire Polarity	Dc +	Dc +	Dc +	Dc +	Dc +	Dc +	Dc +	Dc +			
Shielding Gas	Ar/CO2	Ar/CO2	Ar/CO2	Ar/CO2	Ar/CO2	Ar/CO2	Ar/CO2	Ar/CO2			
Gas Mix (%)	80/20	80/20	80/20	80/20	80/20	80/20	80/20	80/20			
Gas Flow Rate (ltr/min)	30	30	30	30	30	30	30	30			
Starting Time	8.02	8.18	8.24	8.24	8.34	8.34	8.43	8.43			
Finish Time	8.04	8.20	8.26	8.26	8.36	8.36	8.45	8.45			
Start Temperature (°C)	100	130	146	146	211	211	275	275			
Arc Voltage (V)	19.7/19.9	19.7/20.0	19.4/19.8	19.2/19.5	19.5/19.9	19.1/19.7	18.7/19.4	18.6/19.2			
Arc Current (Amp)	272/281	231/255	229/254	235/252	234/255	217/231	215/249	209/237			
Travel Speed (cm/min)	98/103	58/60	49/56	51/56	44/53	46/53	52/78	60/78			
Wire Speed (m/min)	7.4	6.0/6.5	6.0/6.5	6.0/6.5	6.0/6.5	5.0/5.6	5.0/6.2	5.0/6.2			
Osc. Speed (cm/min)	245	125/140	130/145	135/150	140/155	170/180	115/145	115/145			
Osc. Width (mm)	0.3	2.2/2.5	2.4/2.8	2.6/3.1	2.8/3.4	4.0/4.6	2.6/3.7	2.6/3.7			
Dwell Time (sec)	0.00	0.10	0.10	0.10	0.10	0.08	0.02/0.04	0.02/0.04			
Tip/work Distance (mm)	10 - 15	10 - 15	10 - 15	10 - 15	10 - 15	10 - 15	10 - 15	10 - 15			
Heat Input (KJ/mm)	0.31/0.34	0.46/0.53	0.48/0.62	0.48/0.58	0.52/0.69	0.47/0.59	0.31/0.56	0.30/0.46			

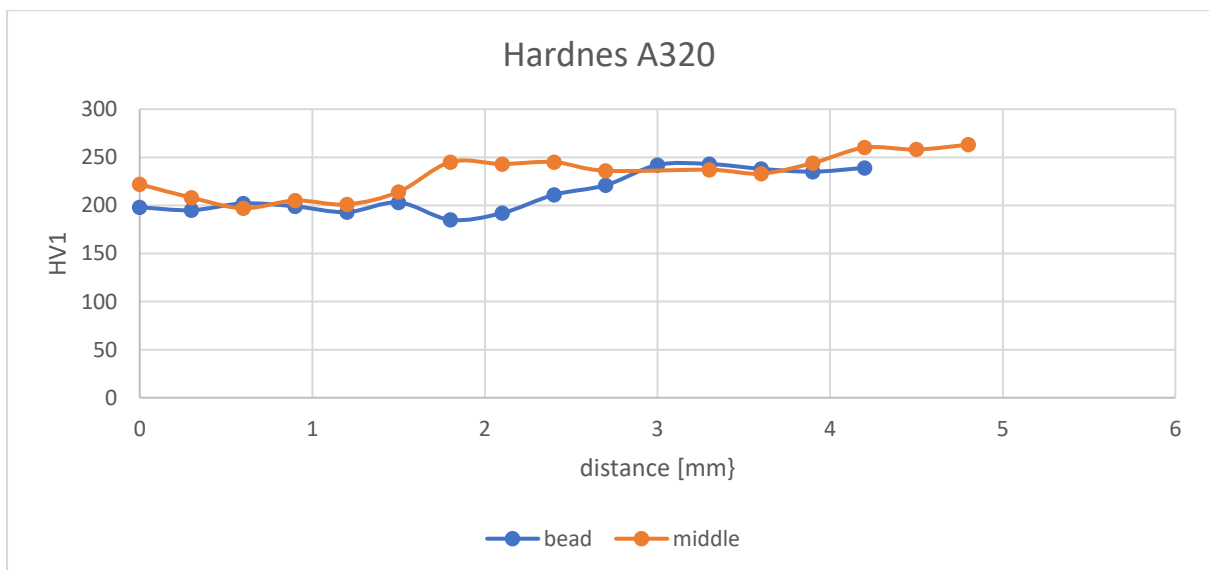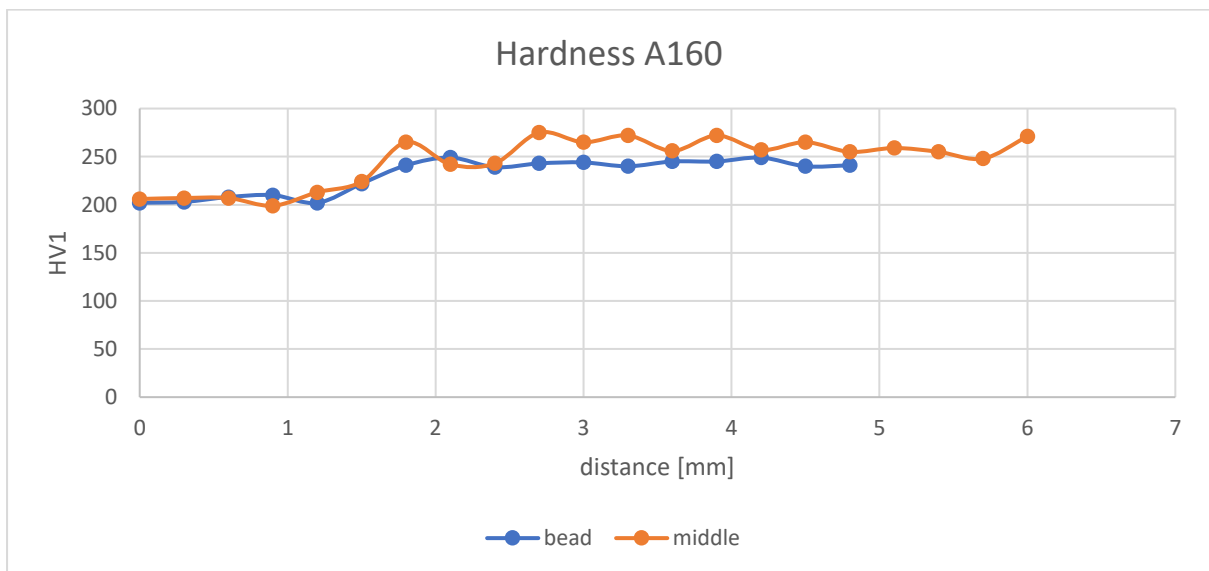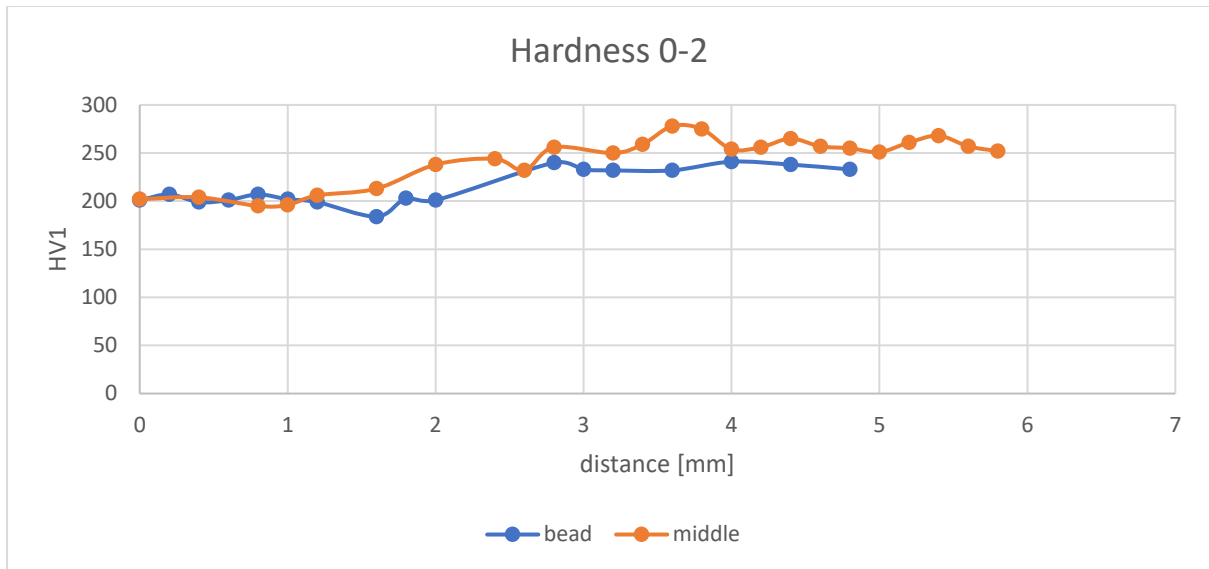| Remarks	ALX unit and Phoenix system display used to record welding parameters
	Preheat by propane torch and temperature control by digital thermometer and Tempil sticks
	Preheat temperatures measured 75mm from bevel and interpass temperatures measured adjacent to the bevel

Allseas		Client		Certifying Authority	
Date	: 03/02/15		05.02.2015		5 Feb 2015

Page 1 of

114

AUT Weld Inspection Report

Allseas

Project:	Over Stressed Root
Client:	Allseas
Project Number:	
Location:	Bright Spark

AUT Procedure Doc No:	N/A
Acceptance Criteria:	DNV-OS-F101
Contractor:	Allseas
Calibration Block:	24 Inch 15.9mm Hebron

Equipment:	Allseas AUT System
Software Version:	V6
Weld Classification:	Welder Training
AUT Location:	Bright Spark

Report Number:	
Report Date:	Friday, 24 August 2018
Shift:	07:00-19:00
Page No:	1 OF 1

Wall Thickness	Diameter		Material Grade	Bevel Prep	Welding Process	Welding Position
15.9mm	24 (Inch)	1915 (mm) (Constant ID)	N/A	J3 / Calibration Frequency 1/1	GMAW	5G

Weld Number	Result		DEFECT CLASIFICATON				UT ZONE		LOCATION (mm)					Comments
	ACCEPT	REJECT	Linear	Transverse	Volumetric	Ident.	Label	Weld Side	Start	End	Length	Depth	Height	Wall Thickness
A2-0001	✓				VI	P	V2_D	DownSteam	242	243	1	10,0	1,0	15,9
	✓				VI	P	V2_D	DownSteam	306	312	6	11,4	1,0	
	✓				VI	P	V2_D	DownSteam	666	667	1	10,6	<1,0	Small Intermittant gaspores from 628 to 680
B-0002	✓				VI	P	V2_D	DownSteam	297	298	1	9,1	1,0	
	✓				VI	P	V2_D	DownSteam	386	387	1	10,9	<1,0	
	✓				VI	P	V2_D	DownSteam	630	631	1	9,8	<1,0	
	✓				VI	P	V2_D	DownSteam	1251	1252	1	9,2	1,0	
C-0001	✓				VI	P	V2_U	UpStream	303	305	2	7,5	1,0	
	✓				VI	P	V2_U	UpStream	1251	1252	1	8,8	1,0	
O-0001	✓				VI	P	V2_D	UpStream	1204	1205	1	10,0	1,0	
TOTALS	10													

Terms and Abbreviations

IF - Incomplete Fusion	LCP - Inadequate Cross Penetration	P - Porosity	HB - Horrow Bead	LS-Linear Surface	VI - Volumetric Individual
IFD - Incomplete Fusion Due to Cold Lap	ESI - Elongation Slag Inclusion	CP - Cluster Porosity	IC - Internal Concavity	LB - Linear Buried	VC - Volumetric Cluster
IP - Incomplete Penetration	ISI - Isolated Slag Inclusion	EU - External Undercut	Cu - Copper	T- Transverse	VR - Volumetric Root
IPD - Incomplete Penetration Due to High Low	BT - Burn Through	IU - Internal Undercut	C - Crack		

Operator:	Nick Stannard	**QC:**		**QC**	**Client:**		Client
UT Certification	PCN Lv II	Affiliation		Allseas QA / QC	Affiliation		
Signature		Signature			Signature		

APPENDIX D: Overview of fatigue specimens

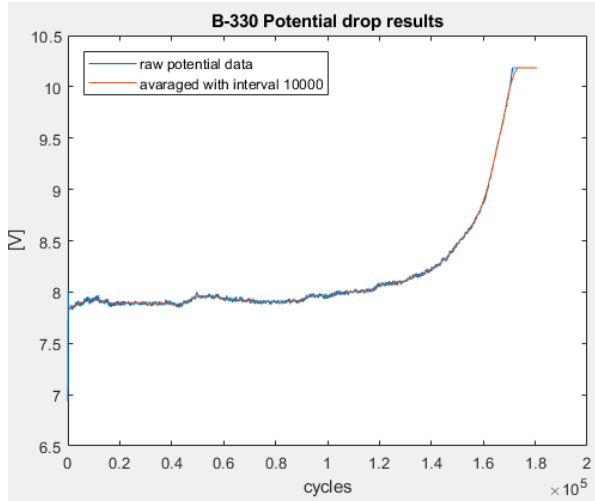|	Specimen	Cycles to failure Nf	[h]	Hi-Lo [mm]	cracked at	initiation phase Optical [% lifetime]	PD [% lifetime]
1	0-280	3,05E+05	05:38	0,42	weld	X	50%
2	0-270	4,23E+05	07:50	0,39	weld	X	46%
3	0-260	3,14E+05	05:49	0,44	weld	X	X
4	0-100	3,29E+05	06:05	0,58	both	X	59%
5	0-1	8,47E+05	15:40	0,4	weld	76%	59%
6	0-2	3,24E+05	06:00	0,88	weld	24%	x
7	0-3	5,66E+05	10:28	0,4	base	60%	57%
8	A-20	3,06E+05	05:40	0,33	base	93%	62%
9	A-40	1,51E+05	02:47	0,87	base	52%	57%
10	A-320	6,91E+05	12:48	0,32	both	70%	63%
11	B-30	7,00E+05	12:57	0,32	weld	X	63%
12	B-40	6,35E+05	11:45	0,48	weld	X	63%
13	B-320	1,80E+05	02:50	1,15	base	X	48%
14	B-330	1,81E+05	03:20	1,03	base	44%	65%
15	B-340	1,82E+05	03:22	0,52	base	38%	50%
16	extra A	1,36E+05	02:30	0,83	base	77%	70%
17	A-140	2,91E+05	05:23	0,17	weld	X	x
18	A-150	3,18E+05	05:53	0,38	weld	65%	x
19	A-160	2,83E+05	05:14	0,42	base	78%	73%
20	A-200	3,71E+05	06:52	0,55	base	75%	x
21	A-210	4,42E+05	08:10	0,48	weld	85%	x
22	A-220	3,87E+05	07:10	0,2	base	x	74%
23	B-240	2,74E+05	05:04	0,53	weld	37%	x
24	B-70	4,10E+05	07:35	0,25	weld	67%	75%
25	B-120	2,33E+05	04:18	0,46	weld	48%	x
26	B-110	1,95E+05	03:36	0,48	weld	35%	x
27	B-250	4,24E+05	07:51	0,26	weld	70%	52%
28	C-270	1,80E+05	03:20	0,77	base	70%	80%
29	C-100	6,34E+05	11:44	0,21	weld	x	x
30	C-260	1,95E+05	03:37	0,76	base	21%	64%
31	C-280	1,64E+05	03:02	0,72	weld	66%	40%
32	C-80	2,75E+05	05:05	0,52	base	84%	63%
33	A-90	2,78E+05	05:09	0,1	weld	78%	59%
34	A-100	3,76E+05	06:58	0,15	weld	90%	70%
35	A-260	3,51E+05	06:30	0,16	base	92%	74%
36	A-270	3,23E+05	05:58	0,14	weld	29%	32%
37	A-280	4,22E+05	07:48	0,5	base	78%	85%
38	A-80	4,42E+05	08:10	0,47	weld	X	52%

Hardness 0-2

Hardness A160

Hardnes A320

Hardness B240

Hardness C100
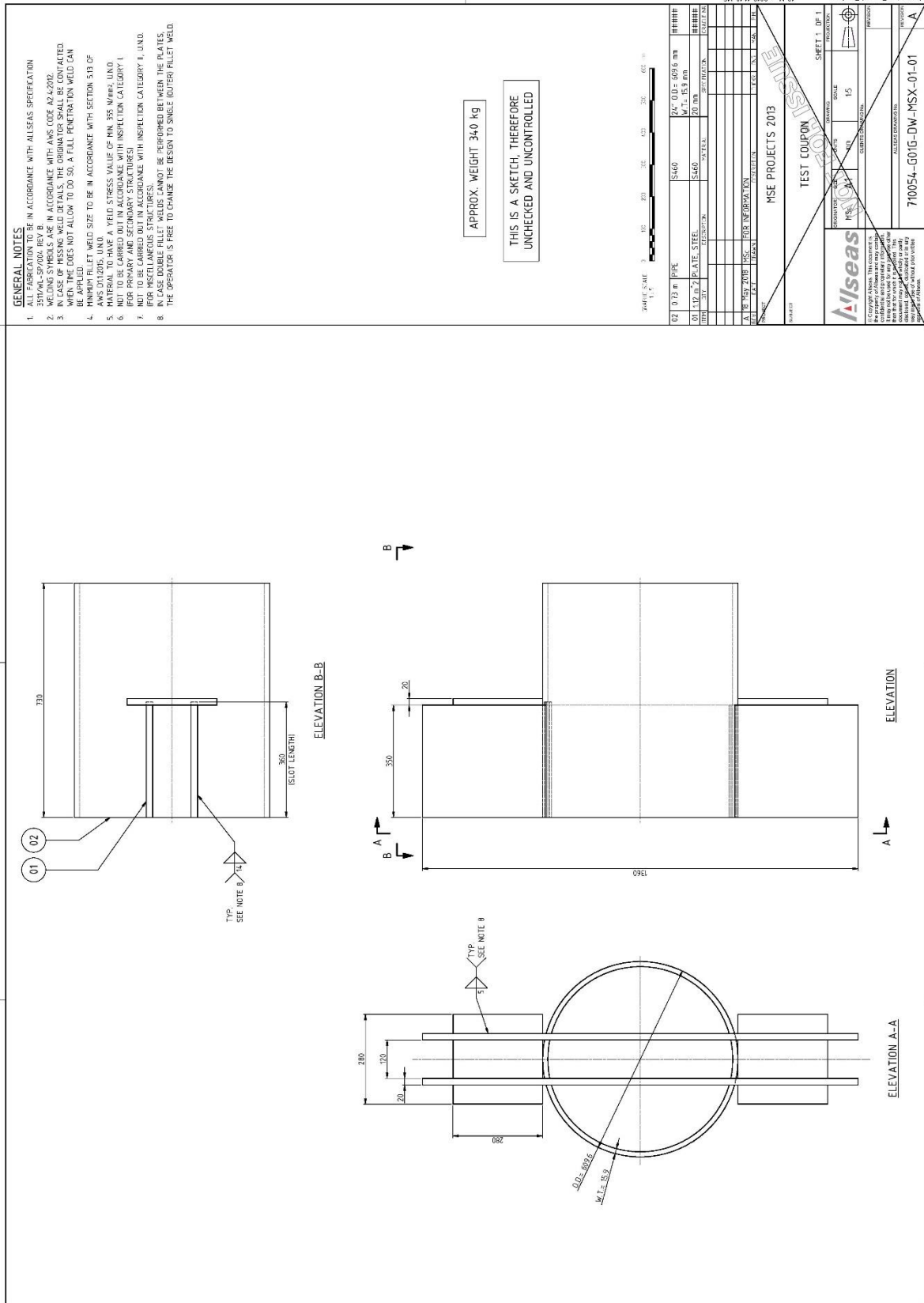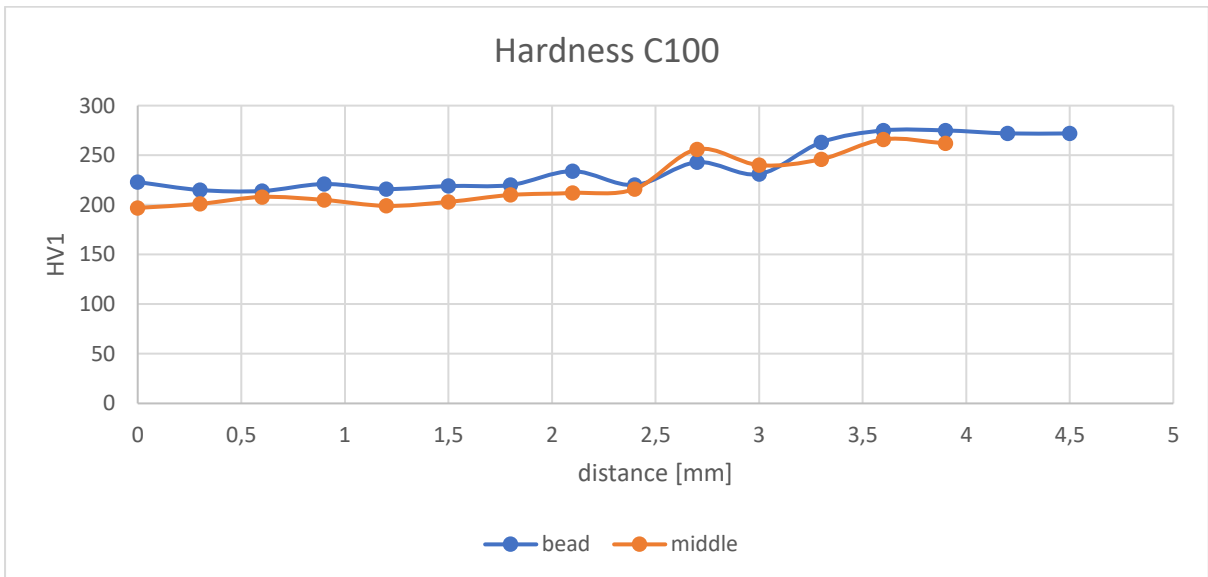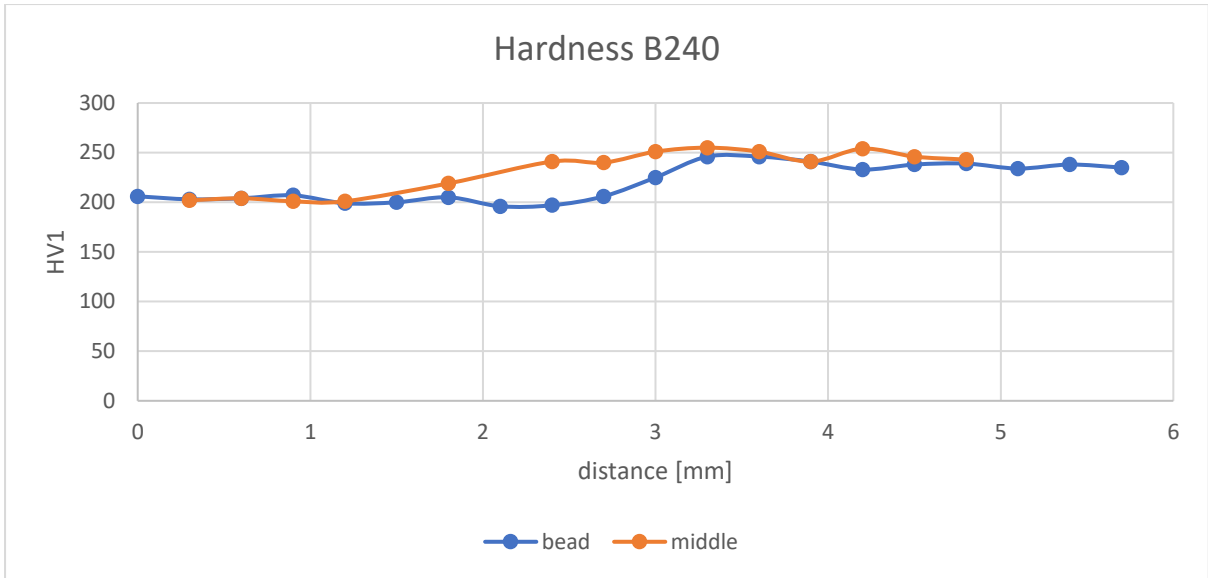
APPENDIX G: PD measurement results

B-40 Potential drop results

B-70 Potential drop results

B-110 Potential drop results

B-240 Potential drop results

B-250 Potential drop cyclic results

B-320 Potential drop results
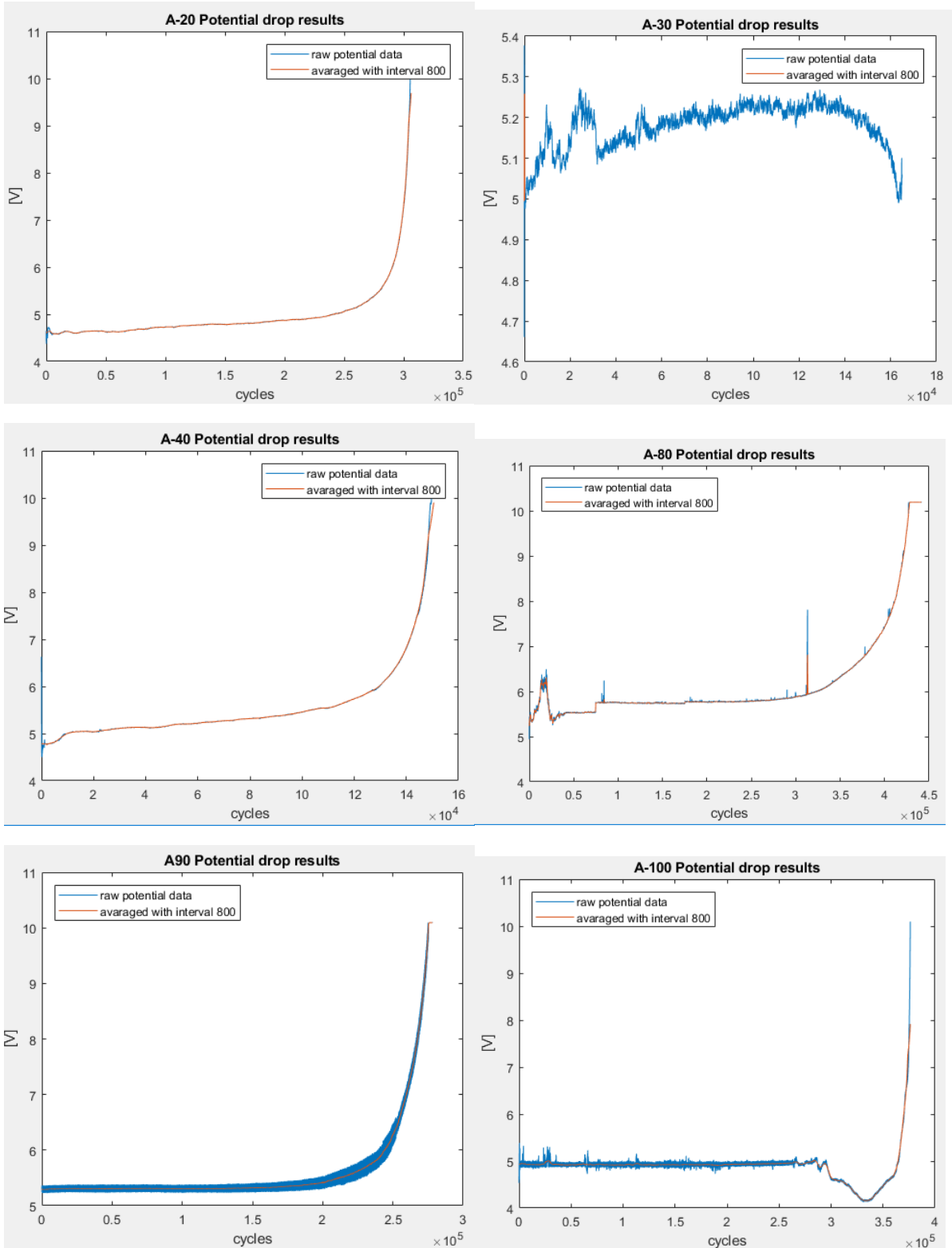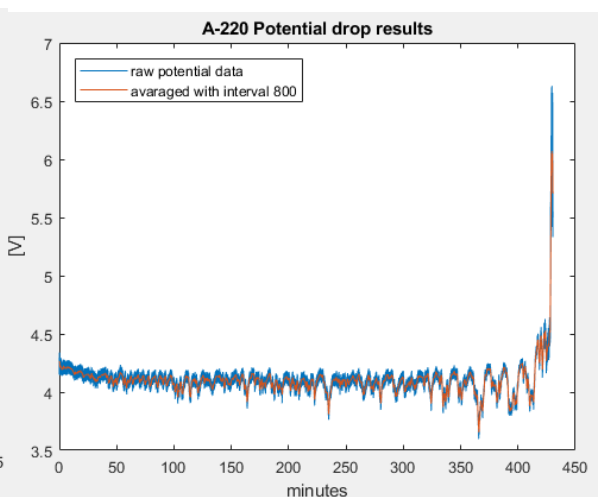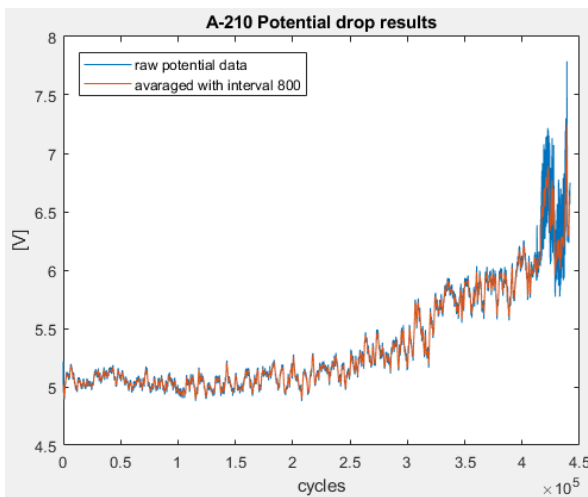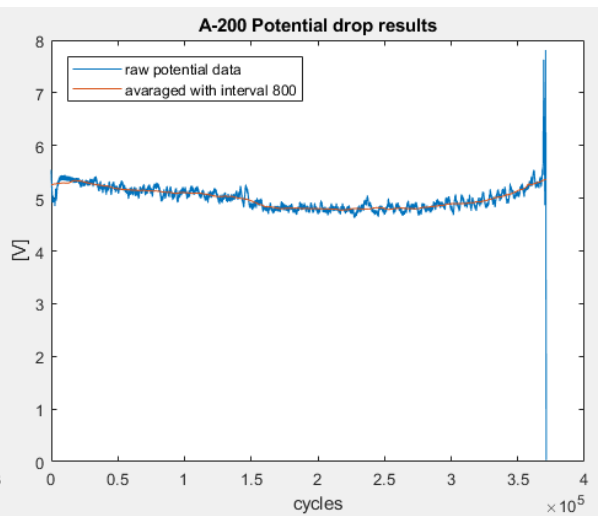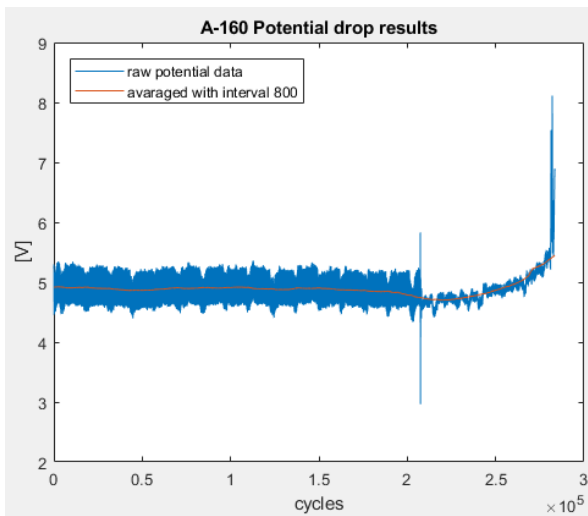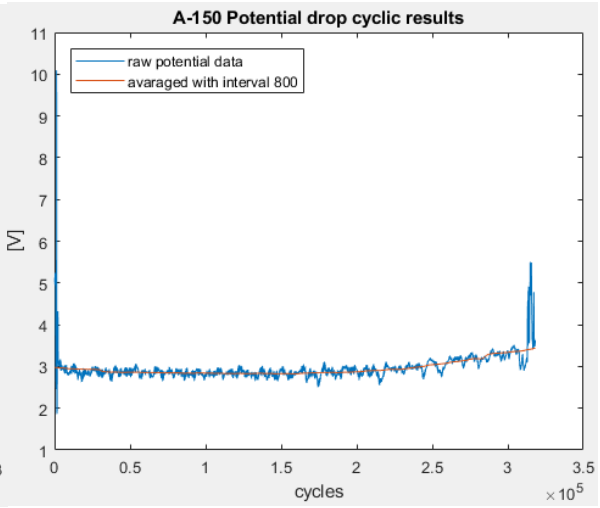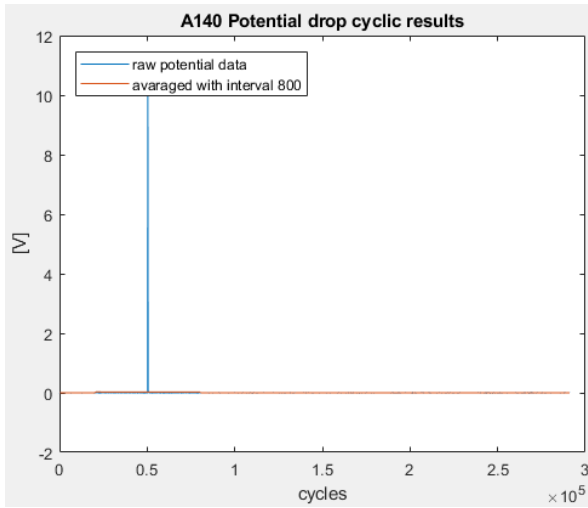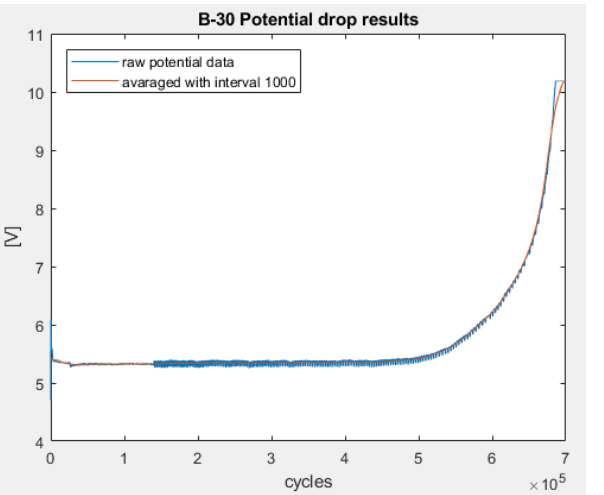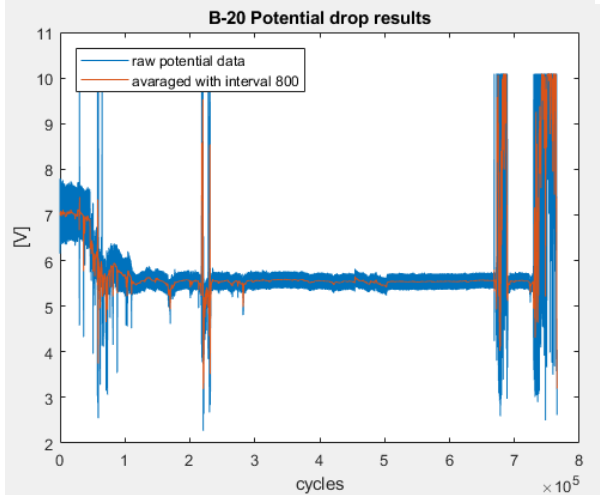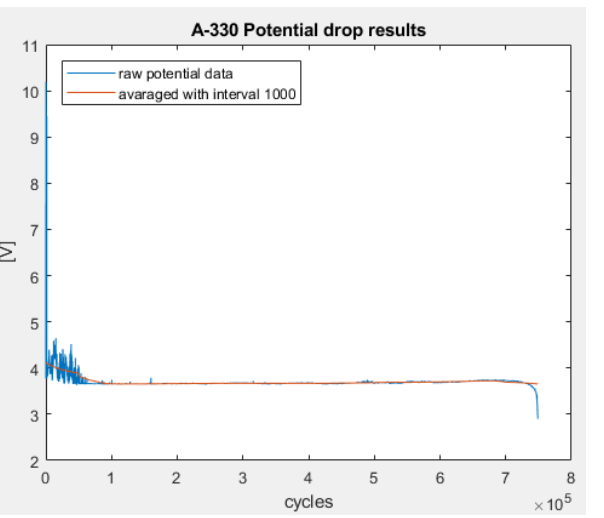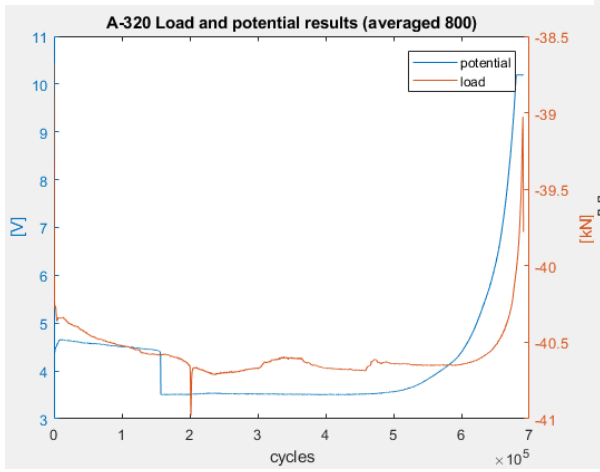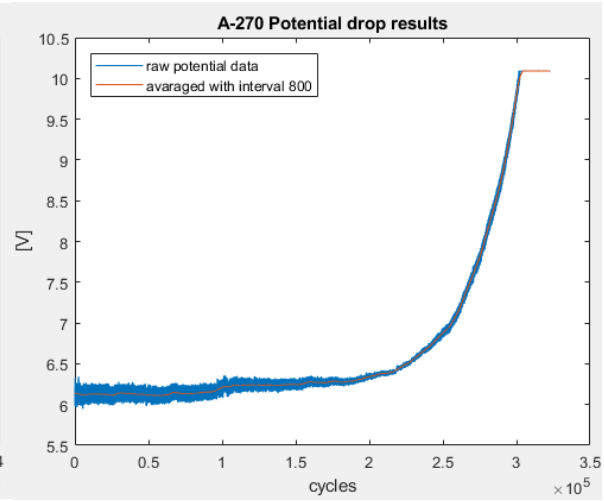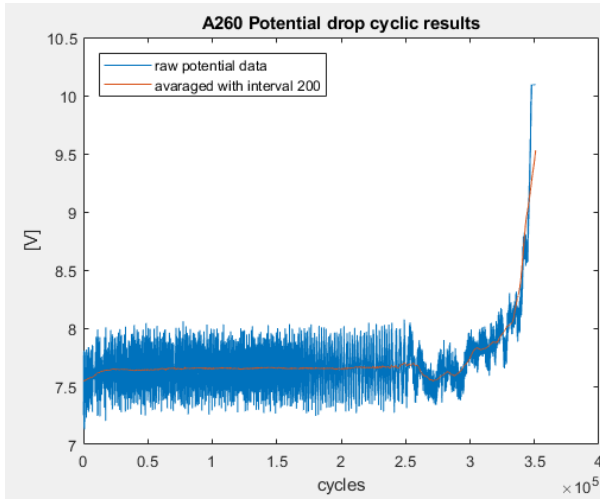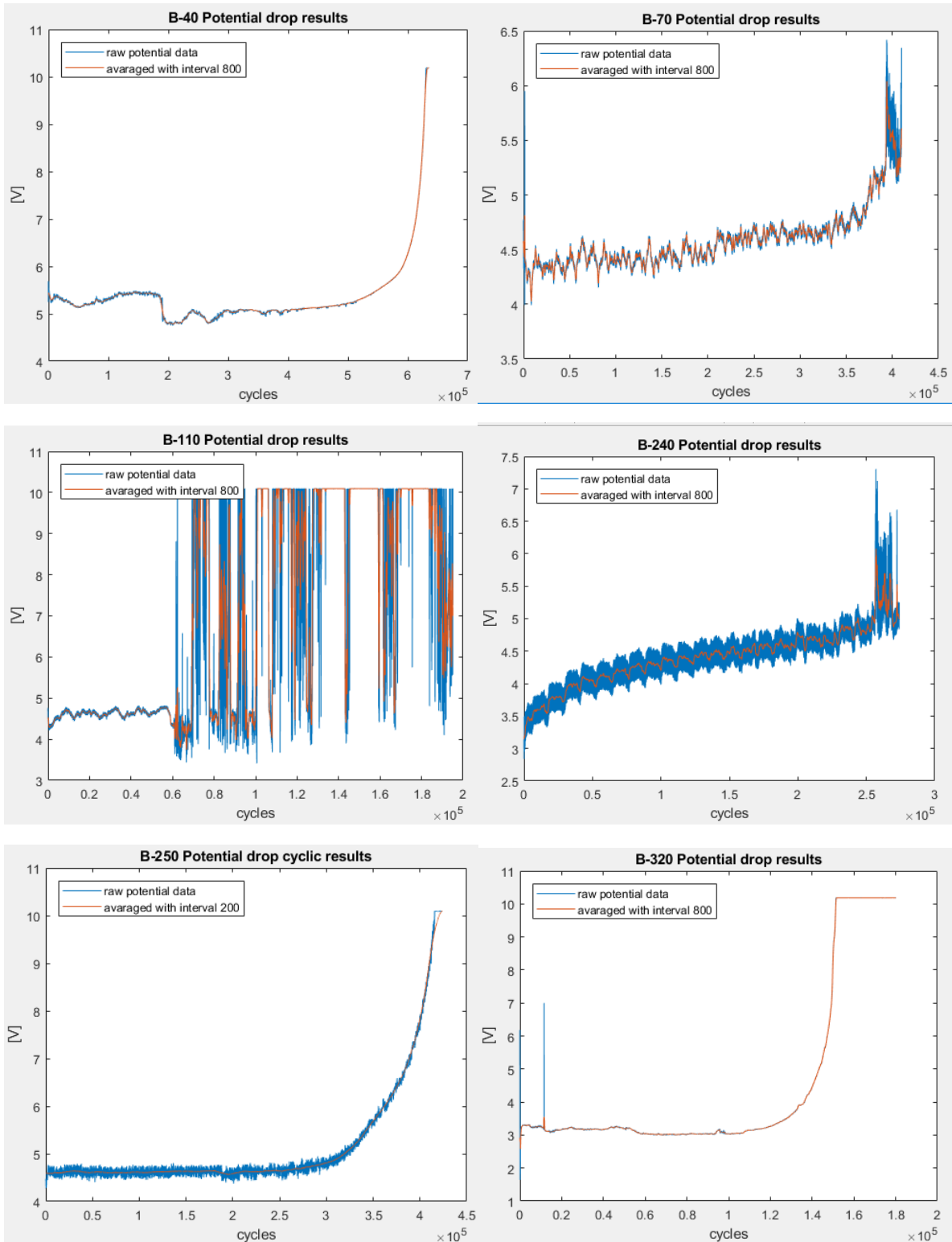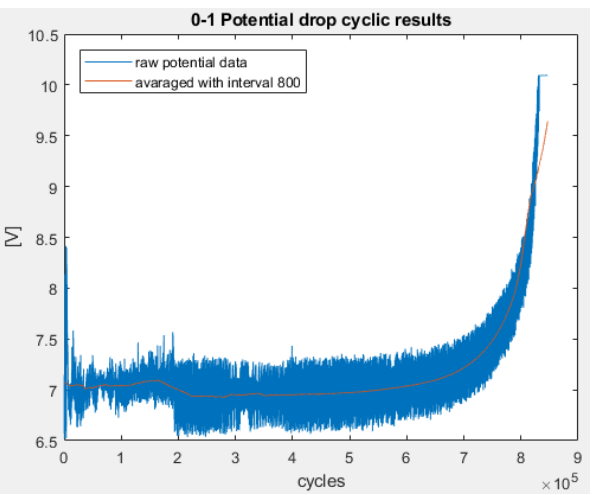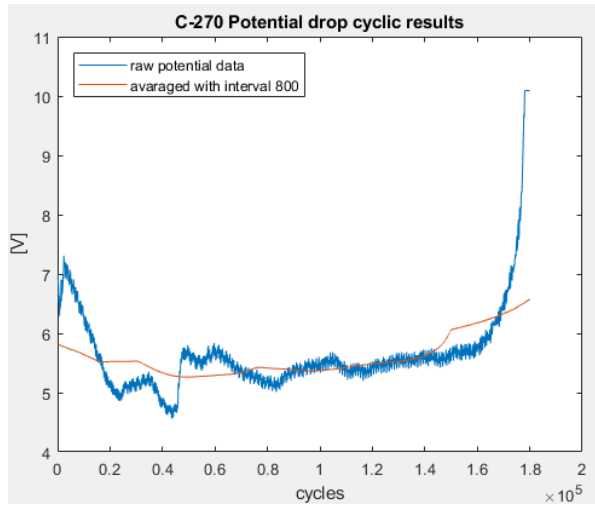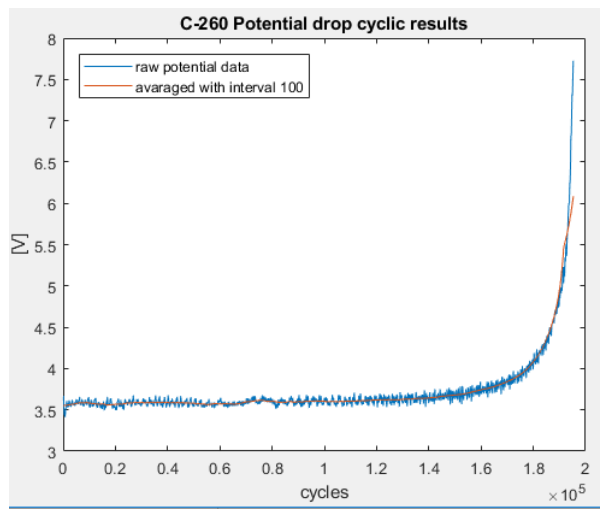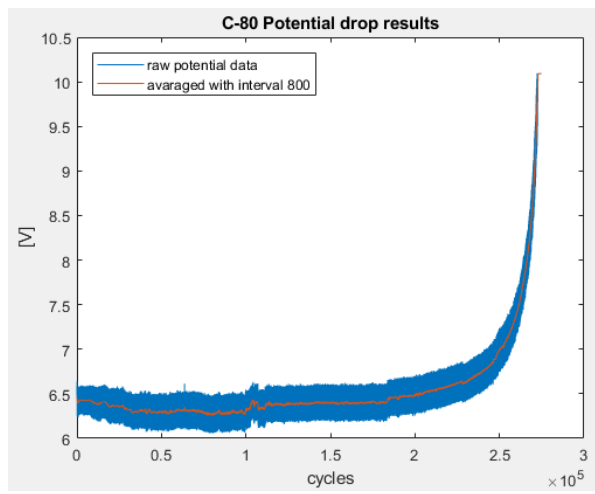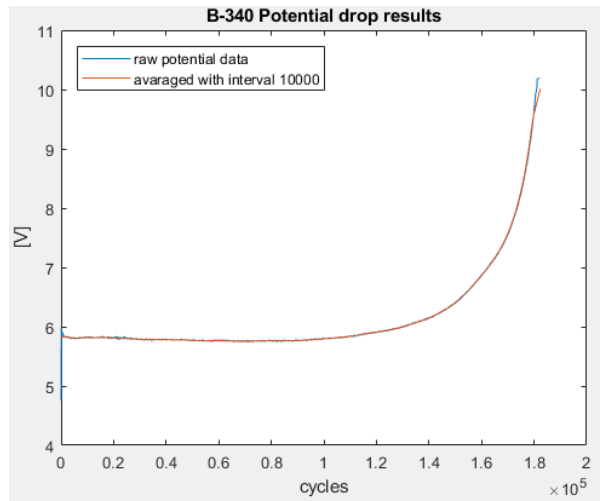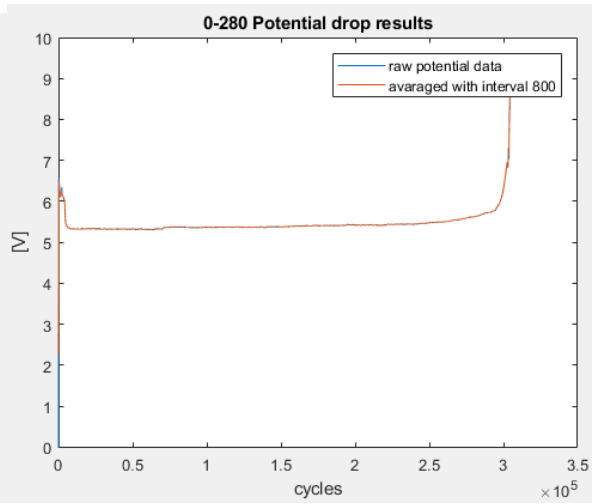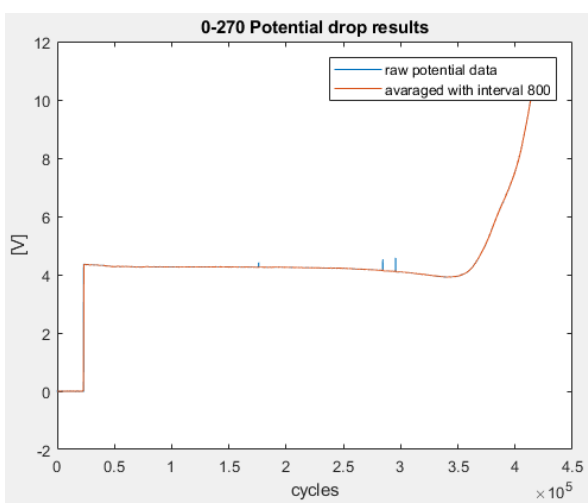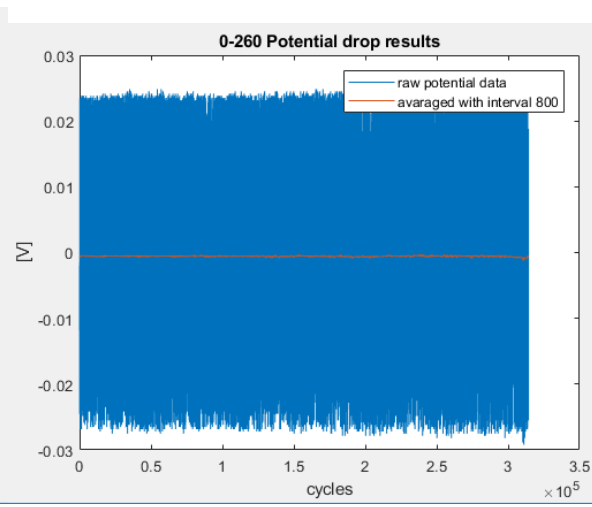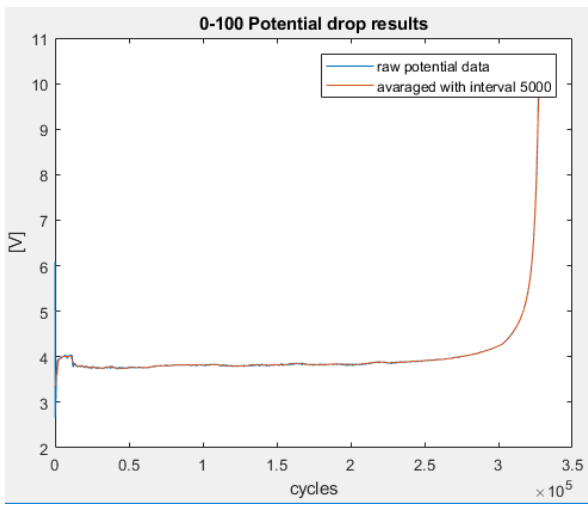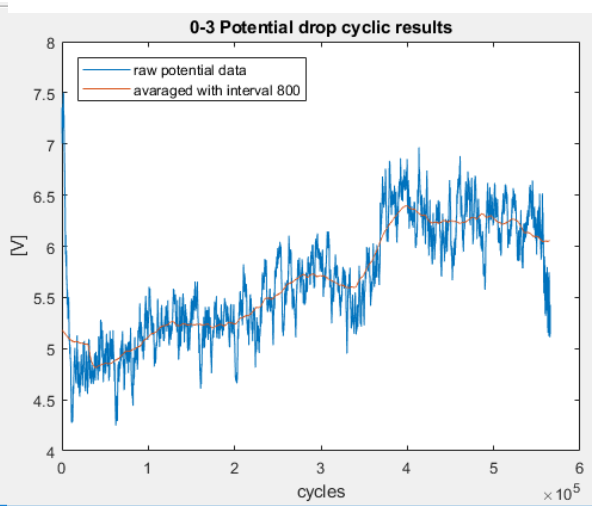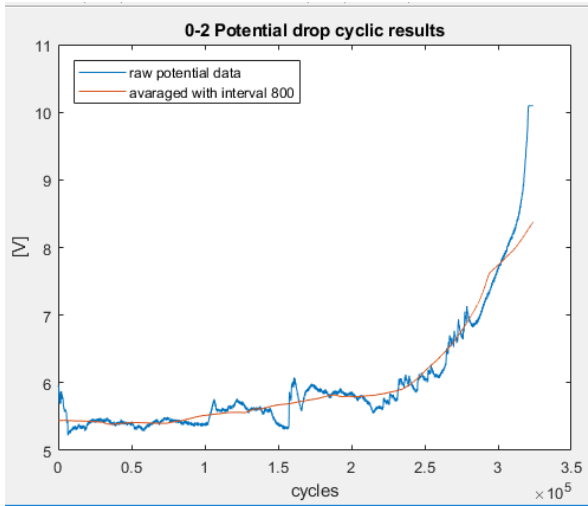
APPENDIX H: Tensile testing results

Specimen 0-1

Specimen 0-2

specimen E1

specimen E2

specimen E3

specimen P1

Specimen P2

Specimen P3

specimen P4
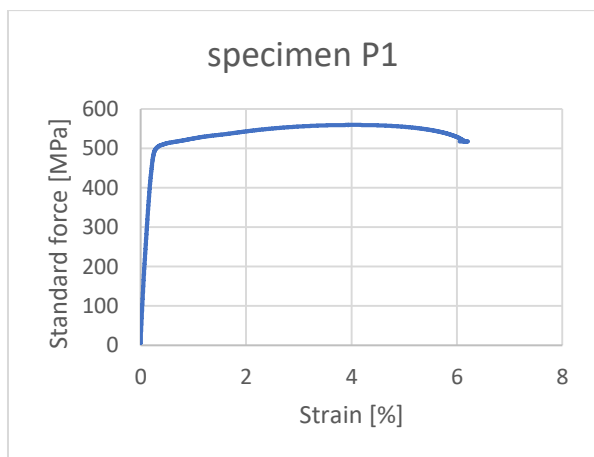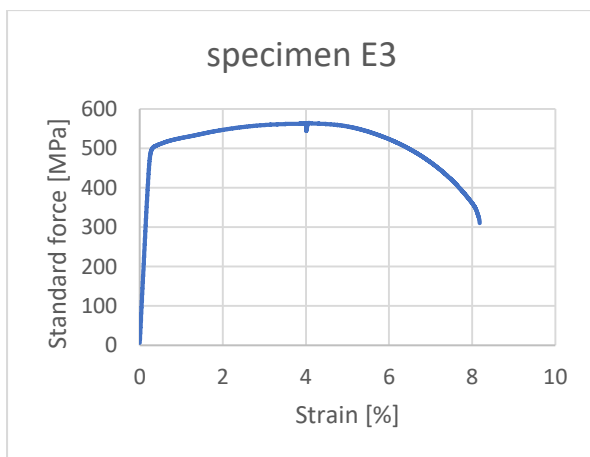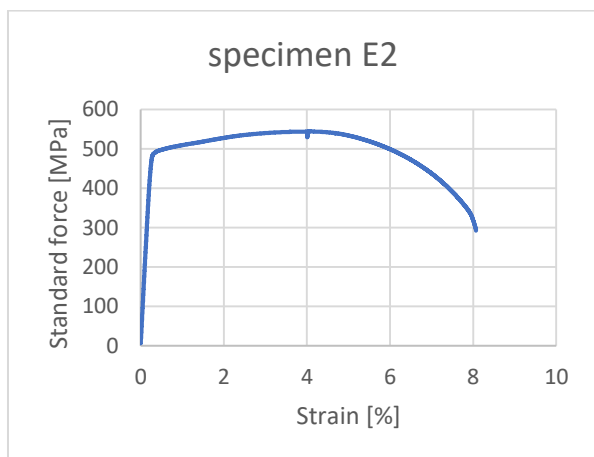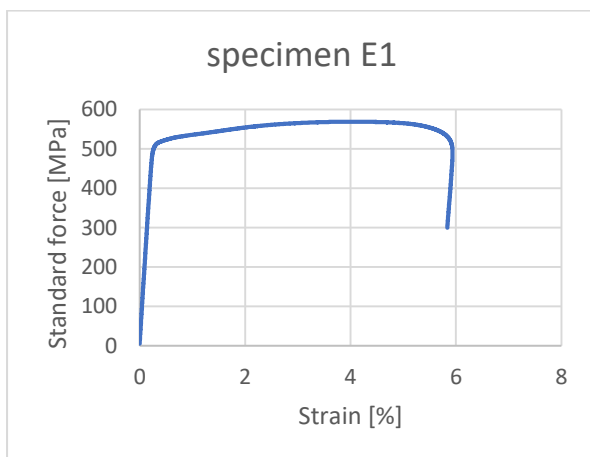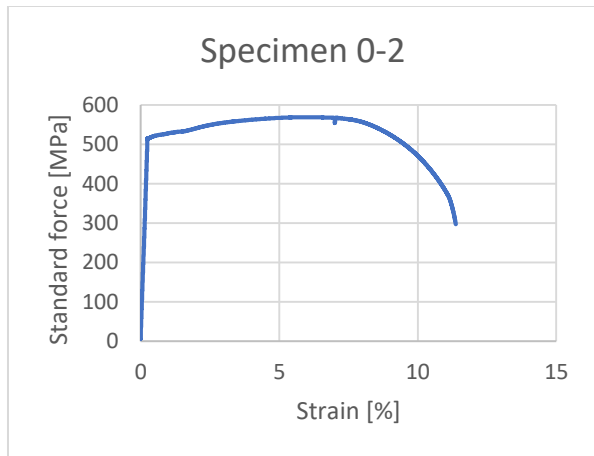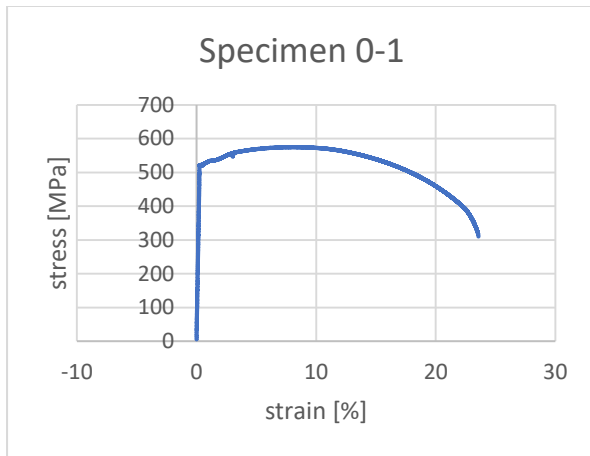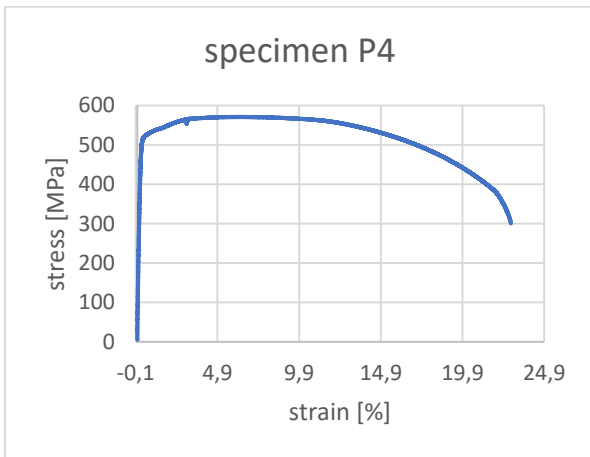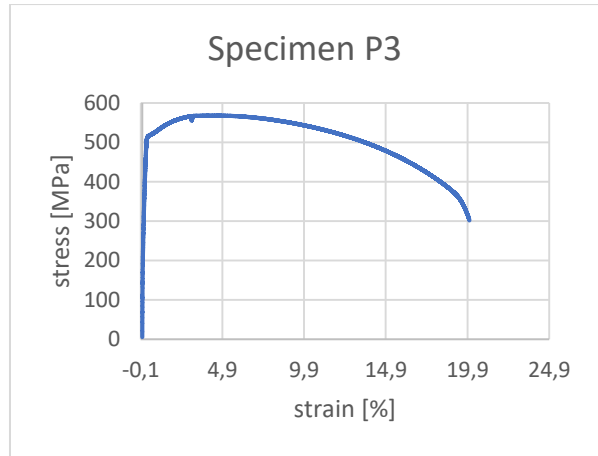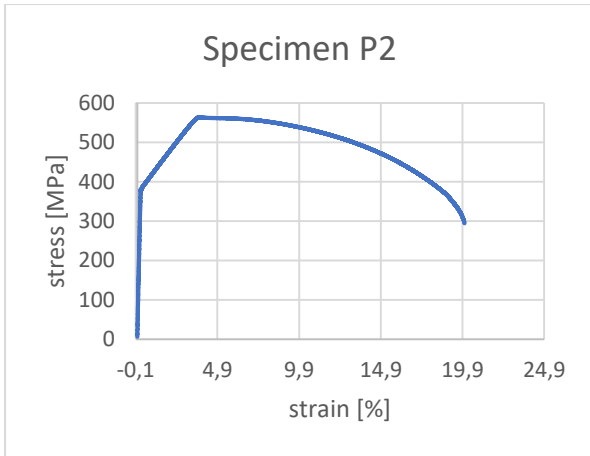
APPENDIX I: Engineering and true stress-strain relationship

Part of the engineering-true curve conversion table. The yield point $R_{p0,2}$ is marked with yellow and the true UTS (end of the true stress-strain curve) is highlighted in orange. True stress and true plastic strain columns (source of input material model for FEA) are marked in blue.

ENGINEERING						TRUE				
Test time	Strain	Strain	Plastic strain	Stress	Nominal strain	True Strain	True Strain	True Stress	Elastic Strain	Plastic Strain
[s]	%	[-]	[-]	MPa	%	[%]	[-]	[Mpa]	[-]	[-]
given	given	Strain/100	Strain-(Stress/E)	given	given	True strain * 100	ln(1+Strain)	Stress (1+Strain)	True Stress/E	True Strain - Elastic Strain
0,00	0,00000	0,00000	-0,00003	5,68	0,00000	0,00000	0,00000	5,68	0,00003	-0,00003
0,02	0,00000	0,00000	-0,00003	5,68	0,00000	0,00000	0,00000	5,68	0,00003	-0,00003
0,04	0,00000	0,00000	-0,00003	5,68	0,00000	0,00000	0,00000	5,68	0,00003	-0,00003
0,06	0,00000	0,00000	-0,00003	5,68	0,00000	0,00000	0,00000	5,68	0,00003	-0,00003
0,08	0,00000	0,00000	-0,00003	5,68	0,00000	0,00000	0,00000	5,68	0,00003	-0,00003
0,10	0,00000	0,00000	-0,00003	5,68	-0,00001	0,00000	0,00000	5,68	0,00003	-0,00003
0,12	0,00000	0,00000	-0,00003	5,68	-0,00001	0,00000	0,00000	5,68	0,00003	-0,00003
148,66	0,49050	0,00490	0,00235	522,90	3,69918	0,48930	0,00489	525,46	0,00256	0,00233
148,68	0,49200	0,00492	0,00237	522,91	3,69968	0,49079	0,00491	525,48	0,00256	0,00234
148,70	0,49400	0,00494	0,00239	522,92	3,70020	0,49278	0,00493	525,50	0,00256	0,00236
148,72	0,49600	0,00496	0,00241	522,91	3,70073	0,49477	0,00495	525,51	0,00256	0,00238
148,74	0,49850	0,00498	0,00243	522,90	3,70128	0,49726	0,00497	525,51	0,00256	0,00241
148,76	0,50150	0,00501	0,00246	522,87	3,70179	0,50025	0,00500	525,50	0,00256	0,00244
148,78	0,50399	0,00504	0,00249	522,84	3,70230	0,50273	0,00503	525,48	0,00256	0,00246
148,80	0,50650	0,00506	0,00251	522,80	3,70278	0,50522	0,00505	525,45	0,00256	0,00249
148,82	0,50900	0,00509	0,00254	522,77	3,70325	0,50770	0,00508	525,43	0,00256	0,00251
148,84	0,51150	0,00511	0,00257	522,73	3,70373	0,51020	0,00510	525,40	0,00256	0,00254
148,86	0,51400	0,00514	0,00259	522,69	3,70419	0,51268	0,00513	525,38	0,00256	0,00256
274,79	6,05750	0,06057	0,05778	573,20	6,33060	5,88112	0,05881	607,92	0,00297	0,05585
274,81	6,05802	0,06058	0,05778	573,25	6,33113	5,88161	0,05882	607,98	0,00297	0,05585
274,83	6,05854	0,06059	0,05779	573,29	6,33164	5,88210	0,05882	608,02	0,00297	0,05586
274,85	6,05901	0,06059	0,05779	573,32	6,33212	5,88255	0,05883	608,06	0,00297	0,05586
274,87	6,05953	0,06060	0,05780	573,35	6,33263	5,88303	0,05883	608,09	0,00297	0,05586
274,89	6,06002	0,06060	0,05780	573,37	6,33312	5,88349	0,05883	608,11	0,00297	0,05587
274,91	6,06052	0,06061	0,05781	573,38	6,33362	5,88397	0,05884	608,13	0,00297	0,05587
274,93	6,06102	0,06061	0,05781	573,40	6,33412	5,88444	0,05884	608,15	0,00297	0,05588
274,95	6,06153	0,06062	0,05782	573,41	6,33464	5,88492	0,05885	608,17	0,00297	0,05588
274,97	6,06202	0,06062	0,05782	573,42	6,33513	5,88539	0,05885	608,18	0,00297	0,05589
274,99	6,06253	0,06063	0,05783	573,43	6,33563	5,88586	0,05886	608,19	0,00297	0,05589

Figure I. Zoom-in view of the specimen Ex-A, presenting the arch-like features along the weld root. Crack growth direction marked with the blue arrow.
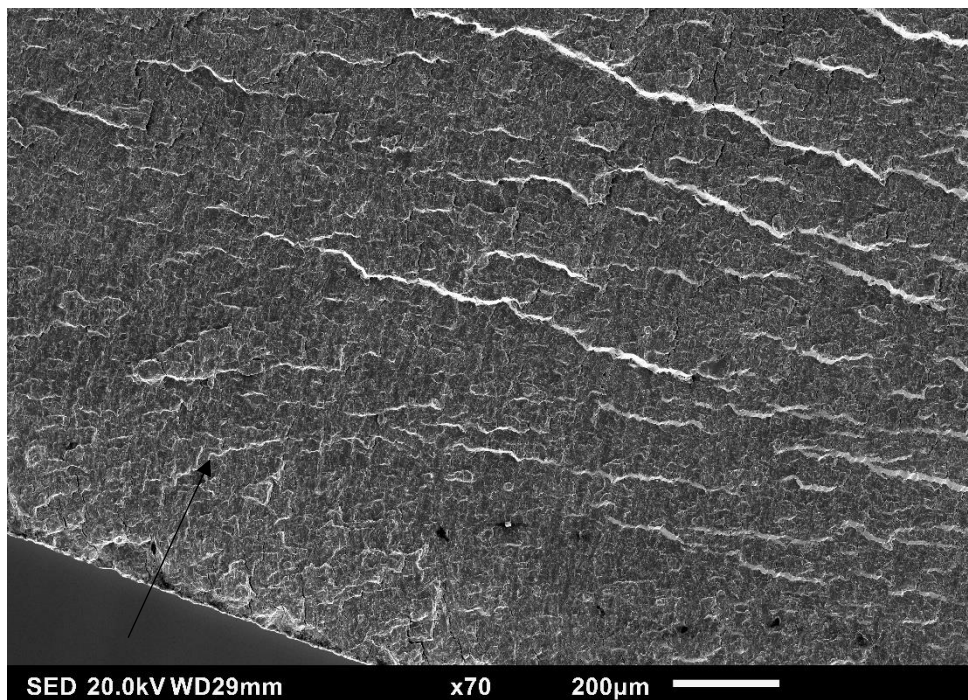

Figure II. SEM image of the A-270 fracture surface at the root weld edge. The direction of the crack growth is marked with the arrow.
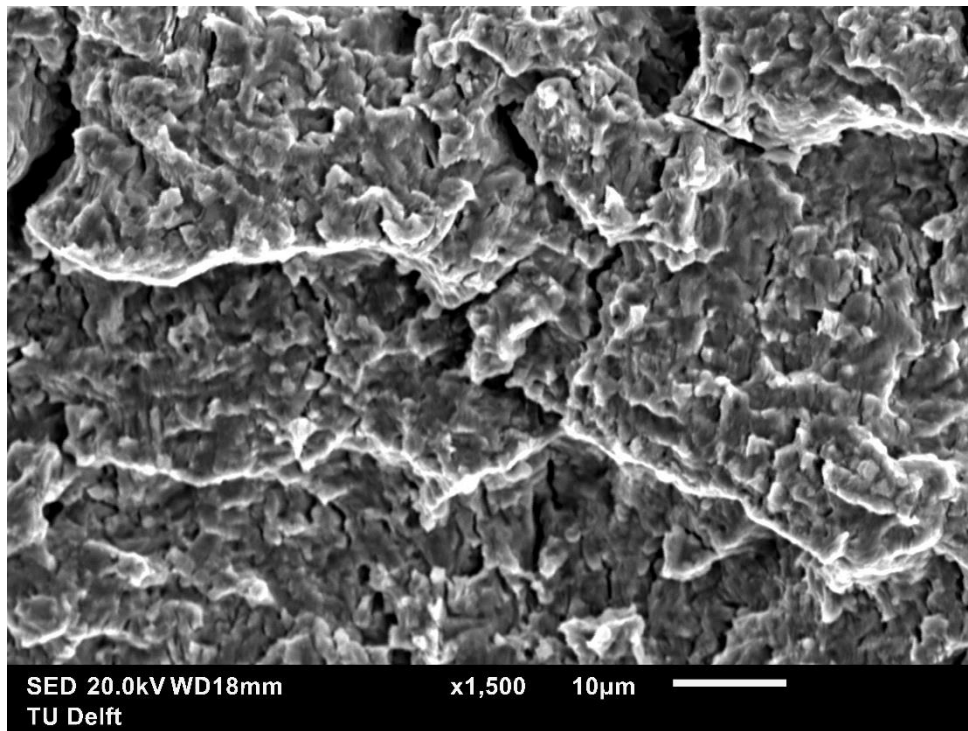
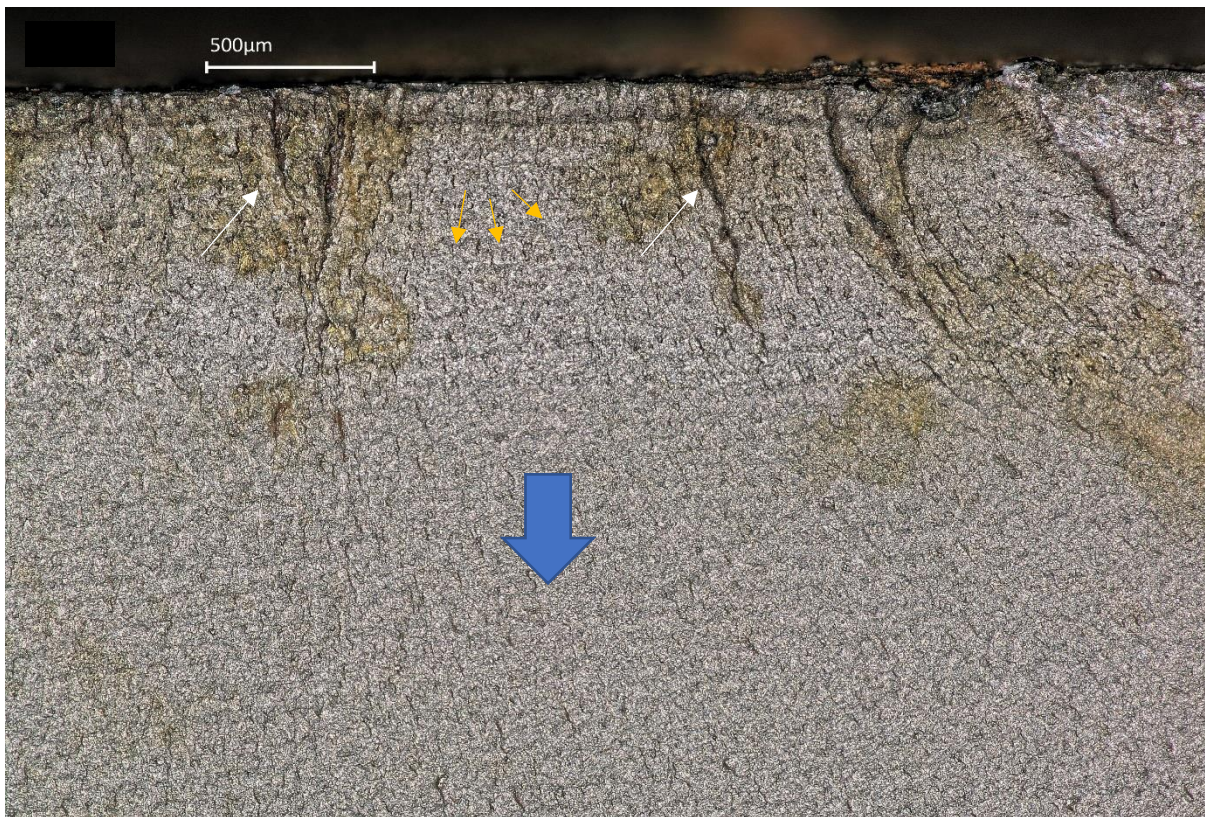Figure III. SEM image of the specimen A-270 fracture surface, magnification x1500.

Figure IV. Weld root of specimen A-270. Ratchet marks and beach marks are visible. Crack growth direction is marked with the blue arrow. Ratchet marks are marked with the white arrows, beach marks- with the yellow ones.
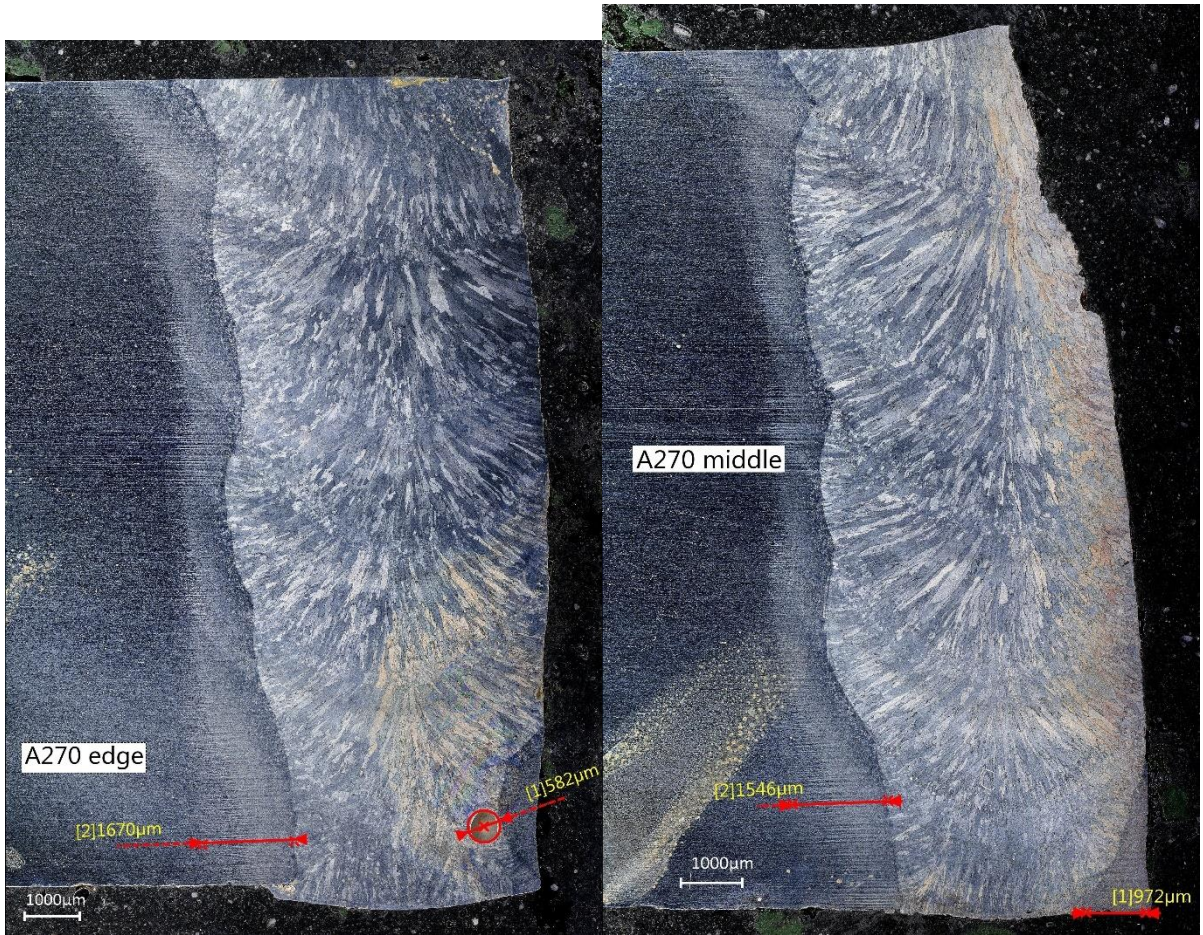
Figure V. Macrographs of the specimen A-270 full weld, view from the edge (left) and middle (right) planes.
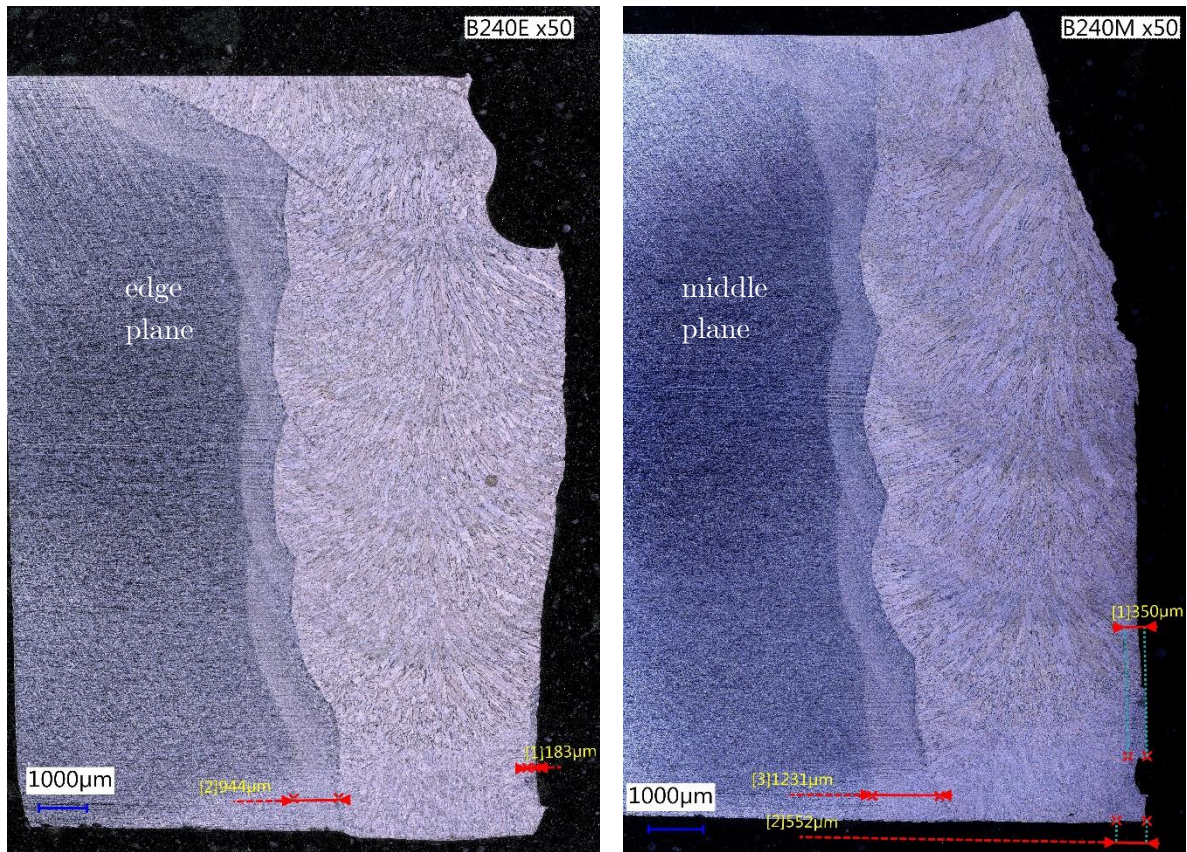
Figure VI. Overview of the full weld microstructure, views from the edge and middle plane of the specimen
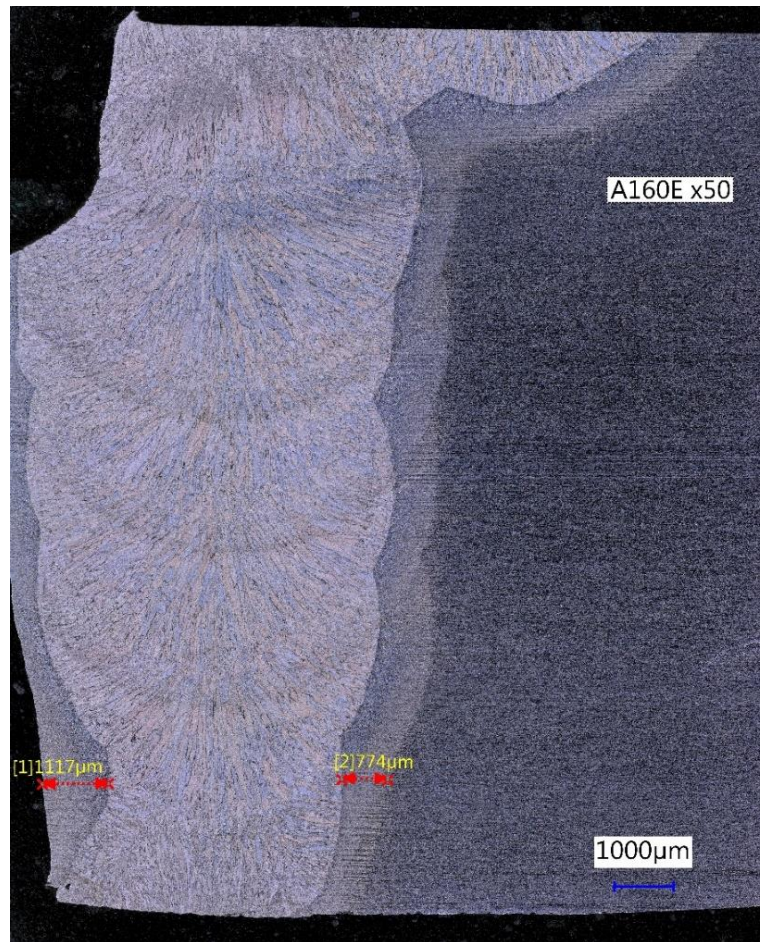
Figure VII. Weld microstructure overview of the specimen A-160. Edge plane view is presented.
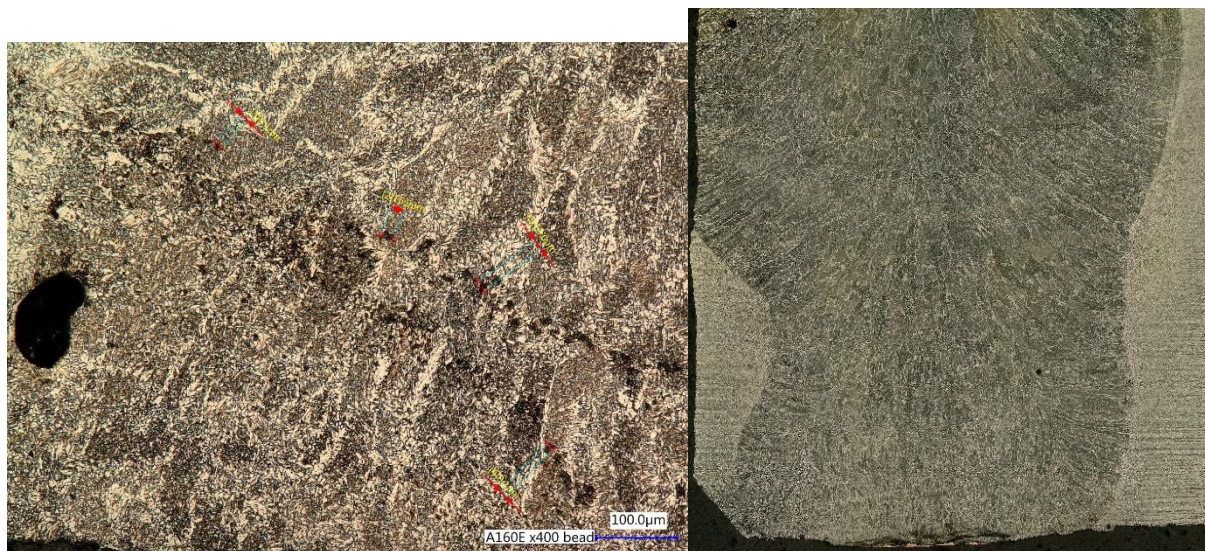

Figure VIII.1 Zoom-in the beadweld microstructure on the edge (left) and middle (right) plane. Magnification x400.